

©Copyright 2023

Spencer Wallace

Planetary Accretion Beyond the Solar System: An Application  
to Systems of Tightly-Packed Inner Planets

Spencer Wallace

A dissertation  
submitted in partial fulfillment of the  
requirements for the degree of

Doctor of Philosophy

University of Washington

2023

Reading Committee:

Thomas Quinn, Chair

Rory Barnes

Eric Agol

Program Authorized to Offer Degree:

Astronomy

University of Washington

## **Abstract**

Planetary Accretion Beyond the Solar System: An Application to Systems of  
Tightly-Packed Inner Planets

Spencer Wallace

Chair of the Supervisory Committee:

Chair Thomas Quinn  
Department of Chair

This sample dissertation is an aid to students who are attempting to format their theses with L<sup>A</sup>T<sub>E</sub>X, a sophisticated text formatter widely used by mathematicians and scientists everywhere.

- It describes the use of a specialized macro package developed specifically for thesis production at the University. The macros customize L<sup>A</sup>T<sub>E</sub>X for the correct thesis style, allowing the student to concentrate on the substance of his or her text.<sup>1</sup>
- It demonstrates the solutions to a variety of formatting challenges found in thesis production.
- It serves as a template for a real dissertation.

---

<sup>1</sup>See Appendix A to obtain the source to this thesis and the class file.

## TABLE OF CONTENTS

	Page
List of Figures . . . . .	iii
Chapter 1: Introduction . . . . .	1
Chapter 2: Formation of Planetary Embryos in the Inner Solar System . . . . .	2
2.1 Introduction . . . . .	2
2.2 Simulations . . . . .	6
2.3 Results . . . . .	12
2.4 Dynamical Friction and Resolution . . . . .	18
2.5 Implications of Simplifying Assumptions . . . . .	33
2.6 Dependence on Initial Planetesimal Mass . . . . .	39
2.7 Summary and Discussion . . . . .	41
2.8 Appendix A: Mean Motion Resonance Test . . . . .	44
2.9 Appendix B: Tree Approximation and Opening Angle . . . . .	46
Chapter 3: Detecting Cold Jupiters via Collisional Grinding of Planetesimals . . . . .	50
3.1 Introduction . . . . .	50
3.2 Overview of Relevant Dynamics . . . . .	52
3.3 Simulations . . . . .	56
3.4 Results . . . . .	62
3.5 Where Does the Dust End Up? . . . . .	65
3.6 Constraining the Mass and Eccentricity of the Planet . . . . .	77
3.7 Summary and Conclusions . . . . .	82
3.8 Appendix A: Timescale for Secular Forcing . . . . .	84
3.9 Appendix B: Libration in Mean Motion Resonance . . . . .	85
3.10 Appendix C: Nonaxisymmetric Structure in Boley 2017 . . . . .	86

Chapter 4: Formation of Planetary Embryos at Short Orbital Periods . . . . .	89
4.1 Introduction . . . . .	89
4.2 Overview of Planetesimal Accretion . . . . .	92
4.3 Numerical Methods . . . . .	98
4.4 Narrow Annulus Simulations . . . . .	100
4.5 Full Disk Simulation . . . . .	104
4.6 Simplifying Assumptions . . . . .	121
4.7 Summary and Discussion . . . . .	126
4.8 Appendix A: Robustness of Timestepping Scheme . . . . .	129
Chapter 5: In-Situ Formation of STIPs . . . . .	132
5.1 Introduction . . . . .	132
5.2 Simulations . . . . .	134
5.3 Results . . . . .	139
5.4 Comparison With Typical Planet Formation ICs . . . . .	144
5.5 Training a Neural Network to Synthesize ICs . . . . .	152
5.6 Summary and Discussion . . . . .	166
Bibliography . . . . .	169
Appendix A: Where to find the files . . . . .	186

## LIST OF FIGURES

Figure Number	Page
2.1 Evolution of the maximum (solid curve) and mean (dashed curve) planetesimal mass in the $N=4000$ and $N=10^6$ particle simulations. At early times, the maximum mass grows more quickly than the mean mass, which is indicative of runaway growth. After a few thousand years, the separation between the curves becomes a constant factor, signalling the start of oligarchic growth. . . . .	9
2.2 Snapshots from the low and high resolution models in the $a - e$ plane. On the left, the light dots represent individual planetesimals, while the contours on the right hand plots represent curves of constant number density. The contour levels are the same between all panels and correspond to $7.8 \times 10^6$ , $1.6 \times 10^7$ , $2.3 \times 10^7$ , and $3.1 \times 10^7$ planetesimals per AU per unit eccentricity. The black circles denote the configuration of the 6 largest bodies in the simulation, with the area of the circles scaled to the mass of the body. The horizontal error bars are scaled to 5 times the Hill radius of the bodies. . . . . . . . . . .	10
2.3 Cumulative number of bodies in each mass bin for the low and high resolution runs, shown at the end of runaway growth (top row) and the end of the simulation (bottom row). The dashed line indicates a slope of -1.5, which is characteristic of runaway growth. . . . . . . . . . .	11
2.4 The rms eccentricity (top) and planetesimal surface density at each mass (bottom) shown for the $N = 4000$ and $N = 10^6$ simulations. The blue points correspond to the quantities at the end of the runaway growth phase (when the mass distribution deviates from a single power law) and the orange points are from the end of the simulations ( $T = 20,000$ years). The vertical dashed lines indicate the value of $M_{stir}$ during that snapshot. . . . . . . . . . .	15
2.5 The average spacing in semi-major axis as a function of mass at the end of the high resolution growth simulation (black points). The gray regions indicate the libration width of planetesimals in each mass bin that are in resonance with the most massive oligarch. The light gray region corresponds to the libration width of the 65:64 (highest non-overlapping) resonance and the dark gray region corresponds to the 15:14 (most distant populated) resonance. . . . .	19

2.6	The cumulative fraction of bodies as a function of mass in the wide (solid dark curve) and narrow (gray curve) high resolution growth simulations. Decreasing the annulus width, which depopulates resonances, produces a less prominent $10^{22}$ g bump. . . . .	23
2.7	The mean scattering time-scale for embryo-embryo (blue curve) and planetesimal-embryo (orange curve) interactions over the course of the high resolution growth simulation. The dashed lines correspond to the simulation time-scale (upper) and longest relevant mean motion resonance time-scale (lower), which is set by the 65:64 resonance. . . . .	25
2.8	Number density profiles of the planetesimals at the end of the $e_{hi}$ (left) and $e_{narrow}$ simulations (right). The blue curves represent the number density of planetesimals less massive than the resonance heating mass ( $2 \times 10^{22}$ g) and the orange curves represent the number density of planetesimals above this mass. The green curves show the surface number density of planetesimals randomly drawn from the low mass bin, such that the total number of bodies matches that of the high mass bin. The vertical lines indicate the positions of first order mean motion resonances with an embryo at 1 AU. . . . .	27
2.9	Time evolution of the eccentricity of the oligarch in the $e_{hi}$ (solid), $e_{narrow}$ (dotted) and $e_{low}$ (dashed) simulation. . . . .	31
2.10	The change in the resonant argument for the oligarch and planetesimals near the 15:14 MMR over a 50 year time interval from the $e_{hi}$ simulation. The solid vertical line designates the nominal resonance location and the dashed vertical lines indicate the minimum libration width. The diagonal blue lines represent the change in $\phi$ due to the Keplerian shear of the disc, which is calculated analytically. . . . .	34
2.11	The cumulative mass distribution of planetesimals at the end of the three high-resolution growth simulations. The vertical lines represent the mass at which the planetesimal spacing in semi major axis falls below the libration width of the MMRs. . . . .	40
2.12	A comparison between the cumulative number of objects in our high resolution growth simulation (black curve) and the present day asteroid belt [19] (gray curve) as a function of size and mass. . . . .	43
2.13	The evolution of the planetesimal in the complex plane defined by equation 2.24. Each point represents the state of the system when the perturber and planetesimal are at opposition. . . . .	47

2.14 Time evolution of the eccentricity of the oligarch (left) and rms eccentricity of the smallest planetesimals (right) in the $e_{hi}$ simulation with an opening angle $\Theta_{BH}$ of 0.7 (solid line) and 0.35 (dashed line). The dotted line shows $\Theta_{BH} = 0.7$ with a timestep that is half as large. . . . .	48
3.1 The positions of the remaining planetesimals at the end of the e1m2 (left), e2m2 (center) and e3m2 (right) simulations. The red dot indicates the position of the giant planet, and the dashed line points in the direction of the planet's longitude of perihelion. Non-axisymmetric gaps are apparent near the locations of MMRs. At higher eccentricities, more resonances become visible. At the 2:1 MMR, gap features at $\theta = 0$ and $\theta = \pi$ follow the giant planet in its orbit. . . . .	57
3.2 The semimajor axes and eccentricities of the remaining planetesimals are shown, with the locations of prominent resonances indicated by the vertical dashed lines. Libration of the critical angle drives large variations in eccentricity, which produce spikes in the a-e plane. Between the resonances, the nonzero eccentricity is due to secular forcing by the planet. . . . .	61
3.3 Shown here are the longitudes of pericenter and semimajor axes of the remaining planetesimals. The dashed lines again indicate the locations of prominent MMRs. Close to the resonances, the critical angle librates and drives fast precession of the longitudes of pericenter of the bodies. This overpowers the secular forcing by the planet and effectively randomizes the orientations of their orbits. . . . .	62
3.4 A PDF of the collision rate in each disc as a function of semimajor axis, generated using a KDE with a Gaussian kernel with a FWHM of 0.02 au. In semimajor axis space, prominent features appear near the 3:1 and 2:1 MMRs. Near the 3:1, the collision rate exhibits a local minimum, while an enhancement appears near the 2:1. . . . .	66
3.5 The collision rate (given by equation 3.6) of bodies in the vicinity of the 3:1 (left) and 2:1 (right) MMRs, relative to the minimum value, as a function of the local eccentricity dispersion. The pairs of points connected by lines show the values of the unperturbed (left-hand points in each subplot) and perturbed (right-hand points in each subplot) collision rates in the e1m2, e2m2 and e3m2 simulations. The unperturbed collision rate, along with the amount of dynamical heating that the planetesimal population experiences determines whether the MMR acts to suppress or enhance the collision rate	67



3.11	The presence of a dip or bump in the collision profile (and therefore the dust profile) near the 2:1 MMR can be used to constrain the mass and eccentricity of the perturbing planet. The color scale indicates the relative strength of the features, while the dashed lines indicate boundaries in parameter space where a dip or a bump will be produced at the resonance. Combinations of mass and eccentricity that fall between the dashed lines correspond to an inner apocenter and outer pericenter separation at the edges of the resonance that is smaller than the resonance width and therefore will not create any significant feature in the collision profile. . . . .	80
3.12	Positions of planetesimals at the end of the simulation presented in [17] in polar coordinates. The dashed line marks the location of a $50 M_{\oplus}$ planet embedded in the disc. First order MMRs with the planet are indicated with arrows. A second planet is also present at 32.3 au, although it is not massive enough to induce any significant structure in the disc near associated resonances.	87
4.1	The ratio between the two-body relaxation and collision timescale for a population of equal-mass planetesimals with an internal density of $3 \text{ g cm}^{-3}$ . <b>The dashed curves show the value of <math>e_h</math> for which the random velocity dispersion is equal to the escape velocity of the planetesimals for a range of sizes.</b> Only in regions where $t_{\text{relax}} \gg t_{\text{coll}}$ can the velocity distribution respond to changes in the mass of the bodies such that oligarchic growth can operate. This condition is no longer satisfied for a dynamically hot disk at sufficiently short orbital periods. . . . .	96
4.2	The initial (blue) and final (orange) states of the narrow annulus simulations described in section 4.4. Relative masses of the bodies are indicated by point size. In the case of large $\alpha$ , almost no residual planetesimal population remains. Regardless of the initial choice of $\beta$ , the protoplanets that form attain similar eccentricities. . . . .	99
4.3	The final state of the mass distributions for the narrow annulus simulations described in section 4.4. For small $\alpha$ , a few embryos form alongside a power law tail of planetesimals. For larger values of $\alpha$ , the mass distribution stops being bimodal. As in the previous figure, the initial choice of $\beta$ does not appear to have any meaningful impact on the end result. . . . .	100
4.4	<b>Top:</b> The evolution of the ratio between the maximum and mean mass for the four simulations presented in section 4.4. The runaway growth phase can be identified by a positive trend in this ratio. For all values of $\alpha$ , an increase in $\beta$ has the effect of delaying runaway growth. <b>Bottom:</b> <b>The evolution of the maximum (solid lines) and mean (dashed lines) shown individually.</b>	101

4.5	The final state of the fdHi simulation. In the top panel, the contours denote the initial period-eccentricity distribution of the planetesimals. Point sizes indicate the relative masses of bodies at the end of the simulation. In the bottom panel, we show the feeding zone width (see equation 5.2) required to produce the final masses of the bodies. The dashed line indicates the feeding zone size expected for bodies on circular orbits. <b>For the shorter period bodies, the feeding zone size exceeds this expected value, which indicates that oligarchic growth is not operating here. This boundary occurs near roughly 60 d in orbital period.</b> . . . . .	110
4.6	The time evolution of the planetesimal surface density (in units of the total solid surface density) in the fdHi simulation. Each curve represents a radial slice of the disk. <b>The time is measured in units of the local accretion timescale at the center of each radial zone. The colors represent the orbital period at the center of each zone.</b> . . . . .	110
4.7	The final state of the full disk simulations listed in table 4.1. Point sizes indicate mass relative to the largest body in each simulation. . . . .	111
4.8	Feeding zone width (see equation 5.2) required to produce the final masses for the protoplanets from the simulations listed in table 4.1. <b>For the fdHi, fdHiSteep and fdHiShallow simulations, we have included the results from five separate iterations of the simulations, each using a different random number seed.</b> The horizontal dashed line indicates $\tilde{b} = 2\sqrt{3}$ . Despite the vastly different initial solid surface density profiles, the feeding zone width reaches the circular orbit value around $\sim 60$ days in all cases. . . . .	112
4.9	<b>For all bodies with <math>m &gt; 100m_0</math> at the end of the high surface density simulations,</b> the fraction of their total mass attained through mergers with initial mass planetesimals (smooth accretion) as a function of total mass. <b>Colors indicate the orbital periods of the bodies in the final simulation snapshot. Bodies interior to <math>\sim 20</math> to 30 days attain up to an order of magnitude less of their mass through minor merger events, while accretion of planetesimals plays a much more significant role at longer orbital periods.</b> . . . . .	119
4.10	<b>The relative separation between the final period of a body and the mean orbital periods of its accretion zone at the end of the fdHi, fdHiSteep and fdHiShallow simulations.</b> The marker type and color denotes the simulation used, while the marker sizes indicate the relative masses of bodies. In each case, all five iterations of the simulations are plotted simultaneously. . . . .	120



5.2	The evolution of the orbits of some of the last surviving bodies in the $\delta = 1.5$ simulations. Collisions are indicated with colored triangles, where the size and color denotes the relative mass of the body that was consumed in the merger. Green curves indicate bodies which survived through the end of the simulation and the line width indicates their relative mass. The vertical blue line marks the time at which the CHANGA snapshots were passed to GENGA.	141
5.3	Final period-mass configurations for the planets formed in all fifteen simulations. Each panel contains a set of simulations using a different mass surface density profile. Points connected by lines represent planets from the same simulation snapshot. Each color represents a set of initial conditions constructed from a different random number seed.	143
5.4	Final compositions of planets from the five $\delta = 1.5$ simulations. Point sizes indicate relative mass and the pie fractions indicate the amount of wet/dry material incorporated into each planet. A snow line is placed at 50 days in orbital period and all planetesimals that originate from beyond this location are assumed to be wet.	144
5.5	The period-mass (left) and period-eccentricity (right) distributions of the simulations starting from planetesimals (colored points) and isolation mass embryos (gray points). Each planetary system is connected by a series of lines.	146
5.6	The combined timing and location of collisions from all five versions of the full (blue) and isolation mass (orange) simulations. Point sizes indicate the relative masses of bodies consumed in each merger. The timings of the isolation mass simulations have been shifted to line up with the ending of the CHANGA segment of the full simulations.	148
5.7	Timing and velocities (in units of the mutual escape speed) of collisions between bodies larger than $0.1 M_{\oplus}$ in the full (colored points) and isolation mass (gray points) simulations. Collisions between subsequent bodies are connected by lines. The dashed horizontal line at $v_{coll}/v_{mut,esc} = 2$ corresponds to boundary above which collisions should be destructive.	150
5.8	Final orbital architectures of planetary systems formed in the full (blue points) and isolation mass (gray points) simulations. Point sizes indicate relative masses. Bodies which underwent a collision where $v_{coll}/v_{mut,esc} > 2$ with a $> 0.1 M_{oplus}$ body are marked with a red X.	151
5.9	Corner plot showing the correlations between all five features (orbital period $P_{orb}$ , mass $M$ , eccentricity $e$ , inclination $inc$ and smooth accretion fraction $s_f$ ) used to train the generator and discriminator. The training data is shown in blue and an example synthetic dataset is shown in orange.	155

5.10	Period-mass and period-eccentricity distributions of planetary systems formed through the full simulations (colored points) and the synthetic simulations (gray points). Planets from the same system are connected with a line. . . . .	156
5.11	The combined timing and location of collisions from all versions of the full (blue) and synthetic (orange) simulations. Point sizes indicate the relative masses of bodies consumed in each merger. Here, T=0 corresponds to the end of the CHANGA simulations and collisions from that phase are not shown. . . . .	157
5.12	Corner plot showing the correlations between bulk properties of the final orbital architectures of the full, isolation mass and synthetic simulations. $q$ is the mass ratio between the initial and final snapshot, $S_c$ is the radial mass concentration statistic, $S_d$ is the angular momentum deficit and $n_{pl}$ is the final number of planets. Blue points are the full simulations, green points are the isolation mass simulations and orange points are the synthetic simulations. . . . .	159
5.13	Timing and velocities (in units of the mutual escape speed) of collisions between bodies larger than $0.1 M_\oplus$ in the full (colored points) and synthetic (gray points) simulations. Collisions between subsequent bodies are connected by lines. The dashed horizontal line at $v_{coll}/v_{mut,esc} = 2$ corresponds to boundary above which collisions should be destructive. . . . .	162
5.14	Final orbital architectures of planetary systems formed in the full (blue points) and isolation mass (gray points) simulations. Point sizes indicate relative masses. Bodies which underwent a collision where $v_{coll}/v_{mut,esc} > 2$ with a $> 0.1 M_\oplus$ body are marked with a red X. . . . .	163
5.15	Occurrence rates of planets as a function of orbital period in 0.25 dex logarithmic bins. The occurrence rate measured from our synthetic simulations is shown in blue and the occurrence rate measured from planet candidates in the California Kepler Survey [140] is shown in orange. . . . .	165

## **ACKNOWLEDGMENTS**

The author wishes to express sincere appreciation to University of Washington, where he has had the opportunity to work with the T<sub>E</sub>X formatting system, and to the author of T<sub>E</sub>X, Donald Knuth, *il miglior fabbro.*

## **DEDICATION**

to my dear wife, Joanna

Chapter 1

**INTRODUCTION**

## Chapter 2

# FORMATION OF PLANETARY EMBRYOS IN THE INNER SOLAR SYSTEM

### **2.1 *Introduction***

The standard scenario of terrestrial planet formation involves the pairwise accretion of small rocky bodies, called planetesimals, that condense from dust out of the protostellar disc [151]. This accretion process can be broken into a series of distinct stages. First, dust particles settle toward the midplane of the disc and clump together via gravitational instability [54, 180], streaming instabilities [81, 80], turbulent concentration [23, 34, 33, 64] or direct sticking [134, 175, 48, 82]. These formation models predict a wide variation in the initial size of planetesimals, ranging from hundreds of meters up to a few hundred kilometers in diameter.

After this condensation process ends, growth continues via pairwise collisions between planetesimals. Above about 1 km in size, gravitational focusing becomes effective and the collision rate strongly increases. This marks the beginning of the intermediate stage of accretion. During this phase, runaway growth [44, 87, 13] quickly increases the size of the largest bodies. Eventually, the largest bodies grow massive enough to heat the small planetesimals, which then inhibits the runaway growth effect. This marks the transition into the phase of oligarchic growth in which the handful of large bodies all tend to grow at the same rate. This produces a bimodal size distribution of planetesimals, with many small bodies and a handful of very large bodies. During this phase, a combination of scattering events between the oligarchs and dynamical friction from the small planetesimals places the oligarchs on nearly circular orbits that are spaced apart by approximately 5-10 Hill radii [88]. Eventually, the oligarchs accrete most of the available material in the vicinity of their orbit, which eventually throttles their growth rate. On much longer time scales, the large bodies

perturb each other onto crossing orbits, forming Mars to Earth sized bodies via occasional collisions. This phase of late stage accretion is highly chaotic and takes much longer to play out than the previous stages [24, 144].

Generally, planetesimal accretion models fail to produce a configuration of planets that resembles that of the Solar System. Planets produced in the vicinity of Mars are systematically too massive [172, 143, 123, 73] and the terrestrial planets that form are too eccentric compared to their Solar System counterparts [24, 2, 22]. In addition, the present day water content of Earth, along with the large D/H ratio of Venus [42] does not match with models of solids that condensed out of the Solar nebula at 1 AU.

These issues all have proposed solutions, which generally involve altering the initial conditions for late-stage accretion simulations. The condition of the Solar System at the beginning of the late stage accretion phase is poorly constrained. This is mostly due to the fact that planetesimal formation, and therefore the intermediate accretion phase which produces the planetary embryos, is not well understood. Although the present day population of small Solar System bodies has continued to evolve since the end of the intermediate accretion phase, the current size frequency distribution (SFD) of asteroid belt and Kuiper belt objects contains some clues about the accretion history. [119] argued that the SFD of asteroid belt objects larger than 100 km in diameter has been largely unchanged, aside from a size independent depletion factor. [44] did a long term stability analysis of small Solar System objects and found that small bodies left over from accretion should still be largely unperturbed. For these reasons, it should be possible to connect observables in the Solar System to planetesimal formation theories by modeling only the intermediate stages of accretion.

There are two common ways to model planetesimal growth. A powerful approach is to use statistical methods to track the evolution of large groups of planetesimals. This is known as the particle-in-a-box method [56, 173]. The evolution of growth is followed by tracking planetesimals in discrete bins of mass and semi-major axis. This removes the need to calculate the motion of every individual body and allows very large collections of planetesimals to be followed. Unfortunately, the dynamics that governs the evolution of

these bodies does not always naturally emerge with this approach. As an example, [167] found that a careful treatment of three body encounters led to a different prediction for the initial size distribution of planetesimals near the asteroid belt. Additionally, the particle-in-a-box method is not well suited for studying oligarchic growth because the largest mass bins, which dominate the evolution in this stage, contain small numbers of bodies. Non-gravitational effects such as gas drag and fragmentation require extra care to implement self-consistently [97], although it has been successfully done [174, 22]. To alleviate some of these issues while still being able to model large populations, a newer hybrid approach, in which large bodies are treated as single entities and planetesimals are treated as statistical ensembles has been developed [169, 83, 100, 121].

The most reliable and straightforward approach is to use N-body methods to follow the evolution and growth of the planetesimals [95]. By tracking the individual motions of bodies, the dynamics governing their evolution naturally emerges, no matter what the distribution of bodies looks like. However, N-body simulations involving collision detection are extremely computationally expensive, which severely limits both the resolution and number of timesteps that can be achieved. This is why there are very few studies of runaway and oligarchic with direct N-body simulations in the literature [87, 88, 89, 13]. Instead, N-body methods are most commonly used to study late stage accretion, where the self-gravity and collisional evolution of the residual planetesimals is largely unimportant [24, 2, 22, 131, 119].

To date, we are not aware of any N-body simulations that resolve both the runaway and oligarchic growth phase with more than about  $10^4$  particles. At this resolution, stochasticity likely has a significant influence on dynamical friction and resonances may not be sufficiently resolved. [144] found that insufficient planetesimal resolution during the oligarchic growth phase limits the effectiveness of dynamical friction felt by the oligarchs, producing a population of embryos with unrealistically high eccentricities. This idea has also been applied to planet migration through a disc of planetesimals. [30] showed that resonances make a significant contribution to the dynamical friction torque exerted by the disc on the planet. This phenomenon requires the planetesimals to be finely resolved [20]. Dynamical friction is

also facilitated via resonances in galactic dynamics [108]. [171, 170] examined the effect of N-body particle counts on galaxy dynamics and showed that resonant interactions between the bar and halo were only effective with sufficient particle phase space coverage.

For these reasons, we motivate the need for a high resolution N-body simulation of planetesimal growth. We do this to better understand the effect that dynamical friction has on the intermediate stages of terrestrial planet growth and to examine what predictions a high resolution model makes about the residual population of planetesimals in the Solar System. In particular, resonances which are only effective with fine enough resolution, may have an important influence on planetesimal growth. In this paper, we investigate planetesimal evolution during the runaway and oligarchic growth phases with a direct N-body model. We begin by simulating an annulus of planetesimals with similar resolution to [88] to validate our model. We then run the same configuration with 100x more particles to better understand the effects of resolution on the intermediate stages of terrestrial planet growth.

In section 2.2, we describe the simulation code that we use and provide a detailed description of the collision model. We also summarize the initial conditions used. In section 5.3, we present the results of the low and high resolution simulation of terrestrial planet growth and highlight differences between the two. We find that a bump develops in the mass distribution of the high resolution simulation, which does not appear in the low resolution run. This feature manifests itself shortly after oligarchic growth commences and we infer that it is produced by extra heating via mean motion resonances between the oligarchs and small planetesimals. To further demonstrate this effect, we re-run the high resolution simulation with a narrower annulus (depopulating many of the resonances) and show that this reduces the prominence of the bump in the mass distribution. In section 2.4, we present a set of collisionless simulations of a planetary embryo embedded in an annulus of planetesimals. This more clearly demonstrates the differences in dynamical behavior between the low and high resolution models. In section 2.6, we present two more simulations of planetesimal growth at intermediate resolutions and demonstrate that the location of the bump is sensitive to the initial planetesimal mass. Finally, section 2.7 connects these new results to our present

understanding of terrestrial planet growth and we discuss the additional steps necessary to use our results to constrain the initial size of planetesimals in the Solar System.

## 2.2 *Simulations*

### 2.2.1 *Numerical Methods*

All of the simulations described in this paper were performed with the highly parallel N-body code CHANGA . CHANGA is written in the CHARM++ programming language and has been shown to perform well when using up to half a million processors [113] simultaneously. Gravitational forces are calculated using a modified Barnes-Hut tree algorithm with hexadecapole order expansions of the moments. For all of the simulations described in this paper, a node opening criterion of  $\Theta_{BH} = 0.7$  was used. [150] was able to resolve mean motion resonances in a terrestrial disc using a similar tree code with the same node opening criterion, so we expect that our model should properly handle resonance effects as well. The equations of motion are integrated using a kick-drift-kick leapfrog scheme. For more information about the implementation of CHANGA see [79].

### 2.2.2 *Collision Model*

CHANGA is a smoothed particle hydrodynamics code originally designed for cosmology simulations. In order to use CHANGA to study planetesimal coagulation, we implemented a hard-body collision model that treats particles as solid objects with a fixed radius, rather than as smooth tracers of a fluid with a characteristic softening length. This work was largely based off of the hard body collision implementation in PKDGRAV, which is described in [149] and [150].

Collisions are predicted at the beginning of each drift step by extrapolating the positions of the particles forward using the velocities calculated during the first kick. For each particle, the closest 64 neighbors are considered in the collision search. Because CHANGA is a tree code, the nearest neighbors of a particle can be retrieved in  $\mathcal{O}(N \log N)$  time. After

extrapolating the positions forward and checking for overlap with any neighbors, the earliest collision time  $t_{coll}$  is stored for each particle.

After the prediction phase, particles with  $t_{coll}$  less than the time step size  $\Delta T$  must have their collisions resolved. For simplicity, all collisions in our simulations result in perfect accretion. [68] showed that excluding the effects of fragmentation and collisional rebound does not qualitatively change the growth modes of the planetesimals. A merger between two particles of mass  $m_1$  and  $m_2$  results in a single particle of mass  $M = m_1 + m_2$ , with the radius set to conserve density. The position and velocity of the resulting particle is set to the centre of mass position and velocity of the colliders at the moment of contact. The resulting merged particle is then drifted to the end of the step. If multiple collisions are predicted during a time step, the earliest collision is resolved first. Because resolving a collision can result in another imminent collision, collisions must be resolved one by one, with a new prediction check being run each time.

As in [87, 88] we accelerate the accretion process by artificially inflating the physical radius of the bodies by a factor of  $f$ . This technique reduces the accretion time-scale by approximately a factor of  $f^2$ , significantly reducing the number of timesteps that must be integrated. Additionally, inflating the particle radii allows us to use a smaller annulus with less planetesimals. The reason we cannot use an arbitrarily skinny annulus is because the edges tend to expand outward due to the unrealistic boundary conditions, decreasing the surface density. The time-scale for this expansion is set by the two body relaxation time-scale, which scales with  $N$ . Reducing the accretion time-scale by increasing  $f$  allows us to study planetesimal growth with a smaller, less computationally expensive annulus.

We must be careful, however, to choose a value of  $f$  that is not too large. The rms eccentricity and inclination of the planetesimal disc grows as gravitational encounters transform energy due to Keplerian shear into random motions. By accelerating the growth rate, we cause the transitions between growth modes to happen early, when the disc is less dynamically excited. This discrepancy is partly compensated for by the fact that our model ignores the effects of gas drag, which would damp the eccentricities and inclinations of the plan-

etesimals. We adopt  $f = 6$  for our calculations, which reduces the amount of gravitational scattering by less than 10% of its true value and does not qualitatively change the modes of planetesimal growth [88].

As previously mentioned, simulation (ii) is meant to be compared with the results of [88]. This allows us to both validate our collision model and also have a baseline to compare our simulations to. In both cases, the planetesimals are distributed randomly in an annulus centred at 1 AU with a width  $\Delta a = 0.085$  AU around a  $1 M_{\odot}$  star. This annulus width was chosen so that the required particle count is minimized without boundary effects influencing planetesimal growth. The surface mass density of the ring is set to  $10 \text{ g cm}^{-2}$ , which approximately corresponds to the minimum-mass solar nebula model [63] at 1 AU. In case (i), the eccentricities and inclinations are taken from a Rayleigh distribution [70] with  $\langle e^2 \rangle^{1/2} = 2\langle i^2 \rangle^{1/2} = 4h/a$ , where  $h$  is the mutual Hill radius. To match the same eccentricity and inclination dispersion with larger planetesimals in case (ii), we use  $\langle e^2 \rangle^{1/2} = 2\langle i^2 \rangle^{1/2} = 0.635h/a$ . In both simulations, the planetesimals are given an internal density of  $2 \text{ g cm}^{-3}$ . We use fixed timesteps with  $\Delta T = 0.0025$  years and evolve the simulations for 20,000 years. Large timesteps diminish the effectiveness of gravitational focusing, which inhibits the collision rate. We find that the collision rate is converged below  $\Delta T = 0.0025$  years. The integration time was chosen to be comparable to the orbital repulsion and Hill radius growth time-scale [86] so that the effects of oligarchic growth are fully realized by the end of the simulation.

It is worth noting that simulation (i) was a very computationally expensive undertaking. In total, the full 20,000 years of integration required approximately 130,000 CPU hours and over 50 days of wall clock time.

### 2.2.3 Initial Conditions

We begin by using our collision model to perform two sets of calculations:

- (i)  $10^6$  equal mass bodies with  $m = 1.2 \times 10^{21} \text{ g}$
- (ii) 4000 equal mass bodies with  $m = 3 \times 10^{23} \text{ g}$

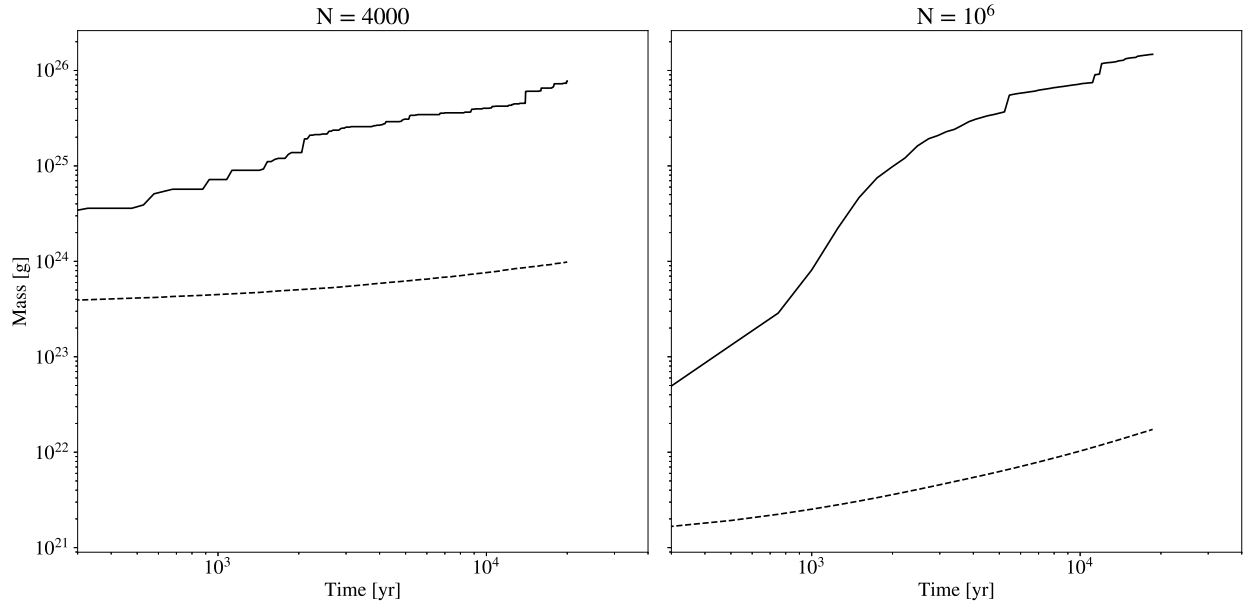


Figure 2.1: Evolution of the maximum (solid curve) and mean (dashed curve) planetesimal mass in the  $N=4000$  and  $N=10^6$  particle simulations. At early times, the maximum mass grows more quickly than the mean mass, which is indicative of runaway growth. After a few thousand years, the separation between the curves becomes a constant factor, signalling the start of oligarchic growth.

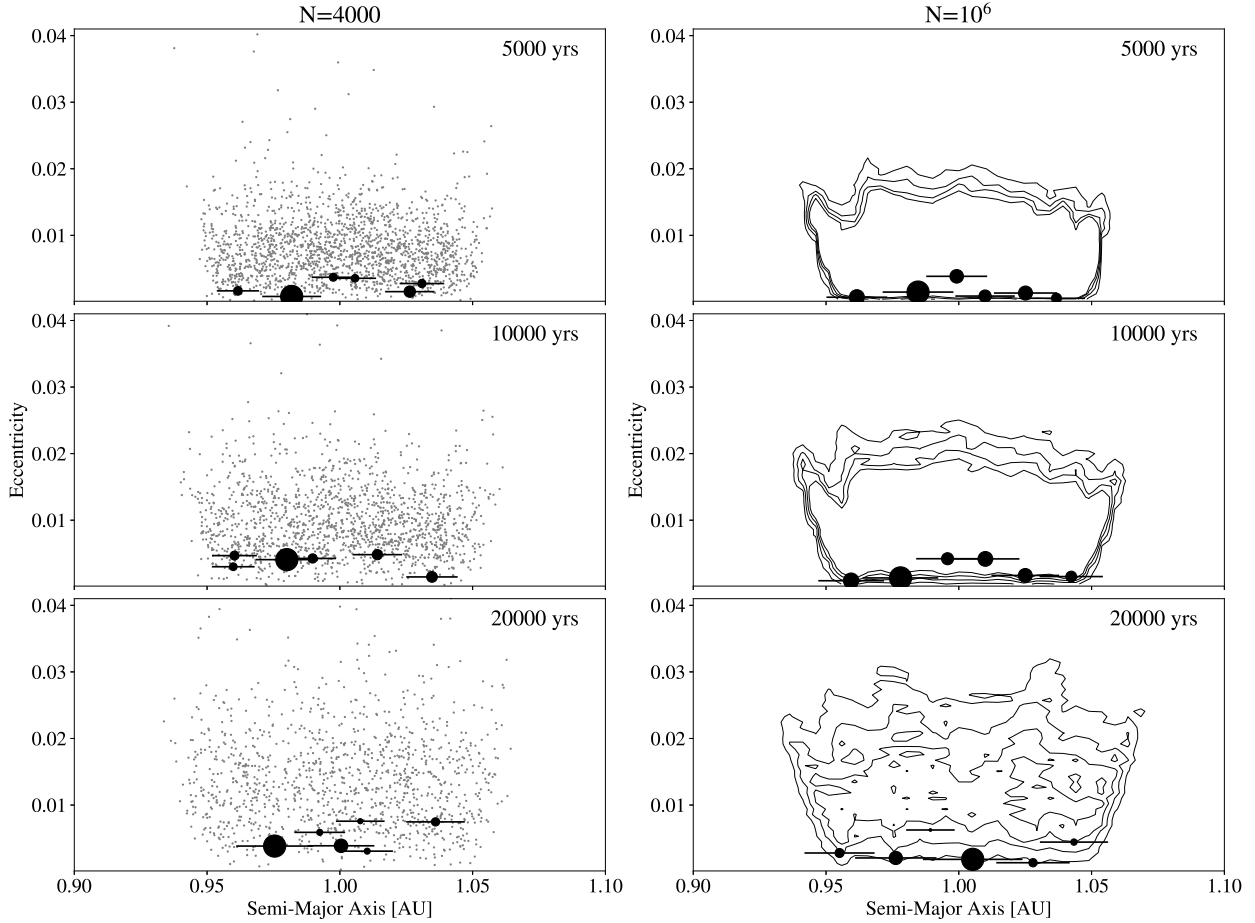


Figure 2.2: Snapshots from the low and high resolution models in the  $a - e$  plane. On the left, the light dots represent individual planetesimals, while the contours on the right hand plots represent curves of constant number density. The contour levels are the same between all panels and correspond to  $7.8 \times 10^6$ ,  $1.6 \times 10^7$ ,  $2.3 \times 10^7$ , and  $3.1 \times 10^7$  planetesimals per AU per unit eccentricity. The black circles denote the configuration of the 6 largest bodies in the simulation, with the area of the circles scaled to the mass of the body. The horizontal error bars are scaled to 5 times the Hill radius of the bodies.

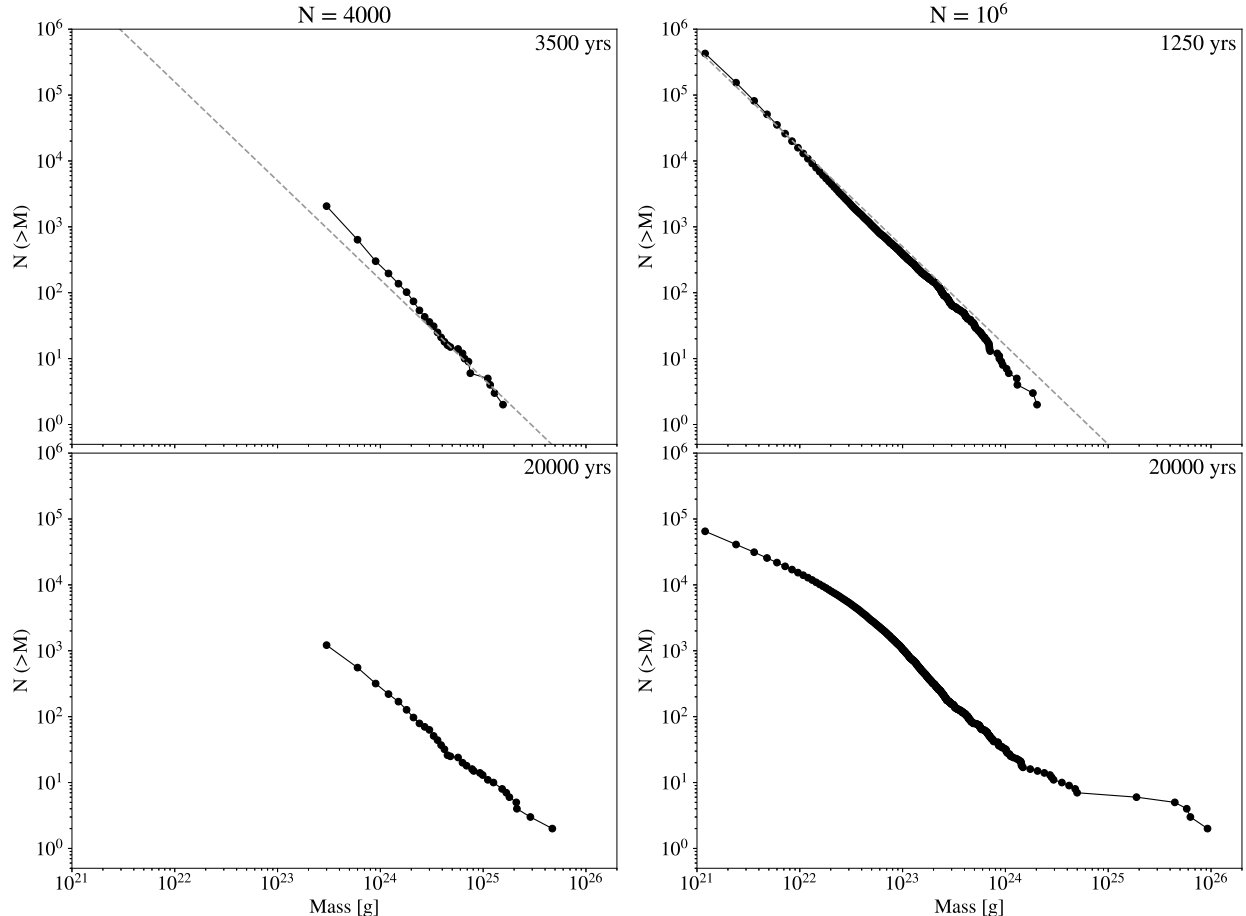


Figure 2.3: Cumulative number of bodies in each mass bin for the low and high resolution runs, shown at the end of runaway growth (top row) and the end of the simulation (bottom row). The dashed line indicates a slope of -1.5, which is characteristic of runaway growth.

## 2.3 Results

### 2.3.1 Low vs High Resolution

We begin by comparing the evolution of growth between the low resolution ( $N=4000$ ) and high resolution ( $N=10^6$ ) models. As planetesimals collide and grow, gravitational focusing becomes increasingly effective and the relative growth rate increases with mass [56]. Figure 2.1 shows the evolution of the average and maximum planetesimal mass in both simulations. Runaway growth at early times is evident from the fact that the maximum mass grows more quickly than the mean mass. Eventually, the largest bodies begin to dynamically heat the neighboring planetesimals, which slows the growth rate of the largest bodies.

When gravitational focusing and dynamical friction are both effective, the growth rate of a planetesimal of mass  $M$  is given by

$$\frac{dM}{dt} \propto \Sigma M^{4/3} e_m^{-2}, \quad (2.1)$$

where  $\Sigma$  is the surface density of solid material and  $e_m$  is the rms eccentricity of the planetesimals [86]. Before the oligarchs form, the eccentricity dispersion is independent of mass and the fractional growth rate scales like  $dM/dt \propto M^{4/3}$  [174]. This implies that large bodies grow more quickly than small bodies, hence the runaway effect. Once the oligarchs form and dynamical friction becomes effective, energy equipartition causes the velocity dispersion to evolve toward  $v_m \propto M^{-1/2}$  [66]. Using  $v_m \propto e_m$  [102], the growth rate during the oligarchic growth phase scales like  $dM/dt \propto M^{2/3}$ . Note that this does not imply that smaller bodies grow more quickly than large bodies. Rather, the growth rates tend towards the same value. This is reflected in figure 2.1, where the slope of the maximum mass curve flattens out to match the slope of the mean mass curve after a few thousand years.

Comparing the two panels in figure 2.1, it is also evident that the rate of growth is more vigorous in the high resolution case. This is due to the fact that the collision time-scale, given by

$$t_{coll} = \frac{1}{n\sigma v}, \quad (2.2)$$

is shorter in the latter case, where  $n$  is the number density of planetesimals,  $\sigma$  is the collision cross section and  $v$  is the typical encounter velocity. The collision cross section depends on both the geometric cross section ( $\propto N^{-2/3}$ ) and an extra term due to gravitational focusing ( $\propto N^{-7/3}$ ), where  $N$  is the total number of particles in the simulation and the total disk mass is fixed. Because the eccentricity and inclination dispersion (and therefore the scale height of the disk) are kept fixed between the low and high resolution simulations, the typical encounter velocity does not vary with  $N$ . Here, we retain only the leading order term for the collision cross section, in which case these quantities scale like  $n \propto N$ ,  $\sigma \propto N^{-2/3}$  and  $v \propto \text{const}$  so that

$$t_{coll} \propto N^{-1/3}. \quad (2.3)$$

Figure 3.2 shows the a-e distribution of planetesimals at three snapshots from both simulations. In both cases, the eccentricity dispersion grows as energy from Keplerian shear is transformed into random motion, an effect known as viscous stirring [133]. The black circles denote the semi-major axis and eccentricity of the 6 largest bodies. The area of the circles indicates the mass of the bodies and the horizontal bars are each scaled to 5 times the Hill radius of the bodies. Gravitational scattering between the oligarchs, coupled with dynamical friction from the surrounding planetesimals, places the oligarchs on low eccentricity orbits that are spaced apart by a 5-10 Hill radii via orbital repulsion [88].

Next, we examine the evolution of the mass distribution of planetesimals. This is shown in figure 2.3. At early times, both models exhibit a power law distribution  $N(< M) \propto m^{-p}$ , where  $p = 1.5$  for the small bodies. A mass distribution with this slope is characteristic of runaway growth [174]. The top panels show the mass distribution from both simulations at the end of the the runaway growth phase. In all subsequent snapshots, the mass distribution deviates from a single power law as the most massive bodies break away from the distribution,

signaling the start of oligarchic growth. This happens sooner in the high resolution case. The bottom panels show the mass distribution at the end of the simulation at  $T = 20,000$  years.

Besides the fact that growth is more vigorous at higher resolution, the final mass distribution of planetesimals in the  $N = 10^6$  case develops a feature that does not appear in the low resolution model. In the low resolution case, the low mass end of the mass distribution of planetesimals retains a single power law slope. The high resolution model, on the other hand, develops a bump in the mass distribution near  $10^{22}$  g.

### *2.3.2 Explaining the Bump in the High Resolution Mass Spectrum*

We would next like to determine what produces the feature at  $10^{22}$  g in the high resolution simulation and why it is absent from the low resolution run. Upon close inspection of the simulation snapshots, both models retain a mass distribution that follows a single power law up until the onset of oligarchic growth. The bump in the high resolution mass spectrum becomes visible shortly after the oligarchs form. Over the course of the simulation, the bump gradually becomes more prominent. Because the bump appears shortly after the first oligarchs do, its presence is likely tied to the formation of the oligarchs.

Other investigations of planetesimal growth have revealed a similar bump in the size frequency distribution (SFD) at intermediate masses. [119] found that the location of this bump was set by the initial size of the planetesimals. Objects smaller than this size were created through disruptive collisions, which resulted in a shallower slope on the SFD to the left of the bump. Our collision model does not allow for fragmentation, so we must look for another explanation.

[?] showed that a bump in the SFD was an artefact of the transition between shear and dispersion dominated growth. Objects in the shear regime, whose encounter velocities are dominated by the differential rotation of the disc, grow more slowly than those in the dispersion regime, whose encounters are set by the random velocity dispersion. Because the velocity dispersion varies with planetesimal mass, both of these growth modes can operate

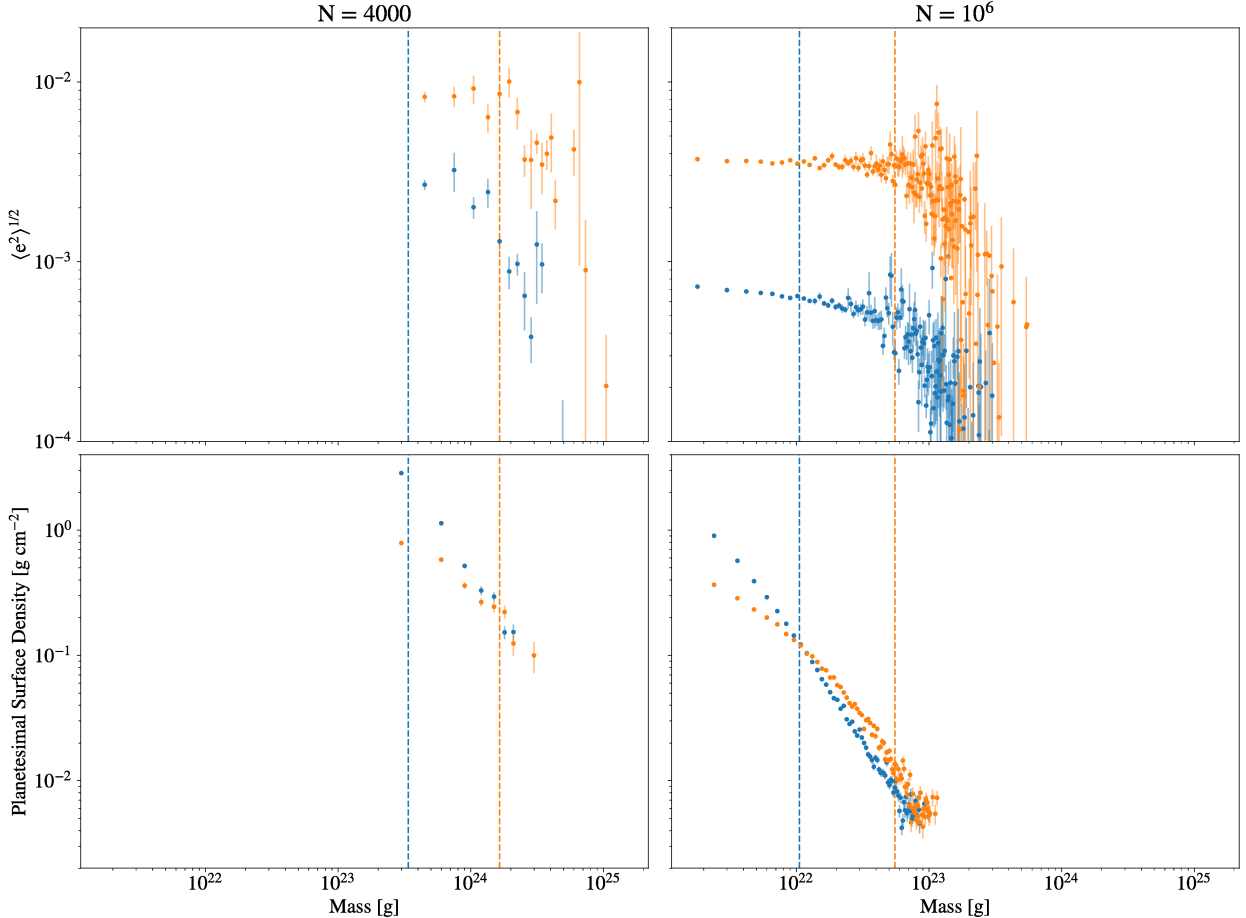


Figure 2.4: The rms eccentricity (top) and planetesimal surface density at each mass (bottom) shown for the  $N = 4000$  and  $N = 10^6$  simulations. The blue points correspond to the quantities at the end of the runaway growth phase (when the mass distribution deviates from a single power law) and the orange points are from the end of the simulations ( $T = 20,000$  years). The vertical dashed lines indicate the value of  $M_{\text{stir}}$  during that snapshot.

simultaneously. Energy equipartition should cause the velocity dispersion to decrease with mass, so the transition between shear and dispersion dominated growth should happen at some intermediate mass. Finally, the smallest bodies have a velocity dispersion that exceeds their escape velocities, which sets a third, slow mode of growth in which gravitational focusing is ineffective. Although our high resolution simulation resolves all three modes of growth, we find that the boundaries between these modes smoothly and steadily evolve. Over the course of the simulation, the shear-dispersion boundary increases from about  $10^{22}$  g to  $10^{25}$  g, while the dispersion- escape boundary evolves from about  $10^{21}$  to  $10^{24}$  g. Any artefacts that these boundaries would leave on the planetesimal mass distribution should get washed out, so we also rule these out as explanations for the  $10^{22}$  g bump.

Although the boundary between shear and dispersion dominated growth does not seem to be producing the bump, there still must be some kind of transition between growth modes occurring near this mass. As shown by equation 2.1, the growth rate is controlled by both the surface density of the planetesimals and their eccentricities. In figure 2.4, we show the rms eccentricity and surface mass density of the planetesimals as a function of mass at the end of the runaway growth phase (blue points) and at the end of the simulation (orange points). In this figure, each point corresponds to the relevant quantity calculated for all planetesimals with the exact same mass. Because the simulations start with equal mass planetesimals which grow via pairwise collisions, the masses take on discrete, linearly spaced values. We found that logarithmically binning the mass values alters the shape of the distributions, especially in the high resolution case where the quantities span many orders of magnitude. For this reason, we chose not to bin any of the data. The error bars in figure 2.4 are obtained via 10,000 iterations of bootstrap resampling. For the high resolution simulation, the error bars at low mass are smaller than the size of the points.

The surface density was determined by calculating an azimuthally averaged density profile using the analysis package PYNBODY [141]. The surface density for each planetesimal mass was taken to be the average surface density for those particles in a single radial bin from 0.9575 to 1.0425 AU, which spans the initial boundaries of the annulus.

One might expect that the rms eccentricity spectrum should eventually reach energy equipartition ( $e \propto m^{-1/2}$ ), but this has been shown to only occur with a sufficiently steep mass distribution [142]. In our case, the mass distribution is shallow enough that the velocity evolution of the low mass bodies is set only by interactions with large planetesimals. The mass below which this occurs, shown by the vertical dashed lines in figure 2.4 is given by [174, 135]

$$M_{stir} = \frac{\langle m^2 \rangle}{\langle m \rangle}. \quad (2.4)$$

Below this mass, planetesimals do not produce a dynamical friction wake and their velocity evolution becomes independent of mass [142]. Because we started with equal mass planetesimals, the mass distribution was steep at early times. A power law slope steeper than  $p = -2$  should produce a mass-dependent velocity distribution everywhere [142]. In the top right panel of figure 2.4, the rms eccentricity distribution is not entirely flat below  $M_{stir}$ , which is likely due to the evolving mass spectrum. The analysis of [142], however, assumes a static mass spectrum.

At late times, a power law break in the surface density distribution forms near  $10^{22}$  g in the high resolution simulation. Because the surface density is tied to both the mass distribution and the spatial distribution of planetesimals, it is difficult to learn anything else about the dynamics that are altering the growth rate from this information alone. We will examine this further in section 2.4.3.

Given the power law break in the surface density distribution below  $10^{22}$  g, we infer that there must be a dynamical mechanism at work that alters the collision rates of the low mass bodies. By the time that the  $10^{22}$  g bump begins to appear, the planetesimals are sufficiently hot enough to render gravitational focusing ineffective (equation 2.1 is also no longer applicable). In this case, any additional heating actually increases the collision rate. Because this effect appears around the time of the onset of oligarchic growth, it likely has something to do with dynamical friction between the oligarchs and the planetesimals. In the next section, we examine how dynamical friction might be more effective with small

planetesimals.

## 2.4 *Dynamical Friction and Resolution*

Although the Chandrasekhar formula [26] contains no dependence on particle mass, the 'granularity' of the surrounding medium has been shown to influence the action of dynamical friction [20]. This is because the individual kicks from gravitational encounters become less frequent and more powerful at coarse resolution, introducing extra stochasticity as the system evolves toward energy equipartition. [131] showed that a finely resolved planetesimal distribution during the oligarchic growth phase produced planetary embryos with low eccentricities. They did not, however, examine the mass spectrum to see if the oligarchs were preferentially heating the smallest planetesimals. In addition, their simulations only contained a few thousand particles, while our high resolution run contains in excess of 200,000 bodies at the onset of oligarchic growth. Comparing the largest embryos at the end of simulation (i) to their results, we find that the largest embryo in our high resolution run has an eccentricity that is a factor of 2 smaller than the embryos produced by [131].

In addition to altering the cumulative effect of close gravitational encounters, there is evidence that energy and angular momentum exchange through resonances is more effective with fine granularity. For example, in collisionless simulations of galaxies, [171, 170] showed that a minimum number of particles was required to populate resonances and couple the rotation of a bar to the central halo cusp through Lindblad resonances. If the resolution was too coarse, gravitational potential fluctuations would scatter particles out of resonances and prevent any strong torque between the bar and the halo. Likewise, [30] showed that resonant torque has a measurable effect on the interaction between a planet and a planetesimal disc.

### 2.4.1 *Resolved Resonances*

During the oligarchic growth phase, a handful of massive bodies lose energy and angular momentum to the surrounding medium. The previous runaway growth phase leaves behind a steadily varying spectrum of planetesimal masses, whose number decreases with mass.

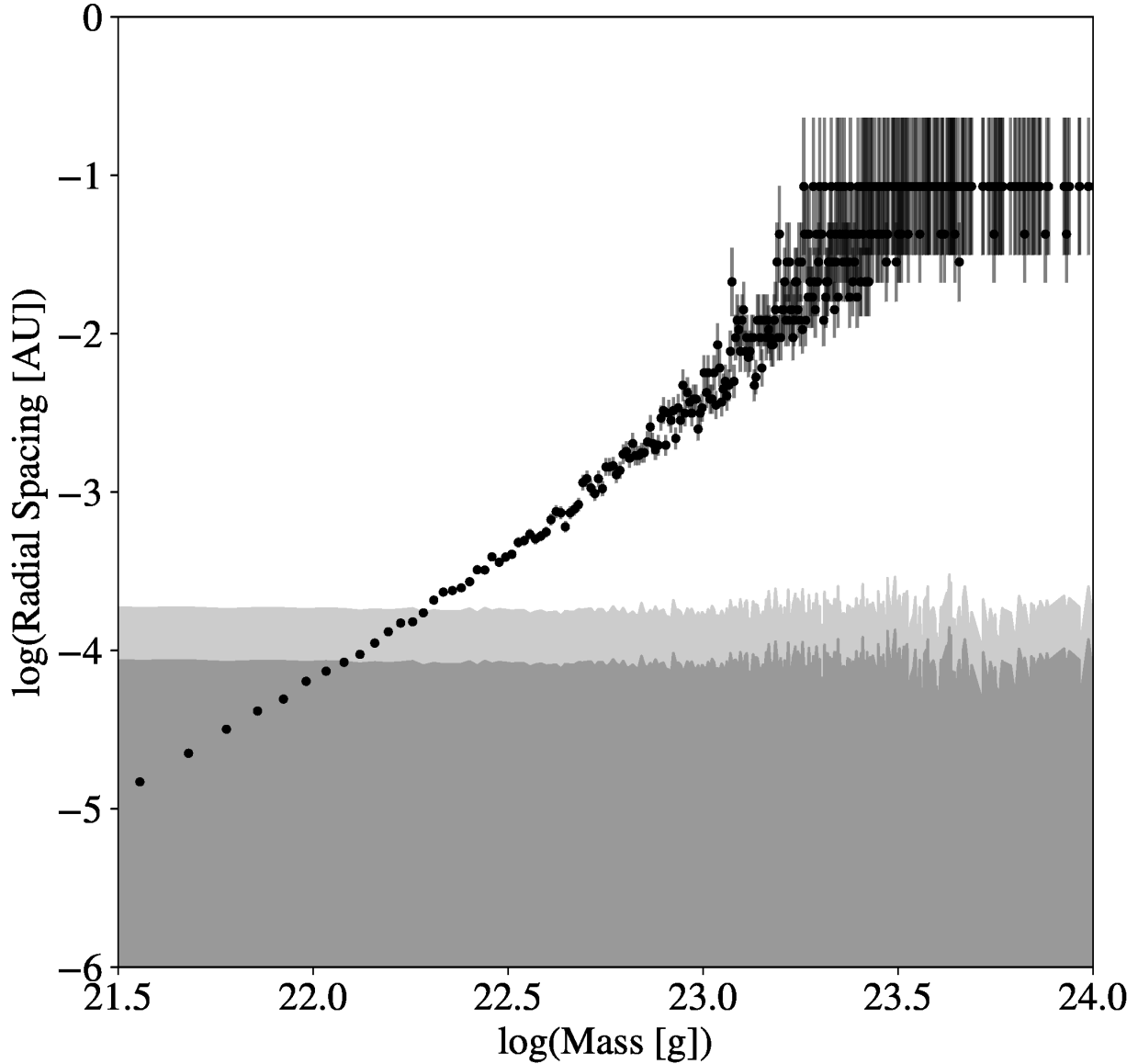


Figure 2.5: The average spacing in semi-major axis as a function of mass at the end of the high resolution growth simulation (black points). The gray regions indicate the libration width of planetesimals in each mass bin that are in resonance with the most massive oligarch. The light gray region corresponds to the libration width of the 65:64 (highest non-overlapping) resonance and the dark gray region corresponds to the 15:14 (most distant populated) resonance.

Assuming the planetesimals are randomly distributed throughout the disc, the granularity can be thought of as increasing with mass. This implies that the dynamical friction should be more effective from the smallest planetesimals. Because the planetesimals appear to be more strongly heated below a certain mass threshold, we hypothesize that the change in growth modes has to do with the activation of resonances, rather than a smooth decrease in the stochasticity of scattering events.

Because spiral features like those seen in [171, 170] and [30] are unlikely to form in such a narrow annulus, we will consider the effects of mean motion resonances (MMRs), which are a subset of the Lindblad resonances considered in the aforementioned studies. In order to determine the resolution required to resolve MMRs, we calculate the libration width of first order MMRs associated with the oligarchs and compare it to the average radial spacing between planetesimals as a function mass. The average radial spacing is given by

$$\langle \Delta r \rangle = \frac{\Delta a}{N(m)}, \quad (2.5)$$

where  $\Delta a$  is the width of the annulus and  $N(m)$  is the number of planetesimals of each mass.

Because the mass distribution has a negative slope and we expect planetesimals of varying mass to be randomly distributed about the disc, the radial spacing between planetesimals should increase with mass. For a fixed resonance width, there should be a cutoff in mass, below which planetesimals are more strongly affected by the resonances. The libration width of a first order mean motion resonance can be derived analytically using the pendulum approximation [126] and is given by

$$\frac{\delta a}{a} = \pm \left( \frac{16}{3} \frac{|C_r|}{n} e \right)^{1/2} \left( 1 + \frac{1}{27j_2^2 e^3} \frac{|C_r|}{n} \right)^{1/2} - \frac{2}{9j_2 e} \frac{|C_r|}{n}, \quad (2.6)$$

where  $a$  is the semi-major axis at the centre of the resonance,  $e$  is the eccentricity of the body in resonance and  $j_2 = -q$  where  $p : q$  is the MMR being considered.  $|C_r|/n = (m'/m_c)\alpha f_d(\alpha)$ , where  $(m'/m_c)$  is the mass ratio of the body associated with the resonance to the central body,  $\alpha$  is the semi-major axis ratio associated with the resonance and  $f_d(\alpha)$

is the disturbing function. For an interior first order resonance, the disturbing function can be expressed as

$$f_d(\alpha) = jb_{1/2}^j + \frac{\alpha}{2} \frac{db_{1/2}^j}{d\alpha}, \quad (2.7)$$

[176] where  $j = 1 - j_2$  and  $b_{1/2}^j$  is a Laplace coefficient which is defined as

$$b_s^j(\alpha) = \frac{1}{2\pi} \int_0^{2\pi} \frac{\cos j\theta d\theta}{(1 - 2\alpha \cos\theta + \alpha^2)^s}. \quad (2.8)$$

The derivative in the second term of equation 2.7 can be written in terms of the Laplace coefficients [126]

$$\frac{db_s^j}{d\alpha} = s \left( b_{s+1}^{j-1} - 2\alpha b_{s+1}^j + b_{s+1}^{j+1} \right). \quad (2.9)$$

Figure 2.5 shows the libration width and average radial spacing of the planetesimals as a function of mass at the end of the high resolution run. To calculate the libration width as a function of planetesimal mass, the  $e$  used in equation 2.6 was taken to be the average eccentricity in each mass bin, while  $a$  was set to the semi-major axis of the largest oligarch in the simulation. The slight variation in the resonance width as a function of mass is due to the variation in eccentricity. The error bars on the radial spacing data are calculated from Poisson statistics.

This calculation was done for the 15:14 and 65:64 mean motion resonances. The 15:14 resonance is the most distant first order resonance relative to an oligarch at 1 AU that still lies within the annulus of planetesimals. The 65:64 resonance is the closest MMR for which the libration width is smaller than the spacing between resonances. Higher first order resonances should not exhibit any resolution dependence because they overlap. For planetesimals less massive than about  $10^{22}$  g, the average particle spacing drops below the libration width. Bodies below this mass cutoff, which we will refer to as the resonance heating mass  $M_{res}$ , are more likely to populate MMRs. This provides an explanation for how the oligarchs are preferentially heating the low mass bodies. Comparing with figure 2.4, the mass of the

power law break in the surface density matches very closely with  $M_{res}$ , which also matches the location of the  $10^{22}$  g bump in figure 2.3. Over the course of the simulation,  $M_{res}$  increases by no more than a factor of 2, so the growth mode boundary could easily leave an imprint on the mass spectrum, unlike the shear/dispersion dominated growth boundary, which evolves from  $10^{22}$  to  $10^{25}$  g.

In the restricted three-body problem, the orbital parameters of a test particle receiving energy and angular momentum via a mean motion resonance will evolve such that [126]

$$\frac{de}{da} = \frac{a^{3/2} - 1}{2a^{5/2}e}, \quad (2.10)$$

where  $a$  is in units relative to the semi-major axis of the perturbing body. In the above equation, the inclination is assumed to be negligibly small.

Equation 2.10 can be used to place an upper limit on the change in eccentricity that a planetesimal in resonance will experience. Because any  $\delta a$  larger than the resonance width will remove the planetesimal from the resonant influence of the oligarch,  $\delta e$  is also restricted by the resonance width. Taking  $a \approx 0.95$  (the location of the 15:14 resonance),  $e \approx 10^{-3}$  and  $\delta a \approx 10^{-4}$  (the libration width of the 15:14 MMR) we predict a first order change in eccentricity of  $10^{-4}$ . This value is small relative to the rms eccentricity of the planetesimals, which explains why the effects of the mean motion resonances are not visible in figure 3.2 or in the top right panel of figure 2.4.

Because the resonances are not possible to pick out by eye on an  $a - e$  plot, we ran a modified version of simulation (i), the purpose of which is to show how planetesimal growth proceeds when the mean motion resonances are not present. The initial conditions are identical to those described in section 5.2.2, except that the annulus only extends from 0.98 to 1.02 AU. This effectively depopulates all of the first order mean motion resonances below the 26:25 resonance. It was not possible to use an annulus skinnier than this without introducing strong boundary effects which influence the growth of the planetesimals. This makes it impossible to depopulate all of the resolved resonances. The mass spectrum at the end of the skinny annulus simulation (also evolved for 20,000 years), along with the mass

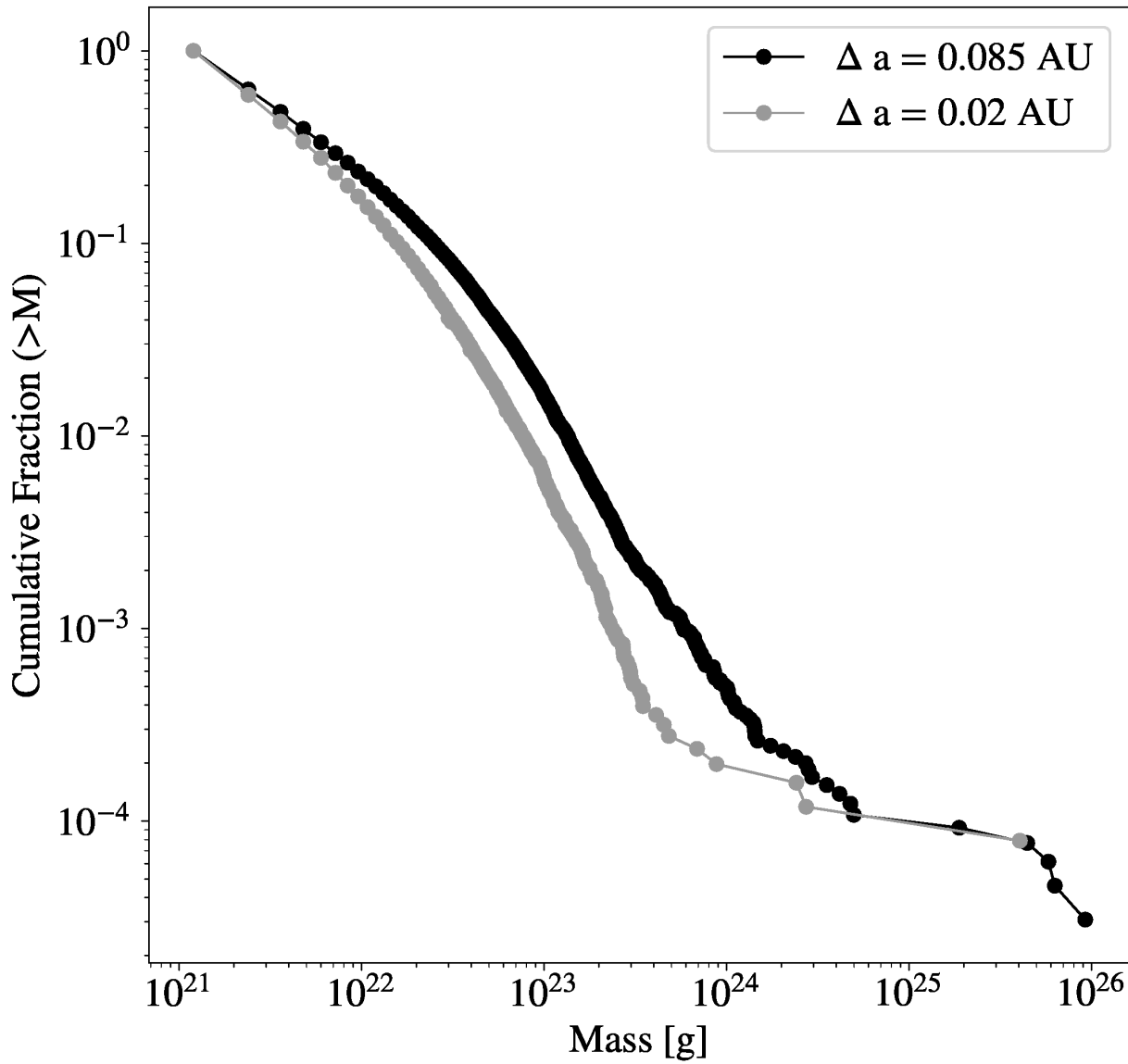


Figure 2.6: The cumulative fraction of bodies as a function of mass in the wide (solid dark curve) and narrow (gray curve) high resolution growth simulations. Decreasing the annulus width, which depopulates resonances, produces a less prominent  $10^{22} \text{ g}$  bump.

spectrum at the end of the high resolution growth simulation, is shown in figure 2.6. With a narrower annulus, the change in slope of the mass distribution below  $10^{22}$  g is noticeably weaker. We attribute this to the fact that the resonant interaction between the planetesimals and oligarchs is diminished because many of the MMRs are now empty.

#### 2.4.2 Planetesimal and Oligarch Mixing

Although figures 2.5 and 2.6 provide strong evidence that the  $10^{22}$  g bump is being produced by mean motion resonances, it is not immediately clear how the resonances affect such a large fraction of the planetesimals. To have a noticeable effect on the mass distribution, the oligarchs must be affecting bodies below  $M_{res}$  everywhere in the disc, not just within the small fraction of space covered by the MMRs at a given time.

We infer that both the oligarchs and planetesimals slowly wander through the annulus due to occasional scattering events. This continually replenishes the population of planetesimals that are sitting inside of resonances. The orbital repulsion effect described by [88], which moves the oligarchs around, alters the location of the mean motion resonances. In addition, we infer that the planetesimals are occasionally scattered by the oligarchs. These two effects slowly cycle different planetesimals through the resonances and allow the oligarchs to eventually heat a large fraction of the small bodies.

In order for this effect to work, the bodies must keep a constant semi-major axis long enough for resonant interactions to play out, while still moving by an appreciable amount over the course of the simulation. The strong scattering time-scale for oligarch- oligarch interactions and oligarch-planetesimal interactions is shown in figure 2.7. This is the timescale over which bodies of mass  $m$  moving with speed  $v$  relative to the local Keplerian velocity will approach each other with an impact parameter  $b \leq Gm/v^2$ . This is sufficient to cause a large deflection and effectively randomize the orbital elements of the bodies. In both cases, the average time between scattering events falls between the longest resonance time- scale (set by the 65:64 resonance) and the growth time-scale (set by the duration of the simulation). This indicates that the scattering is vigorous enough to occur many times over the course of

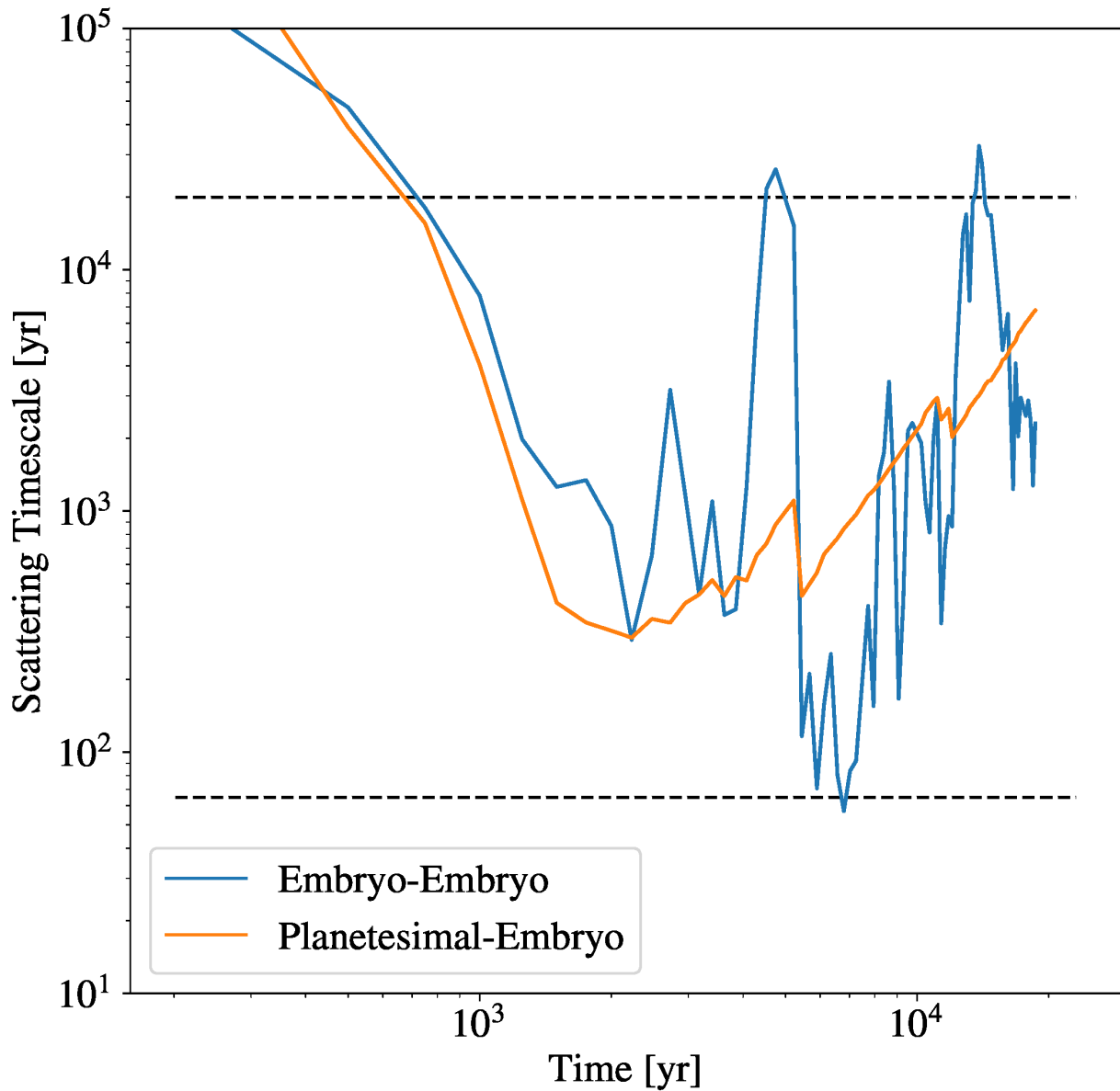


Figure 2.7: The mean scattering time-scale for embryo-embryo (blue curve) and planetesimal-embryo (orange curve) interactions over the course of the high resolution growth simulation. The dashed lines correspond to the simulation time-scale (upper) and longest relevant mean motion resonance time-scale (lower), which is set by the 65:64 resonance.

the simulation, while still being slow enough to allow mean motion resonances to act. The strong scattering rate is given by

$$\dot{N} \approx \frac{\Sigma}{m} \Omega_p R_h^2 \left( \frac{v_h}{v} \right)^4, \quad (2.11)$$

[128] where  $\Sigma$  and  $m$  are the surface density and individual masses of the bodies being scattered,  $\Omega_p$  is the orbital angular velocity of the bodies and  $R_h$  and  $v_h$  are the Hill radius and Hill velocity of the object doing the scattering.

As discussed in section 2.3.1, viscous stirring plays an important role in the dynamical evolution of the planetesimals. The effects of viscous stirring are realized over many weak ( $b \gg Gm/v^2$ ) but frequent encounters. For a population of equal mass planetesimals, the timescale for viscous stirring is given by [68]

$$\tau_{vs} = \frac{\langle e^2 \rangle}{d \langle e^2 \rangle / dt} \approx \frac{1}{40} \left( \frac{\Omega^2 a^3}{2Gm} \right)^2 \frac{4m \langle e^2 \rangle^2}{\Sigma a^2 \Omega}, \quad (2.12)$$

where  $a$  and  $e$  are the semi-major axes and eccentricities of the individual planetesimals. By using the properties of the planetesimal disk at the beginning of simulation (i) in equation 4.12, we find that the viscous stirring timescale is approximately 1000 years. This timescale can be taken as a lower limit because the eccentricity dispersion grows over time.

We also briefly consider the importance of planetesimal-driven migration. This is the coherent change in the semi-major axis of an oligarch due to repeated weak encounters with planetesimals. An upper limit on the planetesimal-driven migration rate of an oligarch is given by [69]

$$\left| \frac{da}{dt} \right| = \frac{a}{T} \frac{4\pi \Sigma a^2}{M_*}, \quad (2.13)$$

where  $a$  is the semi-major axis of the oligarch,  $T$  is the orbital period of the oligarch and  $\Sigma$  is the local surface density of the planetesimal disk. For an oligarch on a 1 AU orbit in a planetesimal disk with  $\Sigma = 10 \text{ g cm}^{-2}$ , the maximum migration rate is roughly  $10^{-5} \text{ AU / yr}$ . [85] showed that this migration rate is greatly reduced for planetesimals whose

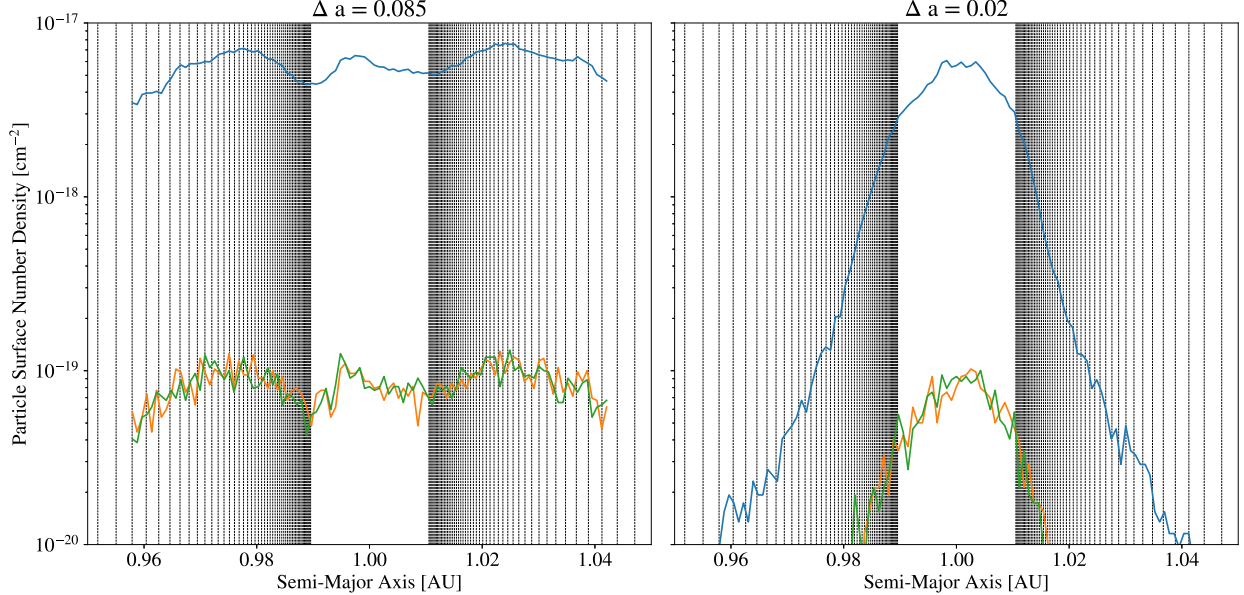


Figure 2.8: Number density profiles of the planetesimals at the end of the  $e_{hi}$  (left) and  $e_{narrow}$  simulations (right). The blue curves represent the number density of planetesimals less massive than the resonance heating mass ( $2 \times 10^{22}$  g) and the orange curves represent the number density of planetesimals above this mass. The green curves show the surface number density of planetesimals randomly drawn from the low mass bin, such that the total number of bodies matches that of the high mass bin. The vertical lines indicate the positions of first order mean motion resonances with an embryo at 1 AU.

encounters are dispersion dominated. In simulation (i), the Hill eccentricity of the smallest planetesimals at the onset of oligarchic growth is larger than 10, in which case the migration rate is reduced by a factor of at least 100 (see figure 7 of [85]). At this rate, it would take an oligarch roughly 1000 years to migrate by a single resonance width ( $10^{-4}$  AU). This is much longer than the resonance timescale and therefore we do not expect that planetesimal-driven migration would disrupt the resonant configuration.

From these results, we conclude that the two simultaneous modes of growth are driven by a difference in the way that loosely and densely packed populations of planetesimals exert dynamical friction on large bodies. In the tightly packed case, energy transfer between the oligarchs and planetesimals is facilitated by mean motion resonances with the largest bodies.

### 2.4.3 Collisionless Dynamics

So far, the most compelling evidence of the resonance heating effect that we have shown is the power law break in the surface density distribution in the bottom right panel of figure 2.4. Because the surface density depends on both the mass distribution and spatial distribution of the planetesimals, it is difficult to tell whether the power law break is caused by resonances moving the planetesimals around or is simply set by the mass distribution. To clear up this ambiguity, we ran an additional set of simulations in which a large planetary embryo is embedded in an annulus of planetesimals, this time ignoring the effects of collisions. This forces the mass distribution to be static.

The initial conditions for these simulations were taken from intermediate snapshots from the runs described in section 5.3. Specifically, the initial conditions are taken from the end of the runaway growth phase, which correspond to the snapshots shown in the top row of figure 2.3. Additionally, a planetary embryo is placed in the centre of the annulus at 1 AU with an eccentricity of 0.02 and an inclination of 0.01. The mass of the embryo is set at  $M = 10^{26}$  g, which is approximately the mass of the largest oligarch at the end of the high resolution simulation. Because collisions are ignored, close encounters are handled with a gravitational softening parameter, the length of which is set to the physical radius of the planetesimals. Both runs are integrated for 2,000 years with fixed timesteps of 0.0025 years. We will refer to the collisionless versions of these simulations as  $e_{low}$  and  $e_{hi}$ , respectively. To further demonstrate that the dynamical excitation of the small planetesimals is driven by mean motion resonances, we also ran a high resolution collisionless simulation with planetesimals outside of the  $a = 0.99$  to 1.01 AU range excluded. We will refer to this simulation as  $e_{narrow}$ .

As we saw previously, the resonance heating effect manifests itself as an increase in the spacing of the low mass planetesimals. Figure 2.8 shows the planetesimal surface number density at the end of the  $e_{hi}$  (left) and  $e_{narrow}$  (right) simulations described above. The vertical dashed lines indicate the locations of the non-overlapping first order mean motion resonances with the embryo. The blue curves show the number density of planetesimals below

the resonance heating mass, which is  $2 \times 10^{22}$  g in this case. The orange curves show the number density of planetesimals above this mass. Finally, to demonstrate that the difference in dynamical behavior between the low and high mass planetesimals is a population effect, the green curve shows the number density of a subsample of planetesimals randomly drawn from the low mass group, such that the total number of planetesimals in the subsample matches that of the high mass group.

In both cases, the particle number density is slightly enhanced around 1 AU, which is due to bodies trapped in the corotation resonance with the embryo. For the wide annulus, the surface number density decreases and then begins to increase again approximately 0.01 AU away from the embryo. As is evident in the left panel of figure 2.8, the location at which the number density begins to increase corresponds to the location of the closest non-overlapping ( $j < 65$ ) mean motion resonances. Due to conservation of the Jacobi energy (see equation 2.10), interior MMRs will push bodies inward, while exterior resonances move bodies outward. This effect was also observed by [150] (see model B) in that the density decreases to the right of interior resonances and increases to the left. Because our setup contains many closely spaced resonances, the cumulative effect is that the density smoothly increases as one moves through the resonances.

Hence, the number density distribution acquires a 'W' shape around the embryo, with the low points corresponding to the inner edges of the resonant regions. An inspection of the earlier snapshots from this simulation shows that the 'W' structure becomes deeper and narrower with time. This is consistent with our resonance heating argument because the resonance time-scale decreases as one moves away from the embryo. The stronger, closer resonances become effective last, causing the profile to deepen and narrow with time.

The strength of the resonance heating effect depends on the number density of bodies outside of the  $0.99 < a < 1.01$  AU region, where the resonances are not overlapping. The 'W' shaped structure relative to the noise of the high mass (orange) and subsampled population (green) is weak compared to the low mass population (blue) due to the fact that there simply aren't many bodies sitting within the resonances. This structure is entirely absent from the

narrow annulus, shown in the right hand panel of figure 2.8 because the planetesimal number density near the resonances is too low. We infer that this decrease in number density of the low mass bodies adjacent to the embryo must also be present in the high resolution growth simulation and is enhancing the collision rate below the resonance heating mass.

We also examine the eccentricity evolution of the planetary embryo in the three collisionless simulations, shown in figure 2.9. A decrease in the eccentricity of the embryo indicates that energy is being lost to the planetesimals. A steeper drop in eccentricity implies that the exchange happens more quickly and that the effects of dynamical friction are stronger. Only when the resonances are properly resolved and populated does the exchange appear to happen quickly. In both the  $e_{narrow}$  and  $e_{low}$  simulations, the decrease in eccentricity of the embryo is gradual. This implies that dynamical friction is stronger and energy and angular momentum exchange between the oligarchs and planetesimals proceeds faster when the mean motion resonance heating is effective. In the  $e_{hi}$  simulation, the eccentricity of the embryo begins to drop more steeply after about 1000 years. This effect is also noticeable for the  $e_{narrow}$  simulation, although it happens sooner. Because we are suddenly dropping a massive body into the annulus of planetesimals, the system likely requires some time to return to a state of quasi-equilibrium. The two-body relaxation time, which is well-described by the viscous stirring timescale [68] appears to roughly coincide with the change in slope for each of the curves in figure 2.9, although the connection between the relaxation of the planetesimals and the eccentricity evolution of the oligarch is not immediately clear. In the  $e_{low}$  simulation, the change in slope may not be visible due to the fact that the two-body relaxation time is nearly instantaneous due to the small particle count (the relaxation time scales as  $N/\ln N$ ).

To verify the effectiveness of the resonant interactions, we next examine the evolution of the resonant arguments. The libration frequency of a planetesimal in resonance with an embryo is given by [126]

$$\omega_0^2 = -3j_2^2 C_r n e^{|j_4|}, \quad (2.14)$$

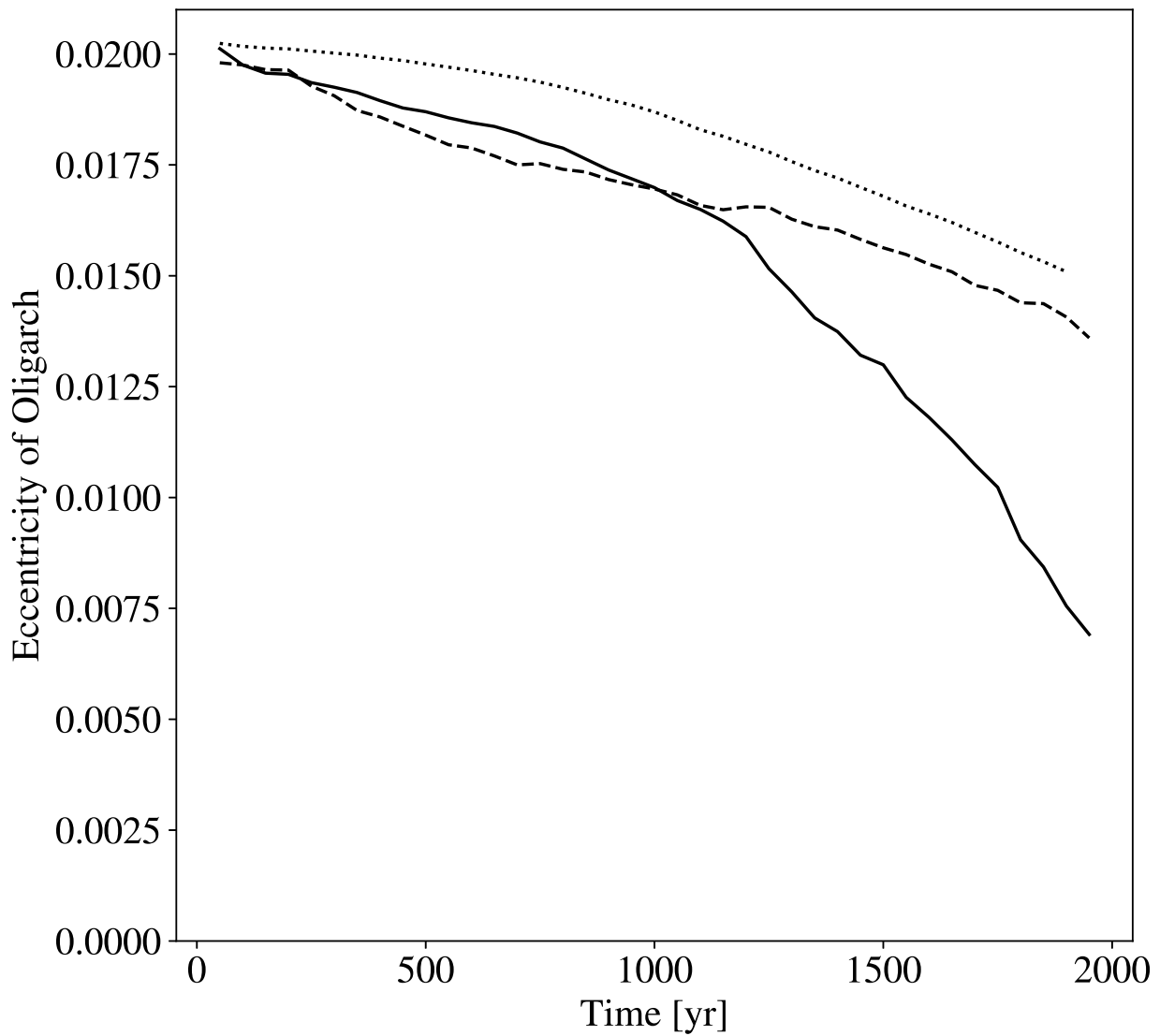


Figure 2.9: Time evolution of the eccentricity of the oligarch in the  $e_{hi}$  (solid),  $e_{narrow}$  (dotted) and  $e_{low}$  (dashed) simulation.

where  $j_2 = -15$  and  $j_4 = -1$  for the 15:14 MMR and  $n = \sqrt{GM_*/a^3}$  is the mean motion of the planetesimal. For a planetesimal with a typical eccentricity of  $10^{-3}$  inside the 15:14 mean motion resonance with a  $10^{26}$  g embryo, the libration period is approximately 1000 years. For this reason, it is likely that a particle will undergo only a partial libration cycle before being removed from the resonance by two-body scattering. This makes it difficult to verify the resonant interaction by searching for libration, rather than circulation of the resonant arguments. However, this also implies that the resonances will cause permanent changes to the energy and angular momentum of the planetesimals. In canonical perturbation theory, the action conjugate to the resonant argument should evolve secularly because there is a near-constant term in the partial derivative of the Hamiltonian with respect to the resonant angle. If the viscous stirring timescale, which is the mechanism responsible for the removal of planetesimals from resonance is short compared to the libration period, this secular interaction produces a permanent change in the action (and therefore the energy and angular momentum) of a planetesimal (see the text following equation 10 in [171] for a further discussion of this).

The typical change in the resonant arguments of the planetesimals from the  $e_{hi}$  simulation over multiple synodic periods is shown in figure 2.10. The resonant argument is given by [126]

$$\phi = j_1\lambda_e + j_2\lambda_p + j_4\varpi_p, \quad (2.15)$$

where  $j_1 = -j_2 - j_4 = 16$  for the 15:14 MMR.  $\lambda_e$  and  $\lambda_p$  are the mean longitudes of the embryo and planetesimal, respectively and  $\varpi_p$  is the longitude of pericenter of the planetesimal. The  $\Delta\phi$  shown in figure 2.10 is the change in this resonant argument between  $t=1500$  and  $t=1550$  years, well after the system has relaxed back to a state of quasi-equilibrium. The blue diagonal lines represent the change in the resonant argument due to the Keplerian shearing of the disc. This quantity is derived by taking the time derivative of equation 2.15, which is given by

$$\frac{d\phi}{dt} = j_1 \left( \frac{d\varpi_e}{dt} + \frac{dM_e}{dt} \right) + j_2 \left( \frac{d\varpi_p}{dt} + \frac{dM_p}{dt} \right) + j_4 \frac{d\varpi_p}{dt}. \quad (2.16)$$

Only the mean anomaly  $M = nt$  changes due to the Keplerian shear and so

$$\Delta\phi_{Kepler} = \sqrt{GM_*} \left( j_1 a_e^{-3/2} + j_2 a_p^{-3/2} \right) \Delta t, \quad (2.17)$$

where  $\Delta t$  is the time interval that we are considering. Note that at the nominal resonance location,  $\Delta\phi_{Kepler} = 0$ .

Over a 50 year time interval, which is approximately 3 times longer than the synodic period with the embryo, the change in the resonant arguments of the planetesimals appear to be dominated by the differential rotation of the disc. Near the nominal resonance location, the change in  $\phi$  is small. The fact that many planetesimals remain within the resonance width and undergo only small changes in  $\phi$  over multiple synodic periods demonstrates that the resonant interaction between the planetesimals and the embryo is able to proceed. Because the libration period is not short compared to the scattering timescale, the resonant interactions will cause permanent changes to the energy and angular momentum of the planetesimals.

## 2.5 Implications of Simplifying Assumptions

### 2.5.1 Gas Drag

Although the effects of gas drag are weak during the planetesimal accretion stage, we will briefly consider its effect to ensure that it would not alter or remove the  $10^{22}$  g bump. One way to describe the importance of gas drag on a planetesimal is with the stopping time [1]. In the Stokes regime, where the mean free path of gas particles is much smaller than the radius of the planetesimals ( $\lambda \ll s$ ), the stopping time is given by

$$t_s = \frac{2m}{C_D \pi s^2 \rho_g v}. \quad (2.18)$$

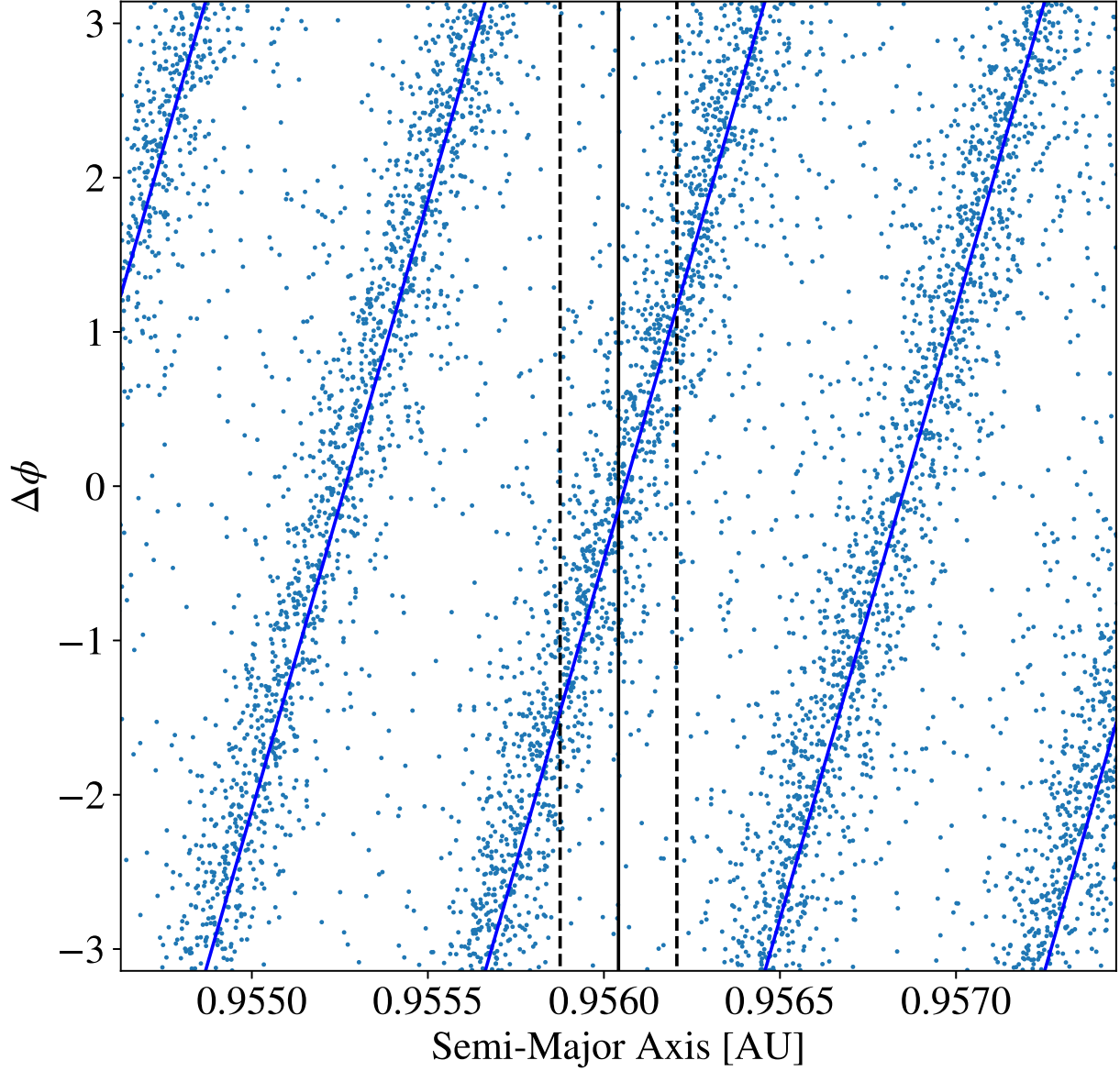


Figure 2.10: The change in the resonant argument for the oligarch and planetesimals near the 15:14 MMR over a 50 year time interval from the  $e_{hi}$  simulation. The solid vertical line designates the nominal resonance location and the dashed vertical lines indicate the minimum libration width. The diagonal blue lines represent the change in  $\phi$  due to the Keplerian shear of the disc, which is calculated analytically.

Here,  $\rho_g$  is the local density of the gas and  $C_D$  is the drag force coefficient, which is of order unity in this regime. The gas density of the solar nebula is approximately  $2 \times 10^{-9}$  g cm $^{-3}$  at 1 AU [63].

The relative velocity between the planetesimals and the gas is set by both the random motions of the planetesimals and the fact that the gas orbits at a sub-Keplerian speed due to its internal pressure support. The planetesimal velocity due to random motions is given by [102]

$$v_{rnd} = v_k \sqrt{\langle e^2 \rangle + \langle i^2 \rangle}. \quad (2.19)$$

At the beginning of the simulation (i),  $v_{rnd}$  is on the order of  $10^3$  cm s $^{-1}$ . The headwind speed due to the sub-Keplerian motion of the gas is given by [1]

$$v_{gas} = v_k \left( 1 - (1 - 2\eta)^{1/2} \right). \quad (2.20)$$

At 1 AU in the solar nebula,  $\eta \approx 0.002$ , which gives  $v_{gas} \approx 6000$  cm s $^{-1}$ . From equation 2.18, the smallest planetesimals in simulation (i) have a stopping time on the order of  $10^4$  years. This is much longer than the synodic period of the relevant planetesimal-oligarch resonances, therefore we expect the dynamics of even the smallest planetesimals to be entirely dominated by the resonances.

Additionally, gas drag can drive the inward radial drift of small bodies. Although the relatively large stopping time of the planetesimals suggests that this effect should be unimportant, the resonances are narrow enough that even a small amount of radial drift could quickly remove planetesimals from their influence. The radial drift velocity of a particle is given by [166]

$$v_r = -\frac{2v_{gas}}{\Omega t_s + (\Omega t_s)^{-1}}. \quad (2.21)$$

where  $\Omega$  is the orbital angular frequency of the body being considered. Using the values for  $v_{gas}$  and  $t_s$  described above, the inward radial drift speed of the smallest planetesimals is 0.1

$\text{cm s}^{-1}$ . At this rate, a planetesimal will drift across a typical resonance width ( $10^{-4}$  AU) in about 1000 years. This is comparable to the viscous stirring timescale, which suggests that radial drift should not have a significant effect on the resonant dynamics.

Massive bodies can create density waves in the gas disk which carry away angular momentum [52, 53] through an effect known as type I migration (for a recent review see [14]). The strength of this effect scales linearly with the mass of the body and should therefore be most effective for planetary embryos. In addition to gas drag causing planetesimals to radially drift across resonances, type I migration can cause planetary embryos to drift inwards, potentially moving the resonances before they have a chance to act on the planetesimals. [159] provides an analytic expression for the torque exerted on a body embedded in a three-dimensional gaseous isothermal disk as

$$\Gamma = -(1.364 + 0.541\alpha) \left(\frac{m}{M_*}\right)^2 \left(\frac{r\Omega}{c_s}\right)^2 \Sigma r^4 \Omega^2, \quad (2.22)$$

where  $\alpha$  is the power law index of the radial surface mass density profile  $\Sigma \propto r^{-\alpha}$  of the gas and  $c_s$  is the local sound speed of the gas,  $m$  is the mass of the body,  $\Omega$  is the orbital angular frequency of the body and  $r$  is the orbital distance of the body. The radial migration velocity is given by

$$\dot{r} = \frac{-2r\Gamma}{L}, \quad (2.23)$$

where  $L = m(GM_*r)^{1/2}$  is the total angular momentum of the body. For a  $10^{26}$  g embryo orbiting at 1 AU and taking  $\alpha = 3/2$ ,  $\Sigma = 1700 \text{ g cm}^{-2}$  and  $c_s = 10^5 \text{ cm s}^{-1}$  [63], the inward migration speed is  $2 \times 10^{-7} \text{ AU yr}^{-1}$ . At this rate, the 15:14 MMR with an embryo will migrate by a entire resonance width in roughly 500 years, which is much longer than the synodic period. It should be noted that the analysis of [159] has been shown to produce migration rates that are up to a factor of  $10^3$  too large to be consistent with observed populations of exoplanets [67, 4, 115]. The migration timescale derived above should therefore be taken strictly as a lower limit.

As migration proceeds, planetesimals can have their spatial distribution altered as they become trapped in exterior resonances with protoplanets [168]. A necessary condition for resonant trapping to occur is that the drift timescale of a planetesimal across a resonance must be much longer than the libration period [37]. As we calculated in section 2.4.3, a typical libration period is around 1000 years. This is comparable to the timescale for **two-body** scattering and also for radial drift of planetesimals across a resonance due to gas drag. Therefore, we do not expect that exterior resonances should be effective at trapping drifting planetesimals.

### *2.5.2 Inflated Collision Cross Section*

As discussed in section 2.2.2, enhancing the geometric collision cross section  $f$  of the planetesimals by a factor of 6 only slightly reduces the effectiveness of gravitational scattering. More importantly, varying  $f$  alters the accretion timescale. The implication of this is that a longer accretion timescale causes oligarchic growth to commence later when the disk is more dynamically excited. The dynamical excitation of the disk, which is set by the rms eccentricity, alters the libration width of planetesimals in resonance with the oligarchs. In section 2.4.1, we argued that the intersection between the libration width and the radial spacing between planetesimals sets the location of the bump in the mass distribution. Because the radial spacing between planetesimals increases with mass and the libration width of the resonances gets larger with time, the mass of the bump would be larger had we used  $f = 1$ .

It is difficult to predict exactly how much  $f$  reduces the accretion timescale, but [87] showed that it is by no more than factor of  $f^2$ . Integrating equation 4.12, the rms eccentricity scales with  $t^{1/4}$ . Having enhanced the collision cross section by a factor of 6, the rms eccentricity should be a factor of  $(f^2)^{1/4} \approx 2.5$  times larger with a realistic collision cross section. Using equation 2.6, a factor of 2.5 increase in the eccentricity of a planetesimal increases the libration width by a factor of about 1.6. Looking at figure 2.5, this would cause an extremely insignificant change in the resonance heating mass.

### 2.5.3 Fragmentation

Because our model does not include the effects of collisional fragmentation, we examine the statistics of the collisions in simulation (i) to estimate its effects had it been included. Here, we find that roughly 60 percent of the collisions occur with a relative velocity larger than the mutual escape velocity of the two planetesimals. Assuming that the planetesimals are rubble piles with no internal strength, these high velocity collisions should be completely disruptive. Previous studies of planetesimal accretion have shown that including the effects of fragmentation tends to slow down the accretion process, but does not qualitatively change it [174, 98].

If we separate the collision statistics into those occurring between bodies below the bump mass ( $< 10^{22}$  g) and those above the bump mass, we do not see a significant difference in the relative amount of catastrophic collisions. Above the bump mass, about 60 percent of collisions occur at disruptive velocities, while 70 percent of collisions between bodies below the bump mass occur at these high relative velocities. Because we do not have multiple simulations to draw from, it is difficult to estimate errors to tell whether this difference is statistically significant.

Assuming that disruptive collisions are not significantly more common below the bump mass, we expect that fragmentation would alter our results by lengthening the accretion timescale. As discussed in the previous section, the location of the bump depends on the rms eccentricity of the planetesimals during the oligarchic growth phase. If this phase takes longer to commence, the libration widths of the resonances would be larger when the embryos form, which increases the mass below which the resonant heating is effective. Although it is difficult to determine by exactly how much fragmentation extends the accretion timescale, statistical models of planetesimal growth show that  $10^{26}$  g embryos can be formed in  $10^5$  years [174] when the effects of fragmentation are included. We showed in the previous section that a factor of 36 increase in the accretion timescale (720,000 years) makes a negligible difference in the location of the bump in the mass spectrum. Similarly, we expect that including the

effects of fragmentation would make a negligible contribution to the bump mass.

## 2.6 Dependence on Initial Planetesimal Mass

In order to demonstrate that our results are robust, and also to gain some insight into how the resonance heating mass is related to the initial planetesimal mass, we ran two more simulations of planetesimal growth at intermediate resolutions. Our choice of initial planetesimal mass in the high resolution simulation was somewhat arbitrary and understanding how this parameter affects the resulting distribution of masses is necessary in order to connect our results with observations of small Solar System bodies.

The configurations used were identical to the high resolution run described in section 5.2.2, except that the particle count was changed. These two additional runs contained 250,000 and 500,000 starting planetesimals, which corresponds to  $m = 2.4 \times 10^{21}$  and  $m = 4.8 \times 10^{21}$  g, respectively, at the same surface density. To match the same eccentricity dispersion as the models described in section 5.2.2, we used  $\langle e^2 \rangle^{1/2} = 3.17h/a$  and  $\langle e^2 \rangle^{1/2} = 2.52h/a$ , with the inclination dispersion set to half of those values.

Figure 2.11 shows the mass spectrum at  $T = 20,000$  years in the high resolution growth simulation, along with the intermediate resolution growth simulations mentioned above. In all three cases, the bump in the mass distribution approximately matches up with the resonance heating mass. There is a clear positive trend between the resonance heating mass and the initial planetesimal mass  $m$ , which we attribute to two things. First, larger planetesimals will be spaced further apart for a fixed disc surface density. This pushes the intersection point between the planetesimal spacing and libration width to higher mass. Secondly, larger initial planetesimals will cause oligarchic growth to begin at a higher mass [122]. This increases the libration width of the resonances, which moves the intersection between planetesimal spacing and resonance width to a higher mass.

The size frequency distribution of asteroid belt objects is known to exhibit a power law break around around  $1.05 \times 10^{21}$  g [77]. The fact that the knee in the mass distribution is reproducible and appears sensitive to  $m_0$  demonstrates that this value could be tuned to

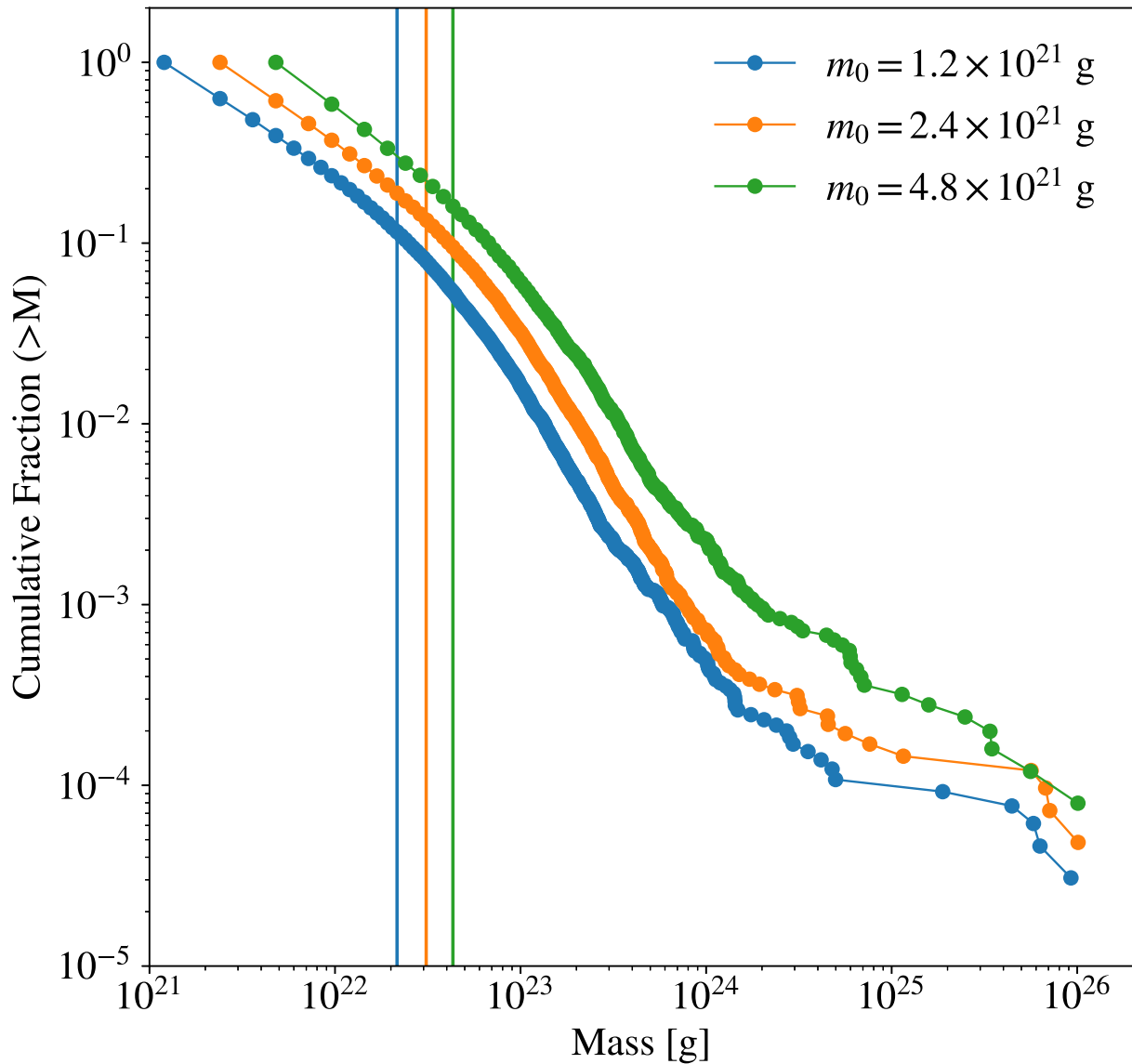


Figure 2.11: The cumulative mass distribution of planetesimals at the end of the three high-resolution growth simulations. The vertical lines represent the mass at which the planetesimal spacing in semi major axis falls below the libration width of the MMRs.

constrain planetesimal formation models by matching the observed mass of the bump with simulations. There is evidence that the shape of the SFD for asteroid belt objects more massive than about 100 km reflects that of the primordial population [119]. Although the purpose of this paper is not to try to tune the model to match observations, we show the mass distribution from the  $N = 10^6$  growth simulation alongside the SFD of asteroid belt objects [19] in figure 2.12 for comparison. Although the bump location in all of our simulations is larger than 100 km, a smaller initial planetesimal mass would probably produce a better match. The slope of the mass distribution above the bump mass matches reasonably well in both cases, but the slopes on the low mass end are discrepant. As the results from figure 2.6 show, a wider annulus tends to produce a shallower slope below the resonance heating mass. A better match might be made by simulating a wider annulus which includes resonances further from the embryos. Unfortunately, simulating an annulus wide enough to resolve all of the first order MMRs would require an extremely large number of particles.

As discussed in section 2.5, we do not expect the simplifying assumptions of perfect accretion and the absence of gas drag, along with the artificially inflated collision cross section to have a significant effect on the size distribution of accreted bodies. Because we have proposed that the initial planetesimal size could be reduced to better match the break in the asteroid belt SFD, we briefly consider the smallest sized planetesimals for which the resonant heating effect is not damped by gas drag. This will occur when the synodic period of the resonance becomes comparable to the stopping time. The latter quantity is given by equation 2.18 and scales linearly with planetesimal size. For 100 km planetesimals, we showed that the stopping time is around  $10^4$  years. The stopping time becomes comparable to the synodic period for bodies smaller than a few km in size, at which point our calculations would become invalid.

## 2.7 Summary and Discussion

We have revealed a new mode of growth during the planetesimal accretion phase by simulating the interaction between oligarchs and planetesimals at unprecedented resolution.

Shortly after the onset of oligarchic growth, a bump develops in the mass distribution of planetesimals. Below the bump mass, the surface density of planetesimals follows a shallower power law distribution. The break occurs near the mass at which the radial spacing of planetesimal matches the libration width of first order mean motion resonances with the oligarchs. These resonances, which are preferentially populated by the more numerous low mass planetesimals, act as effective pathways for dynamical friction to transfer energy and angular momentum from the oligarchs to the planetesimals. This result is analogous to the resolution dependence that [171, 170] found when examining the interaction between the bar and halo of a galaxy. This also matches the results of [131] and [30], which showed that finer granularity in a planetesimal disc increases the effectiveness of dynamical friction. Bodies below the bump mass, which are packed tightly enough together to populate the resonances receive a disproportionate amount of energy and angular momentum from the oligarchs. Because this happens when the disc is hot enough to render gravitational focusing ineffective, this enhances the growth of the smallest planetesimals and produces a bend in the mass distribution.

Additionally, we ran a high resolution planetesimal growth simulation in which the width of the annulus was limited to exclude some of the resonances. Doing so mostly suppressed the formation of the bump near the resonance heating mass, although it did not completely get rid of it. We attribute this to the fact that we cannot make the annulus narrow enough to exclude all of the important resonances without introducing strong boundary effects which interfere with planetesimal growth. The fact that the feature in the mass distribution was greatly diminished when the many of the resonances were excluded is strong evidence that the MMRs are responsible for creating this bump.

We confirmed this dynamical effect by placing a massive oligarch into a smoothly varying distribution of planetesimal masses. Within a few thousand orbits, the low mass planetesimals sitting within the zone of influence of the resonances began to migrate outwards, leaving a dearth of low mass bodies around the embryo. This effect did not appear when we simulated a similar heterogeneous distribution of masses, but limited the width of the annulus to

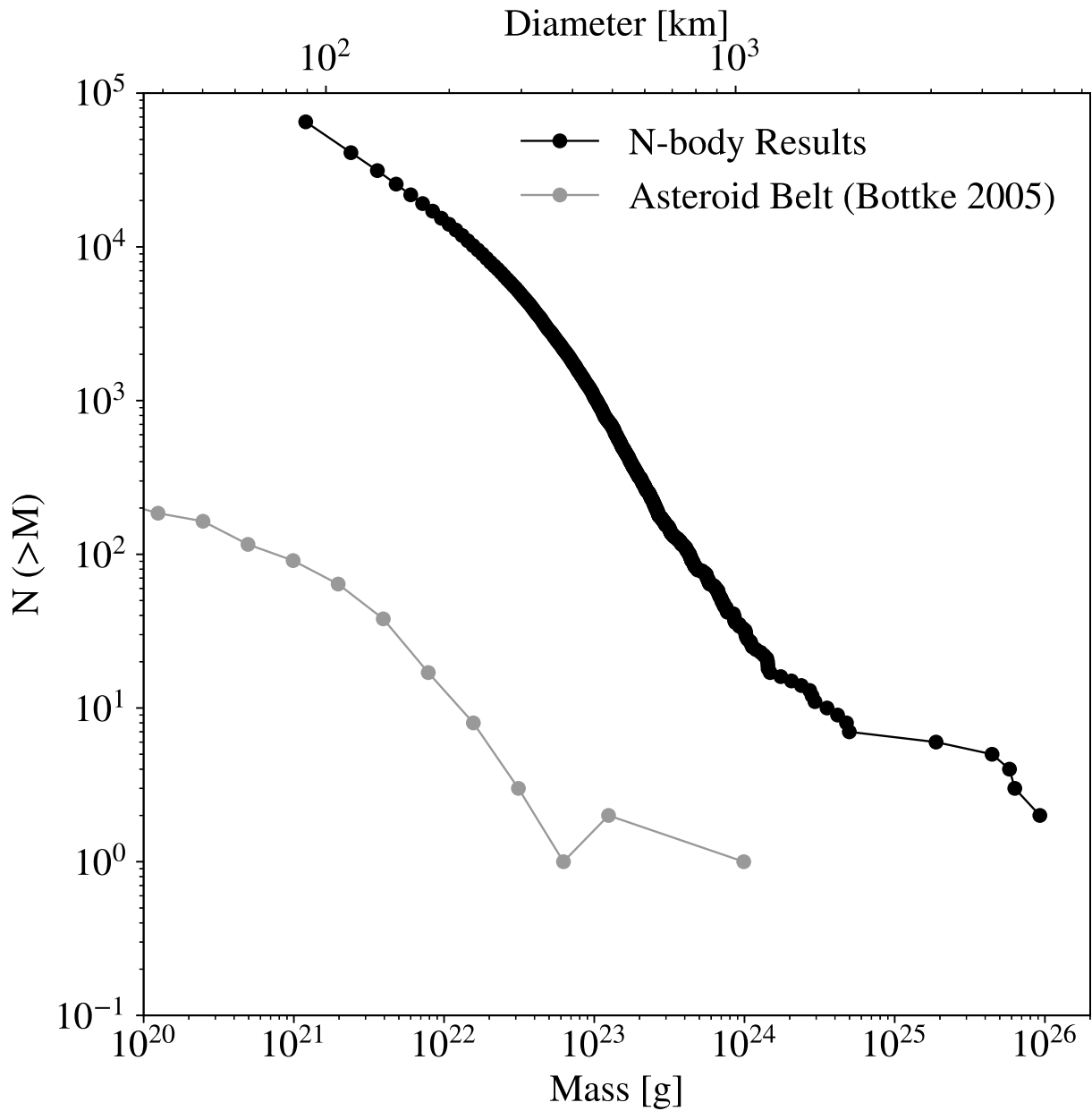


Figure 2.12: A comparison between the cumulative number of objects in our high resolution growth simulation (black curve) and the present day asteroid belt [19] (gray curve) as a function of size and mass.

exclude many of the MMRs. Additionally, the eccentricity of the oligarch decreased much more quickly when placed in a finely resolved disc with populated MMRs.

This result is significant because it suggests a new potentially observable link between the planetesimal formation process and the residual population of planetesimals in the present day Solar System. We showed that the mass distribution in our highest resolution simulation looks qualitatively similar to the SFD of objects in the asteroid belt, which, for objects larger than  $\approx 100$  km, reflects the population of planetesimals at the end of the accretion stage [119]. We demonstrated that tuning the initial planetesimal mass in our simulation changes the location of the bump. This could potentially be matched with the observed 100 km feature in the asteroid belt to constrain planetesimal formation models. Additionally, using a wider annulus, which populates more of the first order MMRs, tends to produce a shallower slope on the low mass end of the mass distribution, which matches more closely with observations.

As discussed in section 2.3.2, there are a couple of explanations for this bump feature which were obtained from statistical models of planetesimal coagulation. It is unlikely that this resonance heating effect would naturally emerge from a statistical growth model unless it was explicitly built in. For this reason, this resonance heating effect has likely not been considered before. To our knowledge, no one has ever run an N-body simulation of planetesimal accretion to the oligarchic growth phase at this resolution.

Our results show that a feature similar to the power law break in the size distribution of asteroid belt objects can be produced without the effects of fragmentation, in contrast to [119]. Although our model does not account for the effects of fragmentation, the statistics of collisions above and below the bump mass are quite similar. We do not expect that including the effects of collisional fragmentation would significantly affect the location or strength of the bump. Regardless, these results demonstrate that a careful treatment of the dynamics is necessary to properly model planetesimal accretion during the oligarchic growth phase.

## 2.8 Appendix A: Mean Motion Resonance Test

To demonstrate that CHANGA can properly track the motions of bodies in a mean motion resonance over many orbits, we present a test case with a central star, a perturbing massive body and a planetesimal. Although the simulations presented in this paper are far more complex than this three body setup, the resonant interactions that produce the bump in the mass distribution are driven by the most massive bodies in the simulation. Because there are only a handful of these massive bodies, the tree approximation should have a negligible effect on the force contribution from these objects. For this reason, the behavior shown here should also apply to the previously presented simulations of planetesimal growth.

To test that the resonant interaction evolves correctly, we follow the evolution of the planetesimal in the complex x-y plane defined by the variable [44]

$$z = (GM_*a)^{1/4} \left\{ 2 \left[ 1 - (1 - e^2)^{1/2} \right] \right\}^{1/2} \exp[i(\bar{\omega} - \lambda)], \quad (2.24)$$

where  $a$ ,  $e$ ,  $\bar{\omega}$  and  $\lambda$  are the semi-major axis, eccentricity, longitude of perihelion and mean longitude of the planetesimal. If these values are recorded at the moment of opposition between the perturber and the planetesimal ( $\lambda - \lambda_p = \pi$ ), the trajectory of the planetesimal should trace out a closed loop in the x-y plane. This indicates that an approximate Hamiltonian of the system is preserved and the resonant interaction is properly accounted for.

Figure 2.13 shows the evolution of the planetesimal over 20,000 years (about 130 synodic periods) in the complex x-y plane. The orbital elements of the planetesimal at the exact moment of opposition are calculated via linear interpolation. The perturbing body is placed at 1 AU on a circular orbit and has a mass of  $10^{26}$  g, which is similar to the final mass of the embryos presented in simulation (i). The planetesimal is given a mass of  $1.2 \times 10^{22}$  g and is placed on a coplanar orbit with a semi-major axis of 0.95501, which corresponds to the nominal location of the 15:14 mean motion resonance with the perturber. To start the planetesimal in a stable equilibirum, its orbital eccentricity is set to  $10^{-2}$  so that the

longitude of pericenter is well-defined. Fixed timesteps of  $\Delta T = 0.0025$  yrs are taken, which is the same as the previous simulations. In this configuration, the Jacobi constant is small and so the planetesimal follows a circular trajectory in the complex plane. Because the perturbing body is on a circular orbit, the forced eccentricity is zero and the trajectory of the planetesimal is centered at the origin. Most importantly, trajectory of the planetesimal appears to follow a closed loop, which indicates that an approximate Hamiltonian is preserved and the integration is accurate enough to follow mean motion resonances in this configuration.

## 2.9 Appendix B: Tree Approximation and Opening Angle

The results we have presented in this work depend on repeated two-body interactions between planetesimals. As discussed in section 2.5, the location of the bump in the mass spectrum depends on the amount of viscous stirring that has occurred before oligarchic growth commences. Additionally, the resonant heating effect presented in this work requires that viscous stirring is not too vigorous as to prevent repeated conjunctions. Here, we examine the impact of force calculation errors from our tree algorithm on these phenomena.

CHANGA calculates the gravitational interaction force between particles via a tree approximation. Particles that only weakly contribute to the gravitational potential are grouped together during the force calculation phase. The opening angle  $\Theta$  controls how likely particles are to get grouped together during this stage. Because the lowest mass particles contribute weakly to the surrounding potential, the gravitational contribution from these bodies is more approximate. This can potentially alter the effectiveness of viscous stirring. For this reason, we re-ran the  $e_{hi}$  simulation with a smaller, more restrictive opening angle of  $\Theta_{BH} = 0.35$  to test whether the tree approximation is noticeably altering the behavior of viscous stirring. Because we expand forces from tree nodes to hexadecapole order, an opening angle that is a factor of 2 smaller should reduce the error in the force calculations by a factor of 16. Additionally, we test  $\Theta_{BH} = 0.7$  with a timestep of  $\Delta T = 0.00125$  years.

A comparison between the three versions of the  $e_{hi}$  simulation is shown in figure 2.14. In all cases, the oligarch slowly loses eccentricity for about 1000 years before the curve

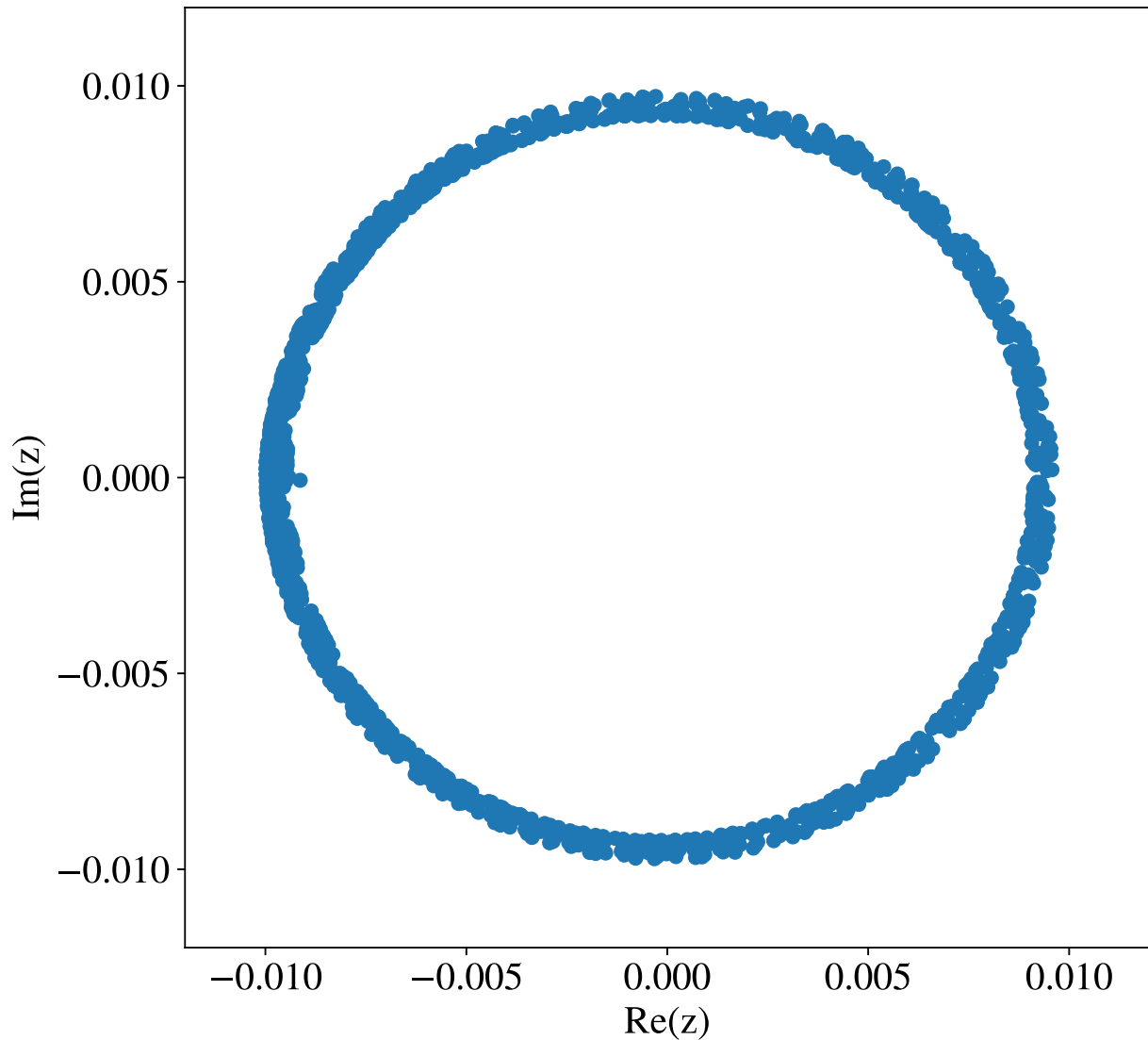


Figure 2.13: The evolution of the planetesimal in the complex plane defined by equation 2.24. Each point represents the state of the system when the perturber and planetesimal are at opposition.

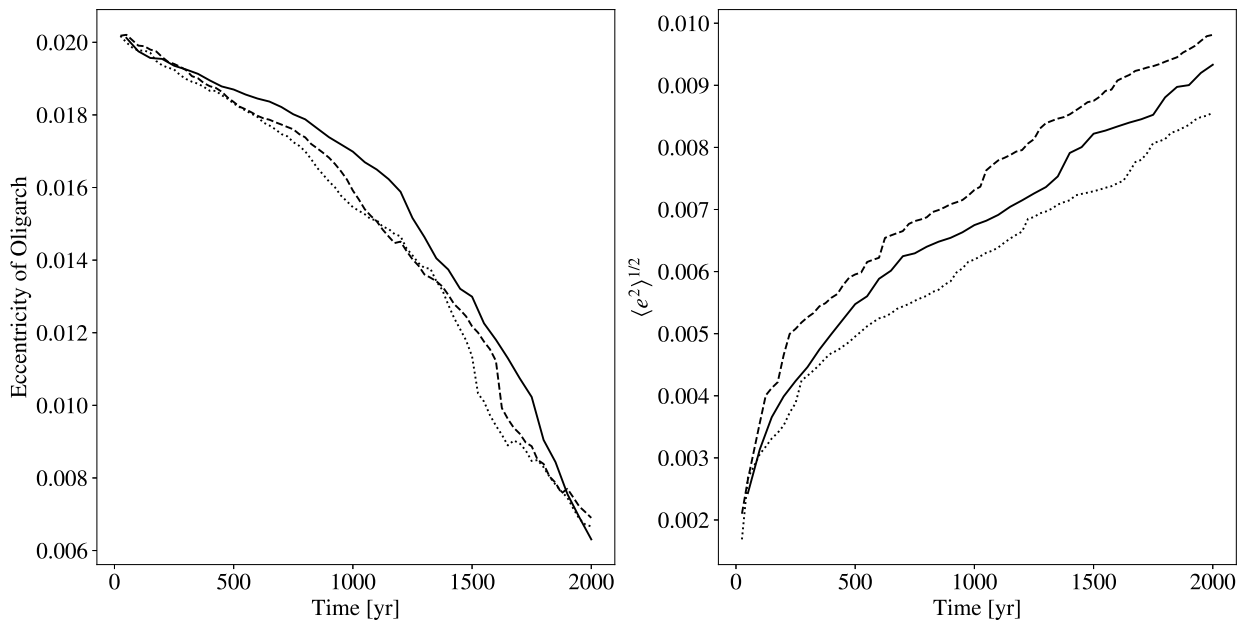


Figure 2.14: Time evolution of the eccentricity of the oligarch (left) and rms eccentricity of the smallest planetesimals (right) in the  $e_{hi}$  simulation with an opening angle  $\Theta_{BH}$  of 0.7 (solid line) and 0.35 (dashed line). The dotted line shows  $\Theta_{BH} = 0.7$  with a timestep that is half as large.

drops more steeply. With a smaller opening angle or a smaller timestep size, the downturn appears to happen slightly sooner. By the end of the simulation, the resulting eccentricities of the oligarchs are still within 10 percent of each other. The right hand panel of figure 2.14 shows the evolution of the rms eccentricity of the lowest mass planetesimals. There is some divergence between the curves early on, but this only lasts for a fraction of the viscous stirring timescale. As was shown in section 2.5, it would take a much larger difference in the rms eccentricity than is seen here here to alter the bump in the mass spectrum. The evolution of the rms inclination of the planetesimals is qualitatively similar in all three cases.

## Chapter 3

# DETECTING COLD JUPITERS VIA COLLISIONAL GRINDING OF PLANETESIMALS

### **3.1 *Introduction***

Recent observations of circumstellar discs by ALMA have revealed a rich variety of substructure. Features such as gaps and asymmetries [5, 139, 72, 6, 29] in the emission provide diagnostics for the physical processes that drive the evolution of the discs. In many gas-rich systems, these gap features are argued to indicate the presence of a giant planet, either embedded in the disc [39] or orbiting adjacent to it, although the details of gas-dust interactions can have strong effects on the resulting morphologies[43]. In gas-poor/debris systems, a giantplanet perturber can also influence the structure of the dust continuum emission. For example, a misaligned giant planet can produce nonaxisymmetric features such as warps [?], highly eccentric perturbers can produce structures through secular interactions [137, 138], and mean motion resonances (MMRs) can open gaps [130, 156, 157].

Collisions between planetesimals are thought to be the principal source of dust for debris discs (see[178]). Although some amount of primordial dust is likely still present during the early stages of debris disc evolution, ongoing collisions between small bodies will augment this and could be used to trace the underlying dynamical activity of the planetesimals. This process was directly detected when the putative object Fomalhaut b was confirmed to be an expanding debris cloud, most likely from a planetesimal collision [49].

[40] showed that collisional dust that is generated near the gap opened by a giant planet in the inner regions of a transition disc should produce a distinct observable marker that could be used to infer the presence of the planet. In a followup study, it was found that morphological differences in the dust emission could be used to determine whether the planet

had a circular or eccentric orbit [41]. Moreover, substructure due to mean-motion resonances (MMRs) with a giant planet may hold additional clues that could be used to constrain the properties of the planet. The width of a resonance is set by both the mass of the perturbing planet and the unperturbed eccentricity of the planetesimals, which is in turn set by the eccentricity of the planet through secular forcing. Therefore, the planetesimal collision profile and potentially the structure of second generation dust produced near MMRs may encode information about both the mass and eccentricity of the planet.

The dynamics governing the motion of bodies near MMRs is extremely nonlinear, as is determining what the collision rates between planetesimals should look like in these regions. For a collection of bodies massive enough to experience the effects of gravitational focusing, a large eccentricity dispersion tends to reduce the probability of collision, while enhancements in surface density tends to increase it. Due to conservation of the Jacobi energy, MMRs simultaneously enhance the local eccentricity dispersion and also enhance the surface density adjacent to the resonance [150, 17]. Unfortunately, collision detection in an N-body simulation is extremely computationally expensive. So far, studies of planetesimal dynamics near MMRs in which the planetesimals are directly resolved have involved either collisionless test particles [17, 156, 157] or integration times that do not fully capture the dynamics of the resonances [150, 40].

To further elucidate this subject, we use the tree based N-body code CHANGA [79, 113] to follow the collisional evolution of a planetesimal disc under the gravitational influence of a Jupiter-sized body. Because particle positions are sorted into a tree structure, neighbor finding and collision detection can be done quickly and efficiently. This considerably relaxes the constraints on resolution and integration time. With this toolset, we explore the collision rate structure of a planetesimal disc in the vicinity of mean-motion resonances with a planet. In particular, we would like to determine (1) what dynamics govern the collision rate profile near MMRs, (2) whether MMRs leave a detectable signature in the collisionally-generated dust, and (3) whether these signatures can be used to determine or constrain the orbital properties of the perturbing planet.

This work is organized in the following way: In section 3.2, we provide an overview of the relevant dynamics that drive the evolution of a planetesimal disc under the gravitational influence of an external perturber. In section 3.3 we provide an overview of the N-body code used and describe the initial conditions chosen for five simulations in which a perturbing giant planet is given various masses and eccentricities. Section 5.3 presents the results of these simulations and we take an in-depth look at the collision rate profiles of the planetesimals near the MMRs. In section 3.5, we extrapolate the collision rate down to smaller bodies and motivate a direct correspondence between the planetesimal collision profile and the resulting dust profile. In section 3.6, we use the resolved collisions to generate synthetic dust emission profiles that would be detected with observing facilities like ALMA. Under our simplifying assumptions, we show that a characteristic bump or dip feature appears in the dust emission near the interior 2:1 MMR, the presence of which depends on the mass and eccentricity of the perturbing planet. If the 2:1 MMR can be identified (presumably, by identifying another prominent MMR, such as the 3:1, and measuring the spacing between the two), we discuss the potential for using this feature to place constraints on the mass and eccentricity of the planet. In addition, we highlight the caveats of connecting the dust and planetesimal collision profiles in such a simple way. Finally, we conclude in section 3.7.

### **3.2 Overview of Relevant Dynamics**

We begin by providing a description of the dynamical effects responsible for shaping the orbital distribution of the planetesimals. The purpose of this is twofold: (1) to motivate the initial conditions used for the simulations described in section 5.2.2 and (2) to justify the exclusion of certain physical effects from our simulations. Here, we focus solely on the physics relevant for full-sized ( $\sim 100$  km) planetesimals and save a discussion of the effects on smaller bodies generated through collisions for section 3.5.

### 3.2.1 Secular Forcing

The most direct and widespread effect that a perturbing giant planet will have on a planetesimal disc is through secular forcing of the planetesimals. This will cause the complex eccentricities of the planetesimals to take on a time-independent forced value, given by [?] as

$$z_f = \frac{b_{3/2}^2(\alpha)}{b_{3/2}^1(\alpha)} e_g \exp i\varpi_g. \quad (3.1)$$

Here,  $\alpha = a_g/a$  where  $a_g$  and  $a$  are the semi-major axes of the giant planet and a planetesimal, respectively.  $e_g$  and  $\varpi_g$  are the eccentricity and longitude of pericenter of the giant planet, and  $b_s^j(\alpha)$  is a Laplace coefficient given by [125] (ch. 6, pg. 237, eq. 6.67) as

$$b_s^j(\alpha) = \frac{1}{\pi} \int_0^{2\pi} \frac{\cos j\psi d\psi}{(1 - 2\alpha \cos \psi + \alpha^2)^s}. \quad (3.2)$$

Without any nearby secular or mean motion-resonances, equation 3.1 will completely describe the eccentricities and longitude of pericenter orientations of the planetesimals. Additional forces due to two-body scattering between planetesimals, along with aerodynamic gas drag will add an additional free component to the complex eccentricity, which will be randomly oriented. The magnitude of the free eccentricity describes how dynamically hot the planetesimal disc is and sets the random encounter speeds of planetesimals. When the dynamical excitation of the disc is driven by gravitational stirring, the magnitude of the free eccentricity can be described by a Rayleigh distribution [70].

For the case of a Jupiter mass planet at 5.2 au perturbing a test particle at 3 au, the timescale for secular forcing is approximately 12,000 years. The details of this calculation can be found in appendix 3.8.

### 3.2.2 Mean-Motion Resonances

In regions where there are commensurabilities between frequencies, Laplace-Langrange secular theory breaks down and bodies are subject to strong perturbations. For the purposes of

this study, we will ignore secular resonances, which generally occur on rather large timescales and will focus on mean-motion resonances. A MMR occurs when the orbital period ratio between two bodies is sufficiently close to

$$\frac{P}{P'} = \frac{p+q}{p}, \quad (3.3)$$

where  $p$  and  $q$  are integers  $> 0$  and the unprimed and primed quantities correspond to the perturber and the body being perturbed, respectively. In terms of these quantities,  $P/P'$  corresponds to a  $p+q:p$  resonance. If the perturber is much more massive than the other body and all of the bodies lie in a near-Keplerian potential, the condition for MMR is set by

$$\frac{a}{a'} = \left( \frac{p}{p+q} \right)^{2/3}. \quad (3.4)$$

If we further assume that the two bodies are orbiting in the same plane, the motion of the bodies near resonance is determined by the behavior of a critical angle

$$\phi = (p+q)\lambda' - p\lambda - q\varpi, \quad (3.5)$$

where  $\lambda = \varpi + M$  is the mean longitude of a body, with  $M$  being the mean anomaly. For bodies in resonance, the critical angle will librate around an equilibrium value, while this angle will circulate outside of resonance. For small eccentricities, this behavior is analogous to the motion of a pendulum. Furthermore, variations in the critical angle are coupled to changes in the mean motion and semimajor axis [125]. An important point to note, which we will revisit later, is that the variation frequency of this angle approaches zero near the edge of a resonance. The width of a resonance can be defined by determining the largest variation in semimajor axis that permits librational, rather than circulatory motion of  $\phi$ . Calculations for the widths of first and second order interior MMRs are shown in appendix 3.9, along with a timescale for the libration. For the most prominent interior mean-motion resonances, including the 2:1 and 3:1, the timescale associated with these oscillations driven by a Jupiter mass planet is  $\sim 1,000 - 2,000$  years.

### 3.2.3 Collisions Between Planetesimals

A simple analytic model for the collision rate of a planetesimal population is given by [151] as

$$n\sigma v = n\pi s^2 \left(1 + 2Gm/sv^2\right) v, \quad (3.6)$$

where  $n$  is the number density of the population,  $s$  and  $m$  are the radii and masses of the bodies and  $v$  is their typical encounter velocity. The encounter velocity is often described in terms of the rms eccentricity  $\langle e^2 \rangle^{1/2}$  and inclination  $\langle i^2 \rangle^{1/2}$  of the population (e.g. [102]) as

$$v = \sqrt{\langle e^2 \rangle + \langle i^2 \rangle} v_k, \quad (3.7)$$

where  $v_k$  is the local Keplerian velocity. The second term in equation 3.6 can be thought of as an additional enhancement to the collision cross section due to gravitational focusing. When the typical encounter velocity is small compared to the mutual escape velocity of the planetesimals, the collision cross section greatly exceeds the geometric value. An important feature of equation 3.6 is that for a fixed value of  $n$ , the collision rate exhibits a global minimum as a function of  $v$ . For small  $v$ , gravitational focusing facilitates more collisions, while for large  $v$  the encounter rate simply becomes so great that the collision rate again increases, even though gravitational focusing is mostly suppressed. This point will become relevant in section 3.4.1 when we examine the qualitative changes in the collision rate near mean-motion resonances.

Although equation 3.6 works well to describe the collision rate for a homogeneous collection of planetesimals, some problems arise when regions of commensurabilities are introduced. Namely, the resonances cause the orbits of planetesimals to precess, and an interface between secularly aligned and randomly oriented orbits arise on each side of the resonance. Additionally, an interface between dynamically cold and hot planetesimals develop. These two effects cause the number density, collision cross section and encounter velocity to rather abruptly vary across the boundaries of the resonance. For this reason, an N-body treatment

in which collisions are directly resolved is necessary to understand how the collision rate varies near the MMRs.

### 3.2.4 Gas Drag on Planetesimals

Over the course of many orbits, the residual gas from the primordial nebula can damp the eccentricities and inclinations of bodies. For a planetesimal-sized body, gas drag operates in the Stokes regime and the timescale for aerodynamic forces to significantly alter its relative velocity is given by [1]

$$t_s = \frac{2m}{C_D \pi s^2 \rho_g v_g}, \quad (3.8)$$

where  $m$  and  $s$  are the mass and radius of the planetesimal.  $C_D$  is a drag coefficient which is of order unity,  $\rho_g$  is the local density of the gas and  $v_g$  is the headwind velocity of the gas experienced by the planetesimal. At 3 au, the gaseous component of the solar nebula has a density of  $3 \times 10^{-11}$  g cm $^{-3}$  and the typical headwind experienced by a body on a Keplerian orbit is  $\sim 5,000$  cm s $^{-1}$  [63]. For a 100 km body with a density of 2 g cm $^{-3}$  (assuming a mixture of ice and rock) the stopping timescale is about 1 Myr. This is much longer than the timescales associated with secular forcing and libration due to mean-motion resonances, as discussed above, but shorter than the typical protoplanetary disk lifetime and potentially shorter than the planetesimal formation timescale. For this reason, we do not model the effects of gas drag in the simulations, although we consider its effects when constructing initial conditions, which is discussed in the next section.

## 3.3 Simulations

### 3.3.1 Numerical Methods

To follow the dynamical and collisional evolution of a planetesimal disc, we use the highly parallel N-body code CHANGA. This code, which is written in the CHARM++ parallel programming language, was originally designed for cosmology simulations and has been

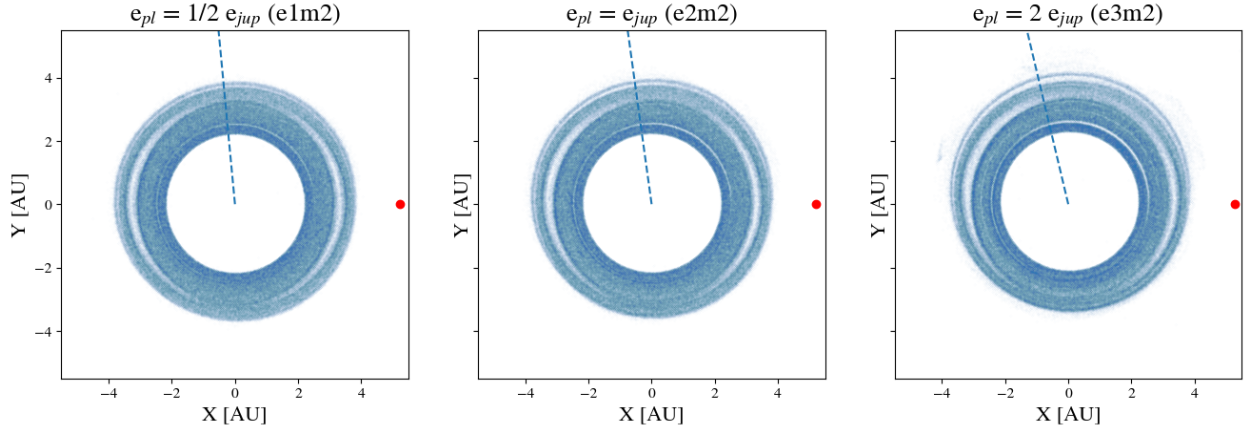


Figure 3.1: The positions of the remaining planetesimals at the end of the e1m2 (left), e2m2 (center) and e3m2 (right) simulations. The red dot indicates the position of the giant planet, and the dashed line points in the direction of the planet’s longitude of perihelion. Non-axisymmetric gaps are apparent near the locations of MMRs. At higher eccentricities, more resonances become visible. At the 2:1 MMR, gap features at  $\theta = 0$  and  $\theta = \pi$  follow the giant planet in its orbit.

shown to perform well on up to half a million processors [113]. Using similar methods to PKDGRAV, which has been used for numerous studies of planet formation [150, 98, 40, 99], CHANGA calculates gravitational forces using a modified Barnes- Hut [12] tree with hexadecapole expansions of the moments and integrates the equations of motion using a kick-drift- kick leapfrog scheme. All of the simulations we perform use a node opening criterion of  $\theta_{BH} = 0.7$ . More information about the code can be found in [79].

We have recently modified CHANGA to handle solid-body collisions between particles, by assigning them a fixed radius, rather than treating them as tracers of a fluid with a characteristic softening length. We provide a brief summary of the collision model here, although a full description is provided in [164]. This work is largely based on the solid-body collision implementation in PKDGRAV, which is detailed in [149] and [150]. Imminent collisions are found during the drift phase of each time step by extrapolating the positions of bodies forward using the velocity calculated during the first kick. For each body, the nearest 64 neighbors are tested for an imminent collision. If an imminent collision is detected, the

Table 3.1: Summary of Simulations Run

Name	Mass of Planet	Eccentricity of Planet
e1m2	$1.0 M_{jup}$	$0.5 e_{jup}$
e2m2	$1.0 M_{jup}$	$1.0 e_{jup}$
e3m2	$1.0 M_{jup}$	$2.0 e_{jup}$
e2m1	$0.5 M_{jup}$	$1.0 e_{jup}$
e2m3	$2.0 M_{jup}$	$1.0 e_{jup}$

two particles of mass  $m_1$  and  $m_2$  are merged together together to form one single larger body with the same density and a mass of  $m_1 + m_2$ . The resulting body is then imparted with the center of mass position and velocity of the two colliders. Because the resolution of a collision can result in another imminent collision, these events must be handled one at a time, with the soonest collision being resolved first. For this reason, another collision search is run each time a collision is resolved, which continues until there are no more imminent collisions during the current time step. During the course of the simulation, no debris is created by collisions. To model the collisionally generated dust distribution, we use the statistics of the resolved planetesimal collisions to build a dust profile. This process is discussed in detail in section 3.5.

### 3.3.2 Initial Conditions

In total, five simulations are run, which are listed in table 3.1. The second is a “nominal” case, in which the perturbing planet’s mass and eccentricity are set to that of Jupiter’s. In the other four cases, the mass or eccentricity is altered by a factor of two from the nominal value. In all cases, the perturbing giant is placed on a 5.2 au orbit around a  $1 M_\odot$  star. The planetesimal disc extends from 2.2 to 3.8 au, which covers the two most prominent mean-motion resonances with the giant planet, the 2:1 at 3.27 au and the 3:1 at 2.5 au. The

planetesimal disc loosely follows a minimum-mass solar nebula surface density profile [63]

$$\Sigma = \Sigma_0 r^{-\alpha}, \quad (3.9)$$

with  $\alpha = 3/2$  and  $\Sigma_0 = 10 \text{ g cm}^{-2}$ . Planetesimals are given a bulk density of  $2 \text{ g cm}^{-3}$ , which corresponds to a mixture of ice and rock, and are given a diameter of 300 km. This choice of parameters is meant to mimic the setup used in simulation B from [150]. One difference from the aforementioned study is that we use a narrower annulus, which reduces the number of particles required from  $10^6$  down to roughly 500,000. This allows us to use a finer base timestep size, which, as we will discuss in section 5.3, appears to be the reason why no features were seen in the collision profile near the resonances by [150].

Another difference from [150] is that the dynamical effects of secular forcing by the giant planet, along with the effects of viscous stirring and gas drag on the planetesimals, are built into the initial conditions. Although we do not model the effects of gas drag on the planetesimals during the simulation, we construct the initial conditions such that the effects of gas drag and viscous stirring are in balance. The viscous stirring timescale of the planetesimal disc is much longer than our chosen integration time, and so the dynamical excitation of the disc (excluding resonances) stays constant, even without the inclusion of damping forces from the gas. This is done by first calculating the equilibrium eccentricity  $e_{eq}$  due to viscous stirring and gas drag as a function of semimajor axis according to equation 12 of [89]. The eccentricities of the bodies are drawn randomly from a Rayleigh distribution with a mode of  $e_{eq}$ , while the inclinations are drawn from a similar distribution with a mode of  $e_{eq}/2$  [66]. The arguments of perihelion  $\omega$ , longitude of ascending nodes  $\Omega$  and the mean anomalies  $M$  of the bodies are drawn uniformly  $\in [0, 2\pi)$ .

To account for the effects of secular forcing by the planet, the eccentricity vectors of the planetesimals are first decomposed into real and imaginary components:

$$z = (k, ih) = e \exp(i\varpi) \quad (3.10)$$

and a forced component is added to  $h$  according to equation 3.1 (where we have set  $\varpi_g = 0$ ).

### 3.3.3 Time Stepping Scheme

For the purposes of the integrator, there are two relevant timescales in this system. The first is the orbital dynamical time  $\sqrt{a^3/GM_\odot}$ . Through experimentation, we have found that using a base timestep size with CHANGA of 3% of an orbital dynamical time at the inner edge of the disc keeps the integration symplectic. Although doing so preserves orbital frequencies, the errors associated with precession frequencies do not average out to zero. This is especially important given the effects of secular forcing by the planet. To mitigate this, we further reduce the base timestep size by a factor of 4 and use  $\Delta t = 0.0025$  yr. Doing so prevents the longitude of perihelia of planetesimals at the inner edge of the disc, where this artificial precession is most severe, from drifting by more than the intrinsic spread in  $\varpi$  due to the free eccentricity over the course of our integrations.

An additional timescale is set by the dynamical time of the planetesimals ( $\sim 1/\sqrt{G\rho}$ ), which is about 45 minutes. This timescale must be resolved in order to properly follow close gravitational encounters between these bodies. To resolve the base time step and the dynamical timescale of planetesimals simultaneously, we use a two-tiered time stepping scheme, following[99]. To start, all bodies are placed on the base time step. A first pass of collision detection is then run in which the radii of all bodies are inflated by a factor of 2.5. Any bodies with imminent collisions predicted using the inflated radii are placed on a time step that is a factor of 16 smaller than the orbital time step. Although this is still a factor of roughly 7 larger than the dynamical time of a planetesimal, we found no difference in the collision rate when using any smaller of a minimum time step size. The purpose of the two-tiered scheme is to properly resolve the gravitational interactions between any bodies that undergo a close encounter. This prevents the coarser base time step from reducing the effectiveness of gravitational focusing, while minimizing the additional computational expense.

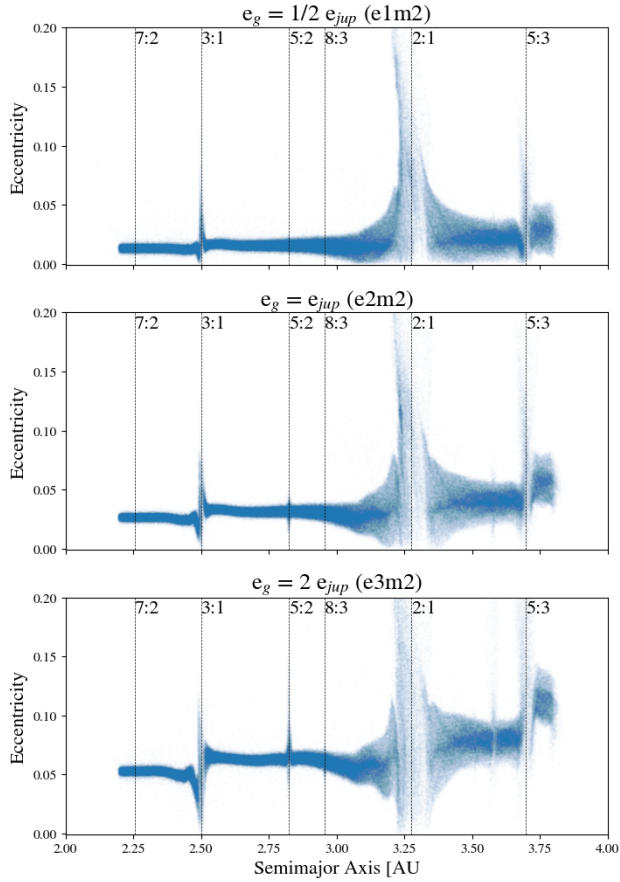


Figure 3.2: The semimajor axes and eccentricities of the remaining planetesimals are shown, with the locations of prominent resonances indicated by the vertical dashed lines. Libration of the critical angle drives large variations in eccentricity, which produce spikes in the a-e plane. Between the resonances, the nonzero eccentricity is due to secular forcing by the planet.

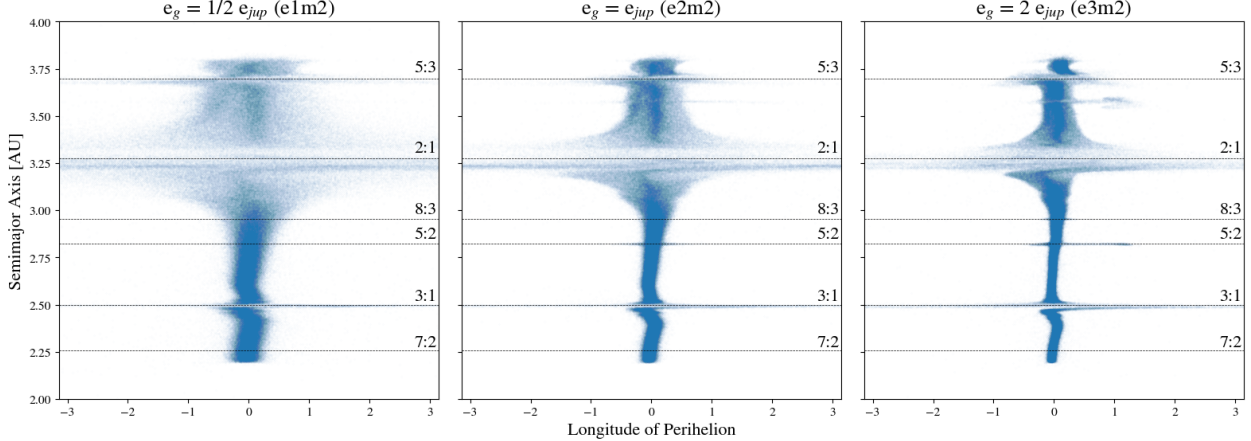


Figure 3.3: Shown here are the longitudes of pericenter and semimajor axes of the remaining planetesimals. The dashed lines again indicate the locations of prominent MMRs. Close to the resonances, the critical angle librates and drives fast precession of the longitudes of pericenter of the bodies. This overpowers the secular forcing by the planet and effectively randomizes the orientations of their orbits.

### 3.4 Results

All five simulations are evolved for 5,000 years, which is roughly 400 complete orbits of the perturbing planet. Because the effects of the mean motion resonances are not built into the initial conditions, the simulations must be run long enough for the distribution of orbital elements to reach equilibrium near the resonances before the collision rate is measured. To do so, we allow each simulation to run for 2,000 years before we begin recording any collision statistics. This is comparable to the libration period, which was calculated in section 3.2.2 for the 3:1 and 2:1 resonance. Although one might worry that a single libration period may not be long enough for the orbital structure due to the resonances to develop, we find that the shape of the semimajor axis-eccentricity distribution of the planetesimals reaches a steady state by this time. This is largely due to the fact that there are enough bodies in or near the resonances to allow an ensemble average of phase space, rather than a time average. As an additional confirmation, we find that the time evolution of the collision rate near the

resonances maintains a steady state in all five simulations after  $\sim 2000$  years.

### 3.4.1 Varying the Eccentricity

We begin by examining simulations e1m2, e2m2 and e3m2. The positions of the planetesimals in the x-y plane after 5,000 years of integration are shown in figure 3.1. In all cases, the coordinate system is rotated so that the giant planet lies at  $\theta = 0$ . The longitude of perihelion of the planet is shown by the dashed line. Resonances with the perturbing planet are visible as nonaxisymmetric gaps in this figure. Upon close inspection of a series of simulation snapshots, these gaps appear to follow the planet in its orbit, rather than aligning themselves with the longitude of perihelion. A similar substructure, which is most noticeable near the 2:1 MMR, reveals itself in [150] (see their figures 3c and 3f) and [156] (see their figure 3a). This structure is also present in the [17] simulations, although it was not reported at the time (see Appendix 3.10). It is worth noting that both [150] and [17] started with a completely cold planetesimal disc. Thus, the presence of these features seems robust to the choice of initial conditions.

The effects of the resonances become much more apparent in semimajor axis-eccentricity space, which is shown in figure 3.2. In all cases, the 3:1, 2:1 and 5:3 resonances are readily visible as “spikes” in the eccentricity that bend slightly inward (due to the conservation of the Jacobi energy). In the e3m2 simulation, features also appear near the 5:2, 7:3 and 5:3 resonances. The absence of these finer features from the e1m2 simulation can be explained by the fact that the strength of a resonance scales with  $e^q$  [109].

Another important effect of the resonances is visible in figure 3.3, which shows the orientation of the longitude of perihelia of planetesimals in the disc. Inside of the resonances, orbits of planetesimals quickly precess, and their orientations are effectively randomized. An important point to note is that this strong precession effect quickly disappears beyond the boundaries of the resonance. This turns out to be key to explaining the nonaxisymmetric structure seen in figure 3.1, which will be addressed in more detail below.

Next, we examine the statistics of collisions resolved in each of the simulations. The 3D

positions and velocities of the two colliding bodies are recorded to a table at the moment of impact. We derive the Keplerian orbital elements of a collision using these positions and velocities. First, we examine the semimajor axis of the first collider, which is shown in figure 3.4. During a collision, the “first” particle is defined as the more massive of the two. However, nearly all of the collisions happen between the initial, equal-mass planetesimals. In this case, the distinction is set by the collision search algorithm and is rather arbitrary. In all of the plots where we show collision statistics, we have verified that using the “first” or “second” collider does not qualitatively change any of the features. We find that some of the features present in figure 3.4 in this and subsequent figures are highly sensitive to the number of bins and the location of the bin edges. For this reason, we construct a probability density function (PDF) of the collisions using a Kernel Density Estimate (KDE). We use the `NEIGHBORS.KERNELDENSITY` function from the `SKLEARN` [?] package to construct our KDEs, using a gaussian kernel with a FWHM of 0.02 au. The curves shown in figure 3.4 are normalized such that the area underneath is equal to 1.

Near the stronger resonances, there are noticeable suppressions or enhancements to the local collision rate. This contrasts with the findings of [150], who simulated a similar setup and found no discernible features near the MMRs. We attribute the differences to a more conservative timestepping criterion in our simulations, along with the inclusion of secular perturbations in our initial conditions. The most prominent features appear as a local maximum in the collision rate near the 2:1 MMR and a local minimum near the 3:1 MMR. At higher forced eccentricities, features near the 5:2, 8:3 and 5:3 resonances are also visible, due to the steep sensitivity of higher order resonant perturbations to eccentricity [109].

Although the features in figure 3.4 near the 3:1 and 2:1 MMRs appear qualitatively different, they can be explained by one single dynamical process. As discussed in section 3.2.3, the collision rate between planetesimals depends on both the encounter rate and the strength of gravitational focusing. The encounter rate grows as the relative velocity  $v$  between the planetesimals increases, while gravitational focusing is most effective for bodies with small relative velocities. There is therefore an intermediate value of  $v$  for which the average collision

rate  $\langle\sigma v\rangle$  is at a minimum, which we will refer to as  $\langle\sigma v\rangle_0$ . The dynamical excitation induced by a mean motion resonance can either increase or decrease the local average collision rate, depending on the unperturbed value of  $\langle\sigma v\rangle$  relative to  $\langle\sigma v\rangle_0$ .

In figure 3.5, we show the effect that the 2:1 MMR and 3:1 MMR have on the local average collision rate. Each pair of points connected by a line represents the average collision rate before and after the effects of the mean-motion resonances develop. Here, the relative velocity between bodies is calculated by measuring the eccentricity and inclination dispersion near each resonance and using equation 3.7. We assume that the eccentricity and inclination dispersions are coupled [66] and use the eccentricity dispersion as a free parameter. Because both the strength of secular forcing and the effects of the resonant perturbations are different near the 3:1 and 2:1 MMRs, the planetesimal population at each of these locations in the disk experiences a qualitatively different change in the collision rate. Near the 3:1 MMR, the unperturbed collision rate is well above the minimum value  $\langle\sigma v\rangle_0$  and the dynamical heating introduced by the resonance acts to suppress it further. Near the 2:1 MMR, the collision rate starts out much closer to the minimum value and the additional perturbations instead act to drive it higher.

This explains the relative drop in the collision rate near the 3:1 MMR and the relative increase near the 2:1 and 5:3 resonances seen in figure 3.4. Although this could potentially serve as a useful diagnostic of the planetesimal size in a disc (because the size and mass of the planetesimals sets the eccentricity dispersion at which  $\langle\sigma v\rangle$  is minimized), a direct measurement of the semimajor axes of the colliding planetesimals is not possible. Furthermore, as we will demonstrate next, collisions due to bodies in resonance do not have a significant effect on the final shape of the radial dust distribution that we predict.

### **3.5 Where Does the Dust End Up?**

To construct a radial dust profile from the collision statistics, we begin by making two assumptions: (1) any dust generated by collisions is strongly coupled to the gas and (2) any subsequent spatial evolution of the collisional debris is insignificant. So long as both of these

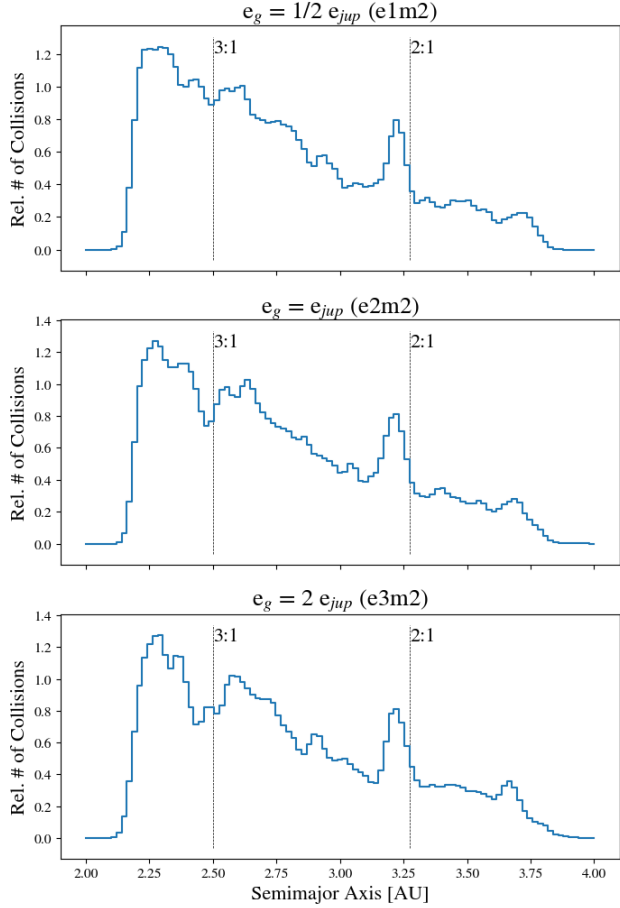


Figure 3.4: A PDF of the collision rate in each disc as a function of semimajor axis, generated using a KDE with a Gaussian kernel with a FWHM of 0.02 au. In semimajor axis space, prominent features appear near the 3:1 and 2:1 MMRs. Near the 3:1, the collision rate exhibits a local minimum, while an enhancement appears near the 2:1.

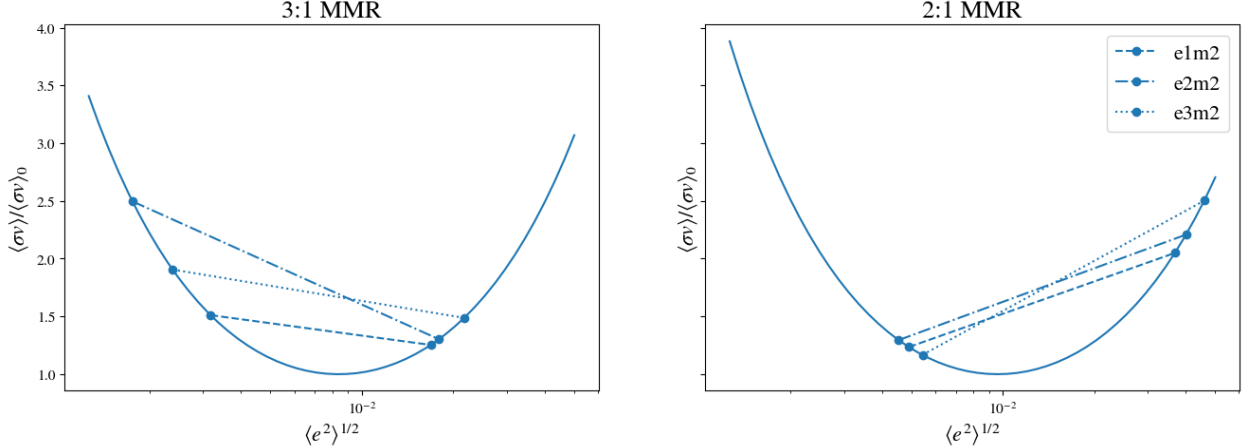


Figure 3.5: The collision rate (given by equation 3.6) of bodies in the vicinity of the 3:1 (left) and 2:1 (right) MMRs, relative to the minimum value, as a function of the local eccentricity dispersion. The pairs of points connected by lines show the values of the unperturbed (left-hand points in each subplot) and perturbed (right-hand points in each subplot) collision rates in the e1m2, e2m2 and e3m2 simulations. The unperturbed collision rate, along with the amount of dynamical heating that the planetesimal population experiences determines whether the MMR acts to suppress or enhance the collision rate

assumptions are true, we can use the radial locations of planetesimal collisions in the plane of the disk to generate a dust profile for each simulation.

We first provide a justification for assumption (1), which is as follows: At 3 au in the protosolar nebula, the mean free path of a gas particle is  $\sim 50$  cm (assuming a composition of pure hydrogen with a local volume density of  $\rho_g = 3 \times 10^{-11} \text{ g cm}^{-3}$ ). This places any dust grains in the Epstein drag regime, with a stopping timescale given by

$$t_s = \frac{\rho s}{\rho_g v_{th}}, \quad (3.11)$$

where  $\rho$  is the bulk density of the dust grain,  $s$  is its size, and  $v_{th}$  is the local thermal velocity of the gas. At 3 au in the protosolar nebula,  $v_{th} \sim 10^5 \text{ cm s}^{-1}$ . Assuming a 1 mm dust grain with a  $\rho = 2 \text{ g cm}^{-3}$ , the stopping time is  $\sim 10^{-4} \text{ yr}$ . This is orders of magnitude smaller than the orbital timescale; therefore, we conclude that collisionally generated dust grains

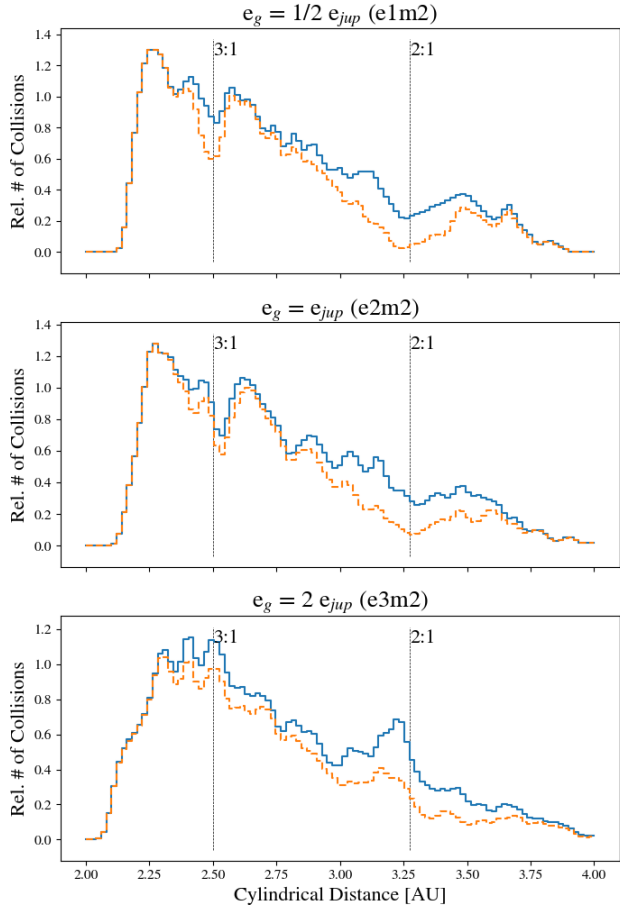


Figure 3.6: Here, collisions are instead ordered by cylindrical distance from the star. Features near the 3:1 and 2:1 MMRs are still present, but appear qualitatively different than in semimajor axis space. At low eccentricities, a dip appears around the center of the resonance. At the highest eccentricity, a bump is formed instead. The dashed lines shown the collision profile with collisions between bodies in resonance removed. The bump and dip features remain qualitatively the same, which suggests that they are produced by bodies outside of the libration width of the resonance.

will immediately couple to the gas.

Assumption (2) is less straightforward to justify and may not be reasonable in all cases. Although the spatial redistribution of the full-sized planetesimals and mm-sized dust grains is insignificant, the radial drift forces experienced by intermediate-sized bodies is much greater. Collisions between planetesimals do not immediately convert the mass to dust grains. Rather, the debris will undergo a collisional cascade process, which gradually grinds the resulting bodies down to smaller sizes. A proper treatment of the collisional cascade process is quite complicated and is well beyond the scope of this work. However, one may be able to ignore this process if the peak radial drift timescale is longer than the timescale for collisions between these bodies.

This occurs for bodies of the size at which  $t_s\Omega = 1$ . In the Stokes drag regime at 3 au, this occurs for bodies of 1 meter in size. Following a similar calculation in 3.2.4 with a 1 m body, we find that an object of this size will drift across the 2:1 MMR on a timescale of  $\sim 300$  years. Although we do not model collisions between bodies of this size, a lower limit on the collision timescale for these objects can be obtained by extrapolating the planetesimal collision rate measured in our simulations down. For the e2m2 simulation, we find that 125 collisions occur within the libration width of the 2:1 MMR from  $T=2,000$  yr to  $T=5,000$  yr. There are a total of 15,000 planetesimals within this region, which means that a single planetesimal undergoes a collision every  $\sim 370,000$  years on average. If the entire planetesimal population in this region were converted to 1 meter bodies with the same bulk density, the number density of bodies increases by a factor of  $10^{15}$ , while the geometric collision cross section decreases by a factor of  $10^{10}$ . The collision timescale would therefore decrease to  $\sim 1$  year, which is 2 orders of magnitude smaller than the drift timescale. As shown above, radial drift in the Stokes drag regime is maximized for bodies of 1 meter in size, which is only a factor of two larger than the mean free path of the gas particles. It is therefore not entirely clear if the Stokes drag law is appropriate here. Because of this, we also repeat the above calculation for bodies that experience Epstein drag. With this assumption, we find that radial drift is maximized for a cm-sized body and both the radial drift and collision timescale for bodies of that size

decrease by a factor of 10 relative to the Stokes values. In both cases, collisions between maximally drifting bodies occur on a timescale two orders of magnitude shorter than the drift timescale. We therefore argue that it is reasonable and, indeed, best practice to start with such simple assumptions understand the physics before additional complexity is later added. We caution, however, that the collision timescale estimates provided here should be interpreted as lower limits.

Operating under these assumptions <sup>1</sup>, a map of the relative concentration of second-generation dust can be constructed from the cylindrical distance at which the collisions occur. Here, cylindrical distance is defined as the separation between the central star and the location of collision in the  $(r, \theta)$  plane. This is shown in figure 3.6. Similar to figure 3.4, we use a KDE with a width of 0.02 au to assemble the collision locations into a radial distribution. Most strikingly, the bump that was present near the 2:1 resonance is no longer visible in cylindrical distance space, although it suddenly appears again in the e3m2 simulation. The local minimum that is visible near the 3:1 MMR also becomes a local maximum in the highest eccentricity case. To determine how the resonant bodies actually contribute to the radial collision profile, we excluded collisions that fall between  $2.495 < a < 2.505$  au (near the 3:1 resonance) and between  $3.2 < a < 3.35$  au (near the 2:1 resonance), which is shown by the dashed curve. As in figure 3.4, the solid curves are normalized such that the area underneath is equal to 1. For the dashed curves, the normalization factor is scaled according to the number of collisions in the entire sample, compared to the number of collisions in the subsample, which excludes the collisions in resonance. Qualitatively, none of the bump or dip features present are removed by making this exclusion. This suggests that the features near resonance seen in semimajor axis space become smeared out in cylindrical distance space due to the large spread in eccentricity and orbital orientation.

This also suggests that the prominent bumps and dips seen in figure 3.6 are mainly

---

<sup>1</sup>As discussed in [17], the local generation of second-generation dust is only one consideration. The dust will also evolve spatially due to drag effects, but can also evolve in size or be re-accreted onto planetesimals. For simplicity, we focus on local dust sourcing only while acknowledging that subsequent evolution could **also** affect the morphology.

produced by bodies outside of the libration width of the resonance, although the resonant population does make some of the features more pronounced. To further understand this, we consider the nonaxisymmetric structure seen in figure 3.1. In figure 3.7, we compare the radial collision profiles to the radial structure seen in the e1m2, e2m2 and e3m2 simulations. In the lowest forced eccentricity case (e1m2), the pileups near the edge of the 2:1 MMR line up with the boundaries of the dip feature seen in the radial collision profile. The locations of the edges of the resonances are calculated using equations 3.18 and 3.14. The pileups not as pronounced near the other resonances. As discussed previously, the planetesimal density enhancements and gaps seen in polar coordinates follow the position of the giant planet in its orbit, which is shown by the vertical line. For the e2m2 case, the density enhancements take up a much larger radial width, which smears out the corresponding collisional dust profile. In the highest forced eccentricity case (e3m2), the density enhancements occur well within an annulus containing the resonant region, completely altering the radial peak-valley dust morphology.

Although the nonaxisymmetric pileup of bodies near the edges of resonances has been seen previously

[150, 156], we could not find a satisfactory explanation for why it happens, which we will try to provide here. As mentioned in section 3.2, the circulation frequency of the critical angle slows as one approaches the edge of the resonance from the outside. Following the pendulum analogy, this is equivalent to approaching the point where the pendulum becomes suspended in the top dead center. When the critical angle stays relatively stationary during an encounter, the net torque will drive the longitude of pericenter towards the point of conjunction [136]. This is the basic mechanism that causes isolated resonances to be stable. Inside of resonance, the critical angle librates about an equilibrium value and this configuration is maintained. Just outside of resonance, however, the critical angle slowly drifts away, with the drift direction changing sign across the location of exact resonance. The net result of this is that bodies just outside of the resonance experience a torque from the planet that temporarily drives their pericenters toward the current orbital position of

the planet. After the encounter ends, differential rotation of the disc slowly undoes the configuration. As the planet again passes by, adjacent planetesimals near the resonance edges temporarily align themselves in this configuration. This explains why the concentration of planetesimals appears to ‘follow’ the planet. Connecting this back to the radial collision profiles shown in figure 3.6, these bodies at the edges of the resonances must be responsible for the bumps and dips morphology seen because excluding collisions between bodies inside of the MMRs does not qualitatively alter the profiles.

[156] provide a different explanation for this phenomenon, suggesting that the nonaxisymmetric structure is the product of the path that a resonant test particle takes in a frame co-rotating with the planet (see figure 8.4 of [125]). In other words, the gap structure is argued to be due to the interfaces between the low eccentricity, non-resonant and high eccentricity, resonant regions of the disc. This explanation, however, does not hold for a large collection of planetesimals, especially when there is no forced eccentricity. In such a case, the orbits of planetesimals near resonance would be randomly aligned, and the axisymmetric structure should become washed out. Furthermore, when the perturbing planet is on a circular orbit, this structure is still present (see figure 3 of [156] and Appendix 3.10). The only connection between the structure of the gaps in the disc and the path of a resonant particle in the corotating frame is that both phenomena produce the same symmetries, which depend on the particular MMR considered.

With no secular forcing, this dynamical phenomena should produce an underdensity in the radial surface density profile near the center of the resonance and an overdensity at each edge in cylindrical distance space. When a forced eccentricity is introduced, the radial location of the resonance edges vary over the course of an orbit. The maximum and minimum radial distance that the resonance edges occupy is indicated by the solid and dashed lines in figure 3.7. If the the aphelion distance of the inner edge becomes close to the perihelion distance of the outer edge, the overdense regions on each side of the resonance meet and we should expect to see the central dip feature in the collision profile disappear. This is exactly what appears to be happening in the middle panel of figure 3.7. As the forced eccentricity is

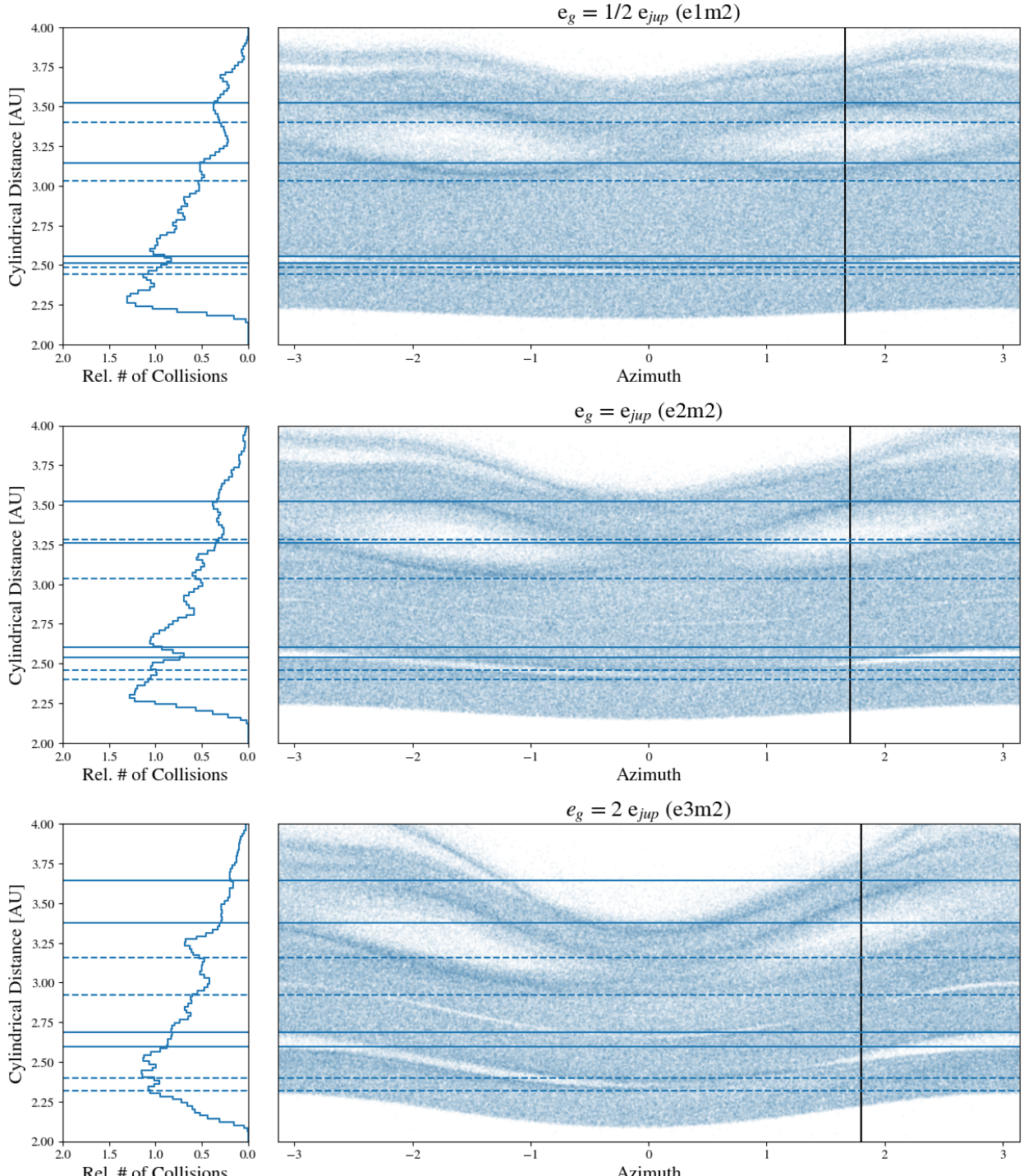


Figure 3.7: The collision profiles in figure 3.6 are shown alongside the positions of the planetesimals, in polar coordinates. The dashed and solid lines show the pericenter and apocenter, respectively, of bodies at each edge of the 3:1 and 2:1 MMR. In these figures, the longitude of pericenter of the planet lies at  $\theta = 0$  and the present position of the planet is indicated by the vertical line. For the 2:1 resonance, a bump, rather than a dip feature appears when the inner edge or the resonance's apocenter and outer edge's pericenter distance cross. The collision profile near the 3:1 resonance does not appear to follow this same qualitative behavior.

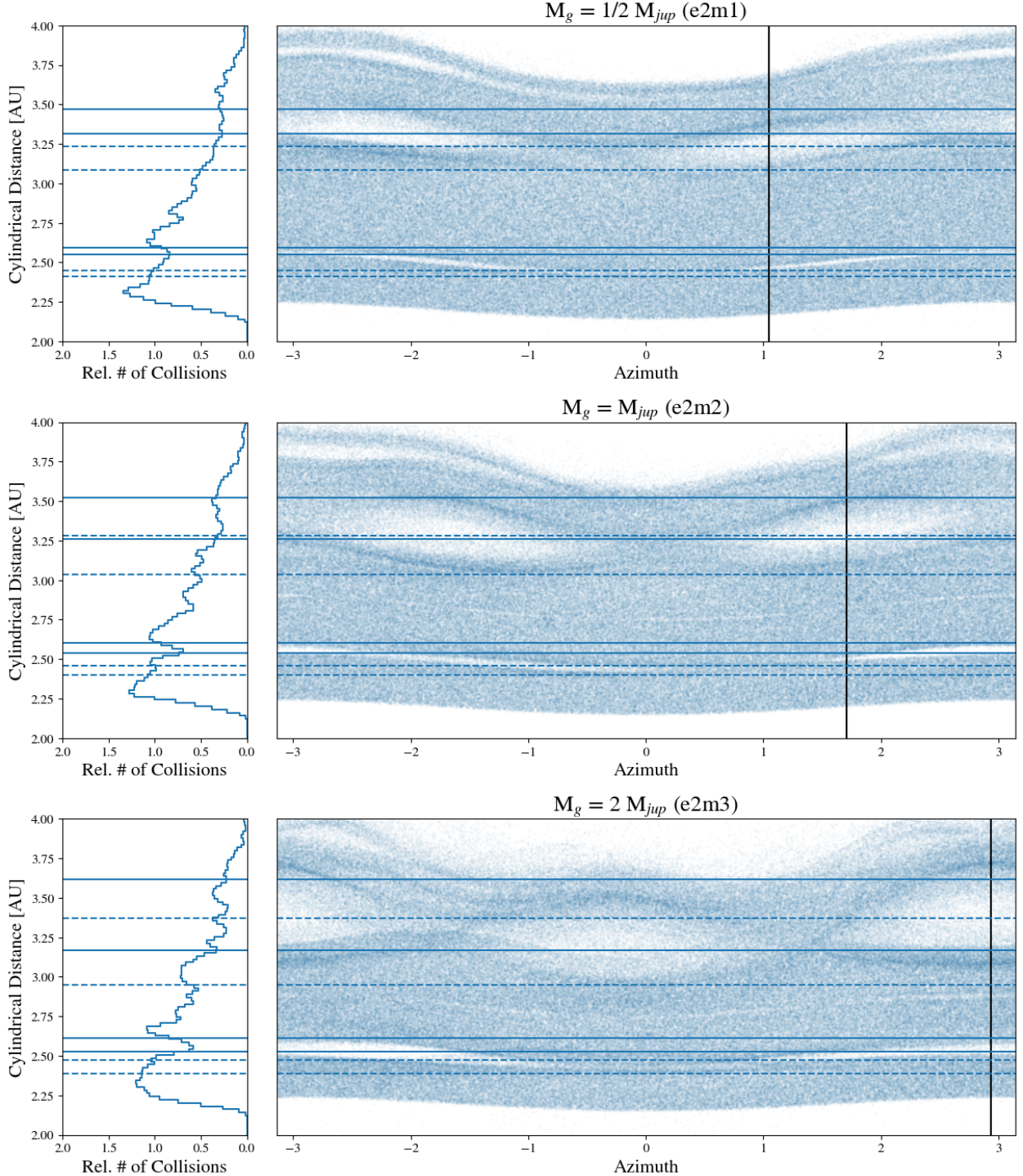


Figure 3.8: Similar to figure 3.7, except the eccentricity of the planet is kept constant and the mass is varied. This has the effect of changing the width of the resonances, without altering the relative apo or peri distances of bodies near the edges. Except for the highest mass case, the apocenter and pericenter distances of the inner and outer edges of the 2:1 resonance are too close together to produce much of a dip or a bump feature.

increased further, a region forms at the center of the resonance where planetesimals on both sides of the resonance spend time (although not simultaneously). When this occurs, a bump feature forms in the collision profile near the center of the resonance. This is apparent in the bottom panel of figure 3.7.

Although the same phenomenon appears to be happening near the 3:1 MMR, the pileups at the edges of the resonance are not as well defined. We attribute this to the more complex symmetry, compared to the 2:1 MMR. In addition, a number of other nearby resonances, including the 7:2 (at 2.25 au), the 10:3 (at 2.33 au), the 8:3 (at 2.71 au) and the 5:2 (at 2.82 au) also likely are contributing to the collision profile in cylindrical distance space near the 3:1 MMR. The 3:1 MMR is also much narrower than the 2:1, which means that any dip or bump features produced by it would require much higher resolution observations. For these reasons, we will focus on the 2:1 MMR as the main diagnostic indicator.

### 3.5.1 Varying the Mass

The dynamical effects of varying the mass of the planet are somewhat simpler, in that doing so does not affect the forced eccentricity of the planetesimal disc. Instead, only the width of the resonances changes. The width of a first order resonance scales with  $m$  (see equation 3.14), while the leading order terms in the resonant part of the disturbing function, which set the strength of the resonance, also scale as  $m$ . For the 2:1 MMR, the dynamics near the resonance are equally sensitive to changes in eccentricity and mass.

We show the polar structure of the e2m1, e2m2 and e2m3 simulations in figure 3.8 alongside the radial collision profile. In all three cases, the eccentricity of the perturbing planet is set to  $e_{jup}$ . Changes in the apocenter and pericenter distances of the edges of the resonances are entirely due to changes in the resonance width. For the e2m1 and e2m2 simulations, the inner apocenter and outer pericenter distances near the 2:1 MMR are quite similar and no strong features appear in the collision profile near this region. For the e2m3 case, the edges of the resonances are sufficiently separated to allow what appears to be the beginning of a gap to form near the center of the 2:1 resonance in the collision profile.

### 3.5.2 Observability of the Dust

While the collisional dust profiles show radial amplitude variations, we still need to assess whether those variations could be observable. To proceed, we create a sky model for simulated ALMA observations as follows. First, we use the radially-averaged collision profile from each simulation (see figures 3.7 and 3.8) as the template for an azimuthally symmetric disc. We then scale the size of each profile by a factor of ten, which places the perturbing planet at 52 au. This scaling is permitted by the dynamics (both the resonance widths and the forced eccentricities are scale-free) and makes the disc comparable in size to the many discs that have now been observed by ALMA [65]. The angular size scale is then set by envisaging a face-on disc at a distance of 100 pc.

The sky model intensity (flux per pixel) is produced by interpolating the radial collision frequency onto a 2D Cartesian grid with cell widths of approximately 2 mas. In doing so, we choose to make the intensity proportional to the collision frequency (i.e., the dust) because it is the most straightforward case. Many different parameterizations are possible, depending on optical depth, grain size, disc temperature, etc., but we will avoid such complications here, as they would affect the overall brightness profile, but not the presence of any gaps or rings. We normalize the intensity by setting the total disc flux density to be 100 mJy at about 350 GHz.

The simulated observations are performed using the `SIMOBSERVE` task in CASA [111]. The disc is given an  $\text{RA} = 11^{\text{h}}01^{\text{m}}52^{\text{s}}$  and a  $\delta = -34^\circ 42' 17''$  (i.e., the J2000 coordinates for TW Hydrae) and is “observed” through transit on March 20, 2020. We observe the disc using configurations 8, 9, and 10 at 350 GHz (cycle 6 antenna file), spending six hours on-source in each configuration<sup>2</sup>. The visibilities are corrupted with thermal noise, setting the precipitable water vapor to 1.5 mm. They are then combined, imaged, and cleaned using the task `tclean`. Imaging uses Briggs weighting with a robustness parameter of -1.

The results for the nominal simulation (e2m2) are shown in figure 3.9. The 3:1 and

---

<sup>2</sup>We have imagined that the TAC really likes us.

2:1 resonances can be easily identified in the cleaned image and in the corresponding radial profile. Moreover, the features are qualitatively similar to the bright rings and dark gaps seen in actual disc profiles [5].

In figure 3.10, we show the azimuthally-averaged radial profiles constructed from the simulated cleaned image from all five simulations. In all cases, a bump or a dip feature is clearly visible at the location of the 3:1 and 2:1 MMRs, indicated by the dashed vertical lines. As mentioned previously, the feature at the 2:1 MMR acts as the actual diagnostic indicator, while the 3:1 resonance (along with the gap that would presumably open at the location of the planet) is mainly useful for determining where the 2:1 MMR is actually located.

### **3.6 Constraining the Mass and Eccentricity of the Planet**

The simple bump vs dip structure that we expect to reveal itself in the dust emission from colliding planetesimals in near- resonance with a giant planet could potentially be used to place constraints on the mass and eccentricity of the planet. Near the 2:1 MMR, the central dip feature is only produced when bodies at the edges of the resonance stay sufficiently separated in cylindrical distance over the course of an orbit. This is achieved when either the resonance width is large or the forced eccentricity is small. The bump feature, on the other hand, is produced when there is a sufficiently large amount of overlap between the apocenters and pericenters of the inner and outer edges of the resonance, respectively. This is achieved when the resonance is narrow and the forced eccentricity is large.

In figure 3.11, we show the constraints that the presence of a bump or a dip or dip at the 2:1 MMR places on possible values of  $(m_g, e_g)$ . The dashedlines indicate regions of parameter space where qualitatively different features in the collision profile are expected to form. Above the upper dashed line, the resonance is wide while the radial excursion distance of planetesimals at the edge of the resonance is small, which gives rise to a dip in the collision profile. Below the lower dashed line, the resonance is narrow, while the radial excursion distance is large, allowing the apocenter and pericenter distances of the edges of the resonance to overlap and produce a bump in the collision profile. Between the dashed

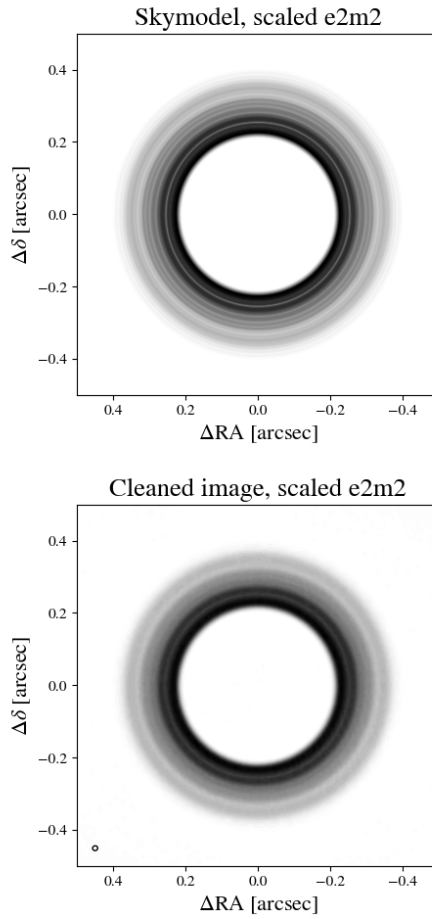


Figure 3.9: Simulated ALMA observations for the nominal (e2m2) case, operating under the assumption that the dust profile closely traces the planetesimal collision profile. Top: The sky model based on the radial collision distribution. The size of the disc has been scaled by a factor of 10 and placed at a distance of 100 pc. Bottom: The cleaned image using combined observations in configurations 8, 9, and 10. The circle in the bottom left indicates the simulated beam size. Gaps in the dust due to the 3:1 and 2:1 resonances are visible.

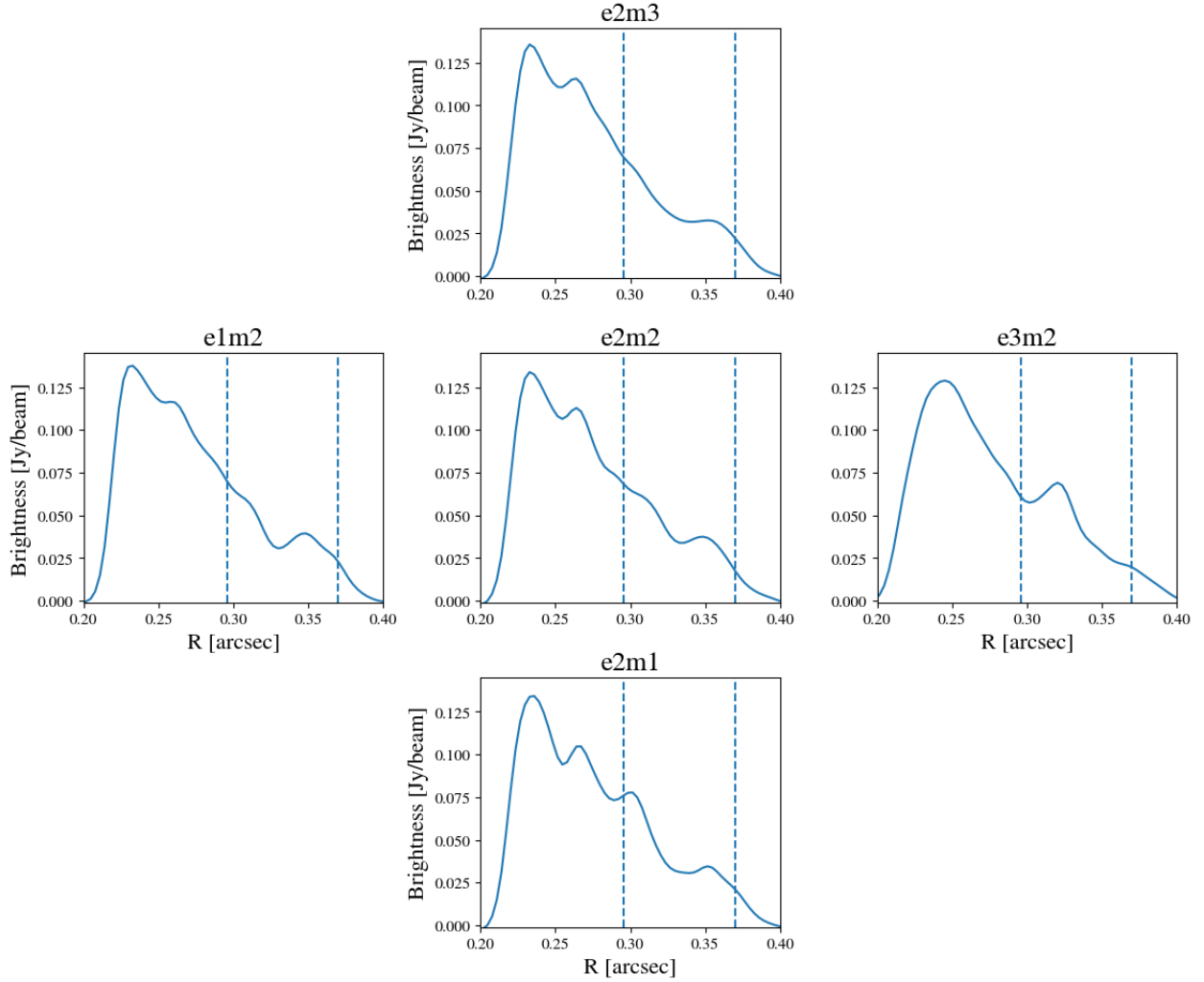


Figure 3.10: The azimuthally-averaged radial profile based on the simulated cleaned images from all five simulations. The eccentricity of the perturbing planet increases from left to right, while the mass of the planet increases from bottom to top. The vertical dashed lines indicate the locations of the 3:1 and 2:1 resonances. As in figure 3.9, the size scale of the disc has been expanded by a factor of 10 and then placed at a distance of 100 pc.

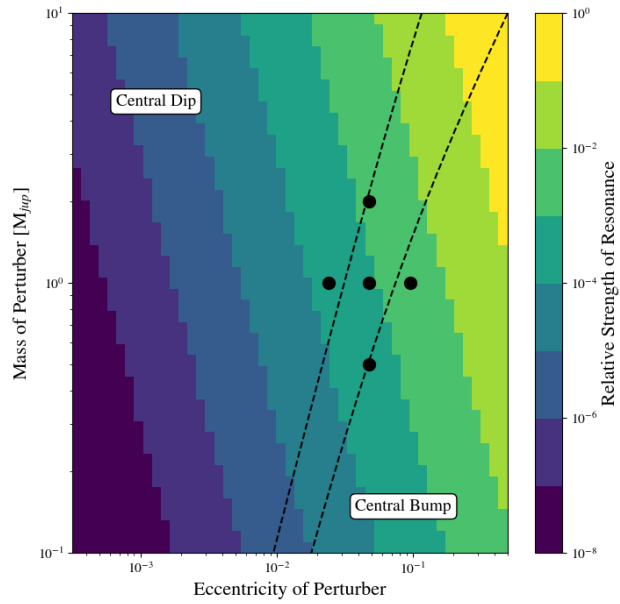


Figure 3.11: The presence of a dip or bump in the collision profile (and therefore the dust profile) near the 2:1 MMR can be used to constrain the mass and eccentricity of the perturbing planet. The color scale indicates the relative strength of the features, while the dashed lines indicate boundaries in parameter space where a dip or a bump will be produced at the resonance. Combinations of mass and eccentricity that fall between the dashed lines correspond to an inner apocenter and outer pericenter separation at the edges of the resonance that is smaller than the resonance width and therefore will not create any significant feature in the collision profile.

lines, the absolute value of separation between the apocenter and pericenter distances of the inner and outer edges of the resonance is less than the resonance width. In this region of parameter space, no significant features in the collision profile near the 2:1 MMR are expected to form.

Because the strength<sup>3</sup> of the 2:1 resonance scales with  $e_g$  and  $m_g$ , a sufficiently low mass and low eccentricity planet will not create enough of a perturbation in the planetesimal disc to produce a detectable bump or dip feature. The colored contours in figure 3.11 indicate the relative strength of the resonance as these quantities are varied. Although the resonance strength is equally sensitive to changes in mass and eccentricity, the peri-apocenter overlap of the resonance edges is more sensitive to changes in eccentricity. This is because changes to eccentricity affect both the resonance width and the forced eccentricity. As we showed in figure 3.8, changing  $m_g$  by a factor of 4 produced very minimal changes to the resulting dust profile.

In order to actually identify the 2:1 MMR in the dust emission, at least one other resonance must be visible. Assuming the gravitational field in the disc is near-Keplerian, the distance ratios between two features can be used to determine period ratios, which can be used to confirm whether the features seen are indeed resonances. Although the 3:1 MMR does not appear to follow the simple bump vs dip dichotomy described above, its presence should be marginally detectable in all of the cases shown above.

We would again like to emphasize that the dust emission profiles in figure 3.10 are constructed upon the assumption that the radial dust structure closely traces the collision profile of the planetesimals. For this assumption to be valid, the resulting dust must remain locally confined, which can be achieved if the grains are reaccreted onto planetesimals [80]. It is also necessary that the collisional cascade from which the dust grains form plays before radial drift has a chance to move debris away from the resonances. Although we showed with a back-of-the-envelope calculation (see section 3.5) that this is plausible for a typical proto-

---

<sup>3</sup>More specifically, the strength of the resonant term in the disturbing potential

planetary disk with properties similar to the protosolar nebula, a more thorough treatment of collisional grinding and the subsequent evolution of the debris is necessary to be able to interpret the dust emission profiles presented here as anything more than upper limits.

### **3.7 Summary and Conclusions**

In this work, we have shown that mean-motion resonances with a perturbing planet produce significant local variations in the collision rate of a planetesimal disc. In contrast to [150], we find that the more prominent interior MMRs, including the 2:1, 3:1 and 5:3, all produce structure in the collision profile as a function of semimajor axis. Furthermore, we find that a series of distinctly different features appear when collisions are ordered by cylindrical distance from the central star. The morphology of these features are tied to dynamical behavior of bodies near the edges of the resonances, where the circulation frequency of the critical angle approaches infinity. Particularly near the 2:1 MMR, we find that a bump or dip in the collision profile forms when collisions are ordered by cylindrical distance. The presence of one of these two features depends on the peri- and apocenter distances of the edges of the resonance, relative to the libration width. Because these quantities depend on the mass and eccentricity of the perturbing planet, these properties of the planet are actually encoded in the collision profile.

Near the interior 2:1 MMR, we find that a distinct bump or dip feature is generated in the collision profile, depending on the properties of the perturbing planet. The presence of one of these two structures can be used to constrain the mass and eccentricity of the planet. For a high mass, low eccentricity planet, a dip will form because the edges of the resonance, where many collisions occur, stay sufficiently separated. If the planet has a low enough mass (which shrinks the size of the resonance) or is sufficiently eccentric (which decreases the separation between the apocenter and pericenter distances of the edges of the resonance), a bump will instead form. We tested this hypothesis for five different combinations of the planet's mass and eccentricity and found that a distinct bump or dip signature is produced as long as the planet properties are sufficiently far from the dividing line in parameter space.

This diagnostic is more useful for massive, eccentric planets, because the strength of the resonant perturbations scale linearly with both of these quantities.

Although the planetesimal collision profile would not be directly observable in a planet-forming disc, the dust from the resulting collisional cascade could potentially be used to trace it. So long as the dust grains are well-coupled to the gas and radial drift does not have a significant effect on the morphology of the dust, the bump or dip features seen in the collision profile will also appear in the dust profile. Assuming that this is the case, we have generated simulated observations of a protoplanetary disk with ALMA and showed that the bump or dip features seen in the collision profiles should be detectable through the dust emission. From a dust emission profile with sufficiently strong radial features, one could constrain the properties of a perturbing planet on an exterior orbit in the following way: (1) identify the locations of two MMRs in the disc (2) measure the spacing between them to verify that one of the features is indeed associated with the 2:1 MMR (3) determine whether an under- or overdensity in the radial dust profile exists near this location (4) use the presence of one of these two features to determine the region of the eccentricity-mass plane in which the planet lies.

In line with [17], the results of this work suggest that, in planet forming discs, the observed dust structure should not be interpreted as simply the result of primordial dust that is perturbed by the planets and gas. Instead, some morphological features could be the product of collisional dynamics between larger bodies. Within the confines of the simulations presented here, we have shown that this second-generation dust can give rise to significant features in the dust emission profile. For this reason, we emphasize that planet-forming discs should be thought of as existing along an evolutionary continuum, with the youngest discs being dominated by primordial dust and gas and the most evolved discs being comprised of mainly collisionally generated dust.

The results presented here appear to be broadly consistent with the planetesimal dynamics seen by [156]. In their case, a dip feature can be seen in the azimuthally averaged surface density profile, although they did not test a high enough eccentricity planet in any

of their simulations to produce a bump. Another thing to note is that the gap morphology seen by [156] was markedly different for the 2:1 exterior MMR. Whether this would alter the radial collision profile for the exterior, rather than the interior 2:1 resonance, is not immediately clear. On one hand, the solid surface density diminishes with distance ( $\sim r^{-3/2}$  for the MMSN [63]), which would weaken the signal from locally generated collisional dust. On the other hand, exterior MMRs are quite effective at capturing inward drifting bodies [168], which could locally enhance the surface density well beyond the MMSN value. A full treatment of the collisional cascade process and the radial drift of debris is a subject that we leave for future work.

Compared to using the corotating gap opened by the planet as a diagnostic [40, 41], measuring variations in the dust emission near MMRs is much more subtle and requires much higher spatial resolution and sensitivity. As we have shown, the bump vs dip feature near the 2:1 MMR is marginally detectable with ALMA for the nearest protoplanetary discs, so long as the dust profile closely matches the collisional profile of the planetesimals. Another complicating factor is that the inner  $\sim 10$  au of most protoplanetary discs are optically thick in the sub-mm. The solution to this problem is to instead observe at longer wavelengths where the inner disc is optically thin. This comes at the expense of much poorer resolution. However, future radio facilities like the NG-VLA are expected to achieve sub-au resolution for nearby planet-forming discs [148]. In the more near-term, techniques like Gaussian process fitting present a promising way to recover substructure at sub-beam resolution [78].

### **3.8 Appendix A: Timescale for Secular Forcing**

The timescale for secular forcing is given by the period at which the free eccentricity of a body cycles in the complex plane. The time-dependent imaginary and real components of the eccentricity of a planetesimal are given by [125] (see ch. 7, pg. 282, eq. 7.51)

$$h = e_1 \sin(g_1 t + \beta_1) + e_2 \sin(g_2 t + \beta_2) \quad (3.12)$$

$$k = e_1 \cos(g_1 t + \beta_1) + e_2 \cos(g_2 t + \beta_2),$$

where  $(e_1, e_2)$  and  $(g_1, g_2)$  are the corresponding eigenvector components and eigenvalues of a matrix, which describes the secular interaction between two bodies, given by [125] (see ch. 7, pg. 276, eq. 7.9 and 7.10, with  $\alpha_{12} = \alpha$  and  $\alpha_{12}^- = 1$ )

$$\begin{aligned} A_{jj} &= n_j \frac{1}{4} \frac{m_k}{m_c + m_j} \alpha b_{3/2}^{(1)}(\alpha) \\ A_{jk} &= -n_j \frac{1}{4} \frac{m_k}{m_c + m_j} \alpha b_{3/2}^{(2)}(\alpha). \end{aligned} \quad (3.13)$$

Here,  $n$  is the mean motion of a body and  $m$  is its mass. In the case of a massless test particle being perturbed by a giant planet,  $m_1 = m_g$  and  $m_2 = 0$ . The frequency of the secular forcing is simply the difference of the two eigenvalue frequencies  $g_1 - g_2$ .

### 3.9 Appendix B: Libration in Mean Motion Resonance

For second order and higher MMRs, the maximum libration width is given by [125] (ch. 8, pg. 338, eq. 8.58) as

$$\frac{\delta a}{a} = \pm \left( \frac{16}{3} \frac{|C_r|}{n} e^{|q|} \right)^{1/2}, \quad (3.14)$$

where  $n$ ,  $a$  and  $e$  are the mean motion, semimajor axis and eccentricity of the unperturbed body.  $C_r$  is a constant defined by  $m'/m_c n \alpha f_d(\alpha)$ , where  $\alpha = a/a'$  and  $f_d$  is the resonant part of the disturbing function. For an interior second-order resonance,

$$\begin{aligned} f_d(\alpha) &= \frac{1}{8} \left[ -5(p+q) + 4(p+q)^2 - 2\alpha D \right. \\ &\quad \left. + 4(p+q)\alpha D + \alpha^2 D^2 \right] b_{1/2}^{p+q}, \end{aligned} \quad (3.15)$$

(see [125] table 8.1, third row, with  $j = p+q$ ) where  $D b_s^j$  is the first derivative with respect to  $\alpha$  of the Laplace coefficient defined in equation 3.2. This is given by [?] as

$$\frac{db_s^j}{d\alpha} = s \left( b_{s+1}^{j-1} - 2\alpha b_{s+1}^j + b_{s+1}^{j+1} \right). \quad (3.16)$$

For a first-order resonance, the associated disturbing function terms are slightly simpler such that

$$f_d(\alpha) = -(p+q)b_{1/2}^{p+q} - \frac{\alpha}{2}Db_{1/2}^{p+q}, \quad (3.17)$$

(see [125] table 8., first row) and there is an additional contribution to the motion of the critical angle by the pericenter precession rate such that

$$\frac{\delta a}{a} = \pm \left( \frac{16}{3} \frac{|C_r|}{n} e \right)^{1/2} \left( 1 + \frac{1}{27p^2e^3} \frac{|C_r|}{n} \right)^{1/2} - \frac{2}{9pe} \frac{|C_r|}{n} \quad (3.18)$$

(see [125] ch. 8, pg. 340, eq. 8.76, with  $j_2 = p$ ).

In mean-motion resonance, the orbital elements of a perturbed body, along with the critical angle described by equation 3.5, will exhibit oscillations. In the circular, restricted three-body case, these small amplitude oscillations exhibit a characteristic frequency, given by (see [125] ch. 8, pg. 332, eq. 8.47, with  $j_2 = -p$  and  $j_4 = -q$ )

$$\omega_0 = 3p^2 C_r n e^{|-q|}. \quad (3.19)$$

### 3.10 Appendix C: Nonaxisymmetric Structure in Boley 2017

As mentioned in section 3.4.1, the nonaxisymmetric gap structure seen in figure 3.1 is present in a number of other studies, including [150] and [156]. One would expect the same dynamics to be at work in the simulation of [17], although the structure is not obviously visible in figure 3 of their work.

Here, we present a closer look at the positions of the planetesimals at the end of the [17] simulation. In figure 3.12, we show the planetesimal positions in polar, rather than Cartesian coordinates as originally presented in the paper. Two planets on circular orbits are present here. The first has mass of  $17 M_\oplus$  and lies at 32.3 au. The second planet has a mass of

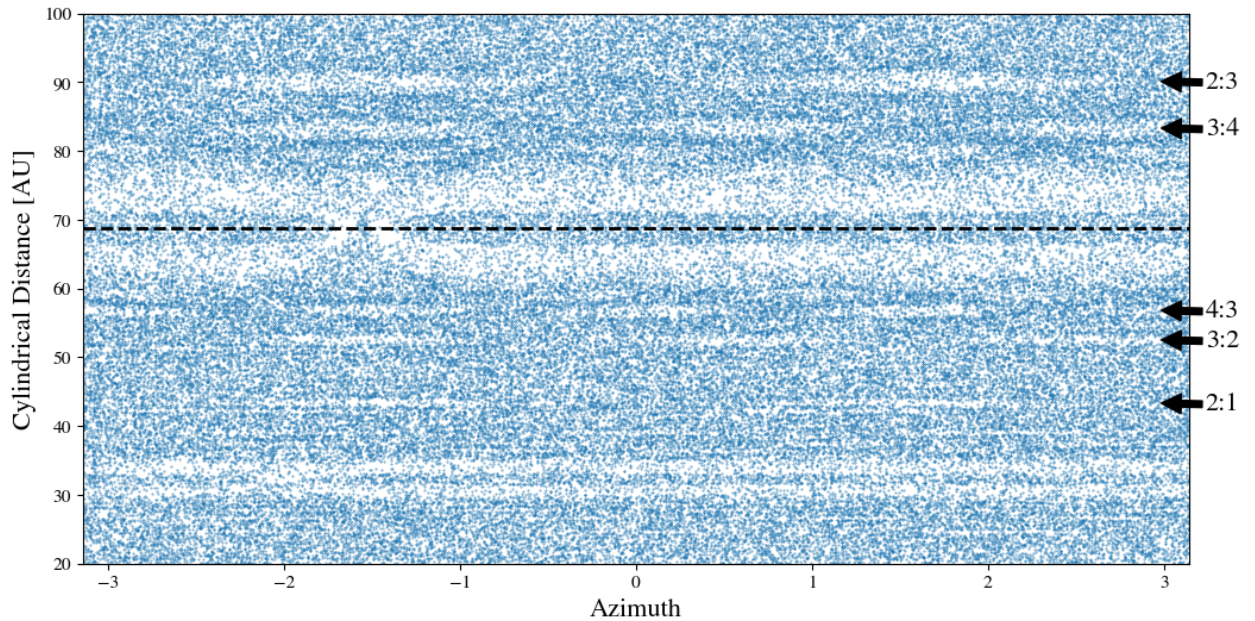


Figure 3.12: Positions of planetesimals at the end of the simulation presented in [17] in polar coordinates. The dashed line marks the location of a  $50 M_{\oplus}$  planet embedded in the disc. First order MMRs with the planet are indicated with arrows. A second planet is also present at 32.3 au, although it is not massive enough to induce any significant structure in the disc near associated resonances.

$50 M_{\oplus}$  and lies at 68.8 au. A horseshoe shaped collection of planetesimals is visible to be corotating with each planet. Nonaxisymmetric gaps are also visible at the locations of first order MMRs with the more massive planet, which are indicated with arrows.

Similar to figure 3.7, a gap is present at the same orbital phase as the planet at the 2:1 MMR, along with a second gap on the opposite side of the disc. Gaps near the 4:3 and 3:2 MMRs are also present in phase with the planet, although the number and spacing between additional gaps appears to be different for each resonance. In addition, the gap structure associated with the exterior MMRs appears markedly different than that of each corresponding interior MMR, which suggests that the structure is related to the symmetry of the path that a planetesimal in a frame corotating with the planet takes.

## Chapter 4

# FORMATION OF PLANETARY EMBRYOS AT SHORT ORBITAL PERIODS

### 4.1 *Introduction*

Planetesimal accretion is a key phase in the terrestrial planet growth process, bridging the gap from kilometer-sized bodies up to roughly moon-sized objects known as planetary embryos. In the earliest stages of the planet formation process, **beginning from  $\mu\text{m}$  sizes**, aerodynamic forces dominate the growth and evolution of the solids and statistical models [?, ?] are appropriate to describe how these numerous, small bodies coagulate.

Due to the internal pressure support of the gas disk, the gas itself orbits at sub-Keplerian speed and exerts a headwind on any solids large enough to decouple from the gas [166]. Around a meter in size, this headwind is maximally effective at sapping away orbital angular momentum, and planet-building material can fall onto the central star on catastrophically short timescales [166, ?]. Additionally, laboratory experiments suggest that collisions between mm- to cm- sized solids tend to result in bounces or destruction, rather than continued growth [?, ?, ?].

For these reasons, a number of mechanisms to radially concentrate solids in a planet-forming disk have been proposed to facilitate fast growth from mm to km sizes [81, ?, ?] in order to surmount these barriers. Interestingly, formation models for the short-period multiplanet systems revealed by Kepler [46] also seem to require enhanced concentrations of planet-building material to reproduce the observed architectures [?, 62].

Regardless of how the mm- to km-sized growth barriers are surmounted, gravity begins to dominate and aerodynamic gas drag plays an increasingly unimportant role beyond this size. During this phase, collision cross sections are enhanced as gravitational focusing [151]

acts to bend the trajectories of bodies undergoing close encounters. Because gravitational focusing becomes more effective as bodies grow larger, a period of runaway growth occurs [173, 87, 13] and a power law spectrum of masses develop. Eventually, the largest bodies (known as oligarchs) dynamically heat the remaining planetesimals, severely limiting further growth [88]. The final outcome of this phase is a bimodal population of dynamically cold oligarchs, surrounded by dynamically hot, difficult to accrete residual planetesimals. Lines of evidence suggest that the asteroid belt [19, 119], Kuiper belt [44, ?, ?] and the Oort cloud [?] are largely composed of the leftovers of this stage of planet formation.

**Tidal interactions between protoplanets and the gaseous disk keep eccentricities and inclinations low until the gas disk dissipates, typically over the course of a few Myr [?]. Eventually, gravitational perturbations eventually trigger an instability which drives bodies onto crossing orbits. This instability occurs on a timescale of  $\sim 10^5$  years and involves large scale oscillations of the eccentricity and inclinations of the bodies as they strongly interact through secular resonances [24].** As a consequence of the instability, the oligarchs are no longer on isolated, stable orbits and coalesce to form Earth-sized planets through a series of extremely energetic giant impacts [89, 147, 144].

Due to the relative ease of modeling the early dust coagulation phases and the final giant impact phase, these steps in the terrestrial planet formation process have received most of the attention in the literature. The planetesimal accretion phase, which we will focus on in this paper, is more difficult and expensive to model because there are too many particles to directly track with traditional N-body codes, while the gravitational interactions between the few massive bodies produced by the runaway growth phase [68, 86, 88] render statistical methods inappropriate. Due to computational expense, N-body simulations of planetesimal accretion are usually modeled in a narrow ring [87, 88], and the results and timescales are then scaled to suit whatever relevant orbital period is being studied. N-body simulations of terrestrial planet assembly typically begin with a series of neatly spaced oligarchs, whose mass varies smoothly with orbital period. As we will show in this paper,

oligarchic growth does not scale to arbitrarily short orbital periods.

Given that Systems of Tightly-packed Inner Planets (STIPs) appear to be a common outcome of planet formation [?, 106, ?], understanding exactly how solids accumulate at short orbital periods is crucial. Although gas-disk driven migration of the planets themselves is often invoked to explain the observed architectures [75, 74], we will focus on an in-situ model in this paper. That is, once the planetesimals themselves form, they largely stay in place, and any subsequent large-scale movement of the solids are the result of mutual gravitational interactions. The focus of this work will be to understand how the outcome of the planetesimal accretion process scales with orbital period by using a high-powered N-body code to directly follow the growth and evolution of the planetesimals across a wide range of orbital periods (1 to 100 days). In doing so, we will assess whether the typical initial conditions (fully formed, evenly spaced protoplanets, e.g. [144]) used in studies of terrestrial planet formation are actually appropriate for understanding STIPs.

In section 4.2 we provide an overview of the theory behind planetesimal accretion and show that assumptions used to derive the well-known modes of growth are only valid at sufficiently long orbital periods. We then motivate the need for N-body simulations to study this problem and describe the code used, along with how our initial conditions were constructed in section 4.3. In section 4.4, we present a parameter study of planetesimal accretion using a series of simulations of narrow annuli that exhibit both oligarchic and non-oligarchic growth. In section 4.5 we present a set of simulations starting with a wide planetesimal disk and demonstrate that a transition between accretion modes occurs at moderately small orbital periods. Next, we assess the impact of simplifications made to our collision model on this result in section 4.6. In section 5.6, we discuss the implications of this multimodal accretion behavior throughout the disk for planet formation models and conclude.

## 4.2 Overview of Planetesimal Accretion

### 4.2.1 Oligarchic and Runaway Growth

We begin our analysis by considering a disk of equal mass planetesimals with radius  $r_{pl}$ , mass  $m_{pl}$  and surface density  $\Sigma_{pl}$ . The collision rate in the vicinity of an orbit defined by Keplerian frequency  $\Omega$  can be written as  $n\Gamma v$ , where  $n = \Sigma_{pl}\Omega/2m_{pl}v$  (where we have assumed that the scale height of the planetesimal disk goes as  $2v/\Omega$ ).  $\Gamma$  describes the effective collision cross section and  $v$  is the typical encounter velocity between planetesimals. For a swarm of planetesimals on randomly oriented orbits,  $v$  is typically taken to be the rms velocity,  $\langle v^2 \rangle^{1/2}$ , which can be related to the eccentricity and inclination distribution  $(e, i)$  in the following way [102]:

$$\langle v^2 \rangle^{1/2} = \left( \frac{5}{4} \langle e^2 \rangle^{1/2} + \langle i^2 \rangle^{1/2} \right) v_k. \quad (4.1)$$

The dynamical interactions between growing planetesimals can be somewhat simplified by scaling the orbital elements of the bodies by the Hill radius

$$r_h = \left( \frac{m_{pl}}{3M_*} \right)^{1/3}, \quad (4.2)$$

where  $M_*$  is the mass of the central star. The Hill radius of a body describes the size scale over which the gravity of the growing planetesimal dominates over the gravity of the star. Using equation 4.2, the eccentricity, inclination and separation between orbiting bodies can be defined as

$$e_h = \frac{ae}{r_h}, \quad i_h = \frac{ai}{r_h}, \quad \tilde{b} = \frac{a_2 - a_1}{r_h}. \quad (4.3)$$

Using this formalism,  $e_h$  and  $i_h$  describe the radial and vertical excursions of an orbiting body in units of its Hill radius. For  $e_h > 1$ , the random velocity dispersion dominates over the shearing motion across a separation of  $1r_h$  and encounters can be treated with a two-body formalism.

Assuming that every collision results in a perfect merger, the growth rate of a planetesimal is given by

$$\frac{1}{M} \frac{dM}{dt} = \frac{\Sigma\Omega}{2m_{pl}} \Gamma. \quad (4.4)$$

In the case where the collision cross section depends only on the physical size of the planetesimals, the growth scales sub-linearly with mass and the mass distribution is expected to evolve in an “orderly” fashion, in which mass ratios between bodies tend toward unity. However, bodies larger than  $\sim 100$  km in size are expected to exert a significant gravitational force on each other during encounters and the collision cross section depends on both the size of the bodies and their encounter velocities. In this case,

$$\Gamma = \pi r_{pl}^2 \left( 1 + v_{esc}^2/v^2 \right) \quad (4.5)$$

[151], where  $v_{esc}$  is the escape velocity from the two bodies at the point of contact.

In the limit that  $v_{esc} \gg v$ , it can be shown that  $dM/dt \propto M^{4/3}$ , which implies a runaway scenario where growth accelerates with mass. This mode of growth was confirmed with N-body simulations by [87] and appears necessary to construct protoplanets within the lifetime of a protoplanetary disk [?], **although one should note that pebble accretion [?, ?, ?] is a viable alternative scenario.** Due to the velocity dependence of the gravitational focusing effect, it is not clear how ubiquitous this mode of growth is. In particular, encounter velocities at short orbital periods will be rather large (because  $v \sim v_k$ ) and the  $v_{esc} \gg v$  condition may not always be satisfied. The effect that a dynamically hot disk has on runaway growth will be examined in detail in section 4.4.

An important feature is missing from the model described above, which limits its applicability at late times. Gravitational stirring, which converts Keplerian shear into random motion, raises the typical encounter velocity between planetesimals over time [?, ?] and diminishes the effectiveness of gravitational focusing. As the mass spectrum of the system evolves away from uniformity, these velocity differences become even more pronounced. As the system evolves, it tends toward a state of energy equipartition where  $v \sim m^{1/2}$ . For a system of equal mass bodies in which encounters are driven by random motions rather than

Keplerian shear (dispersion dominated), the timescale for gravitational stirring is described by the two-body relaxation time [68]

$$t_{relax} = \frac{v^3}{4\pi n G^2 m_{pl}^2 \ln \Lambda}, \quad (4.6)$$

where  $\ln \Lambda$  is the Coulomb logarithm, typically taken to be  $\approx 3$  for a planetesimal disk [?, ?]. Despite the fact that the behavior of gravitational stirring is well-described by a two-body formula, [68] found that the stirring in a planetesimal disk is actually driven by close encounters, which requires a three-body formalism. As we will show in section 4.4, gravitational stirring effectively shuts off when the Hill sphere of a body becomes comparable to its physical size. In this case, close encounters tend to result in collisions, and the main pathway for energy exchange between planetesimals and growing protoplanets is unable to operate.

[88] showed that **the runaway growth process described above** is actually self-limiting. As the runaway bodies develop, they become increasingly effective at **dynamically** heating the remaining planetesimals, which diminishes the gravitational focusing cross sections and throttles the growth rate. Around the time that the mass of the runaway bodies exceeds the mass of the planetesimals by a factor of  $\sim 50 - 100$  [68] a phase of less vigorous “oligarchic” growth commences, in which the largest bodies continue to accrete planetesimals at similar rates, independent of mass.

**Regardless of the mechanism that eventually limits the growth of the planetary embryos, a maximum estimate for the masses produced during this stage of accretion can be obtained using the initial solid surface density profile. A growing protoplanet will eventually accrete material within a distance  $b = \tilde{b}r_h$  of its orbit. The total mass of planetesimals within this distance is then  $2\pi a (2\tilde{b}r_h) \Sigma_{pl}$ , where  $a$  is the semimajor axis of the growing protoplanet. The “isolation mass” of the protoplanet can then be obtained by setting the protoplanet mass equal to the total mass of planetesimals within accretionary reach such that**

$$M_{iso} = 4\pi a^2 \tilde{b} \left( \frac{M_{iso}}{3M_*} \right)^{1/3} \Sigma_{pl}. \quad (4.7)$$

Solving for  $M_{iso}$  gives

$$M_{iso} = \left[ \frac{(2\pi a^2 \Sigma_{pl} \tilde{b})^3}{3M_*} \right]^{1/2}. \quad (4.8)$$

For bodies on circular, non-inclined orbits,  $\tilde{b} = 2\sqrt{3}$  is the smallest orbital separation that produces a non-negative Jacobi energy and permits a close encounter [?]. This value of  $\tilde{b}$  is typically used to calculate the final isolation mass of a protoplanet because oligarchic growth tends to maintain near-circular orbits for the growing protoplanets.

The picture described above relies upon a crucial assumption, which is that the mass distribution evolves slowly enough for gravitational stirring to maintain energy equipartition. In other words, the relaxation timescale must remain short relative to the **collision** timescale. For typical conditions near the terrestrial region of the solar system, this timescale condition is satisfied. Due to the steep dependence of the relaxation time on encounter velocity, however, this condition can easily be violated at shorter orbital periods.

In figure 4.1, we show the ratio between the relaxation and collision timescale for a population of equal-mass planetesimals as a function of orbital period. Here, the encounter velocity is described by equation 4.1. For simplicity, we assume that  $\langle e^2 \rangle^{1/2} = 2 \langle i^2 \rangle^{1/2}$  [66] and that the eccentricity dispersion is constant with orbital period. The coloring indicates the ratio between  $t_{relax}$  and  $t_{coll}$ . The dashed lines denote the eccentricity at which the random encounter velocity (calculated according to equation 4.1) is equal to the mutual escape velocity of the bodies. This is shown for planetesimals with an internal density of  $3 \text{ g cm}^{-3}$  ranging from 10 to 200 km in size.

A physically realistic value of  $e_h$  for a population of planetesimals is going to depend on the structure of the gaseous disk (which we will address in section 4.5). However, the eccentricity dispersion will typically increase over time until  $\langle v^2 \rangle^{1/2} = v_{esc}$  and this is often used to construct the initial conditions (e.g. [13]). Therefore, the curves in this figure should be interpreted as upper limits.

The timescale criterion for oligarchic growth is only satisfied in regions where the disk is

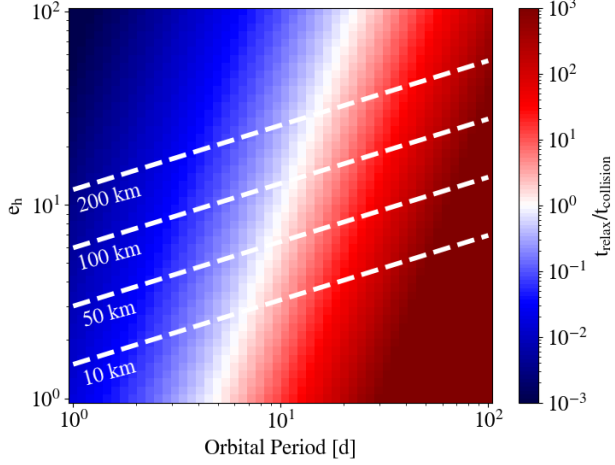


Figure 4.1: The ratio between the two-body relaxation and collision timescale for a population of equal-mass planetesimals with an internal density of  $3 \text{ g cm}^{-3}$ . **The dashed curves show the value of  $e_h$  for which the random velocity dispersion is equal to the escape velocity of the planetesimals for a range of sizes.** Only in regions where  $t_{\text{relax}} \gg t_{\text{coll}}$  can the velocity distribution respond to changes in the mass of the bodies such that oligarchic growth can operate. This condition is no longer satisfied for a dynamically hot disk at sufficiently short orbital periods.

sufficiently dynamically cold and the orbital period is sufficiently long. In sections 4.4 and 4.5 we will explore the behavior and outcome of planetesimal accretion in regions where this criterion is *not* satisfied.

#### 4.2.2 Planetesimal Size and Extent of Hill Sphere

In the formalism described above, the mass and velocity distribution of the bodies are both a function of time. Due to the interdependence of these quantities, it is not clear whether the **ratio between the relaxation and collision timescales will remain constant** as the oligarchs develop. In the case of the solar system,  $t_{\text{relax}} \ll t_{\text{coll}}$  likely continued to remain true, otherwise runaway growth would have consumed all of the small bodies and there would be nothing left to populate the asteroid or Kuiper belt. In the case where  $t_{\text{coll}} \ll t_{\text{relax}}$ , however, it is not clear how the system might evolve.

An insight into the expected behavior in this regime can be gained by defining a dimensionless parameter,  $\alpha$ , which is the ratio between the physical size of a body and its Hill radius,  $r_h$

$$\alpha = \frac{r_{pl}}{r_h} = \frac{1}{a} \left( \frac{9M_\star}{4\pi\rho_{pl}} \right)^{1/3}, \quad (4.9)$$

where  $a$  is the semimajor axis of the body and  $\rho_{pl}$  is its bulk density. Assuming that the bulk density stays constant as bodies collide and grow, and that no large-scale migration occurs, the scaling of both  $r_{pl}$  and  $r_h$  as  $m_{pl}^{1/3}$  means that  $\alpha$  will be constant with time. For a composition of ice and rock,  $\alpha$  is small for any presently populated region of the solar system ( $\alpha \sim 10^{-2}$  near Earth and  $\alpha \sim 10^{-4}$  in the Kuiper belt). As one moves closer to the sun,  $\alpha$  becomes larger than 1, which implies that the Hill sphere of a body becomes smaller than its physical size. **As an additional note, the Roche limit of the central body and the distance at which  $\alpha = 1$  are equivalent for a rigid spherical body. Applying a hydrostatic correction to the Roche limit,  $a_{Roche} \simeq 0.6a_{\alpha=1}$ . This accretion mode should therefore be relevant for ring systems, which is a topic that deserves further study using high resolution N-body techniques.**

The magnitude of  $\alpha$  controls the relative importance of gravitational scattering and collisions in driving the evolution of the planetesimal disk. When  $\alpha$  is small, most close encounters will result in a gravitational interaction, moving the system toward a state of relaxation. If, however, the Hill sphere is largely filled by the body itself, these same encounters will instead drive evolution of the mass spectrum. Because  $\alpha$  stays constant with mass, the boundary in the disk where collisions or gravitational encounters dominate, will stay static with time.

We also introduce a second dimensionless quantity, which relates the physical size of the bodies to the velocity state of the system

$$\beta = \frac{r_{pl}}{r_g}. \quad (4.10)$$

where  $r_g = Gm_{pl}/v^2$  is the gravitational radius of a body (see eq 4.1 of [?]). Encounters between bodies inside of a distance of  $r_g$  result in significant deflections of their trajectories. It should be noted that the gravitational focusing enhancement factor  $v^2/v_{esc}^2$  is equal to 1

for  $\beta = 1$ . In the case where  $r_g$  is smaller than the size of a planetesimal, the gravitational focusing enhancement factor will be between 0 and 1 and the collision cross section is mostly set by the geometric value. **For very large values of  $r_g$  ( $\beta \ll 1$ ), the effective collision cross section is almost entirely set by gravitational scattering.**

These scaling considerations motivate the range of parameters we choose for the numerical experiments presented in the next section, where we aim to understand where and when runaway and oligarchic growth can operate.

### 4.3 Numerical Methods

We use the tree-based N-body code CHANGA to model the gravitational and collisional evolution of a swarm of planetesimals. CHANGA is written using the CHARM++ parallel programming language and has been shown to perform well on up to half a million processors [113] and can follow the evolution of gravitationally interacting collections of up to billions of particles. Using a modified Barnes-Hut tree with hexadecapole expansions of the moments to approximate forces, CHANGA integrates the equations of motion using a kick-drift-kick leapfrog scheme. For all of the simulations presented in this paper, we use a node opening criteria of  $\theta_{BH} = 0.7$ . Additional information about the code is available in [79, 113].

Using the neighbor-finding algorithm in CHANGA, originally designed for SPH calculations, we have recently implemented a solid body collision module in the code. This work is largely based on the solid-body collision implementation in PKDGRAV, which is described in [149] and [150]. To summarize, imminent collisions are detected during the “drift” phase by extrapolating positions of bodies forward in time, using the velocity calculated at the opening “kick”. For each body, any neighboring particles which fall within a search ball of radius  $2\Delta T v + 2r_{pl}$ , where  $\Delta T$  is the current timestep size for the particle and  $v$  is magnitude of its heliocentric velocity, are tested for an imminent collision. In the case that a collision is detected, the particles are merged into a single larger body, which is given the center of mass position and velocity of the two **parents**. Resolving a collision can produce another imminent collision, so collisions are handled one-by-one and another full collision check is run

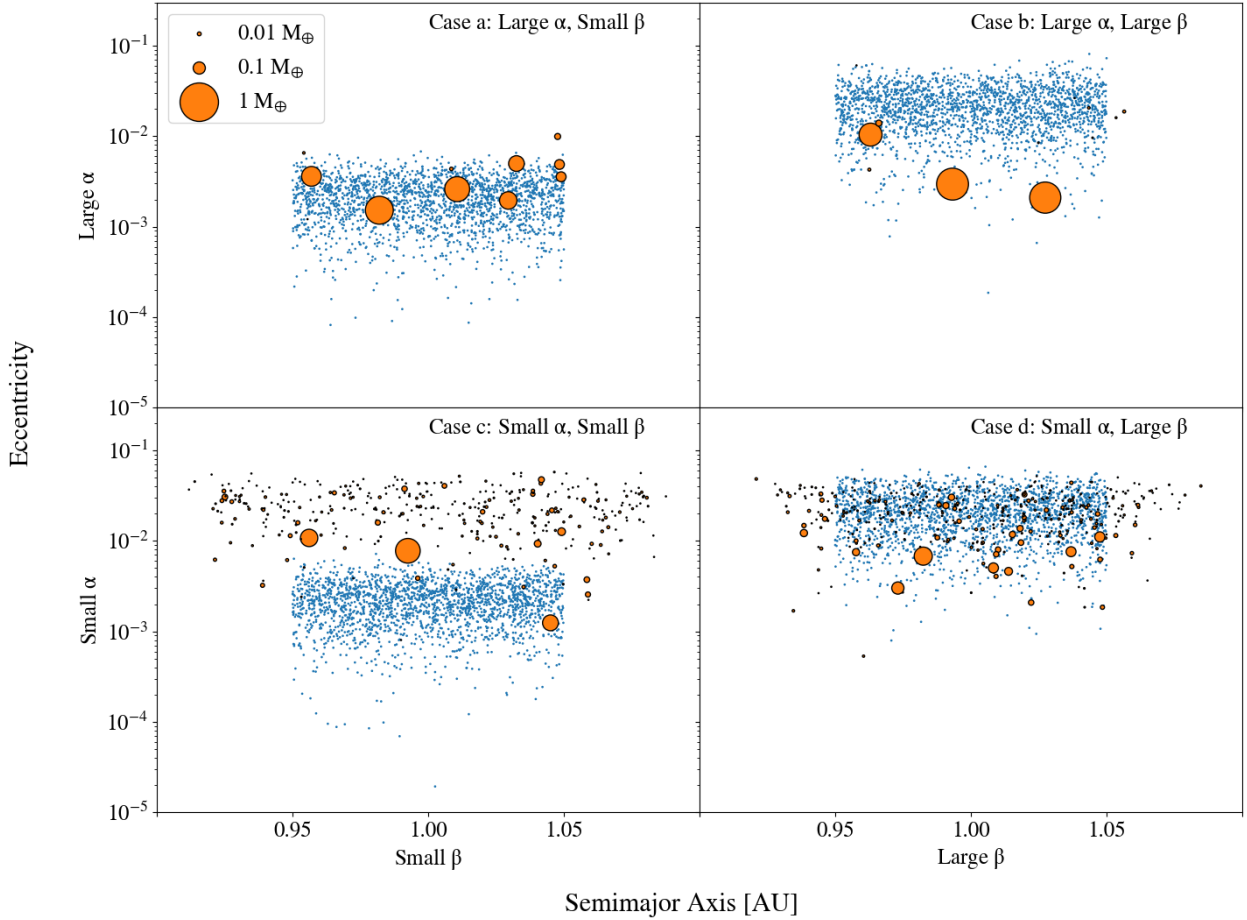


Figure 4.2: The initial (blue) and final (orange) states of the narrow annulus simulations described in section 4.4. Relative masses of the bodies are indicated by point size. In the case of large  $\alpha$ , almost no residual planetesimal population remains. Regardless of the initial choice of  $\beta$ , the protoplanets that form attain similar eccentricities.

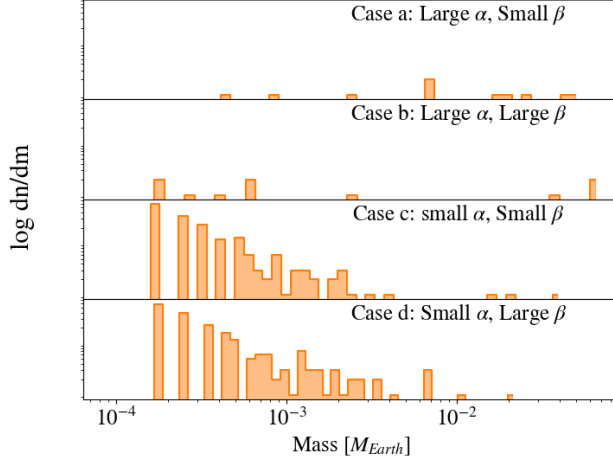


Figure 4.3: The final state of the mass distributions for the narrow annulus simulations described in section 4.4. For small  $\alpha$ , a few embryos form alongside a power law tail of planetesimals. For larger values of  $\alpha$ , the mass distribution stops being bimodal. As in the previous figure, the initial choice of  $\beta$  does not appear to have any meaningful impact on the end result.

after the previous event is resolved. For a more detailed description of the collision module in CHANGA, see [164]. Particles are advanced on individual timesteps chosen as a power of two of a base timestep. The timestep for an individual particle is based on an estimate of the gravitational dynamical time determined by the minimum of  $\sqrt{d_{node}^3/(G(M_{node} + m_{pl}))}$  across all nodes in the tree that are accepted by the Barnes-Hut opening criterion. Here  $d_{node}$  is the distance from the planetesimal to the center of mass of the tree node and  $M_{node}$  is the total mass of the tree node. For nearby particles  $M_{node}$  is replaced with the mass of the nearby particle.

#### 4.4 Narrow Annulus Simulations

We begin by **exploring the outcome of planetesimal accretion in different parts of the  $(\alpha, \beta)$  parameter space**. The choices of  $\alpha$  and  $\beta$  are motivated by two questions raised in section 4.2. 1) Does runaway growth still operate when the condition that  $v \ll v_{esc}$  is not satisfied? 2) How does planetesimal accretion proceed when the planetesimals themselves

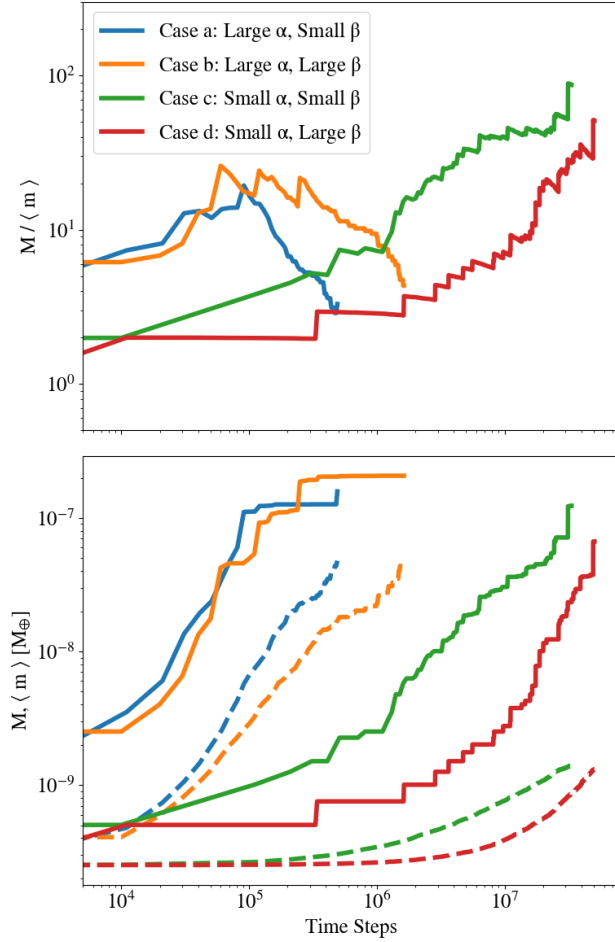


Figure 4.4: **Top:** The evolution of the ratio between the maximum and mean mass for the four simulations presented in section 4.4. The runaway growth phase can be identified by a positive trend in this ratio. For all values of  $\alpha$ , an increase in  $\beta$  has the effect of delaying runaway growth. **Bottom:** The evolution of the maximum (solid lines) and mean (dashed lines) shown individually.

occupy a significant fraction of their Hill spheres?

To answer these questions, we run a series of simulations in which a narrow annulus of planetesimals orbits a star. The values of  $\alpha$  and  $\beta$  are varied individually. 4000 planetesimals with individual masses of  $8.37 \times 10^{-5} M_{\oplus}$  are placed with semimajor axes drawn **from a uniform distribution** between 0.95 and 1.05 AU about a  $1 M_{\odot}$  star. **In total, the disk contains  $\sim 0.33 M_{\oplus}$  of material.** The argument of perihelion,  $\omega$ , longitude of ascending node,  $\Omega$ , and mean anomaly,  $M$ , for each body is drawn from a uniform distribution  $\in [0, 2\pi)$ . The inclinations and eccentricities are drawn from a Rayleigh distribution with  $\langle i^2 \rangle = 1/2 \langle e^2 \rangle$  [66].

In the “fiducial” case, we give the bodies a bulk density of  $3 \text{ g cm}^{-3}$  (**for a radius of 341 km**), and  $\langle e^2 \rangle^{1/2} = 4e_h$ , which corresponds to  $\alpha = 3.6 \times 10^{-2}$  and  $\beta = 3.4 \times 10^{-3}$ . These parameters are chosen to match the initial conditions of [88], which gave rise to oligarchic growth. To vary the value of  $\alpha$ , we alter the bulk density of the particles. In the high- $\alpha$  case, the bulk density is reduced by a factor of  $\sim 7100$ , which produces  $\alpha = 1$ . **This corresponds to a bulk density of  $4.2 \times 10^{-4} \text{ g cm}^{-3}$  and a radius of 6,500 km.** Although this is most certainly unphysical, the purpose of this modification is to have a planetesimal completely fills its Hill sphere so that no strong gravitational scattering should occur. To vary  $\beta$ , the eccentricity dispersion is increased. For the high- $\beta$  case,  $\langle e^2 \rangle^{1/2}$  is increased to  $1500e_h$ , which corresponds to  $\beta = 15,000$ . **This is the largest value of  $\beta$  that permits a particle at 1 AU to still have an apocenter and pericenter distance that lies within the boundaries of the disk.** This choice of  $\beta$  places the system firmly in the  $v > v_{esc}$  regime, while still allowing growth to occur in a reasonable number of timesteps.

In all cases, the simulations are evolved with a base timestep of 1.7 days, which corresponds to 3% of an orbital dynamical time  $\sqrt{a^3/GM_*}$ . Due to the vastly differing growth timescales in each case, a simulation is stopped when the growth of the most massive body flattens out. In figure 4.2, we show the a-e distribution of bodies in the initial (blue) and final (orange) snapshots from each of the 4 simulations. The size of the points indicates the

relative masses of the bodies. Only **with small  $\alpha$  (case c, d)** does a residual population of dynamically hot planetesimals develop. The lack of high eccentricity planetesimals (**relative to the protoplanets**) in the large  $\alpha$  (**case a, b**) **simulations** suggests that most encounters result in accretion rather than scattering. **For large  $\beta$  (case b, d), the growing protoplanets and end up in a dynamically cool state, relative with the initial conditions.** This is due to kinetic energy being lost as particles inelastically collide. One last point we note is the difference between the eccentricities of protoplanets in the large  $\alpha$ , large  $\beta$  (**case b**) and the small  $\alpha$ , large  $\beta$  (**case d**) **simulation**. The dynamically cooler result of the **former** case is likely due to the dominant role that inelastic collisions play here.

In figure 4.3, we show the mass distribution of bodies from the final snapshot in each of the four **simulations**. In addition to leaving fewer residual planetesimals, the large  $\alpha$  (**case a, b**) simulations produce **embryos that are a factor of a few larger**. Despite the vastly different encounter velocities of each population of bodies, the initial size of  $\beta$  (so long as bodies remain in the dispersion-dominated regime) appears to have no significant effect on the final distribution of masses. **For reference, the boundary between shear and dispersion-dominated encounters ( $e_h = 1$ ) lies around  $e = 4 \times 10^{-4}$  for the planetesimal mass we have chosen. The eccentricity at which  $\langle v^2 \rangle^{1/2} = v_{esc}$  for the planetesimals is around  $10^{-2}$ .**

To investigate whether any of these planetesimal rings underwent runaway growth, we examine the time evolution of the maximum and mean masses in each simulation. The ratio  $M/\langle m \rangle$  is plotted in **the top panel of** figure 4.4. **Here**, a positive slope indicates that the quantities are diverging (i.e. the growth rate is accelerating with mass). This behavior is evident in all four cases **although the small  $\alpha$  simulations eventually reach a stage where the curves turn over as the planetesimal supply depletes..** Even with a large  $\beta$ , where the effective collision cross section is nearly equal to the geometric value, runaway growth still appears to operate. The ubiquity of the early positive trends in this figure suggests that as bodies collide and grow, the relative difference in gravitational focusing factors between bodies is what drives the system towards runaway growth, no matter

how close the collision cross sections lie to the geometric value. Although larger encounter velocities lengthen the growth timescales, runaway growth appears to be inevitable, so long as gravity is the dominant force in the system. For large  $\alpha$  (**case a, b**), the curves in this figure eventually turn over and begin to decline. **In the bottom panel of figure 4.4, we separately show the evolution of the maximum (solid lines) and mean (dashed lines) mass for each case.** Here, it is evident that the turnover in  $M/\langle m \rangle$  is driven by an increase in the average mass as the planetesimal population becomes depleted. For small  $\alpha$ , one would expect that planetesimal accretion should also eventually come to a halt as the growth timescale lengthens due to the planetesimal surface density decreasing and the residual bodies being scattered onto high eccentricity orbits with negligible gravitational focusing factors. Many more timesteps, however, would be required to reach this point.

Additionally, these results suggest that the value of  $\alpha$ , which is a function of only the initial conditions, controls the qualitative outcome of accretion. Across most of a planet-forming disk,  $\alpha$  is small, and frequent gravitational encounters between the growing bodies will facilitate oligarchic growth. In the dispersion-dominated regime, close encounters drive the stirring between planetesimals and embryos [?, ?]. **When  $\alpha \ll 1$ , the Hill sphere of a body is mostly empty space and the majority of close encounters result in viscous stirring, rather than accretion.** **In the opposite regime,** we observe that runaway growth still occurs, but nearly all of the planetesimals are consumed by the forming protoplanets, rather than being scattered onto higher eccentricity orbits, where they would otherwise remain as a remnant of the early stages of planet formation [88, ?].

## 4.5 Full Disk Simulation

### 4.5.1 Initial Conditions

Motivated by the qualitative dependence of accretion on  $\alpha$ , we next investigate whether this highly efficient, non-oligarchic growth should be expected to operate near the innermost

regions of a typical planet-forming disk. Given that N-body simulations of short-period terrestrial planet formation typically begin with a chain of neatly-spaced, isolation mass (see [?] eq. 20) protoplanets, it is pertinent to determine whether the high  $\alpha$  growth mode we revealed in the previous section invalidates this choice of initial conditions.

Given the dearth of short-period terrestrial planets observed around M stars (e.g. TRAPPIST-1 [50, 51, 3]), we chose to model the evolution of a series of wide planetesimal disks, which span from 1 to 100 days in orbital period, orbiting a late-type M star of mass  $0.08 M_{\odot}$ . For a population of planetesimals with a bulk density of  $3 \text{ g cm}^{-3}$ , this orbital period range corresponds to  $\alpha \in (0.7, 0.05)$ . By simultaneously modeling a broad range of orbital periods, we can determine the critical value of  $\alpha$  that divides these two modes of accretion, and also explore how the oligarchic/non-oligarchic accretion boundary affects the resulting distribution of protoplanets.

Four wide-disk simulations are run in total (see table 4.1). In each case, the solid surface density follows a power law profile

$$\Sigma(r) = 10 \text{ g cm}^{-2} \times A \left( \frac{M_*}{M_{\odot}} \right) \left( \frac{r}{1 \text{ AU}} \right)^{-\delta} \quad (4.11)$$

where  $M_*$  is the mass of the central star,  $10 \text{ g cm}^{-2}$  is the surface density of the minimum-mass solar nebula [63, MMSN] at 1 AU,  $A$  is an enhancement factor and  $\delta$  is the power law index. In the first case (fdHi), we model a disk that follows a MMSN power law slope ( $\delta = 1.5$ ), with the overall normalization enhanced by a factor of 100. This choice of normalization for the solid surface density profile appears necessary in order to reproduce many observed short period terrestrial worlds in-situ [62]. **The most current planetesimal formation models all involve streaming instabilities triggered by solid material concentrating at preferential locations in the disk. This can occur via zonal flows [?, ?], vortices [?], or through mechanisms that produce a pressure bump in the gas disk, such as an ionization [?] or condensation front [?, ?], or even the perturbations from an existing planet [?]. [?] showed that evolution of the snow line boundary can cause planetesimal formation over a significant area of the disk, producing mass**

concentrations at least as large as the ones we use here. We argue that this is a particularly attractive mechanism for widespread planetesimal formation around low-mass stars, as their extreme pre-main sequence evolution is particularly conducive to significant movement of the condensation fronts [11].

Additionally, we vary the power law index (fdHiShallow, fdHiSteep) and overall normalization (fdLo) of  $\Sigma(r)$ . Although there is no way to reliably measure the uncertainty on the MMSN power law slope, [28] applied a similar analysis to a sample of Kepler multiplanet systems and found a variation of  $\sim 0.2$ . Sub-millimeter observations of the outer regions of cold protoplanetary disks find that  $\delta$  can be as low as 0.5 [?, ?, ?]. Therefore, we vary  $\delta$  by a value of 1.0 relative to the MMSN value for the fdHiShallow and fdHiSteep simulations.

In all cases, the eccentricities and inclinations of the bodies are randomly drawn from a Rayleigh distribution, with  $\langle e^2 \rangle^{1/2} = 2 \langle i^2 \rangle^{1/2} = e_{eq}$  [68]. Following [88], the value of  $e_{eq}$  is chosen such that the timescales for viscous stirring and aerodynamic gas drag on the planetesimals are in equilibrium. Although this approach assumes that these two mechanisms are in balance, there is nothing preventing planetesimal accretion from getting underway before the disk is sufficiently hot to be limited by gas drag. However, as we showed in the previous section, the initial dynamical state of the planetesimals does not seem to affect the outcome of accretion, so it is safe to assume that the resulting distribution of protoplanets would remain unchanged had we started with a colder disk. The viscous stirring timescale is given by [68] as

$$t_{vs} = \frac{\langle e^2 \rangle}{d \langle e^2 \rangle / dt} \approx \frac{1}{40} \left( \frac{\Omega^2 a^3}{2Gm_{pl}} \right)^2 \frac{4m_{pl} \langle e^2 \rangle^2}{\Sigma a^2 \Omega}, \quad (4.12)$$

where  $\Omega$ ,  $a$  and  $e$  are the orbital frequencies, semi-major axes and eccentricities of the individual planetesimals, respectively. In the Stokes regime, where the mean-free path of the gas is much smaller than the solid particles, the gas can be treated as a

**fluid and** the drag timescale is given by [1] as

$$t_s = \frac{2m_{pl}}{C_D \pi r_{pl}^2 \rho_g v_g}, \quad (4.13)$$

where  $C_D$  is a drag coefficient of order unity,  $\rho_g$  is the local gas volume density and  $v_g$  is the headwind velocity of the gas experienced by the planetesimal. The local gas volume density is given by

$$\rho_g = \frac{\Sigma_g}{\sqrt{2\pi} h_g} \exp\left[-z^2/(2h_g^2)\right], \quad (4.14)$$

where  $\Sigma_g$  is the gas surface density (taken to be 240 times the solid surface density [63],  $h_g = c_s/\Omega$  is the local gas scale height and  $z$  is the height above the disk midplane. The sound speed profile is given by  $c_s = \sqrt{k_B T(r)/(\mu m_H)}$ , where  $k_B$  is Boltzmann's constant,  $T(r) = T_0 (r/1\text{AU})^{-q}$ ,  $\mu = 2.34$  and  $m_h$  is the mass of a hydrogen atom. For a protoplanetary disk around a typical M star,  $T_0 = 148$  K and  $q = 0.58$  [?].

Finally, the headwind velocity of the gas, due to the fact that the gas disk is pressure supported, is given by

$$v_g = v_k \left[ 1 - \sqrt{qc_s^2/v_k^2} \right], \quad (4.15)$$

where  $v_k$  is the local Keplerian velocity (see eq. 4.30 of [?]). As in section 4.4, the argument of perihelion  $\omega$ , longitude of ascending node  $\Omega$ , and mean anomaly  $M$  for the planetesimals are drawn from a uniform distribution  $\in [0, 2\pi]$ .

**One should note that this choice for the gas disk profile almost certainly does not capture the wide range of possibilities in real planet-forming disks.** On one hand, a larger initial gas surface density could act to completely remove solids via radial drift, rendering in-situ accretion of solids impossible. On the other hand, a more tenuous gas disk might render aerodynamic drag forces completely unimportant. In this case, the random velocity of the initial planetesimals should be close to their mutual escape velocity. As we showed in section 4.4, the initial dynamical state of the solids seems to have a very minimal effect on the final

outcome of planetesimal accretion. In a similar vein to [62], we choose to use a MMSN-like profile for the gas disk and instead vary the solid surface density profile to capture the range of mechanisms that might have acted to facilitate planetesimal formation in the first place.

#### 4.5.2 Gas Drag Force

In addition to the mutual gravitational forces, a Stokes drag force due to the the gas disk is applied to each particle, following the prescription described in section 2.2.1 of [123]. For the initial mass planetesimals, the **Stokes number ( $St = t_s\Omega$ ) at the inner and outer disk edge is roughly  $2 \times 10^5$  and  $10^7$ , respectively**. For  $t_s \gg 1$ , bodies are decoupled from the gas and are only weakly affected by it. Because  $t_s \sim m^{1/3}$ , the Stokes number grows as planetesimal accretion proceeds, and the drag force plays an increasingly minor role. Although the aerodynamic gas drag is not expected to significantly alter the final protoplanet distribution, we include its effects here to be self-consistent with the initial conditions, which were constructed by balancing the effects of viscous stirring with gas drag.

#### 4.5.3 Timestepping Criterion

In the case of the fdHi simulation, there are nearly 1 million particles, whose orbital periods vary by two orders of magnitude. Because the interaction timescales near the inner edge of the disk are exceedingly short, a fixed timestep size would required a prohibitively large number of steps to follow planetesimal growth throughout the entire disk. For this reason, we use a multi-tiered timestepping scheme, in which particles are placed onto the nearest power of two timestep based on their most recently calculated gravitational acceleration. **This scheme is used on almost all works using ChaNGa, and is common among large-scale simulation codes.**

This more efficient scheme introduces two issues, however. Firstly, momentum is not completely conserved when bodies switch timestep tiers. The error introduced becomes par-

ticularly severe for a particle on an eccentric orbit, whose perihelion and aphelion distances straddle a timestep boundary. For a large collection of particles, this problem manifests itself as the development of a V-shaped gap in the a-e plane, centered on the boundary itself. To correct this problem, we introduce a slightly modified timestepping criterion, which is based on the expected gravitational acceleration of the particle at pericenter. Only in the case of a close encounter with another planetesimal (in which the acceleration is no longer dominated by the star) is the timestep allowed to reduce based on the original instantaneous criterion.

A second issue is introduced when two particles on different timesteps undergo a collision. As in the previous case, momentum is not completely conserved because the most recent ‘kick’ steps did not happen simultaneously for these bodies. Early in the simulation, we find that this problem tends to trigger runaway growth at the timestep boundaries first. This issue carries itself forward through the embryo formation phase, and protoplanets tend to form at the boundaries. To correct this issue, we ignore collisions between bodies on different timesteps early in the simulation. We find that preventing multi-timestep collisions until after the maximum mass grows by a factor of 10 prevents any artifacts from developing at the timestep boundaries, while also minimizing the number of ‘skipped’ collisions. **In the case of the fdHi simulation, only about 20 collisions out of an eventual 900,000 are ignored. To verify that this timestepping scheme does not affect protoplanet growth, we tested an annulus of growing planetesimals with both fixed steps and our two-phase variable timestepping scheme. The results of these tests are shown in appendix 4.8.**

#### 4.5.4 Results

The timescales for embryo formation depend on the chosen surface density profile, along with the local orbital timescale. Protoplanets form first at the inner edge of the disk, where the dynamical timescales are short. Growth proceeds in an inside-out fashion, with the outermost regions of the disk completing the protoplanet assembly phase last (**as an example, see figure 1 of [89]**). This radial timescale dependence is not typically accounted for in

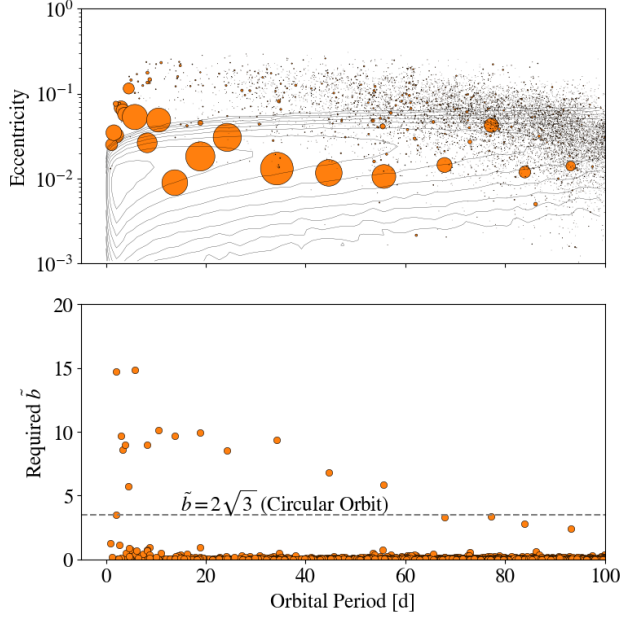


Figure 4.5: The final state of the fdHi simulation. In the top panel, the contours denote the initial period-eccentricity distribution of the planetesimals. Point sizes indicate the relative masses of bodies at the end of the simulation. In the bottom panel, we show the feeding zone width (see equation 5.2) required to produce the final masses of the bodies. The dashed line indicates the feeding zone size expected for bodies on circular orbits. **For the shorter period bodies, the feeding zone size exceeds this expected value, which indicates that oligarchic growth is not operating here. This boundary occurs near roughly 60 d in orbital period.**

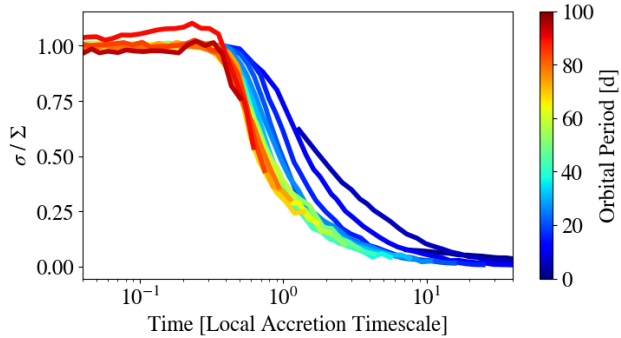


Figure 4.6: The time evolution of the planetesimal surface density (in units of the total solid surface density) in the fdHi simulation. Each curve represents a radial slice of the disk. **The time is measured in units of the local accretion timescale at the center of each radial zone. The colors represent the orbital period at the center of each zone.**

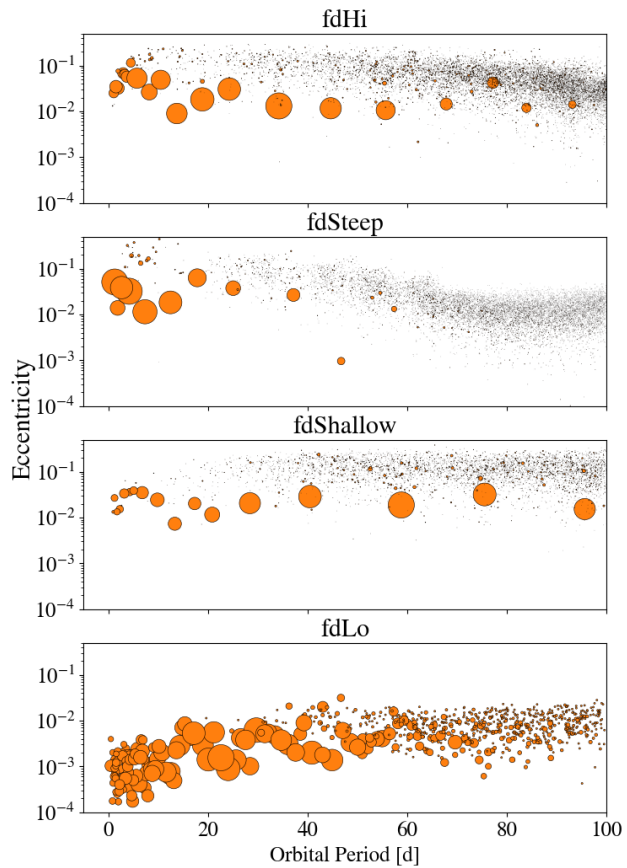


Figure 4.7: The final state of the full disk simulations listed in table 4.1. Point sizes indicate mass relative to the largest body in each simulation.

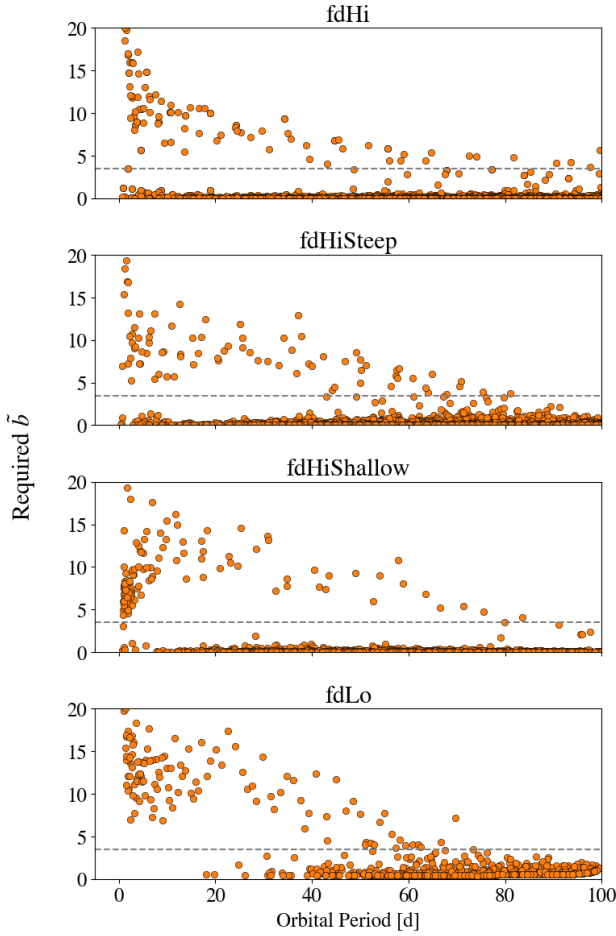


Figure 4.8: Feeding zone width (see equation 5.2) required to produce the final masses for the protoplanets from the simulations listed in table 4.1. **For the fdHi, fdHiSteep and fdHiShallow simulations, we have included the results from five separate iterations of the simulations, each using a different random number seed.** The horizontal dashed line indicates  $\tilde{b} = 2\sqrt{3}$ . Despite the vastly different initial solid surface density profiles, the feeding zone width reaches the circular orbit value around  $\sim 60$  days in all cases.

Table 4.1: Summary of Full Disk Simulations

Simulation Name	$m_{pl}[M_{\oplus}]$	$N_{pl}$	A	$\delta$	$M_{PP}[M_{\oplus}]$	$T_{int}[yr]$	$T_{int,1}[yr]$
fdHi	$8.37 \times 10^{-6}$	903,687	100	1.5	1.00	456	16,377
fdHiSteep	$8.37 \times 10^{-6}$	903,687	100	2.5	1.19	456	16,377
fdHiShallow	$8.37 \times 10^{-6}$	903,687	100	0.5	1.08	456	16,377
fdLo	$8.37 \times 10^{-6}$	45,185	1	1.5	$1.77 \times 10^{-3}$	3,713	133,651

*Note:* A summary of the four ‘full disk’ simulations presented in section 4.5.  $m_{pl}$  and  $N_{pl}$  are the initial masses and number of planetesimals.  $A$  and  $d$  is the initial power law normalization and slope of the solids in the disk.  $M_{PP}$  is the maximum protoplanet mass at the end of the simulation and  $T_{int}$  is the amount of time each simulation was integrated.  $T_{int,1}$  is the integration time scaled by a factor of  $f^2$ , which accounts for the fact that the accretion timescale has been shortened by the inflated collision cross sections.

planet formation simulations **a notable exception being** [?, ?], and appears to be an important component to forming realistic solar system analogs [?]. As with the narrow annulus simulations, we stop the integration once the masses of protoplanets in the outermost region of the disk reach a steady value. In table 4.1, we summarize the outcomes of the four “full disk” cases.

We show the final state of the “fdHi” simulation in figure 4.5. In the top panel, the initial (contours) and final (points) state of the simulation is shown in the orbital period-eccentricity plane. The size of the points indicates the relative mass of the bodies. In the bottom panel, the final masses of the bodies (in units of feeding zone size  $\tilde{b}$ ) are shown as a function of orbital period. **The y-values in the bottom panel of figure 4.5 are calculated by solving equation 5.2 for  $\tilde{b}$ , and inputting the initial surface density and final particle mass into the expression. In other words,  $\tilde{b}$  is describing the size of the annulus that must be cut out of the planetesimal disk in order to produce a protoplanet of the current mass.** By plotting the derived value of  $\tilde{b}$  as a function of orbital period, differences in the dynamical interactions at different locations of the disk are made more clearly visible. **The feeding zone size  $\tilde{b} = 2\sqrt{3}$  permitted by bodies on circular, non-inclined orbits [?] is shown by the horizontal dashed line.** In typical oligarchic growth simulations [88], protoplanets tend to space themselves apart by  $\tilde{b} = 10$ , although it should be noted that they do not consume all of the planetesimals within this distance.

A qualitative shift in the protoplanet and planetesimal distribution is visible **inside of**  $\sim 60$  days. Interior to this location, there are very few remaining planetesimals and the embryos formed have larger feeding zones. Exterior to the boundary, the residual planetesimal population is much more visible, and protoplanets more closely follow the  $\tilde{b} = 2\sqrt{3}$  line. This suggests that the transition between the low  $\alpha$  and high  $\alpha$  accretion modes seen in section 4.4 is happening near this location.

In section 4.4, we postulated that the increased importance of inelastic damping in the inner, non-oligarchic growth region of the disk should lower the overall eccentricity of the

protoplanets there. This behavior is not immediately apparent in the top panel of figure 4.5. **In fact, the opposite appears to be true.** There are, however, a couple of factors in the wide disk simulations that could make this extra dynamical cooling mechanism difficult to see. Firstly, the initial eccentricity distributions of the inner and outer disk are different because of the dependence of the viscous stirring and gas drag timescales on orbital period. **The mean eccentricity at the outer disk edge is 4x larger than at the inner disk edge.** Additionally, the protoplanet formation timescales for the inner and outer disk are vastly different, making a comparison between these regions at the same moment in time somewhat inappropriate. **A quick back of the envelope calculation yields  $\langle e^2 \rangle^{1/2} = 0.05$  for a population of  $\sim 1M_{\oplus}$  bodies with a random velocity dispersion equal to their mutual escape velocity.** It is therefore likely the case that the innermost protoplanets have had ample time to self-stir.

To ensure that the boundary seen **around** 60 days in orbital period is not simply a transient product of the inside-out growth throughout the disk, we examine the time evolution of  $\sigma/\Sigma$ , which compares the planetesimal and total solid surface density at multiple orbital periods. In figure 4.6, the value of  $\sigma/\Sigma$  is plotted as a function of time in 10 orbital period bins, each with a width of 10 days. **To determine whether the evolution of the planetesimal surface density behaves self-similarly across the disk, we normalize the time values in each bin by the local accretion timescale at the beginning of the simulation, which is given by**

$$t_{acc} = (n\Gamma v)^{-1} = \left( \frac{\Sigma_0 \Omega}{2m_{pl}} \Gamma \right)^{-1}, \quad (4.16)$$

where we have assumed the local number density of particles  $n$  is set by the surface density and the local scale height of the disk (see section 4.2). The effective collision cross section is set by gravitational focusing and is given by equation 4.5.

The color of the curves indicate the orbital period bin which is being measured. From about 40 to 100 days in orbital period, the planetesimal surface

density follows a similar trajectory as accretion proceeds. Interior to about 40 days,  $\sigma$  actually decays more slowly. In other words, growth is actually fueled less vigorously by planetesimals in this region. This highlights the fact that accretion proceeds in a qualitatively different way in the inner disk. For the outer disk, gravitational focusing tends to facilitate collisions between protoplanets and preferentially smaller bodies. At short period, however, all close encounters result in a collision, regardless of mass. In a rather counterintuitive fashion, planetesimals in the inner disk actually persist for longer. In section 4.5.5, we examine the assembly history of the embryos and show that there is much less of a preference for planetesimal-embryo collisions at short period as well.

In the inner disk, this value asymptotes to zero as the planetesimal population entirely depletes. In the outer disk, dynamical friction between the embryos and planetesimals eventually throttles subsequent accretion and leaves  $\sim 10$  percent or more of the mass surface density as planetesimals. **It should be noted that in a typical oligarchic growth scenario, where protoplanets space themselves apart by  $10 r_h$  and settle onto circular orbits (giving  $\tilde{b} = 2\sqrt{3}$ ), roughly 30 percent ( $2\sqrt{3}/10 \simeq 0.3$ ) of the planetesimals should remain out of reach of the protoplanets.**

Next, we investigate how the resulting planetesimal and protoplanet distribution changes as we vary the initial solid surface density profile. The final orbital period-eccentricity state of the particles in the fdHi, fdHiSteep, fdHiShallow and fdLo simulations are shown in figure 4.7, with point sizes indicating the relative masses of the bodies. In all cases, the inner disk is largely depleted of planetesimals, while the outer disk contains a bimodal population of planetesimals and embryos, with a clear separation in eccentricity between the two. Despite having significantly different masses, the **semimajor axis-eccentricity** distributions of the planetary embryos formed in all simulations **are** remarkably similar. This is likely due to the fact that inelastic collisions play a more significant role where the solid surface density is highest, which offsets the fact that the initial bodies started off in a dynamically hotter state (due to the increased effectiveness of viscous stirring). The only exception to this is the

fdLo simulation, where the resulting eccentricities are a couple orders of magnitude smaller. Inelastic damping likely plays an even more significant role here, due to the much larger masses of the initial planetesimals.

In figure 4.8, we plot the masses of the resulting protoplanets and planetesimals in all four simulations in units of  $\tilde{b}$  (see equation 5.2). **To make the trend between  $\tilde{b}$  and orbital period more clear, we ran four more versions of the fdHi, fdHiSteep and fdHiShallow simulations using different random number seeds and included these in the figure as well.** As mentioned previously,  $\tilde{b} = 2\sqrt{3}$  (indicated by the horizontal dashed line) is the feeding zone width that a body on a circular orbit will have. In all four simulations, the feeding zone width exceeds the minimum value in the inner disk and approaches  $2\sqrt{3}$  around  $\sim 40$  to  $60$  days. The orbital periods at which this transition occurs are quite similar between simulations, despite the vastly different solid surface density profiles used. This indicates that the boundary between accretion modes is driven entirely by the local value of  $\alpha$ , and also supports our conclusion that planetesimal accretion is largely complete everywhere in the disk.

#### 4.5.5 Assembly History of Embryos

Further insight regarding the difference between the short vs long period accretion modes can be gained by looking at the growth history of the planetary embryos. Because all collisions are directly resolved by the N-body code, a lineage can be traced between each planetary embryo and the initial planetesimals. **For the fdHi, fdHiSteep and fdHiShallow simulations, protoplanets gain a factor of  $\sim 10^6$  in mass relative to the initial planetesimals. For the fdLo simulation, this growth factor is nearly a thousand times smaller, which produces rather shallow and noisy collision histories. For this reason, we choose to exclude the fdLo simulation from our analysis in this section.**

We begin by investigating the “smoothness” of the accretion events that give rise to each embryo. Drawing from a common technique used for cosmological simulations of galaxy formation, we divide growth events for a given body into “major” and “minor” mergers

[?, ?, ?]. Here, we define minor events as any collision involving an initial mass planetesimal, while major events consist of a merger between any two larger bodies. In figure 4.9, we retrieve the collision events for all bodies in all five iterations of the fdHi, fdHiSteep and fdHiShallow simulations and plot the total mass fraction attained through minor merger (smooth accretion) events as a function of the final mass of the body. Here, we define a minor merger to be any collision involving a planetesimal with  $m < 100m_0$ . The color of the points indicates the final orbital period of the body. Beyond  $\sim 20$  to 30 days in orbital period, minor mergers make up a significant fraction of the final mass of a body. Interior to this, the smooth accretion fraction drops significantly and the mass contribution to minor mergers can vary by over an order of magnitude.

The variation in smooth accretion fraction with mass for the short period bodies suggests that the planetesimal and embryo populations interact differently than those in the outer disk. Exterior to the accretion mode boundary, the growing embryos continue to accrete planetesimals while avoiding each other as they near their final mass. Inside the boundary, however, any and all bodies collide with each other, and the occasional embryo-embryo collision tends to dominate growth and drive down the smooth accretion fraction. Gravitational scattering between embryos and planetesimals is a key ingredient for orbital repulsion [88], and so a lack of gravitational scattering in the inner disk should prevent the embryos from settling onto neatly-spaced, isolated orbits. As we showed in figure 4.8, the embryos in the inner disk appear to reach well beyond the typical feeding zone size predicted by an oligarchic growth model. Figure 4.9 suggests that the extra mass here obtain comes from mergers with the other nearby embryos.

Another line of evidence pointing to a lack of gravitational scattering and orbital repulsion in the inner disk can be seen in figure 4.10. Here, we measure the initial orbital period distribution of bodies used to construct each embryo and calculate its mean  $\langle P_{acc} \rangle$ . Point sizes indicate the relative final masses of bodies. As in the previous figure, we have included data from all five versions of the fdHi, fdHiSteep and

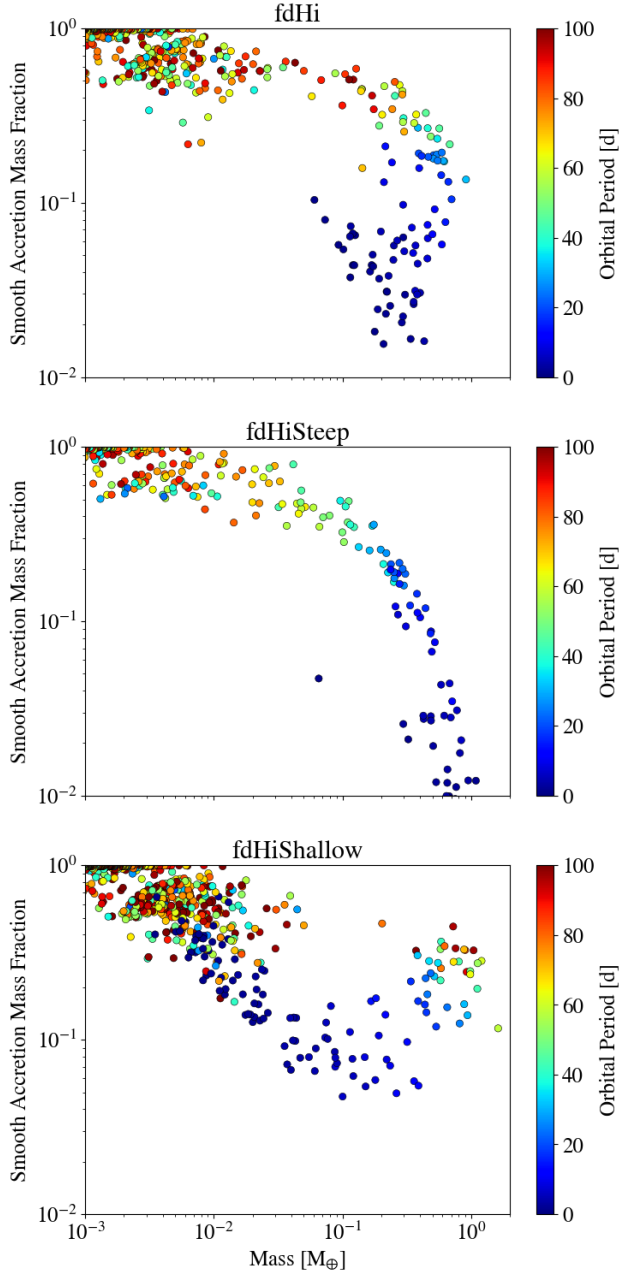


Figure 4.9: For all bodies with  $m > 100m_0$  at the end of the high surface density simulations, the fraction of their total mass attained through mergers with initial mass planetesimals (smooth accretion) as a function of total mass. Colors indicate the orbital periods of the bodies in the final simulation snapshot. Bodies interior to  $\sim 20$  to 30 days attain up to an order of magnitude less of their mass through minor merger events, while accretion of planetesimals plays a much more significant role at longer orbital periods.

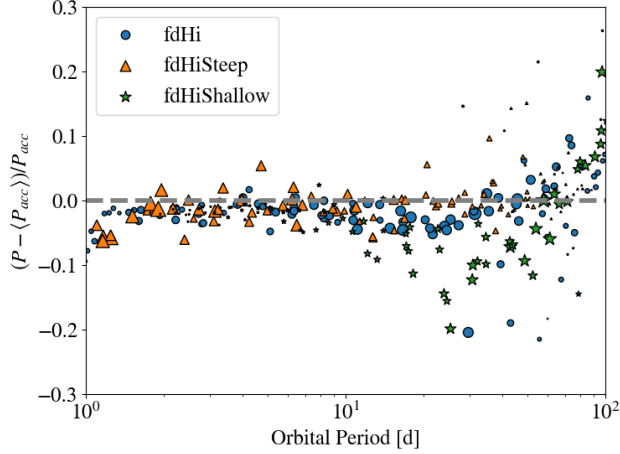


Figure 4.10: The relative separation between the final period of a body and the mean orbital periods of its accretion zone at the end of the fdHi, fdHiSteep and fdHiShallow simulations. The marker type and color denotes the simulation used, while the marker sizes indicate the relative masses of bodies. In each case, all five iterations of the simulations are plotted simultaneously.

fdHiShallow simulations. For each body, this quantity is then compared with its final orbital period. In this figure, bodies that closely follow the gray dashed line still reside close to their initial feeding zones. On the other hand, bodies further from the dashed line must have experienced a strong gravitational scattering event during or after their accretion has completed. For all of the high surface density simulations, the accretion zones and present positions of the embryos appear to diverge beyond  $\sim 20$  days in orbital period.

Coupled with the strong decrease in smooth accretion fraction for bodies in this region (seen in figure 4.9), it appears as if the relative importance of collisions and gravitational scattering seems to shift around  $\sim 20$  days. For the shortest period bodies, growth events are sudden and stochastic, often involving collisions between bodies of comparable mass. For longer period bodies, a significant amount of growth is driven by accretion of smaller planetesimals. We postulate that this qualitative difference is driven by the role that embryo-embryo close

encounters play in the inner and outer disk. In the inner disk, these encounters tend to result in a merger, which drives down the smooth accretion fraction. In the outer disk, these encounters tend to result in a scattering event which moves bodies away from their initial feeding zones. We find that the accretion zone shapes for the longer period bodies are also much more smooth and unimodal, which suggests that scattering tends to occur after accretion has largely completed.

## 4.6 Simplifying Assumptions

### 4.6.1 Collision Cross Section

In all cases shown so far, the boundary between the oligarchic growth and the highly-efficient short period accretion region lies **between 40 and 70** days in orbital period. As discussed in section 4.2.2, the mode of accretion is set entirely by the local value of  $\alpha$ , which scales with both distance from the star and the bulk density of the planetesimals (see equation 4.9). Because we chose to artificially inflate the collision cross section of the particles in our simulations **by a factor of  $f$** , the bulk densities of the particles are reduced, and the accretion boundary is shifted outward. However, the scaling relation between  $\alpha$  and  $\rho$  ( $\alpha \sim \rho_{pl}^{-1/3}$ ) can be used to predict where this accretion boundary should lie in a disk with realistic-sized planetesimals. The simulations presented in this paper use a collision cross section enhancement factor of 6, which moves the boundary outward in orbital period by a factor of approximately 15 (**For a fixed value of  $\alpha$ , equation 4.9 gives  $a \sim r_{pl} \sim f$  and therefore  $P_{orbit} \sim f^{-3/2}$** ). One would therefore expect the accretion boundary to lie **between 3 and 5** days in orbital period for  $3 \text{ g cm}^{-3}$  bodies.

Although a simulation with  $f = 1$  is not computationally tractable, we can test whether the accretion boundary moves in the way we expect by modestly changing the value of  $f$ . In figure 4.11, we compare the fdHi simulation to a nearly identical run using  $f = 4$ . In the top panel, we show the feeding zone width required for each particle to attain its present

mass. As in figure 4.8, we indicate the feeding zone size expected for oligarchic growth with a horizontal dashed line. In the bottom panel, the value of  $\alpha$  as a function of orbital period is shown for  $3 \text{ g cm}^{-3}$  bodies with an artificial radius enhancement of  $f = 1, 4$  and  $6$ . The horizontal dashed line indicates the empirical value of alpha below which the accretion mode switches to oligarchic. Comparing the top and bottom panels, the intersection of the feeding zone width seen in our simulations and the feeding zone width predicted by oligarchic growth matches well with the orbital period at which  $\alpha \sim 0.1$  for both values of  $f$ . Also shown by the shaded region are the expected  $\alpha$  values for realistic-sized bodies with  $\rho_{pl}$  between  $1$  and  $10 \text{ g cm}^{-3}$ . Although the removal of the cross section enhancement greatly reduces the size of the non-oligarchic region, it still should be expected to cover a portion of the disk where planetesimals might be expected to form [124] for a wide range of  $\rho_{pl}$ .

#### 4.6.2 Collision Model

For the simulations presented in this work, every collision results in a perfect merger between pairs of bodies, with no loss of mass or energy. Although simpler and less computationally expensive to model, allowing every collision to produce a perfect merger might result in overly efficient growth, particularly in the innermost region of the disk where the encounter velocities are largest. **Given that we have just shown that a distinctly non-oligarchic growth mode emerges in the inner disk when the collision timescale is short relative to the gravitational scattering timescale, one might be concerned that a more realistic collision model would act to lengthen the growth timescale enough for this condition to no longer be true. In the outer regions of the disk where oligarchic growth still operates, more realistic collision models have been shown to simply lengthen the timescale for planetary embryos to form [174, 98].** A proper way to handle this would be to allow for a range of collision outcomes, based on a semianalytic model (see [?]). However, resolving collisional debris, or even prolonging growth by forcing high-velocity pairs of bodies to bounce is too expensive to model, even with CHANGA.

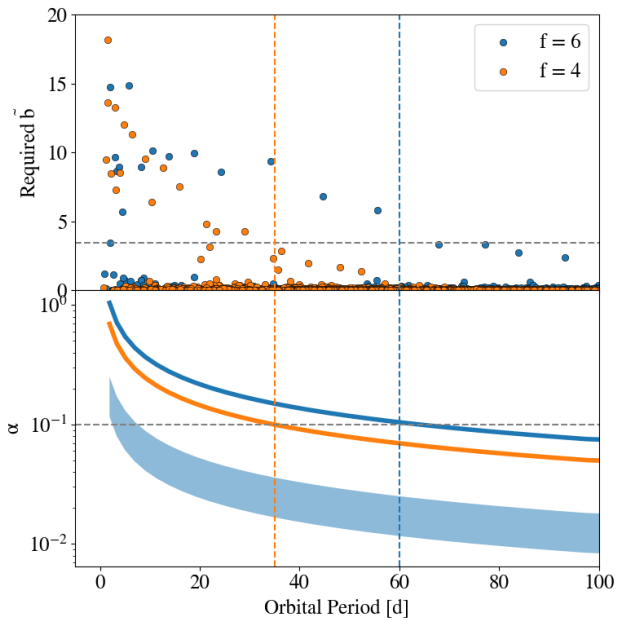


Figure 4.11: In the top panel, we show the required feeding zone sizes to produce the masses of the bodies seen at the end of the fdHi and fdHif4 simulations. The bottom panel shows the variation of  $\alpha$  with orbital period for the bodies used in each case (solid curves). The orbital period at which  $\alpha \simeq 0.1$  matches well with the location at which  $\tilde{b}$  exceeds  $2\sqrt{3}$  **This is highlighted by the vertical dashed lines..** The shaded region in the bottom panel show the values of alpha for realistic-sized ( $f = 1$ ) planetesimals with bulk densities between 10 and 1 g cm<sup>-3</sup>.

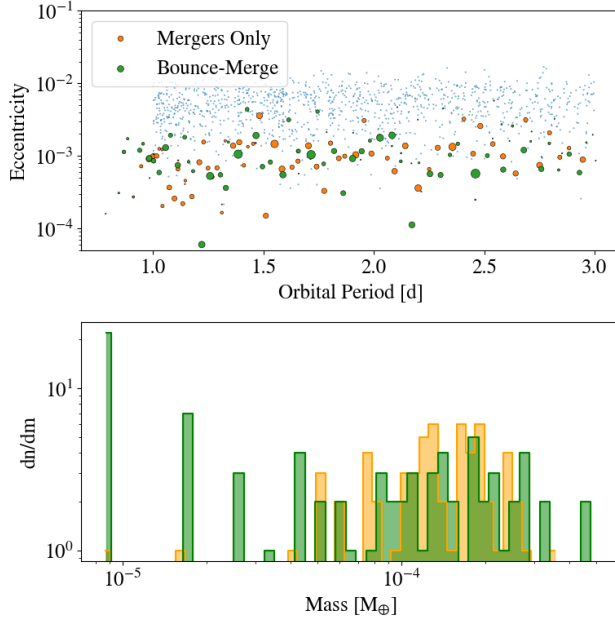


Figure 4.12: A comparison between the innermost region of the fdLo (orange) simulation, and a second version using a bounce- merge collision model (green). In the top panel, the period-eccentricity state of the particles is shown, with marker sizes indicating relative mass. The blue points represent the initial state of the simulations. The bottom panel compares the final **differential** mass distributions of the bodies.

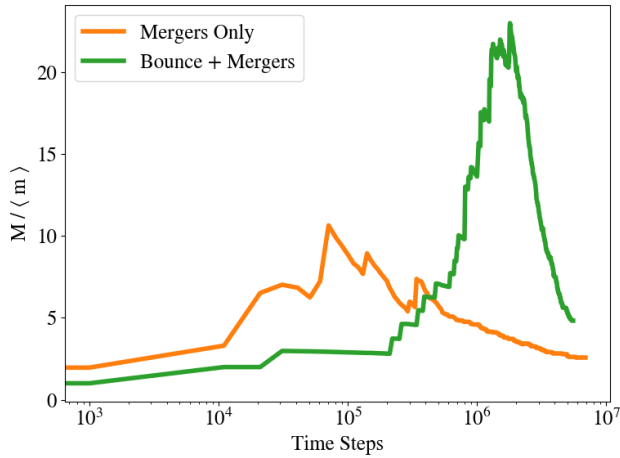


Figure 4.13: The evolution of the ratio between the maximum and mean mass of the simulations shown in figure 4.12. In both cases, the system first evolves through a phase of runaway growth, before the massive bodies consume the smaller bodies, driving down the mean mass. With the bounce-merge model, the mass ratio takes much longer to begin decreasing.

To test whether a more restrictive collision model should alter the growth mode of the inner disk, we ran a smaller scale test using a more restrictive collision model. In this case, a collision can result in one of two outcomes: if the impact velocity is smaller than the mutual escape velocity of the colliding particles, defined as

$$v_{mut,esc} = \sqrt{\frac{2G(m_1 + m_2)}{r_1 + r_2}}, \quad (4.17)$$

where  $m_1, m_2$  and  $r_1, r_2$  are the masses and radii of colliding particles 1 and 2, then the bodies merge. For impact velocities larger than  $v_{mut,esc}$ , no mass is transferred, and the bodies undergo a completely elastic bounce. Because the accretion outcome is all or nothing, this model should restrict growth more than a partial accretion model [?]. Below, we will show that the bounce-merge model does not meaningfully affect the outcome of the inner disk's planetesimal accretion phase, and so a more realistic partial accretion model should do the same.

To compare the outcome of the two collision models, we have chosen to use the initial conditions from the fdLo simulation, but have truncated the disk beyond 3 days in orbital period. This offsets the increased computational cost of the more restrictive collision model, while still allowing the disk to evolve in the region where mergers would be most difficult to achieve. For the initial conditions we have chosen, the typical encounter velocity (defined by  $v_{enc} = \langle e^2 \rangle^{1/2} v_k$ , where  $v_k$  is the local Keplerian velocity) is about 25 percent larger than  $v_{mut,esc}$ . Because the encounter velocities follow a Gaussian distribution, there should still be a small subset of collisions that still meet the merger criteria to occur early on. In addition,  $v_{mut,esc}$  becomes larger as the bodies grow and the merger criteria should become easier to meet as the system evolves. For these reasons, one would expect the inhibition of growth due to the more restrictive collision model to be temporary.

In figure 4.12, we compare the outcomes of the simulations, one with mergers only (shown in orange) and one with the bounce-merge model (shown in green). The blue points in the top panel show the initial conditions used for both cases. Although the bounce-merge simulation takes much longer to reach the same phase of evolution, the resulting orbital properties are

indistinguishable from the merger-only case. **Performing a Kolmogrov-Smirnov test on the two mass distributions yields a p-value of  $2 \times 10^{-5}$** , which tells us that the two mass distributions are quite firmly statistically different. If we remove the initial mass planetesimals, a KS test yields a p-value of 0.1. We conclude that the embryo populations are nearly indistinguishable, while the bounce-merge model produces a small amount of residual planetesimals.

To investigate the differences in growth between the two collision models early on, we show the time evolution of the ratio between the maximum and mean mass in figure 4.13. In both cases, this ratio first increases, which indicates that runaway growth still operates, regardless of the collision model used. In the bounce-merge case, the mass ratio peaks at a higher value, while also undergoing a longer runaway growth phase. This suggests that the mass distribution becomes much less unimodal during this growth process, but as figure 4.12 shows, this does not affect the resulting embryos or allow for a residual planetesimal population.

As a final note, [?] found that a more realistic collision model also enhanced radial mixing in their simulations. Upon calculating the planetesimal accretion zones using the same method as was done to produce figure 4.10, we find that the embryos in the bounce-merge simulation annulus do have modestly wider accretion zones than those produced in the merger-only simulation.

#### **4.7 Summary and Discussion**

In this work, we have demonstrated that planetary embryo growth can simultaneously operate in two distinct modes in a planet-forming disk. In the first mode, gravitational feedback from the growing embryos heats the remaining planetesimals and results in a dynamically cold population of embryos with a modest amount of residual planetesimals. This corresponds to the “oligarchic growth” case revealed by [88], which is often used as a starting point for late-stage accretion models (e.g. [89, 147, 144]). In the second mode, the gravitational feedback does not play a significant role, embryos quickly sweep up all planetesimals, and grow

larger and less uniformly spaced than those produced by oligarchic growth.

We have demonstrated the outcome of both accretion modes through a simple parameter study using a narrow annulus of planetesimals (**section 4.4**). The initial planetesimal distribution can be described in terms of two dimensionless constants,  $\alpha$  and  $\beta$ , which describe the ratio between the physical radius of the planetesimals and the Hill ( $r_h$ ) and gravitational ( $r_g$ ) radius, respectively. For a fixed planetesimal composition,  $\alpha$  scales with the orbital period and  $\beta$  scales with the level of dynamical excitation of the disk. We showed that  $\alpha \ll 1$  leads to oligarchic growth, while **an  $\alpha$  close to unity** produces this newly revealed non-oligarchic growth mode (**see figure 4.2**). Within this non-oligarchic mode, we find that the resulting masses and eccentricities of the embryos come out **very similar**, regardless of the initial value of  $\beta$ .

So long as the density of the bodies do not significantly change as their mass distribution evolves, this ratio is set entirely by the distance from the star. Because both the physical and Hill radii of the bodies grows as  $M^{1/3}$ , the growth mode boundary remains stationary in the disk during the planetesimal accretion process.

We have verified that the growth boundary location **does not strongly depend** of the solid surface density distribution by testing the outcome of the planetesimal accretion process for a variety of solid profiles. Although altering the surface density does affect the resulting masses of the embryos, the location of the boundary separating the growth modes is remarkably similar among all of our simulations. In addition, the sizes of the feeding zones, along with qualitative differences in the accretion history of embryos on both sides of the boundary (**see figures 4.9 and 4.10**) provide further evidence to suggest that oligarchic growth is not operating in the inner disk.

**Finally, we have examined how our assumption of perfect accretion, along with the collision cross section enhancement used, might alter our results. We verified that these modifications, meant to make the simulations less computationally expensive, would still allow for the emergence of this non-oligarchic growth mode.** We showed that a much more restrictive collision model, in which only low-velocity collisions

produce a merger, still allows for this growth mode to occur at the innermost part of the disk, where encounter speeds are most vigorous. In a real planet-forming disk, partial accretion events should allow growth to happen more quickly than what was seen in this test case (**see figure 8 of [99]**), so this growth mode should certainly still occur. We also showed that the collision cross section enhancement moves the accretion boundary outward. We verified this by deriving a scaling relation between the boundary location and the bulk density of the planetesimals, and showing that the boundary moves to the predicted location when running a simulation with a slightly smaller inflation factor. For rocky planetesimals with a realistic bulk density, **3 g cm<sup>-3</sup>**, our results suggest that this boundary should lie around 5 days in orbital period.

#### 4.7.1 *Connections to Satellitesimal Accretion*

To date, there have been no other studies of planetesimal accretion with such a large value of  $\alpha$ . **Typically, it is assumed that  $\alpha \ll 1$  (e.g. [?]), which is certainly true for material at and beyond the Earth's orbit.** However, a value of  $\alpha = 1$  corresponds to the Roche limit of a three-body system, and so one might wonder this high- $\alpha$  accretion mode might be relevant for a circumplanetary accretion. There is a collection of previous works which use N-body methods to examine in-situ satellitesimal accretion [?, 150, ?, ?], although some of these simulations involve a complex interaction between spiral density waves formed inside of the Roche limit and the material exterior to it, **making the dynamics driving accretion distinctly non-local, in contrast to what we have presented in this work.** [?] was able to form 1-2 large moons just exterior to the Roche limit, depending on the extent of the disk with very little satellitesimal material left over. The widest disk they modeled extended out to  $\alpha = 0.5$ . Qualitatively, this result is very similar to the short period planetesimal accretion mode observed in our simulations. [?] modeled a much wider satellitesimal disk, which extends out to about  $\alpha \approx 0.05$ . Inside to the  $\alpha = 0.1$  accretion boundary (which lies near 15 **planetary radii** in figure 1 of [?]), bodies grow beyond the isolation mass, while the opposite is true on the other side of the boundary. In addition,

a residual population of satellitesimals is still present beyond the boundary, which suggests that oligarchic growth is indeed operating only on the far side.

Presently, the implications that this non-oligarchic accretion mode has for the formation of short-period terrestrial planets, and whether the accretion boundary would leave any lasting imprint on the final orbital architecture, is unclear. The extreme efficiency of planetesimal accretion at the inner edge of the disk suggests that no residual populations of small bodies should be expected to exist here. A crucial point that our results do highlight is that the initial conditions used for most late-stage planet formation simulations are overly simplistic. [?] recently simulated planetesimal accretion in a disk extending from the orbit of Mercury to the asteroid belt and found that the disk never reaches a state in which equally-spaced, isolation mass embryos are present everywhere simultaneously. Instead, different annuli reach a ‘giant impact’ phase at different times, preventing the onset of a global instability throughout the entire disk, as is common in classic terrestrial planet formation models [22, 143].

To connect these accretion modes to the final orbital architecture, and to ultimately determine what implications an in-situ formation model has for the growth of STIPs, we will evolve the final simulation snapshots presented here with a hybrid-symplectic integrator for Myr timescales. The final distribution of planets formed, along with composition predictions generated by applying cosmochemical models to our initial planetesimal distributions and propagating compositions through the collision trees, will be examined in a follow-up paper.

#### **4.8 Appendix A: Robustness of Timestepping Scheme**

As described in section 4.3, CHANGA evolves the motions of the particles in the planetesimal disk using a multi-tiered timestepping scheme. Due to the extremely short dynamical timescale at the inner edge of the disk, the outer disk would require a prohibitive number of timesteps to reach the protoplanet phase using a fixed timestep scheme. To circumvent this, particles are evolved in discrete power-of-two timestep groups. In the event that a collision occurs

between two particles on different timesteps, a slight error is introduced to the energy and angular momentum of the merged particle. Due to the nonlinear nature of the runaway growth phase, this slight error tends to trigger more subsequent collisions at the timestep boundary in the disk, and causes protoplanets to preferentially form at the boundaries.

To circumvent this issue, we prohibit particles on different timesteps from merging until the runaway growth phase is well underway. For the fdHi simulation, multi-tiered mergers are not allowed during the first thousand steps. To verify that this technique does not alter the resulting protoplanet distribution in any meaningful way, we ran two test simulations of the inner part (1 to 4 days in orbital period) of the disk from the fdHi simulation. In the first case, the aforementioned timestepping scheme is used. In the second case, all particles are evolved on the timestep appropriate for the inner edge of the disk.

In figure 4.14, we compare the final period-eccentricity state and final mass distributions to each other. There do not appear to be any differences between the two protoplanet distributions, particularly near the timestep boundary at 2 days. In addition, the masses of both the protoplanets and the remaining growing planetesimals are indistinguishable. In this case, a KS test of the two mass distributions yields a p-value of  $\sim 0.34$ . We therefore safely conclude that the timestepping scheme used in this work does not alter the growth of the protoplanets in any meaningful way.

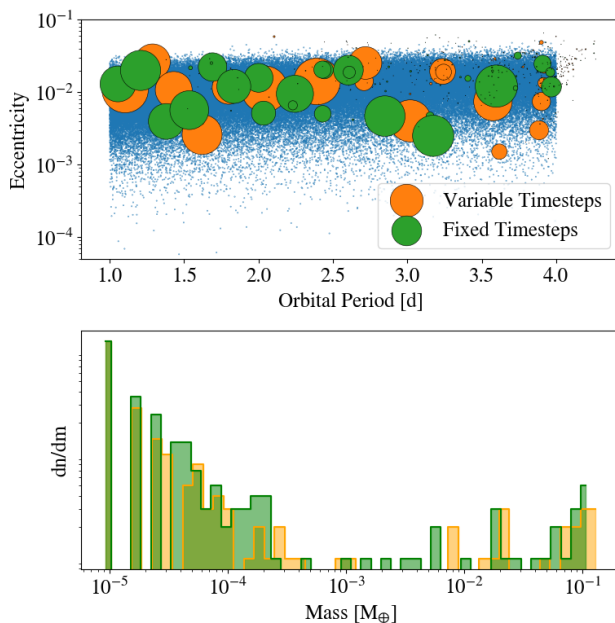


Figure 4.14: A comparison between the innermost region of the fdHi (orange) simulation, and a second version using a fixed timestep appropriate for the inner edge of the disk (green). In the top panel, the period-eccentricity state of the particles is shown, with marker sizes indicating relative mass. The blue points represent the initial state of the simulations. The bottom panel compares the final mass distributions of the bodies.

## Chapter 5

# IN-SITU FORMATION OF STIPS

### 5.1 *Introduction*

One of the most surprising and intriguing results from NASA’s *Kepler* mission was the prevalence of sub-Neptune-sized exoplanets with orbital periods shorter than that of Mercury [18]. These planets are often found in closely-spaced groups, known as systems of tightly-packed inner planets (STIPs) [94, 106, 104]. STIPs are found to often be coplanar [47, 160], have low eccentricities [162, 61] and are usually not in mean-motion resonance with each other [46, 155]. In addition these systems have been shown to exhibit a compelling amount of uniformity between adjacent planets, in terms of mass, radius and orbital spacing [116, 117].

All of these characteristics provide a rich set of constraints for planet formation models. One of the most intriguing questions that arises is why the structure of the present-day solar system appears so different than that of STIPs. Extending the minimum-mass solar nebular (MMSN) model [63] down to  $\sim 0.05$  AU, where the inner edge of many protoplanetary disks are thought to be [114] (and where planetesimals are thought to form [124]) yields several extra Earth masses of material. Explaining why this material is missing from the solar system, but not some exoplanetary systems, is a key question that a complete theory of planet formation must be able to provide.

There are two categories of formation theories meant to explain the ubiquity of these compact, short-period systems. The first involves the gradual assembly of these worlds as they migrate inwards. For Mars-sized bodies and larger, torques at the Lindblad resonances drive the exchange of angular momentum between the gaseous disk and the planet [165]. A key prediction of migration models is that multiplanet systems should end up in resonant chains [32]. Although this is not unheard of (see Kepler 223 [118] and Trappist-1 [50, 51, 3]),

the majority of these systems are found to not be in resonant chains [106, 46]. One potential explanation for this discrepancy involves a later phase of destabilization after convergent migration has completed and the gaseous disk subsequently dissipates [75, 74]. However, the detailed behavior of tidal torque-driven migration is still very uncertain and it is not entirely clear when and how convergent migration should operate. The strength and even direction of tidal migration depends sensitively on the thermodynamic structure of the gas disk [9, 16]. Furthermore, resonant locking often requires a specific amount of dissipation for a given planet mass [15].

Alternatively, these planets may have formed *in situ*, having been constructed only from the local mass budget of the disk. This appears to be the case for the gaseous envelopes of hot Jupiters formed near the inner edge of the disk [10], although it is not clear whether the cores of these worlds require a migration model. Currently, there are no measurements constraining the mass budget of the innermost regions of planet-forming disks, so the initial conditions for *in situ* models tend to rely on wild speculation. By enhancing the solid surface density by a factor of  $\sim 100$  relative to the inner solar system, [62] was able to form compact multiplanet super-Earth systems without invoking any kind of planet migration. *In situ* formation may be particularly prevalent around low mass stars, as magnetically-driven disk winds tend to flatten out the radial gas density profile, which balances out the inner and outer torques from tidally-driven migration [132]. One should note that no *in situ* models have yet to produce resonant chains of planets, so it seems likely that gas disk migration likely plays a role at least for the subset of planetary systems found in this type of configuration.

Compared to planet formation models that involve gas disk-driven migration, an *in situ* model is relatively straightforward (although expensive) to model, involving only mutual gravitational interactions and the occasional collision. In (Wallace + Quinn 2023, cite once published), we used a tree-based N-body code to follow the accumulation of near realistic-sized planetesimals into protoplanets at short orbital period. We showed that oligarchic growth [88], which gives rise to a bimodal population of protoplanets and residual planetesimals, does not operate at arbitrarily short orbital periods. In addition, the boundary

between oligarchic and non-oligarchic growth should be expected to lie somewhere in the middle of a typical STIP.

In this work, we use a hybrid symplectic N-body code to grow the protoplanet systems from (Wallace + Quinn 2023, cite once published) to completion. These comprise the first ever end-to-end N-body simulations that directly follow the growth of the smallest gravitational aggregates to full-sized terrestrial planets. In section 5.2, we describe the simulation code we use, along with how previous protoplanet simulations are used to construct the initial conditions for the final assembly phase. In section 5.3, we examine the final orbital architectures of the simulated STIPs, and investigate whether the accretion mode boundary persists in any measurable way. In section 5.4, we compare our results with a set of simulations run starting with a more ‘typical’ distribution of fully-formed, evenly spaced protoplanets and show that a more self-consistent treatment tends to result in a subset of systems undergoing a potentially destructive phase in the inner disk. Due to the stochasticity of our results, we use the simulation snapshots from (Wallace + Quinn 2023, cite when published) to train a neural network to produce an infinite set of qualitatively similar, but numerically distinct initial conditions and then compare these with the full simulation runs in section 5.5. We also use this much larger set of simulated planets to make a statistical comparison with compact multiplanet systems observed by Kepler. Finally, we conclude in section 5.6 and discuss whether the absence of any short-period planets in the solar system might point toward a largely *in situ* formation history.

## 5.2 *Simulations*

### 5.2.1 *Numerical Methods*

A direct N-body model of the full collisional evolution of a system of terrestrial planets, starting from planetesimals, covers over 6 orders of magnitude in mass growth. Although main physics drivers are gravity and solid body collisions, the wide range of timescales that must be resolved during the accretion process necessitate the use of a multi-phase

integration scheme. Early on, interactions between planetesimals are frequent and encounter timescales can be as short as  $\sim$  hours (check this). As planetary embryos form, the timescale for gravitational instability can lengthen to  $10^5$  years [25], while the final planet assembly process can take Myrs. For traditional N-body codes that use a leapfrog integrator, Myr integrations of a planetary system require  $\sim 10^{10}$  timesteps, which is prohibitively long for even the most modest resolutions. To circumvent this problem, a hybrid mixed variable symplectic (MVS) scheme [21] can be used, which greatly reduces the number of timesteps required so long as close encounters are extremely infrequent.

However, close encounters are certainly frequent during the planetesimal accretion process, and so a hybrid MVS scheme is not appropriate here. To properly resolve the planetesimal accretion process, while still being able to integrate the planet formation process to completion, we split our simulations into two separate phases. In the first phase, we track planetesimal growth using the highly parallel N-body code CHANGA. Gravitational forces are calculated using a modified Barnes-Hut [12] tree with hexadecapole expansions of the moment. For all of our simulations, we use a node opening criterion of  $\Theta_{BH} = 0.7$ . The equations of motion are integrated using a kick-drift-kick leapfrog scheme and collisions are treated as solid spherical bodies which produce a complete and instantaneous merger. A more complete description of CHANGA can be found in [79, 113] and a description of the collision detection and resolution module, which is largely based off of the implementation in PKDGRAV [149, 150], can be found in [164].

As the particle count diminishes and the encounter timescales lengthen, the final simulation snapshots from CHANGA are passed to the hybrid MVS code GENGA [57, 58]. Like MERCURY [21], GENGA splits the Hamiltonian into a Keplerian and perturbing part and solves these independently using a mixed variable symplectic scheme. For close encounters, the perturbing part of the Hamiltonian becomes large and a Bulirsch-Stoer integrator takes over to update the equations of motion for these particles. To permit larger close encounter groups, a hierarchical method with multiple changeover functions is used, which acts to break the close encounters into multiple subgroups which can be integrated independently. All of

this work is done on GPU hardware, and can be done with up to 60,000 particles while running up to 30x faster than MERCURY. For all of the GENGA simulations presented in this work, we use a maximum subgroup size of 512 particles and allow for 2 substeps on each level of the changeover function.

### 5.2.2 Initial Conditions

Each simulation begins with an equal-mass disk of planetesimals with  $m_{pl} = 5 \times 10^{22}$  g and  $\rho_{pl} = 3$  g cm<sup>-3</sup> orbiting a 0.08  $M_\odot$  star. Semimajor axes of the bodies are randomly drawn between 1 and 100 days in orbital period such that the mass surface density profile follows

$$\Sigma(r) = 10 \text{ g cm}^{-2} \times A \left( \frac{M_*}{M_\odot} \right) \left( \frac{r}{1 \text{ AU}} \right)^{-\delta} \quad (5.1)$$

where  $M_*$  is the mass of the central star, 10 g cm<sup>-2</sup> is the surface density of the minimum-mass solar nebula [63, MMSN] at 1 AU,  $A$  is an enhancement factor and  $\delta$  is the power law index. Following [62] we use  $A = 100$ . To test the influence that the surface density profile has on the final planet configuration, we use  $\delta = 0.5, 1.5$  and  $2.5$ .

Due to the stochasticity of the final assembly phase, we generate 5 distinct initial conditions with each configuration, each using a different random number seed. In all cases, the eccentricities and inclinations are drawn from a Rayleigh distribution with  $\langle e^2 \rangle^{1/2} = 2 \langle i^2 \rangle^{1/2} = e_{eq}$  [68]. The eccentricity dispersion is set such that the viscous stirring timescale is in balance with the aerodynamic gas drag timescale. In both phases of the simulations, the gas surface density is a factor of 240 times larger than the solid surface density, and a power law index of 1.5 is used, even in the cases where the profile of the solids is steeper or shallower than this. In addition to being used to construct the initial conditions, the prescribed gas profile is used to apply a Stokes drag force to the growing planetesimals and protoplanets.

To make the planetesimal accretion phase more computationally tractable, the collision cross sections of particles are inflated by a factor of 6. This acts to shorten the growth

timescale and number of timesteps required to produce protoplanets without qualitatively changing the growth modes. The collision cross section inflation, however, does move the boundary between oligarchic and non-oligarchic growth in the disk outward by a factor of  $\sim 10$  in orbital period. In figure 5.1, we show the eccentricity and mass distribution at the end of the planetesimal accretion phase for a simulation using  $\delta = 1.5$ . For a full description of how the initial conditions were constructed, along with the details of the simulations and the limitations created by expanding the collision cross sections, see Wallace + Quinn 2023.

Once the simulations reach a point where the remaining planetesimals and protoplanets reach a quasi-steady state, the results are converted into a set of initial conditions for GENGA. When doing so, the inflated collision cross sections are removed and the particle radii are reduced back to their proper physical values. Each of the simulation snapshots passed to GENGA contain roughly 10,000-15,000 particles. These are each integrated for 1 Myr using a timestep size of 0.05 days a fully interacting set of particles. Bodies which fall within the radius of the star ( $X$  solar radii) or beyond the truncation radius (0.24 AU) are removed from the simulation. In all cases, roughly half of the remaining planetesimals eventually scatter beyond the outer truncation radius and are considered ejected. This allows the particle count to reduce enough to allow the simulations to complete in a reasonable amount of time.

As with the CHANGA simulations, every collision results in a perfect merger, where the resulting particle takes on the center of mass position and velocity of the participating particles. For high-velocity impacts which happen towards the final assembly stage, this is almost certainly not a realistic assumption [110]. We will explore the implications of destructive giant impacts in section 5.4.

### 5.2.3 Typical Planet Formation ICs: Isolation Mass Embryos

We also construct a set of initial conditions to match a more typical scenario for an N-body simulation of terrestrial planet formation. Here, protoplanets throughout the disk are already fully formed and roughly evenly spaced. Although not as realistic, this type of setup is much simpler to construct and requires far fewer self-interacting bodies, which is a common point

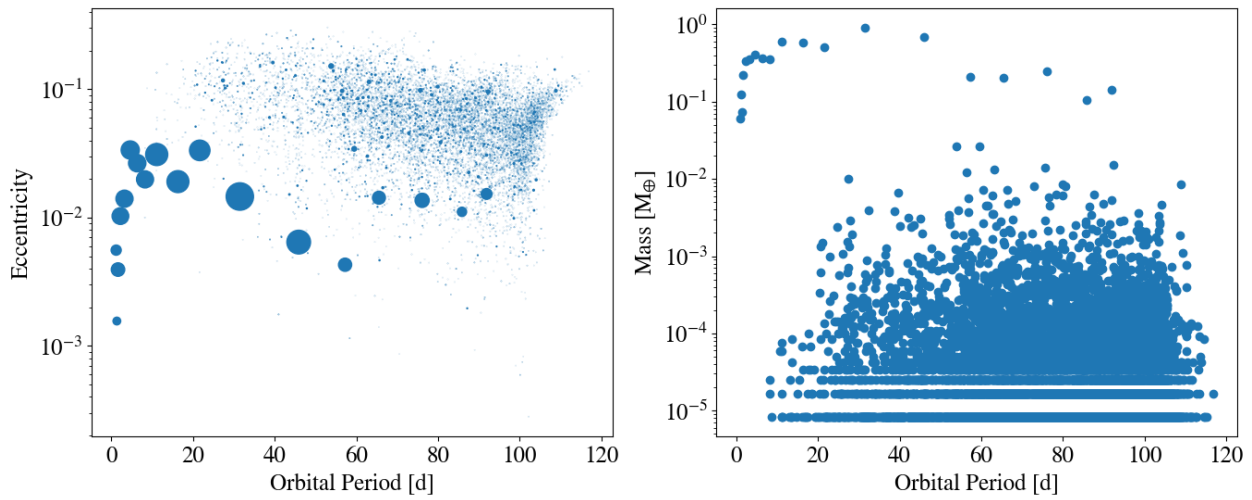


Figure 5.1: The period-eccentricity (left) and period-mass (right) distribution of a planetesimal growth simulation run to completion with CHANGA. A transition between non-oligarchic and oligarchic growth is visible around 40-60 days and is characterized by a change in the amount of residual planetesimals, along with a change in the masses of the protoplanets. The positions, velocities and masses of these bodies are then used as initial conditions for a GENGA simulation, which is run until a fully-formed set of terrestrial planets are constructed.

of trouble for most planet formation simulations.

As with the planetesimal disk, the protoplanets are placed on orbits between 1 and 100 days in orbital period, and the disk is constructed to contain the same amount of total mass (X earth masses). To place protoplanets, we begin at the outer disk edge and calculate the local isolation mass [89]

$$M_{iso} = \left[ \frac{(2\pi a^2 \Sigma \tilde{b})^3}{3M_*} \right]^{1/2}, \quad (5.2)$$

where  $a$  is the current semimajor axis,  $\Sigma$  is the local solid surface density (using  $\delta = 1.5$ ) and  $\tilde{b}$  is the local feeding zone size (in units of the Hill radius). Starting at the outer disk edge, protoplanets are placed one-by-one and  $\tilde{b}$  is then randomly chosen to be between 5 and 10. The current semimajor axis is then decremented by  $\tilde{b}$ , the local isolation mass is recalculated and another protoplanet is placed. This process repeats until the inner disk edge is reached.

The eccentricities and inclinations are randomly drawn from a uniform distribution  $\in [0, 0.01]$  and the longitude of periastron, longitude of ascending node and mean anomaly are randomly drawn from a uniform distribution  $\in [0, 2\pi]$ . In total, 5 sets of initial conditions using different random number seeds are constructed and integrated for 1 Myr.

### 5.3 Results

#### 5.3.1 In-Situ Formation Starting from Planetesimals

One of the motivating questions for this work is whether a fully in-situ formation model leaves any distinct imprints of the orbital architecture of the resulting planets. By stitching together the snapshots from both phases of the simulation and reconciling the particle IDs, we can construct and examine the full history of the collision and phase space evolution for the entire ensemble of particles. In all cases, the planetesimal disks start out with just under  $10^6$  particles and eventually consolidate into 5-10 super Earths, with around  $10^4$  particles being ejected during the giant impact phase.

In figure 5.2, we show the evolution of the orbits and the timing of collisions between bodies in the standard MMSN profile ( $\delta = 1.5$ ) simulations. The gray curves show the orbital periods of the last 100 bodies to exist in each iteration of the simulation. The green curves indicate bodies which survived until the end of the simulation, where the line width denotes relative mass. Overlaid on top of the evolution curves are triangle markers, whose position on the plots indicates the instantaneous orbital period and timing of each collision event. The size of the markers indicates the relative mass of the body participating in the collision. In all cases, the secondary (less massive) body's state is used to determine the size and placement of the marker. Finally, the vertical blue line indicates the time at which the simulation state was transferred from CHANGA to GENGA.

In all cases, it's apparent that the bodies in the non-oligarchic growth region ( $P < 40$  d) behave in a qualitatively different way during the giant impact phase. Rather than scattering events and instability propagating from inside-out in the disk, the opposite appears to be true. The inner disk remains in a meta-stable state while the outer bodies undergo scattering and giant collisions first. We postulate that this is due to the presence of a residual planetesimal population in the outer disk, which acts to facilitate a gradual inward ‘random walk’ of the protoplanets until they have a close encounter with another large body. This effect was also seen in [128] when modeling the outer solar system, and was even seen to facilitate capture of the planets into resonance. This effect was found to be largely resolution dependent and resonance capture was only possible with a sufficiently fine-grained planetesimal disk. In any case, we attribute the much more static state of the inner disk to the lack of residual planetesimals in this region.

Next, we examine the final configurations of the simulated planetary systems. In figure 5.3, we show the final period-mass distributions for all three choices of the initial surface density profile. Planets in the same system are connected by a solid line and each choice of random number seed for the initial conditions is shown as a different color. In most cases, the planet mass increases with orbital period and then turns over at some intermediate value. The turnover distance appears to be inversely proportional to the power law slope of the

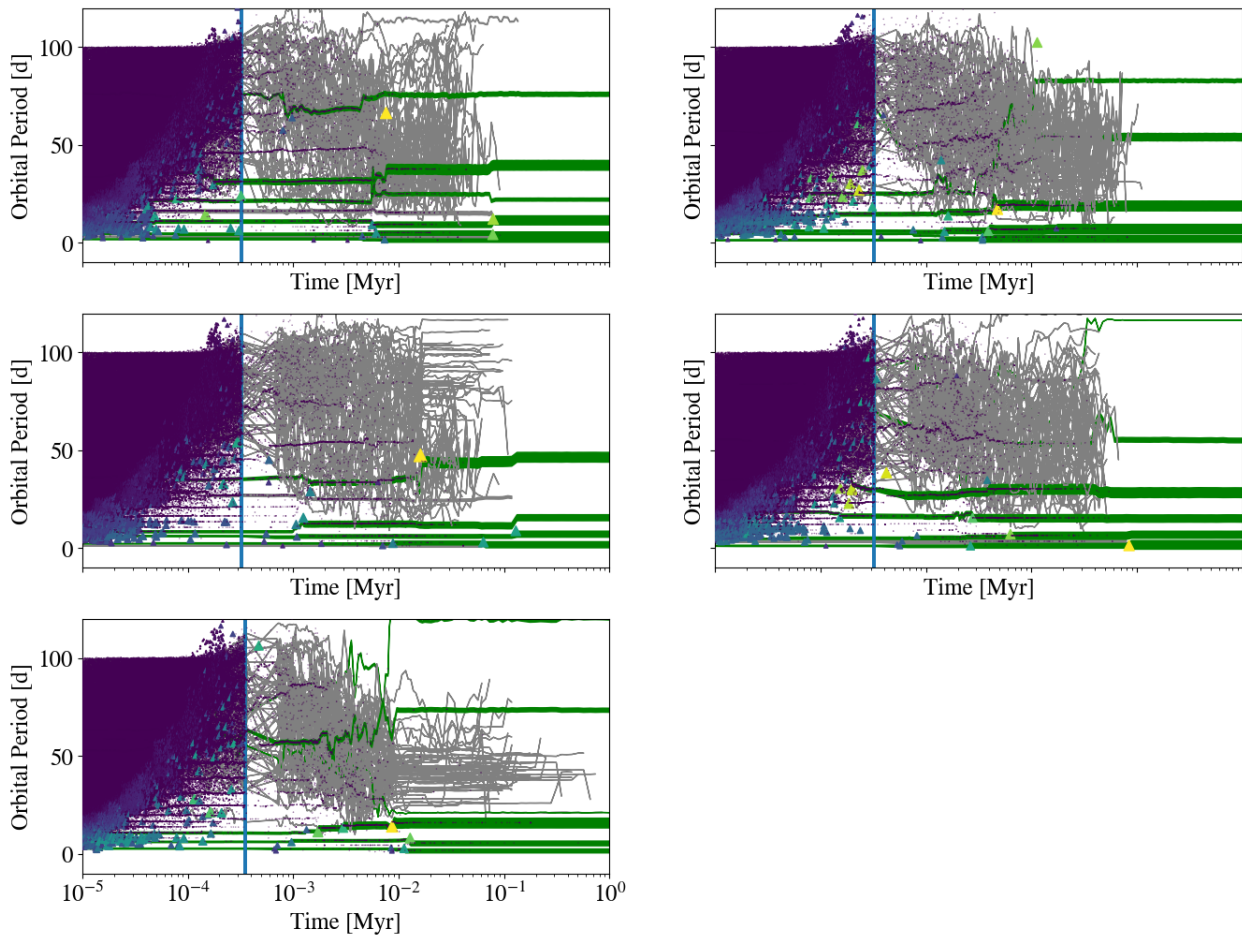


Figure 5.2: The evolution of the orbits of some of the last surviving bodies in the  $\delta = 1.5$  simulations. Collisions are indicated with colored triangles, where the size and color denotes the relative mass of the body that was consumed in the merger. Green curves indicate bodies which survived through the end of the simulation and the line width indicates their relative mass. The vertical blue line marks the time at which the CHANGA snapshots were passed to GENGA.

initial planetesimal disk  $\delta$ . In addition, there is some significant scatter in the final planetary architectures formed which is particularly prevalent for smaller values of  $\delta$ . This is driven by the role that chaos plays during the giant impact phase. In section 5.5, we will revisit this aspect of the simulations and use a neural network to generate a much larger set of late-stage initial conditions which can then be evolved with GENGA.

Having directly tracked every collision starting from the planetesimal phase allows us to make composition predictions for the resulting planets. To do so, we construct a collision tree for each planet in the final simulation snapshots, where the root node is the planet itself and the leaf nodes correspond to the initial mass planetesimals that went into its assembly. We place a snowline partway through the disk and for each planet, calculate the fraction of consumed planetesimals which originated from beyond the snowline location. Due to the fact that the inflated collision cross sections used during the planetesimal accretion phase alter the location of the accretion mode boundary in the disk (see Wallace + Quinn 2023), along with the fact that the snow line locations should be expected to vary widely over the course of the central star’s pre-main sequence evolution [11], we choose to simply place a static snowline at 50 days in orbital period.

Figure 5.4 shows the expected wet/dry compositions of the planetary systems formed in the  $\delta = 1.5$  simulations. Each row of points on the y-axis corresponds to a separate iteration of the simulation and the point sizes indicate relative masses. The blue shading represents the total mass fraction of accreted planetesimals that originated from beyond the snowline, which is indicated by a vertical line. In all cases, we see that water-rich material is able to be incorporated into planets far interior to the snowline location. In one case, a significantly dry planet eventually ends up well beyond the snowline.

As our model is purely in-situ and does not incorporate any significant dissipative forces from the gas disk, one would not expect any resonant chains to form. However, some recent work [75, 145] has shown that super-Earths in resonant chain configurations can later destabilize. One would therefore wonder whether there is any distinguishable difference between a super-Earth system that had formed purely in-situ, and one that underwent

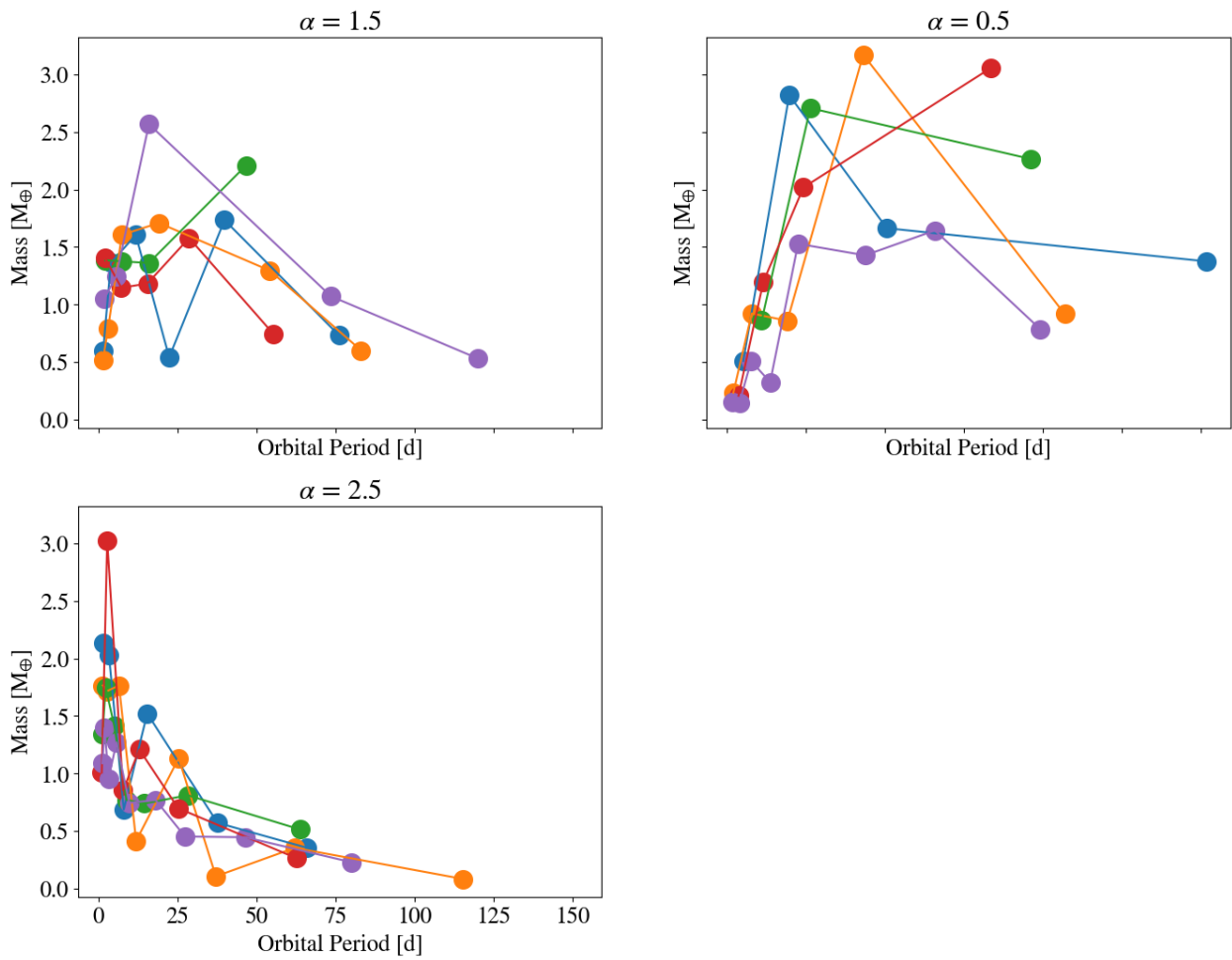


Figure 5.3: Final period-mass configurations for the planets formed in all fifteen simulations. Each panel contains a set of simulations using a different mass surface density profile. Points connected by lines represent planets from the same simulation snapshot. Each color represents a set of initial conditions constructed from a different random number seed.

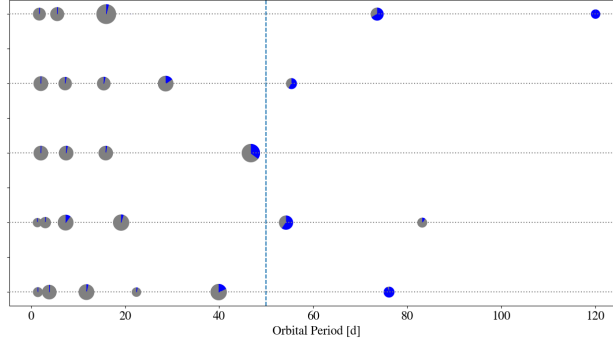


Figure 5.4: Final compositions of planets from the five  $\delta = 1.5$  simulations. Point sizes indicate relative mass and the pie fractions indicate the amount of wet/dry material incorporated into each planet. A snow line is placed at 50 days in orbital period and all planetesimals that originate from beyond this location are assumed to be wet.

convergent migration and was then destabilized. [145] found that the inward migration of wet embryos can actually concentrate and consolidate rocky material near the inner edge of the disk. This quality is also present in our in-situ systems. [75], however, found that only about 50 percent of resonant chains eventually go unstable, while 75 percent must do so to match observations. Given that our in-situ systems appear rather qualitatively similar to the convergent migration, followed by destabilization driven systems seen by [145], it may be the case that disk-driven migration simply doesn't operate for some fraction of STIPs.

#### 5.4 Comparison With Typical Planet Formation ICs

The simulations presented in this work are not the first to investigate the outcome of an in-situ model on the formation of STIPs (see [62]). However, this work does self-consistently follow the terrestrial planet formation process from some of the smallest gravitationally bound objects, which is not the case for most planet formation N-body simulations. Typically, these types of simulations begin with either a set of equal-mass embryos placed in a wide annulus [131], or a set of regularly spaced embryos that follow the local isolation mass of the disk (e.g. [147, 144, 62]). There are two implicit assumptions made in these models:

1. The embryo formation process behaves in a self-similar manner everywhere in the disk. 2. The embryo formation process has fully completed everywhere in the disk before the giant impact phase initiates. Assumption number two is generally valid for the inner solar system, as the planetesimal accretion timescale is much shorter than the instability timescale which gives rise to the giant impact phase [25]. However, assumption number one is not physically motivated.

As we showed in (Wallace + Quinn 2023), the oligarchic growth process, which gives rise to planetary embryos, should only be expected to operate down to  $\sim 5$  days in orbital period. Furthermore, the late-stage instability that initiates collisions between protoplanets is a nonlinear process and there have yet to be any investigations of how it behaves at short period. Both of these concerns are naturally addressed in the simulations we present in this chapter. Except for the fact that the non-oligarchic accretion boundary has been moved out by a factor of a few in orbital period due to the inflation of the collision cross sections during the planetesimal growth phase, the state of the protoplanets at the beginning of the GENGA simulations is free from any simplifying assumptions. To understand the influence that these simplifications made in typical N-body simulations of planet formation have on the final architectures of the systems, we compare our  $\delta = 1.5$  simulations with a set of late-stage simulations which begin with fully-formed, isolation mass embryos in a disk with an identical mass profile.

In figure 5.5, we compare the period-mass and period-eccentricity distributions of the planetary systems formed starting from planetesimals and starting from isolation mass embryos (shown in gray). Qualitatively, the eccentricity distributions are remarkably similar between the two sets of initial conditions, despite the fact that the protoplanet eccentricities at the end of the planetesimal accretion simulations start off nearly an order of magnitude smaller than the isolation mass embryos. The period-mass distributions, however, show some noticeable differences.

Overall, the isolation mass embryo simulations tend to form larger planets. There are twice as many  $> 2M_{\odot}$  planets using the fully formed isolation mass set of initial conditions.

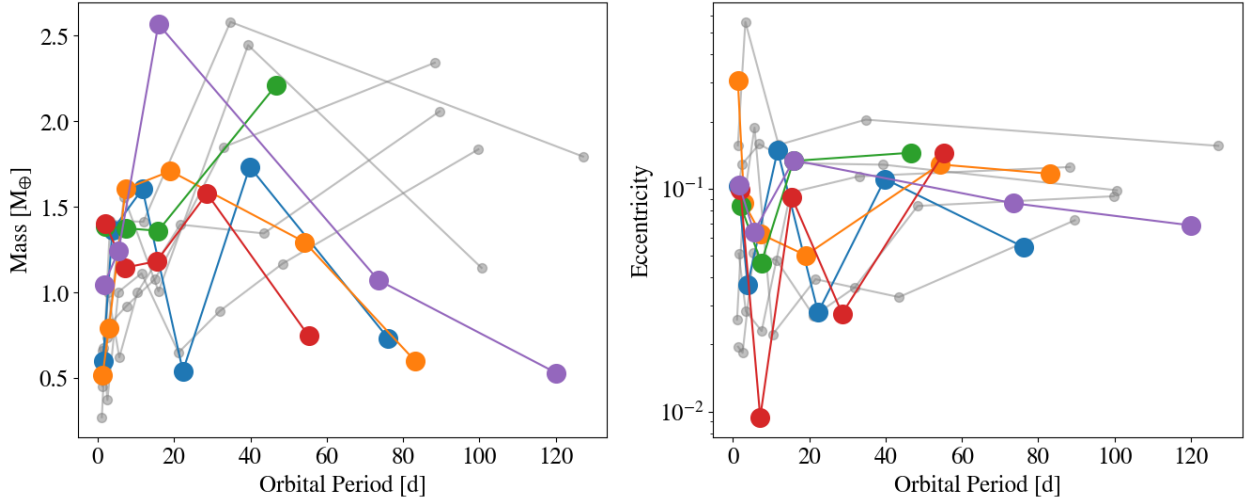


Figure 5.5: The period-mass (left) and period-eccentricity (right) distributions of the simulations starting from planetesimals (colored points) and isolation mass embryos (gray points). Each planetary system is connected by a series of lines.

In addition, the mass in these simulations tends to be less radially concentrated, with every single set of initial conditions producing a super-Earth beyond 80 days in orbital period. In contrast, two of the simulations starting from planetesimals produce a truncated set of planets that do not extend beyond 60 days. Most noticeably, the isolation mass embryo simulations produce a wider variety of masses and eccentricities between sets of initial conditions. This highlights the more influential role that stochasticity plays in these simulations. One possibility for this difference comes from the fact that the isolation mass embryo simulations do not contain any planetesimals, and the gravitational kicks between embryos do not get damped out. A second possibility comes from the way in which the instability which gives rise to the giant impact phase propagates through the disk in each case. For the simulations starting from planetesimals, there is a qualitative difference between the inner and outer disk, and the onset of chaos may occur in a different fashion.

To test this second hypothesis, we examine the timing and location of collisions in the disk for each set of simulations. In figure 5.6, we show ensemble of collisions recorded in all

five versions of the simulations starting from planetesimals (blue points) and isolation mass embryos (orange points). The point sizes indicate the relative masses of bodies consumed in the merger events. The orbital period of each collision is calculated using the phase space state of the consumed body at the moment of impact. For the isolation mass simulations, the collision times are offset by the integration time of the CHANGA simulations because there is no prior planetesimal accretion phase.

During the giant impact phase, there is a clear qualitative difference in the location and timing of protoplanet collisions between the two sets of simulations. For the isolation mass embryo simulations, giant impacts begin almost immediately at the inner edge of the disk and propagate outward over a timescale of  $\sim 10^4$  years. For the simulations starting from planetesimals, the commencement of giant impacts is nearly simultaneous everywhere in the disk. Additionally, this phase seems to be much longer-lived, particularly beyond about 20 days in orbital period.

The near-instantaneous initiation of the giant impact phase in the simulations starting from planetesimals is a possible explanation as to why the variation in the final masses and eccentricities of the resulting planets is smaller. In contrast to the isolation mass simulations, giant impacts occur nearly everywhere in the disk simultaneously, which acts to damp eccentricities and reduces the distance over which protoplanets can communicate. A smaller interaction distance therefore reduces the possible outcomes of the giant impact phase and produces a smaller scatter in the final masses and eccentricities. Because collisions tend to happen at perihelion [101], protoplanets that are simultaneously excited in the outer disk tend to collide in the inner disk, which explains why there are so few planets end up in the outer disk for this set of simulations. The isolation mass embryos, on the other hand, interact with the rest of the disk in an inside-out fashion. This dynamically excited outward-propagating boundary has the opportunity to interact the entire outer disk, which is still in a non-excited state. Between different iterations of the simulation, scattering events happen at different points along an excited protoplanets orbit, which widens the possibilities for the final orbital configurations of the resulting planets.

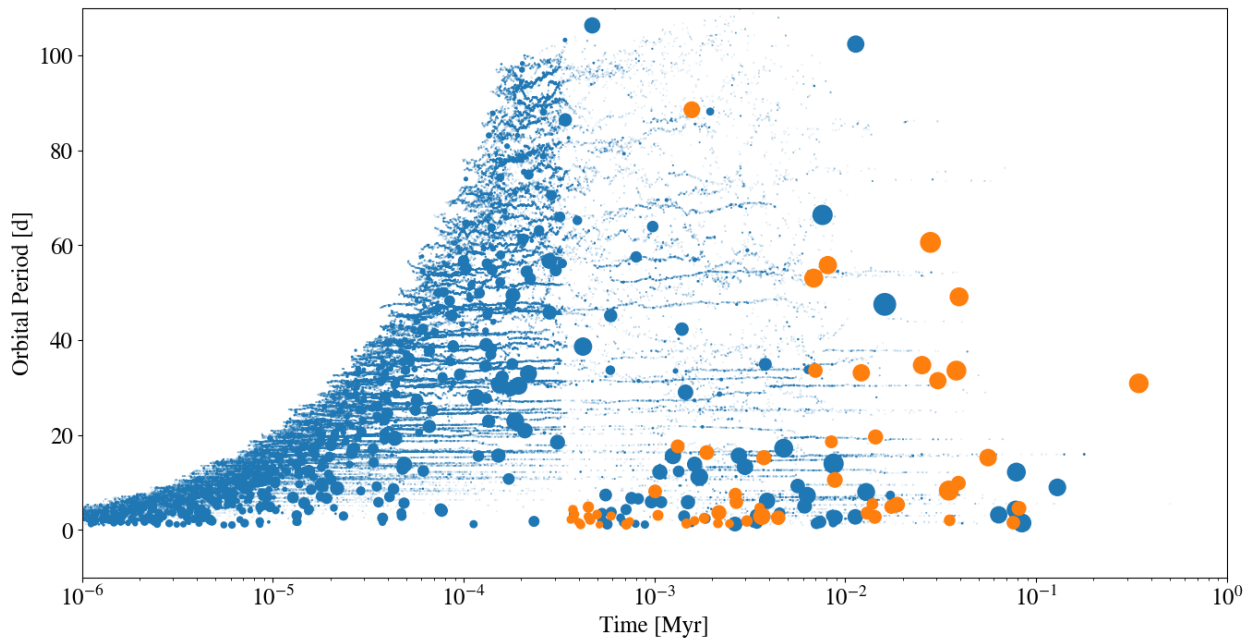


Figure 5.6: The combined timing and location of collisions from all five versions of the full (blue) and isolation mass (orange) simulations. Point sizes indicate the relative masses of bodies consumed in each merger. The timings of the isolation mass simulations have been shifted to line up with the ending of the CHANGA segment of the full simulations.

Lastly, we examine the relative collision velocities of growing protoplanets during the giant impact phase. [163] proposed that the lack of short-period planets in the solar system is due to an earlier phase of violent instability in the inner disk which destroyed any such worlds. Given the sudden onset of instability in our simulations starting from planetesimals, one might wonder whether some of the later collisions should be destructive. Because all collisions result in perfect mergers in our simulations, this effect is not self-consistently captured, but we can examine the collision statistics afterwards to determine which planets might have undergone earlier destruction.

In figure 5.7, we show the timing and speed of collisions between bodies larger than  $0.01 M_{\odot}$  in each set of simulations. The gray points denote collisions from the isolation mass simulations, while the colored points indicate collisions from the simulations started from planetesimals. The collision speeds on the y-axis are shown in units of the mutual escape velocity of the colliding particles. For super-Earth and smaller sized bodies,  $v_{coll}/v_{esc} > 2$  tends to produce destructive collisions [110] and so we have marked this region of the figure with a horizontal dashed line. Solid lines connecting points indicate subsequent collisions between the same body.

With the exception of a single high-speed collision around  $T = 20,000$  yr, (and another collision right on the destruction/accretion boundary) none of the collisions from the isolation mass simulations can be roughly categorized as destructive. In contrast, every simulation starting from planetesimals eventually produces at least one destructive collision. In three of these cases, multi-collision excitation eventually leads to a destructive encounter, which is the same mechanism seen by [163].

In figure 5.7, we show the final orbital architectures of all ten simulations. Here, point sizes indicate relative mass and the simulations starting from planetesimals are colored blue, while the isolation mass embryo simulations are colored gray. Planets that underwent a destructive collision during their giant impact phase are marked with a red X. For the simulations starting from planetesimals, the destructive collisions all involve the planets at the innermost edge of the disk. This is only the case for one of the isolation mass embryo

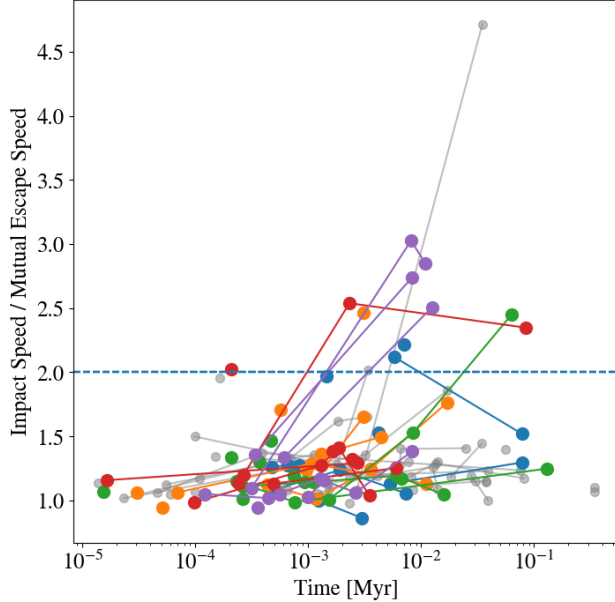


Figure 5.7: Timing and velocities (in units of the mutual escape speed) of collisions between bodies larger than  $0.1 M_{\oplus}$  in the full (colored points) and isolation mass (gray points) simulations. Collisions between subsequent bodies are connected by lines. The dashed horizontal line at  $v_{coll}/v_{mut,esc} = 2$  corresponds to boundary above which collisions should be destructive.

simulations.

Although  $v_{coll}/v_{esc} > 2$  are expected to be at least partially destructive [110], it is not immediately clear whether the debris should be expected to re-accrete onto other bodies or be entirely removed from the system. For small grains (1-10 microns), dust blow out can entirely eject material from the system on timescales much shorter than re-accretion. Larger grains (cm-sized) can be removed by PR drag on  $10^5$  yr timescales. This is particularly efficient if the timescale for collisional grinding of debris is fast [112]. For planetesimal-sized objects (100 km), gravitational scattering can eventually eject material. This was the eventual fate of most remaining planetesimals at the end of the CHANGA simulations.

Another caveat is that the integration time we use (1 Myr) is only a small fraction of the age of most STIPs [154] and our results should only be interpreted as applicable to

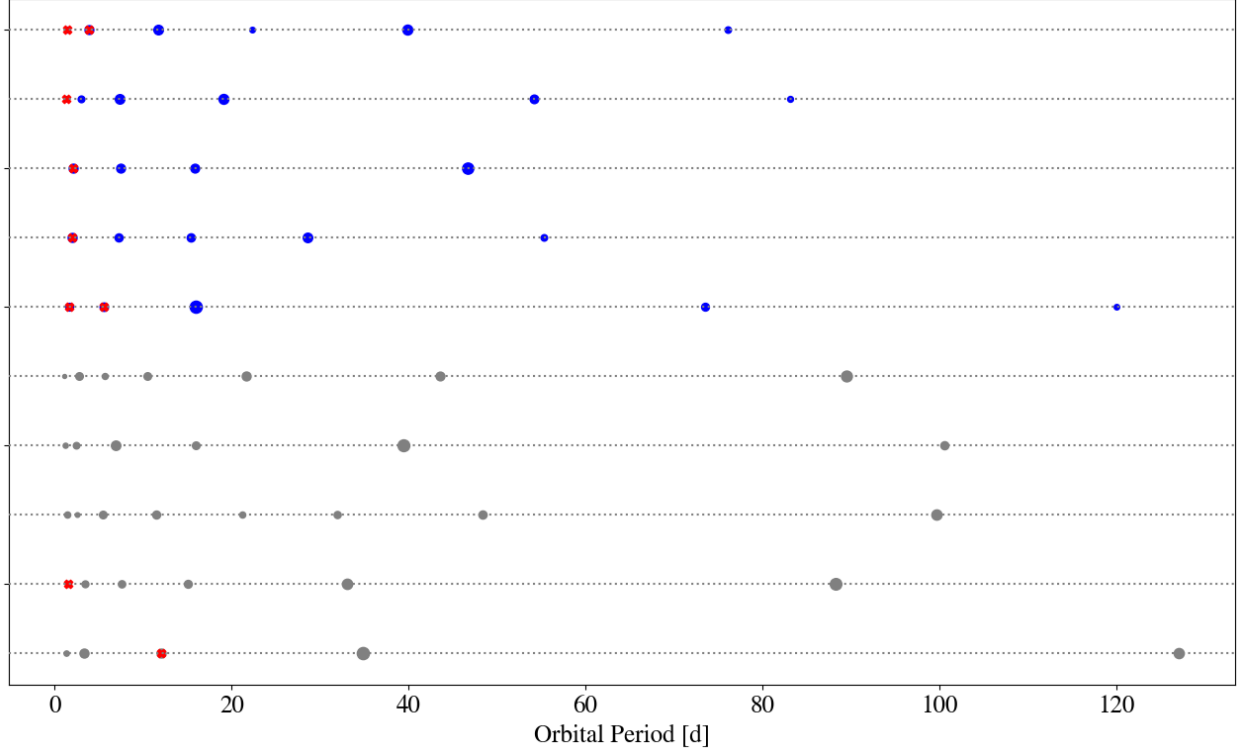


Figure 5.8: Final orbital architectures of planetary systems formed in the full (blue points) and isolation mass (gray points) simulations. Point sizes indicate relative masses. Bodies which underwent a collision where  $v_{coll}/v_{mut,esc} > 2$  with a  $> 0.1M_{oplus}$  body are marked with a red X.

expected behavior during the gaseous disk phase of the planet formation process. The solar system is thought to be in a state of constant metastability, having an instability timescales that matches its current age [93]. The same is likely true for many exoplanetary systems as well (see [36, 105, 103]). In addition, the small sample size of our 5 simulations in each configuration is unlikely to have captured the full extent of the effects of dynamical chaos during the giant impact phase. To address this second point, we train a neural network to produce a much larger set of qualitatively similar, but numerically distinct initial conditions to pass to GENGA, which we describe in detail in the next section.

## 5.5 Training a Neural Network to Synthesize ICs

To fully capture the role that stochasticity plays during the protoplanet assembly phase, a much larger set of simulations is required. As we have shown in the previous section, using a typical arrangements of isolation mass embryos to set up the giant impact phase does not seem to be sufficient. Each of the planetesimal accretion simulations run with CHANGA, however, require about 80,000 CPU hours. Passing each of these simulations to GENGA and integrating to 1 Myr requires another 200 or so GPU hours. The large particle count, in addition to the fact that different parts of the disk evolve semi-independently of each other, means that stochasticity does not play an important role during the planetesimal accretion phase and a small number of simulations is sufficient to capture the outcome of the embryo formation process. When trying to capture the full breadth of planetary architectures possible with our in situ model, it is most useful to focus our computational resources on the GENGA simulations. Doing so requires a much larger set of late-stage initial conditions.

Although there is very little qualitative variation between the CHANGA simulations run in each initial disk configuration, slight differences in the masses, positions and velocities of the embryos and planetesimals lead to significantly different planetary systems, due to the chaotic nature of the giant impact phase. To generate numerically distinct late-stage initial conditions requires an underlying model for orbital distributions of the planetesimals and embryos. Given the presence of the accretion boundary at short period, an analytic model is likely insufficient. Instead, we use the existing simulation snapshots to construct posterior distributions for the particles, and then randomly draw from these distributions to generate more initial conditions.

### 5.5.1 Training a Generative Adversarial Network

We use an unsupervised machine learning technique known as a Generative Adversarial Network (GAN). A GAN is a deep learning method [55], that uses two separate neural networks, a generator and a discriminator, to train itself to produce an infinite collection of

qualitatively similar datasets based on some input training data.

GANs are most well-known for use in synthetic image generation, and first gained traction in the astronomy community when they were used to enhance [152] and even produce entirely new galaxy images [38]. GANs have also recently been applied to N-body simulations to do things such as map large-scale gas and temperature distributions [161] and generate mock galaxy catalogs [76]. In the planetary domain, GANs have been used for exoplanet atmosphere retrieval [181] and even to supplement transit detection models [45].

In a traditional GAN, the discriminator and generator are pitted against each other. A noise vector is fed to the generator which is used to produce a synthetic dataset. The synthetic data is then fed to the discriminator, alongside the original training data. The discriminator then determines whether the two datasets are distinguishable. In the case that the synthetic data is classified as ‘fake’, a loss function is calculated and the result is used in a backward pass through both neural networks to update the weights. Over many iterations, the generator improves its ability to produce authentic-looking synthetic data and the discriminator gets better at distinguishing between real and fake data. Once the discriminator reaches a point where roughly 50 percent of the synthetic data is classified as fake, the algorithm reaches an equilibrium and the generator is considered to be fully trained.

To construct a generator, we use the CTGAN [179] package to train a neural network on our planetesimal accretion simulation results. Traditional GANs are notoriously sensitive to issues such as non-convergence and mode collapse, both of which prevent the generator from ever being able to produce sufficiently varied and useful results. To combat these issues, CTGAN models are trained using a WGAN loss function with a gradient penalty [60]. Updates to the generator and discriminator between iterations are done using an Adam optimizer [84], which is a stochastic gradient descent algorithm. Both neural networks are updated using a learning rate of  $2 \times 10^{-4}$ .

One challenge when working with unsupervised machine learning techniques is determining the best way to format and represent the training data. In the case of the our planetesimal accretion simulations, the residual planetesimals greatly outnumber the protoplanets, which

causes the neural networks to place much more emphasis on the planetesimal distribution. One solution to this problem is to modify the loss function to give more weight to the protoplanets. CTGAN, however, does not provide a way to modify the loss functions, and we found that this approach did not work well in our own experiments when constructing a toy model. A simpler solution is to give every particle in the data set a mass of  $m_0$  and then duplicate points based on their original mass. In addition to expanding the size of the training data set by a factor of nearly 100, this causes the GAN algorithm to fall into a perpetual state of non-convergence.

An even simpler solution that works well with our simulation data is to simply split the dataset in two, with a mass cut that cleanly separates the protoplanets from the remaining planetesimals. To train our GAN, we concatenate all of the final  $\delta = 1.5$  CHANGA snapshots into a single table and place a mass cut at  $0.03 M_{\oplus}$  to split the dataset into two parts. The state of the particles are passed to the deep learning algorithm in terms of orbital period, and logarithmic eccentricity, logarithmic inclination and logarithmic mass. To quantify the accretion histories of the particles, we also include the ‘smooth accretion fraction’ (see Wallace + Quinn 2023) as a separate column in the training sets. Doing so naturally incorporates the effects of the oligarchic and non-oligarchic accretion modes into the data and substantially helps to tighten up the period-mass relation of the synthetic protoplanets.

In figure 5.9, we show the correlations between the features used to train the GANs in the training (blue) and synthetic (orange) datasets after 5,000 epochs. The discretization of the masses (due to growth via perfect mergers) is clearly visible in the synthetic data, despite no enforcement of this property in the model. This characteristic of the mass data, however, appear to produce some additional small artificial peaks in the synthetic mass distribution at equal intervals in logarithmic space. To circumvent this issue, we also tried training the models using linear masses but it did not appear to reconcile the match between the real and synthetic mass distributions. Due to the weak, indirect role that planetesimals play during the giant impact phase, we chose to leave the synthetic mass distribution as-is.

To construct initial conditions from the synthetic data, particles are drawn one-by-one

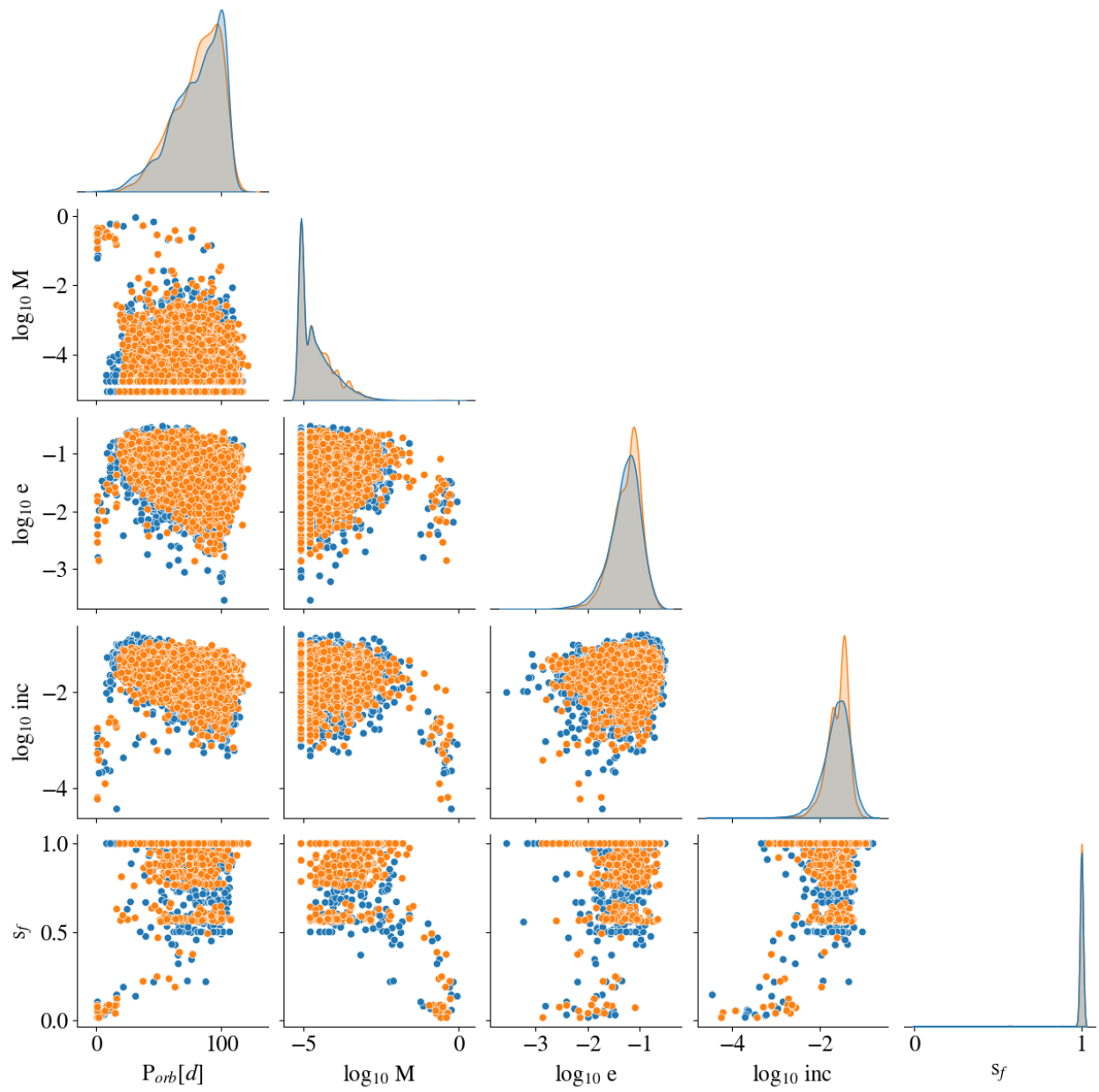


Figure 5.9: Corner plot showing the correlations between all five features (orbital period  $P_{orb}$ , mass  $M$ , eccentricity  $e$ , inclination  $\text{inc}$  and smooth accretion fraction  $s_f$ ) used to train the generator and discriminator. The training data is shown in blue and an example synthetic dataset is shown in orange.

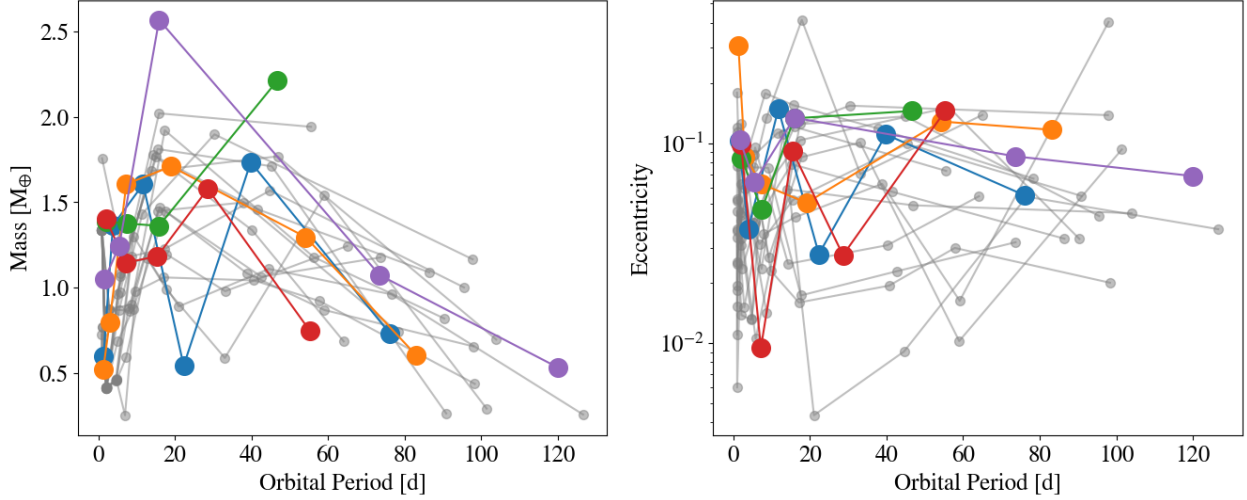


Figure 5.10: Period-mass and period-eccentricity distributions of planetary systems formed through the full simulations (colored points) and the synthetic simulations (gray points). Planets from the same system are connected with a line.

until the total mass exceeds the average disk mass of the full simulations. This is done separately for the planetesimal and embryo populations, and the total masses of each are matched accordingly. Out of the 100 sets of initial conditions we construct, the synthetic particle count matches the original particle count to within 5 percent, which is an encouraging sign that the generator is properly capturing the physical state of the disk.

Once particles are drawn using the five features that the neural networks were trained on, the longitude of periastron, longitude of ascending node and mean anomaly are randomly drawn  $\in [0, 2\pi)$  for each particle. The six orbital elements are then converted to cartesian coordinates and particle radii are calculated using the synthetic masses under the assumption that the bulk density is  $3 \text{ g cm}^{-3}$ . All 100 sets of initial conditions are passed to GENGA and integrated to 1 Myr.

In figure 5.10, we show the resulting period-mass and period-eccentricity distributions of the synthetic simulations (gray points) alongside the full simulations (colored points). Here, planets from the same system are connected by solid lines. The masses of the synthetic

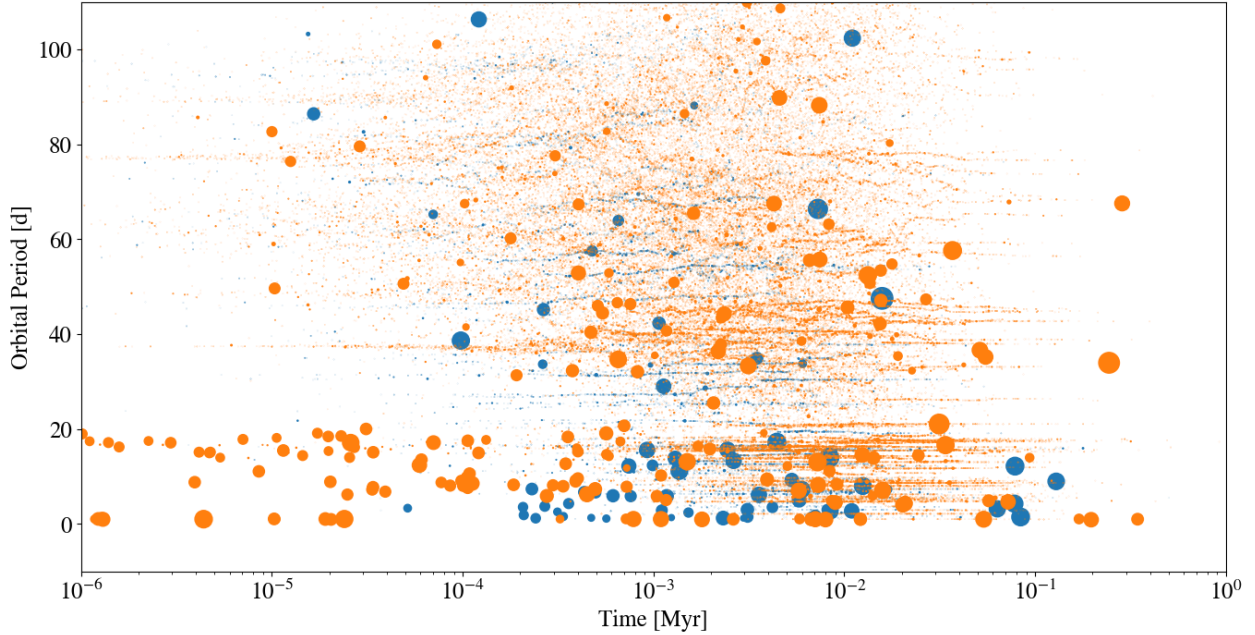


Figure 5.11: The combined timing and location of collisions from all versions of the full (blue) and synthetic (orange) simulations. Point sizes indicate the relative masses of bodies consumed in each merger. Here,  $T=0$  corresponds to the end of the CHANGA simulations and collisions from that phase are not shown.

planets are quite similar to those in the full simulation, with the turnover in the period-mass relation occurring at roughly the same orbital period (20 days). The period-eccentricity distribution of both sets of simulations appears quite flat and both exhibit a similar mean eccentricity, which indicates that the giant impact phase plays out in a very similar way for the synthetic simulations. We perform a Kolmogorov-Smirnov test on the mass and eccentricity distributions for both the full and synthetic simulations. A KS test for the planet masses yields a p-value of 0.063, which marginally suggests that the two distributions are statistically different. The eccentricity distributions, however are much more firmly statistically similar, with a p-value of 0.0084.

Next, we examine the timing and location of collisions between the full and synthetic simulations. This is shown in figure 5.11, where point sizes indicate relative mass of the

body consumed in a merger and the point location indicates the timing and orbital period (calculated from the instantaneous position and velocity at the moment of impact) of the body. In the inner disk, collisions take about 100 yr to get underway for the full simulations, while giant impacts begin almost immediately for the synthetic simulations. Despite the features of the training set and the synthetic dataset matching up well in this region of the disk, the generator does not appear to be producing embryos in a metastable configuration here. To date, most deep learning techniques require more than just particle phase space information at a single snapshot in time to make accurate stability classifications (see [158, 31]), so it is not unexpected that our neural network can't reproduce a metastable configuration of embryos.

With the exception of the inner 20 day orbital period region of the disk, giant impacts occur in a nearly instantaneous fashion for both the full and synthetic simulations, which is promising evidence that the synthetic data is still reproducing some of the same dynamical behavior as the training dataset. This also suggests that the early onset of giant impacts in the synthetic inner disk is not affecting the growth of planets elsewhere and is not a major concern. In addition, the resulting planetary masses in the inner disk are quite similar.

In addition to examining the mass and eccentricity distributions, along with the collisional evolution of the simulations, we quantify some global properties of the planetary systems and compare these values between each set of simulations. The first of these quantities  $\alpha$ , is the total disk mass ratio between the initial and final simulation snapshots. This value quantifies the change in the solid disk mass and is a measure of how much material has been ejected during the giant impact phase. We also measure the mean eccentricity of each planetary system, along with the total number of planets.

In addition, we calculate the radial mass concentration (RMC)  $S_c$  of each planetary system, which is a measure of how centrally concentrated the solid material is about the star. Following [22], we define the radial mass concentration statistic as

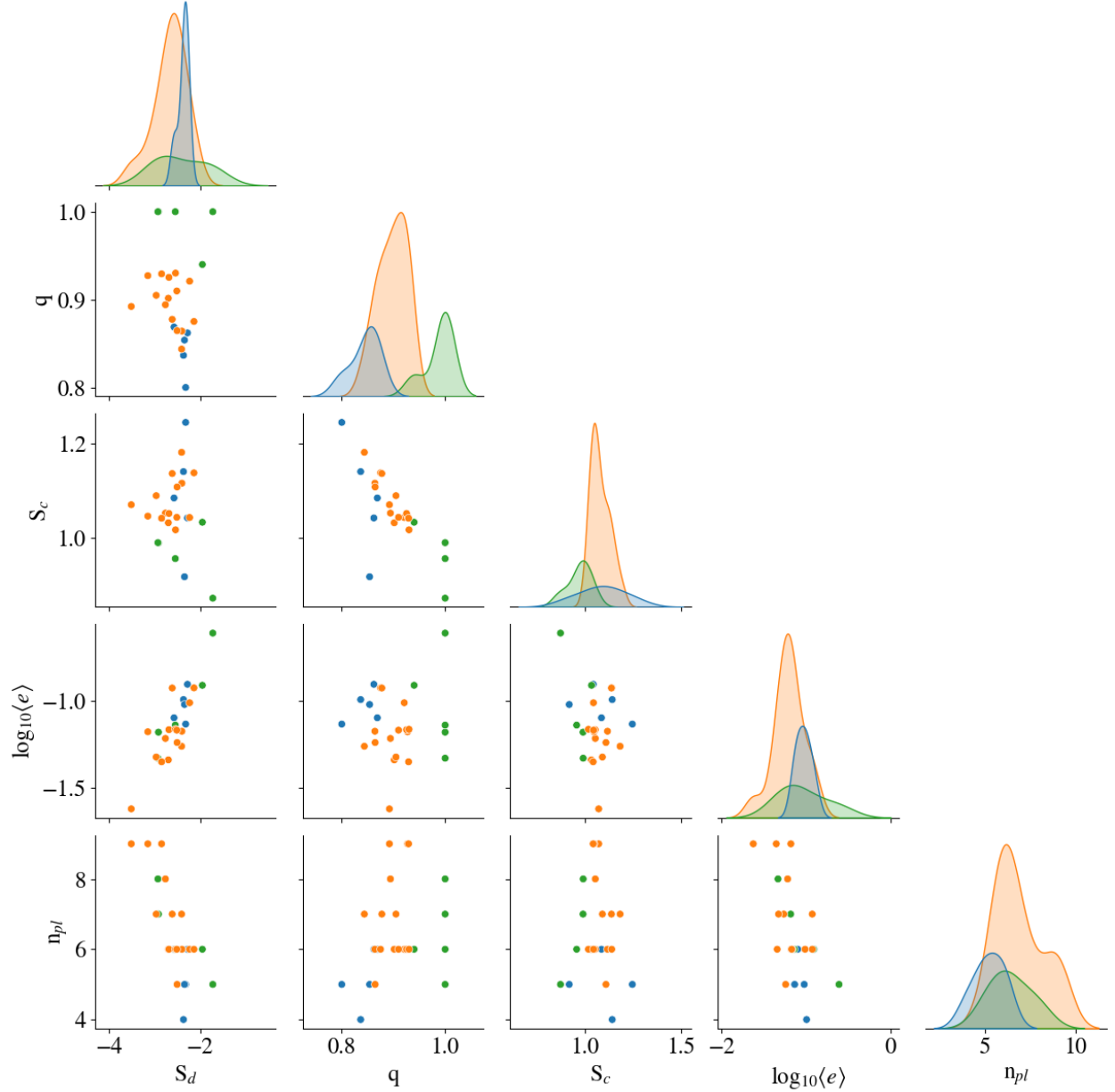


Figure 5.12: Corner plot showing the correlations between bulk properties of the final orbital architectures of the full, isolation mass and synthetic simulations.  $q$  is the mass ratio between the initial and final snapshot,  $S_c$  is the radial mass concentration statistic,  $S_d$  is the angular momentum deficit and  $n_{pl}$  is the final number of planets. Blue points are the full simulations, green points are the isolation mass simulations and orange points are the synthetic simulations.

$$S_c = \max \left( \frac{\Sigma_j m_j}{\Sigma_j m_j [\log_{10} (a/a_j)]^2} \right), \quad (5.3)$$

where  $a_j$  and  $m_j$  are the semimajor axis and mass of the  $j$ th planet and  $S_c$  is the maximum value of the bracketed quantity evaluated over all  $a$ .

Lastly, we measure the angular momentum deficit (AMD)  $S_d$  for each planetary system, which is defined as

$$S_c = \frac{\Sigma_j m_j \sqrt{a_j (1 - e_j^2)} \cos i_j - \Sigma_j m_j \sqrt{a_j}}{\Sigma_j m_j \sqrt{a_j}}, \quad (5.4)$$

[92, 22] where  $e_j$  and  $i_j$  are the eccentricity and inclination of the  $j$ th plane. Physically,  $S_c$  can be thought as the fractional difference between the z-component of the actual total angular momentum of the system and the angular momentum if all of the planets were on circular, non-inclined orbits.

In figure 5.12, we show a corner plot highlighting the correlations between these quantities for the full (color), isolation mass (color) and synthetic (color) simulations. Most obviously, the initial to final mass ratio  $\alpha$  changes between the three distributions, with the isolation mass simulations preserving the most amount of mass. Although the  $\alpha$  values overlap for the full and synthetic simulations, the synthetic simulations seem to preserve about 5 to 10 percent more mass. Similarly, the full simulations produce a few less planets overall, although the synthetic and isolation mass simulations both produce 5 to 9 planets each, despite ejecting different amounts of mass. There is a noticeable negative correlation between the radial mass concentration  $S_c$  and  $\alpha$ . As a reminder, large values of  $S_c$  correspond to a planetary system that is concentrated into a more narrow annulus. The full simulations, which tend to end up with few outer planets, produce larger values of  $S_c$  because the orbital architectures lie over a smaller radial distance.

Interestingly, there appears to be no measurable correlation between the number of planets and  $\alpha$  or  $S_c$  for the synthetic or isolation mass simulations, although  $\alpha$  and  $n_{pl}$  both tend to be smaller for the full simulations. This lack of correlation in the first two cases is likely

due to the inside-out behavior of the giant impact phase for these simulations (see figures 5.6 and 5.11, which leads to a wider variety of possible protoplanet interactions throughout the disk and therefore more final potential orbital configurations. Finally, there is a positive correlation between the angular momentum deficit  $S_c$  and the mean eccentricity and a negative trend between  $S_c$  and the number of planets. The first trend is not surprising, as larger eccentricities directly increase the z-component of the total angular momentum vector relative to a system with circular orbits. The negative correlation in the latter case suggests that the planetary systems lose angular momentum overall when outer bodies get ejected and  $n_{pl}$  decreases.

An important question that figure 5.12 helps to answer is whether the full and synthetic simulation results are sampling the same distributions. Because there are only five full simulations, a quantitative statistical test is not possible. However, all of the correlations present in the synthetic simulation results also appear to be present in the real simulations. We conclude that the data synthesizer is producing a set of useful and dynamically similar set of initial conditions relative to the full simulations that were started from planetesimals, with the caveat that the behavior and final structure of the outer disk is probably not fully captured by the synthetic simulations.

In figure 5.13, we show the timing and impact speed (in units of the mutual escape velocity of the colliding bodies) as a function of time for the full (colored points) and synthetic (gray points) simulations for bodies larger than  $0.01M_\oplus$ . Subsequent collisions between the same body are connected by lines and the horizontal dashed line at  $v_{coll}/v_{mut,esc}$  indicates the speed at which giant impacts should be expected to become destructive [110]. For both the synthetic and full simulations, subsequent collisions speeds begin to ramp up and exceed the destructive limit around  $10^{-2}$  Myr. With the exception of many more low-velocity collisions in the synthetic dataset at early times, the two datasets follow a very similar trend on this plot, which is another promising piece of evidence that the data synthesizer is capturing the same dynamical behavior as the full simulations. In addition, the eventual destructive events in both datasets come from sequences of collisions, rather than one-time events. The cluster

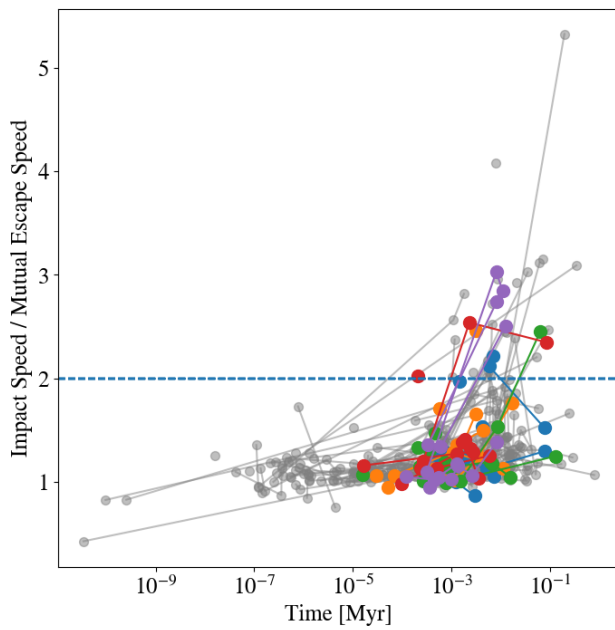


Figure 5.13: Timing and velocities (in units of the mutual escape speed) of collisions between bodies larger than  $0.1 M_{\oplus}$  in the full (colored points) and synthetic (gray points) simulations. Collisions between subsequent bodies are connected by lines. The dashed horizontal line at  $v_{coll}/v_{mut,esc} = 2$  corresponds to boundary above which collisions should be destructive.

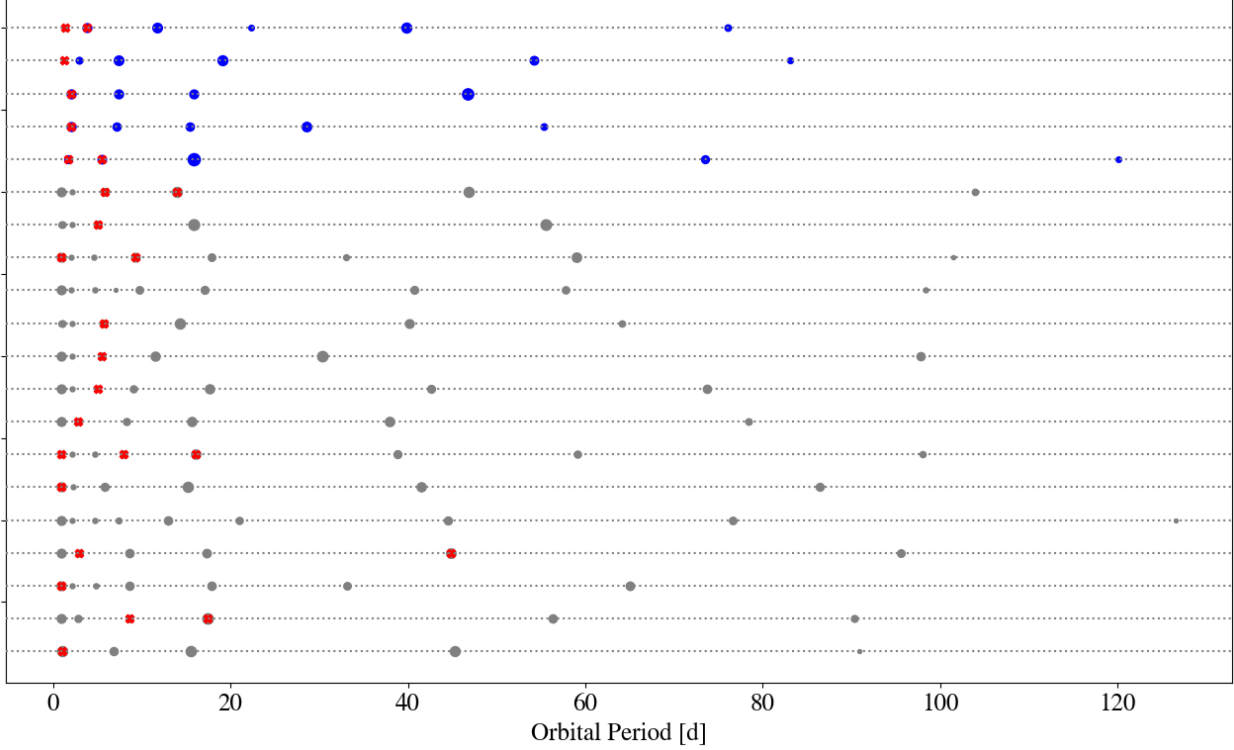


Figure 5.14: Final orbital architectures of planetary systems formed in the full (blue points) and isolation mass (gray points) simulations. Point sizes indicate relative masses. Bodies which underwent a collision where  $v_{coll}/v_{mut,esc} > 2$  with a  $> 0.1M_{\oplus}$  body are marked with a red X.

of low velocity collisions around  $10^{-6}$  Myr in the synthetic simulations is likely due to the early consolidation of protoplanets at the inner edge of the disk seen in figure 5.11. However, as we will show in the next figure, this additional phase of giant impacts does not seem to affect the eventual onset of destruction for the inner planets.

The final orbital architectures of the full (blue points) and synthetic simulations (gray points), including planets that underwent  $v/v_{esc} > 2$  collisions during the giant impact phase are shown in figure 5.14. Point sizes indicate the relative masses of planets, and red X's denote planets with a destructive collision in their accretion history. With the exception of two simulations, every synthetic system has a potentially destroyed planet within the

inner  $\sim 10$  or so days in orbital period. Unlike the full simulations, however, it is often not the innermost planet that undergoes a destructive collision. Instead, a much wider range of planets in the inner 20 days of the disk experience a destruction event. We attribute this difference to the much more immediate and widespread group of giant impacts that occur for  $P < 20$  d in the synthetic case (see figure 5.11). Regardless of this difference, both sets of simulations should be expected to destroy or erode the innermost planets in most cases, although the region of destruction is a little bit narrower for the simulations followed from planetesimals.

### 5.5.2 Matching Occurrence Rates With Kepler Planets

Having a much larger sample of simulated planets from the synthetic simulations opens up the possibility of making some statistical comparisons with observed occurrence rates. [140] performed an analysis of 2,025 planet candidates from the California Kepler Survey and found a turnover in the orbital occurrence rate for super-Earths around 6.5 days. This turnover was only very weakly present for sub-Neptune planets, and was found to be entirely absent for sub-Saturns and Jupiters.

In figure 5.15 we show the occurrence rates of planets from the synthetic simulations as a function of orbital period, in bins of 0.25 dex. Alongside the synthetic occurrence rates are the super-Earth occurrence rates measured by [140]. Beyond about 10 days, the two distributions match up remarkably well. Although we do not perform a full MCMC analysis as [140] does, it appears likely that the turnover in the synthetic simulations lies slightly further out than 6.5 days. Both the inferred initial solid surface density distribution of the CKS sample (see figure 2 of [35]), along with the solid surface density distribution of our synthetic planets follow a single power law all the way to the shortest-period planets. This suggests that the steeper slope seen for the synthetic occurrence rate must be due to a difference in the way protoplanets consolidate in the inner disk.

Regardless of what drives the difference in the short period occurrence rate, the observed turnover at 6.5 days was postulated by [140] to be a sign of in-situ formation. [96] found

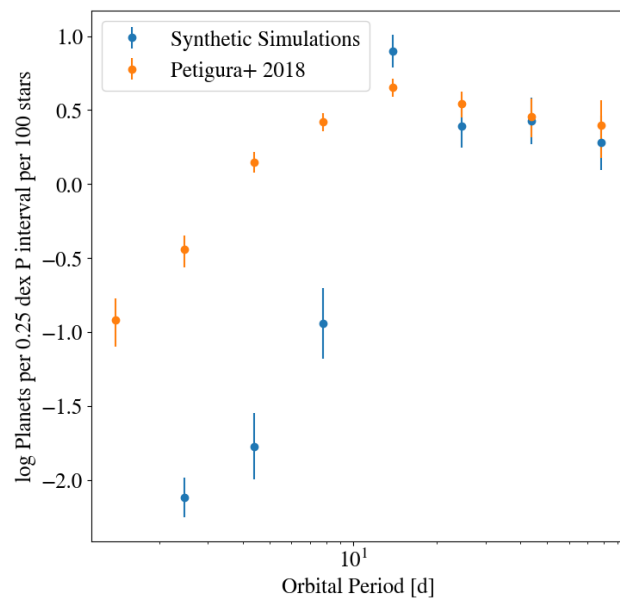


Figure 5.15: Occurrence rates of planets as a function of orbital period in 0.25 dex logarithmic bins. The occurrence rate measured from our synthetic simulations is shown in blue and the occurrence rate measured from planet candidates in the California Kepler Survey [140] is shown in orange.

that the turnover in the period occurrence rates of Kepler planets could be reproduced by assuming that in-situ formation distributed planets randomly throughout the disk and then truncating the disks at the location of the stellar co-rotation radius. Our results in figure 5.15, however, show that this cannot be the case. In all of our simulations, the disk is truncated at 1 day, but the turnover is closer to 10 days. This is a sign that even with an in-situ model, the connection between the solid surface density profile and the final orbital configuration is more nuanced. Furthermore, [15] found that the magnetospheric truncation radius should lie closer to 3 days and should not vary with the type of host star.

Lastly, the observed turnover period for super-Earths is found to be dependent on the metallicity of the host star (see figure 9a of [140]). Assuming that stellar metallicity is broadly correlated with the bulk densities of the planet-building material, this suggests that fluffier planetesimals should move the turnover in occurrence rate to longer orbital periods. Given that the collision cross sections were artificially enhanced in our planetesimal accretion simulations, one would expect that the simulated location of the turnover should move further out. If this is the case, it also suggests that the boundary between oligarchic and non-oligarchic accretion seen by (Wallace + Quinn 2023) may play a role in producing the turnover in the observed super-Earth occurrence rate and is therefore another piece of evidence to suggest that in-situ formation may be the primary pathway to build these compact multi-planet systems.

## **5.6 Summary and Discussion**

In this work, we have presented the first-ever N-body simulations that directly follow the planet formation process from the smallest gravitationally bound bodies (planetesimals) up to super-Earth sized planets using a disk wide enough to produce an entire terrestrial system. There are no tidal interactions with the gas disk and the final positions of the planets are set entirely by gravitational scattering and collision events, so the formation mechanism is largely in-situ. Because aerodynamic gas drag is the only dissipative force present, there is no large-scale inward migration of volatile-rich material. Despite this, some mass from

the outer disk does manage to eventually incorporate itself into the innermost planets. In contrast, planet formation models that invoke convergent migration tend to produce some purely refractory worlds at the inner edge of the disk, even in cases where the resulting resonant chains eventually destabilize [145].

We also compare the outcome of our simulations to a set of planet formation simulations that use a more typical and computationally inexpensive set of initial conditions which skip the planetesimal accretion phase and begin with a set of fully-formed planetary embryos [147, 144, 62]. In this case, the instability which gives rise to the giant impact phase occurs in an inside-out fashion and tends to produce a less radially concentrated set of planets. We attribute this difference to the fact that the protoplanet distribution in our fully simulations does not follow the ‘isolation mass’ in the inner disk, where the conditions for oligarchic growth are not met. In addition to more centrally concentrating the solid mass, the self-consistent initial conditions result in much more violent collisions in the inner disk that have the potential to either completely destroy or strip the mantle off [110] of the innermost planets.

Furthermore, the simulated planetary systems presented in this work bear some striking similarities to the compact multiplanet systems observed by Kepler. To facilitate a statistical comparison, we train a neural network to produce a set of initial conditions consistent with outcome of our short-period planetesimal accretion simulations (see Wallace + Quinn 2023). These are then used to run a much larger set of simulations that follow evolution through the giant impact phase to construct a fully-formed collection of planets. From these results, we measure the occurrence rate of planets as a function of orbital period and find a turnover in the distribution around 10 days. This is only slightly larger than the turnover measured for super-Earths in the California Kepler Survey ( $6.5^{+1.6}_{-1.2}$  d) [140] and is a promising sign that in-situ formation might be the dominant pathway for forming compact multiplanet systems.

Although the turnover location of the occurrence rate for the CKS planets appears to be statistically different than the one seen in our simulations, the difference may be reconcilable. [140] also found a negative correlation between host star metallicity and turnover

period. Given that the densities of our simulated bodies are artificially reduced during the planetesimal accretion phase (to inflate the collision cross sections), it is not surprising that the turnover location would be shifted outward. The complicated connection between the distribution of planetesimals and embryos before the giant impact phase and the resulting short-period planetary system, however, make it difficult to determine how the turnover location should move had we started with realistic-sized planetesimals.

In any case, the large distance between the inner disk edge and the turnover location highlights an important feature of in-situ formation. Although the properties of the final planets broadly reflect the initial local reservoir of solids, it is clear that the state of a much larger section of the planet-forming disk must taken into account. The final planet occurrence rate does not simply mirror the initial solid surface density profile, which is often assumed to be the case when in-situ formation is invoked (see [28, 35]). Furthermore, material from the most distant parts of the disk can still incorporate itself into the innermost planets.

## BIBLIOGRAPHY

- [1] I. Adachi, C. Hayashi, and K. Nakazawa. The gas drag effect on the elliptical motion of a solid body in the primordial solar nebula. *Progress of Theoretical Physics*, 56:1756–1771, December 1976.
- [2] C. B. Agnor, R. M. Canup, and H. F. Levison. On the Character and Consequences of Large Impacts in the Late Stage of Terrestrial Planet Formation. *Icarus*, 142:219–237, November 1999.
- [3] Eric Agol, Caroline Dorn, Simon L. Grimm, Martin Turbet, Elsa Ducrot, Laetitia Delrez, Michaël Gillon, Brice-Olivier Demory, Artem Burdanov, Khalid Barkaoui, Zouhair Benkhaldoun, Emeline Bolmont, Adam Burgasser, Sean Carey, Julien de Wit, Daniel Fabrycky, Daniel Foreman-Mackey, Jonas Haldemann, David M. Hernandez, James Ingalls, Emmanuel Jehin, Zachary Langford, Jérémie Leconte, Susan M. Lederer, Rodrigo Luger, Renu Malhotra, Victoria S. Meadows, Brett M. Morris, Francisco J. Pozuelos, Didier Queloz, Sean N. Raymond, Franck Selsis, Marko Sestovic, Amaury H. M. J. Triaud, and Valerie Van Grootel. Refining the Transit-timing and Photometric Analysis of TRAPPIST-1: Masses, Radii, Densities, Dynamics, and Ephemerides. *PSJ*, 2(1):1, February 2021.
- [4] Y. Alibert, C. Mordasini, W. Benz, and C. Winisdoerffer. Models of giant planet formation with migration and disc evolution. *A&A*, 434(1):343–353, Apr 2005.
- [5] ALMA Partnership, C. L. Brogan, L. M. Pérez, T. R. Hunter, W. R. F. Dent, A. S. Hales, R. E. Hills, S. Corder, E. B. Fomalont, C. Vlahakis, Y. Asaki, D. Barkats, A. Hirota, J. A. Hodge, C. M. V. Impellizzeri, R. Kneissl, E. Liuzzo, R. Lucas, N. Marcelino, S. Matsushita, K. Nakanishi, N. Phillips, A. M. S. Richards, I. Toledo, R. Aladro, D. Broguiere, J. R. Cortes, P. C. Cortes, D. Espada, F. Galarza, D. Garcia-Appadoo, L. Guzman-Ramirez, E. M. Humphreys, T. Jung, S. Kamenó, R. A. Laing, S. Leon, G. Marconi, A. Mignano, B. Nikolic, L. A. Nyman, M. Radiszcz, A. Remijan, J. A. Rodón, T. Sawada, S. Takahashi, R. P. J. Tilanus, B. Vila Vilaro, L. C. Watson, T. Wiklind, E. Akiyama, E. Chapillon, I. de Gregorio-Monsalvo, J. Di Francesco, F. Gueth, A. Kawamura, C. F. Lee, Q. Nguyen Luong, J. Mangum, V. Pietu, P. Sanhueza, K. Saigo, S. Takakuwa, C. Ubach, T. van Kempen, A. Wootten, A. Castro-Carrizo, H. Francke, J. Gallardo, J. Garcia, S. Gonzalez, T. Hill, T. Kaminski, Y. Kurono, H. Y. Liu, C. Lopez, F. Morales, K. Plarre, G. Schieven, L. Testi, L. Videla,

- E. Villard, P. Andreani, J. E. Hibbard, and K. Tatematsu. The 2014 ALMA Long Baseline Campaign: First Results from High Angular Resolution Observations toward the HL Tau Region. *ApJ*, 808:L3, Jul 2015.
- [6] Sean M. Andrews, David J. Wilner, Zhaojuan Zhu, Tilman Birnstiel, John M. Carpenter, Laura M. Pérez, Xue-Ning Bai, Karin I. Öberg, A. Meredith Hughes, Andrea Isella, and Luca Ricci. Ringed Substructure and a Gap at 1 au in the Nearest Protoplanetary Disk. *ApJ*, 820:L40, Apr 2016.
  - [7] P. J. Armitage. *Astrophysics of Planet Formation*. October 2013.
  - [8] J. C. Augereau, R. P. Nelson, A. M. Lagrange, J. C. B. Papaloizou, and D. Mouillet. Dynamical modeling of large scale asymmetries in the beta Pictoris dust disk. *A&A*, 370:447–455, May 2001.
  - [9] Ben A. Ayliffe and Matthew R. Bate. Planet migration: self-gravitating radiation hydrodynamical models of protoplanets with surfaces. *MNRAS*, 408:876–896, October 2010.
  - [10] Elizabeth Bailey and Konstantin Batygin. The Hot Jupiter Period-Mass Distribution as a Signature of in situ Formation. *ApJL*, 866(1):L2, Oct 2018.
  - [11] Isabelle Baraffe, Derek Homeier, France Allard, and Gilles Chabrier. New evolutionary models for pre-main sequence and main sequence low-mass stars down to the hydrogen-burning limit. *A&A*, 577:A42, May 2015.
  - [12] Josh Barnes and Piet Hut. A hierarchical  $O(N \log N)$  force-calculation algorithm. *Nature*, 324(6096):446–449, Dec 1986.
  - [13] R. Barnes, T. R. Quinn, J. J. Lissauer, and D. C. Richardson. N-Body simulations of growth from 1 km planetesimals at 0.4 AU. *Icarus*, 203:626–643, October 2009.
  - [14] C. Baruteau, A. Crida, S. J. Paardekooper, F. Masset, J. Guilet, B. Bitsch, R. Nelson, W. Kley, and J. Papaloizou. Planet-Disk Interactions and Early Evolution of Planetary Systems. In Henrik Beuther, Ralf S. Klessen, Cornelis P. Dullemond, and Thomas Henning, editors, *Protostars and Planets VI*, page 667, Jan 2014.
  - [15] Konstantin Batygin and Antoine C. Petit. Dissipative Capture of Planets into First-order Mean-motion Resonances. *ApJL*, 946(1):L11, March 2023.
  - [16] B. Bitsch, A. Crida, A. Morbidelli, W. Kley, and I. Dobbs-Dixon. Stellar irradiated discs and implications on migration of embedded planets. I. Equilibrium discs. *A&A*, 549:A124, January 2013.

- [17] A. C. Boley. On the Origin of Banded Structure in Dusty Protoplanetary Disks: HL Tau and TW Hya. *ApJ*, 850:103, November 2017.
- [18] William J. Borucki, David Koch, Gibor Basri, Natalie Batalha, Timothy Brown, Douglas Caldwell, John Caldwell, Jørgen Christensen-Dalsgaard, William D. Cochran, Edna DeVore, Edward W. Dunham, Andrea K. Dupree, Thomas N. Gautier, John C. Geary, Ronald Gilliland, Alan Gould, Steve B. Howell, Jon M. Jenkins, Yoji Kondo, David W. Latham, Geoffrey W. Marcy, Søren Meibom, Hans Kjeldsen, Jack J. Lissauer, David G. Monet, David Morrison, Dimitar Sasselov, Jill Tarter, Alan Boss, Don Brownlee, Toby Owen, Derek Buzasi, David Charbonneau, Laurance Doyle, Jonathan Fortney, Eric B. Ford, Matthew J. Holman, Sara Seager, Jason H. Steffen, William F. Welsh, Jason Rowe, Howard Anderson, Lars Buchhave, David Ciardi, Lucianne Walkowicz, William Sherry, Elliott Horch, Howard Isaacson, Mark E. Everett, Debra Fischer, Guillermo Torres, John Asher Johnson, Michael Endl, Phillip MacQueen, Stephen T. Bryson, Jessie Dotson, Michael Haas, Jeffrey Kolodziejczak, Jeffrey Van Cleve, Hema Chandrasekaran, Joseph D. Twicken, Elisa V. Quintana, Bruce D. Clarke, Christopher Allen, Jie Li, Haley Wu, Peter Tenenbaum, Ekaterina Verner, Frederick Bruhweiler, Jason Barnes, and Andrej Prsa. Kepler Planet-Detection Mission: Introduction and First Results. *Science*, 327(5968):977, February 2010.
- [19] W. F. Bottke, D. D. Durda, D. Nesvorný, R. Jedicke, A. Morbidelli, D. Vokrouhlický, and H. Levison. The fossilized size distribution of the main asteroid belt. *Icarus*, 175:111–140, May 2005.
- [20] Adrián Brunini, Pablo J. Santamaría, Héctor R. Viturro, and Rodolfo G. Cionco. On the number of particles in N-body simulations of planet disk interaction. *Planetary and Space Science*, 55:2121–2127, November 2007.
- [21] J. E. Chambers. A hybrid symplectic integrator that permits close encounters between massive bodies. *MNRAS*, 304(4):793–799, April 1999.
- [22] J. E. Chambers. Making More Terrestrial Planets. *Icarus*, 152:205–224, August 2001.
- [23] J. E. Chambers. Planetesimal formation by turbulent concentration. *Icarus*, 208:505–517, August 2010.
- [24] J. E. Chambers and G. W. Wetherill. Making the Terrestrial Planets: N-Body Integrations of Planetary Embryos in Three Dimensions. *Icarus*, 136:304–327, December 1998.
- [25] J. E. Chambers, G. W. Wetherill, and A. P. Boss. The Stability of Multi-Planet Systems. *Icarus*, 119(2):261–268, February 1996.

- [26] S. Chandrasekhar. Dynamical Friction. I. General Considerations: the Coefficient of Dynamical Friction. *ApJ*, 97:255, March 1943.
- [27] Subrahmanyan Chandrasekhar. *Principles of stellar dynamics*. 1960.
- [28] Eugene Chiang and Gregory Laughlin. The minimum-mass extrasolar nebula: in situ formation of close-in super-Earths. *MNRAS*, 431(4):3444–3455, June 2013.
- [29] Lucas A. Cieza, Simon Casassus, John Tobin, Steven P. Bos, Jonathan P. Williams, Sebastian Perez, Zhaohuan Zhu, Claudio Caceres, Hector Canovas, Michael M. Dunham, Antonio Hales, Jose L. Prieto, David A. Principe, Matthias R. Schreiber, Dary Ruiz-Rodriguez, and Alice Zurlo. Imaging the water snow-line during a protostellar outburst. *Nature*, 535:258–261, Jul 2016.
- [30] R. G. Cionco and A. Brunini. Orbital migrations in planetesimal discs: N-body simulations and the resonant dynamical friction. *MNRAS*, 334:77–86, July 2002.
- [31] Miles Cranmer, Daniel Tamayo, Hanno Rein, Peter Battaglia, Samuel Hadden, Philip J. Armitage, Shirley Ho, and David N. Spergel. A Bayesian neural network predicts the dissolution of compact planetary systems. *Proceedings of the National Academy of Science*, 118(40):e2026053118, October 2021.
- [32] P. Cresswell and R. P. Nelson. On the evolution of multiple protoplanets embedded in a protostellar disc. *A&A*, 450(2):833–853, May 2006.
- [33] J. N. Cuzzi, R. C. Hogan, and W. F. Bottke. Towards initial mass functions for asteroids and Kuiper Belt Objects. *Icarus*, 208:518–538, August 2010.
- [34] J. N. Cuzzi, R. C. Hogan, and K. Shariff. Toward Planetesimals: Dense Chondrule Clumps in the Protoplanetary Nebula. *ApJ*, 687:1432–1447, November 2008.
- [35] Fei Dai, Joshua N. Winn, Kevin Schlaufman, Songhu Wang, Lauren Weiss, Erik A. Petigura, Andrew W. Howard, and Min Fang. California-Kepler Survey. IX. Revisiting the Minimum-mass Extrasolar Nebula with Precise Stellar Parameters. *AJ*, 159(6):247, June 2020.
- [36] Katherine M. Deck, Matthew J. Holman, Eric Agol, Joshua A. Carter, Jack J. Lissauer, Darin Ragozzine, and Joshua N. Winn. Rapid Dynamical Chaos in an Exoplanetary System. *ApJL*, 755(1):L21, August 2012.
- [37] Stanley F. Dermott, Renu Malhotra, and Carl D. Murray. Dynamics of the Uranian and Saturnian satellite systems: A chaotic route to melting Miranda? *Icarus*, 76(2):295–334, Nov 1988.

- [38] M. Dia, E. Savary, M. Melchior, and F. Courbin. Galaxy Image Simulation Using Progressive GANs. In R. Pizzo, E. R. Deul, J. D. Mol, J. de Plaa, and H. Verkouter, editors, *Astronomical Data Analysis Software and Systems XXIX*, volume 527 of *Astronomical Society of the Pacific Conference Series*, page 175, January 2020.
- [39] Giovanni Dipierro, Daniel Price, Guillaume Laibe, Kieran Hirsh, Alice Cerioli, and Giuseppe Lodato. On planet formation in HL Tau. *MNRAS*, 453:L73–L77, Oct 2015.
- [40] Jack Dobinson, Zoë M. Leinhardt, Sarah E. Dodson-Robinson, and Nick A. Teanby. Hiding in the Shadows: Searching for Planets in Pre-transitional and Transitional Disks. *ApJ*, 777:L31, Nov 2013.
- [41] Jack Dobinson, Zoë M. Leinhardt, Stefan Lines, Philip J. Carter, Sarah E. Dodson-Robinson, and Nick A. Teanby. Hiding in the Shadows. II. Collisional Dust as Exoplanet Markers. *ApJ*, 820:29, Mar 2016.
- [42] T. M. Donahue, J. H. Hoffman, R. R. Hodges, and A. J. Watson. Venus was wet - A measurement of the ratio of deuterium to hydrogen. *Science*, 216:630–633, May 1982.
- [43] Ruobing Dong, Shengtai Li, Eugene Chiang, and Hui Li. Multiple Disk Gaps and Rings Generated by a Single Super-Earth. II. Spacings, Depths, and Number of Gaps, with Application to Real Systems. *ApJ*, 866(2):110, October 2018.
- [44] M. Duncan, T. Quinn, and S. Tremaine. The long-term evolution of orbits in the solar system - A mapping approach. *Icarus*, 82:402–418, December 1989.
- [45] Elad Dvash, Yam Peleg, Shay Zucker, and Raja Giryes. Shallow Transits-Deep Learning. II. Identify Individual Exoplanetary Transits in Red Noise using Deep Learning. *AJ*, 163(5):237, May 2022.
- [46] Daniel C. Fabrycky, Jack J. Lissauer, Darin Ragozzine, Jason F. Rowe, Jason H. Steffen, Eric Agol, Thomas Barclay, Natalie Batalha, William Borucki, and David R. Ciardi. Architecture of Kepler’s Multi-transiting Systems. II. New Investigations with Twice as Many Candidates. *ApJ*, 790(2):146, Aug 2014.
- [47] Julia Fang and Jean-Luc Margot. Architecture of Planetary Systems Based on Kepler Data: Number of Planets and Coplanarity. *ApJ*, 761(2):92, Dec 2012.
- [48] P. Garaud, F. Meru, M. Galvagni, and C. Olczak. From Dust to Planetesimals: An Improved Model for Collisional Growth in Protoplanetary Disks. *ApJ*, 764:146, February 2013.

- [49] Andras Gaspar and George Rieke. New HST data and modeling reveal a massive planetesimal collision around Fomalhaut. *Proceedings of the National Academy of Science*, 117(18):9712–9722, April 2020.
- [50] Michaël Gillon, Emmanuël Jehin, Susan M. Lederer, Laetitia Delrez, Julien de Wit, Artem Burdanov, Valérie Van Grootel, Adam J. Burgasser, Amaury H. M. J. Triaud, Cyrielle Opitom, Brice-Olivier Demory, Devendra K. Sahu, Daniella Bardalez Gagliuffi, Pierre Magain, and Didier Queloz. Temperate Earth-sized planets transiting a nearby ultracool dwarf star. *Nature*, 533(7602):221–224, May 2016.
- [51] Michaël Gillon, Amaury H. M. J. Triaud, Brice-Olivier Demory, Emmanuël Jehin, Eric Agol, Katherine M. Deck, Susan M. Lederer, Julien de Wit, Artem Burdanov, James G. Ingalls, Emeline Bolmont, Jeremy Leconte, Sean N. Raymond, Franck Selsis, Martin Turbet, Khalid Barkaoui, Adam Burgasser, Matthew R. Burleigh, Sean J. Carey, Aleksander Chaushev, Chris M. Copperwheat, Laetitia Delrez, Catarina S. Fernandes, Daniel L. Holdsworth, Enrico J. Kotze, Valérie Van Grootel, Yaseen Almleaky, Zouhair Benkhaldoun, Pierre Magain, and Didier Queloz. Seven temperate terrestrial planets around the nearby ultracool dwarf star TRAPPIST-1. *Nature*, 542(7642):456–460, February 2017.
- [52] P. Goldreich and S. Tremaine. The excitation of density waves at the Lindblad and corotation resonances by an external potential. *ApJ*, 233:857–871, Nov 1979.
- [53] P. Goldreich and S. Tremaine. Disk-satellite interactions. *ApJ*, 241:425–441, Oct 1980.
- [54] P. Goldreich and W. R. Ward. The Formation of Planetesimals. *ApJ*, 183:1051–1062, August 1973.
- [55] Ian J. Goodfellow, Jean Pouget-Abadie, Mehdi Mirza, Bing Xu, David Warde-Farley, Sherjil Ozair, Aaron Courville, and Yoshua Bengio. Generative Adversarial Networks. *arXiv e-prints*, page arXiv:1406.2661, June 2014.
- [56] R. Greenberg, W. K. Hartmann, C. R. Chapman, and J. F. Wacker. Planetesimals to planets - Numerical simulation of collisional evolution. *Icarus*, 35:1–26, July 1978.
- [57] Simon L. Grimm and Joachim G. Stadel. The GENGA Code: Gravitational Encounters in N-body Simulations with GPU Acceleration. *ApJ*, 796(1):23, November 2014.
- [58] Simon L. Grimm, Joachim G. Stadel, Ramon Brasser, Matthias M. M. Meier, and Christoph Mordasini. GENGA. II. GPU Planetary N-body Simulations with Non-Newtonian Forces and High Number of Particles. *ApJ*, 932(2):124, June 2022.

- [59] Evgeni Grishin and Hagai B. Perets. Application of Gas Dynamical Friction for Planetesimals. I. Evolution of Single Planetesimals. *ApJ*, 811:54, Sep 2015.
- [60] Ishaan Gulrajani, Faruk Ahmed, Martin Arjovsky, Vincent Dumoulin, and Aaron Courville. Improved Training of Wasserstein GANs. *arXiv e-prints*, page arXiv:1704.00028, March 2017.
- [61] Sam Hadden and Yoram Lithwick. Kepler Planet Masses and Eccentricities from TTV Analysis. *AJ*, 154(1):5, Jul 2017.
- [62] Brad M. S. Hansen and Norm Murray. Migration Then Assembly: Formation of Neptune-mass Planets inside 1 AU. *ApJ*, 751:158, June 2012.
- [63] C. Hayashi. Structure of the Solar Nebula, Growth and Decay of Magnetic Fields and Effects of Magnetic and Turbulent Viscosities on the Nebula. *Progress of Theoretical Physics Supplement*, 70:35–53, 1981.
- [64] P. F. Hopkins. Jumping the gap: the formation conditions and mass function of ‘pebble-pile’ planetesimals. *MNRAS*, 456:2383–2405, March 2016.
- [65] Jane Huang, Sean M. Andrews, Cornelis P. Dullemond, Andrea Isella, Laura M. Pérez, Viviana V. Guzmán, Karin I. Öberg, Zhaohuan Zhu, Shangjia Zhang, Xue-Ning Bai, Myriam Benisty, Tilman Birnstiel, John M. Carpenter, A. Meredith Hughes, Luca Ricci, Erik Weaver, and David J. Wilner. The Disk Substructures at High Angular Resolution Project (DSHARP). II. Characteristics of Annular Substructures. *ApJL*, 869(2):L42, December 2018.
- [66] S. Ida, E. Kokubo, and J. Makino. The Origin of Anisotropic Velocity Dispersion of Particles in a Disc Potential. *MNRAS*, 263:875, Aug 1993.
- [67] S. Ida and D. N. C. Lin. Toward a Deterministic Model of Planetary Formation. I. A Desert in the Mass and Semimajor Axis Distributions of Extrasolar Planets. *ApJ*, 604(1):388–413, Mar 2004.
- [68] S. Ida and J. Makino. Scattering of planetesimals by a protoplanet - Slowing down of runaway growth. *Icarus*, 106:210, November 1993.
- [69] Shigeru Ida, Geoffrey Bryden, D. N. C. Lin, and Hidekazu Tanaka. Orbital Migration of Neptune and Orbital Distribution of Trans-Neptunian Objects. *ApJ*, 534(1):428–445, May 2000.

- [70] Shigeru Ida and Junichiro Makino. N-Body simulation of gravitational interaction between planetesimals and a protoplanet . I. velocity distribution of planetesimals. *Icarus*, 96:107–120, March 1992.
- [71] Satoshi Inaba, Hidekazu Tanaka, Kiyoshi Nakazawa, George W. Wetherill, and Eiichiro Kokubo. High-Accuracy Statistical Simulation of Planetary Accretion: II. Comparison with N-Body Simulation. *Icarus*, 149(1):235–250, Jan 2001.
- [72] Andrea Isella, Greta Guidi, Leonardo Testi, Shangfei Liu, Hui Li, Shengtai Li, Erik Weaver, Yann Boehler, John M. Carpenter, Itziar De Gregorio-Monsalvo, Carlo F. Manara, Antonella Natta, Laura M. Pérez, Luca Ricci, Anneila Sargent, Marco Tazzari, and Neal Turner. Ringed structures of the hd 163296 protoplanetary disk revealed by alma. *Phys. Rev. Lett.*, 117:251101, Dec 2016.
- [73] A. Izidoro, S. N. Raymond, A. Morbidelli, and O. C. Winter. Terrestrial planet formation constrained by Mars and the structure of the asteroid belt. *MNRAS*, 453:3619–3634, November 2015.
- [74] André Izidoro, Bertram Bitsch, Sean N. Raymond, Anders Johansen, Alessandro Morbidelli, Michiel Lambrechts, and Seth A. Jacobson. Formation of planetary systems by pebble accretion and migration. Hot super-Earth systems from breaking compact resonant chains. *A&A*, 650:A152, June 2021.
- [75] Andre Izidoro, Masahiro Ogihara, Sean N. Raymond, Alessandro Morbidelli, Arnaud Pierens, Bertram Bitsch, Christophe Cossou, and Franck Hersant. Breaking the chains: hot super-Earth systems from migration and disruption of compact resonant chains. *MNRAS*, 470(2):1750–1770, September 2017.
- [76] Yesukhei Jagvaral, François Lanusse, Sukhdeep Singh, Rachel Mandelbaum, Siamak Ravanbakhsh, and Duncan Campbell. Galaxies and haloes on graph neural networks: Deep generative modelling scalar and vector quantities for intrinsic alignment. *MNRAS*, 516(2):2406–2419, October 2022.
- [77] R. Jedicke, J. Larsen, and T. Spahr. *Observational Selection Effects in Asteroid Surveys*, pages 71–87. 2002.
- [78] Jeff Jennings, Richard A. Booth, Marco Tazzari, Giovanni P. Rosotti, and Cathie J. Clarke. Frankenstein: Protoplanetary disc brightness profile reconstruction at sub-beam resolution with a rapid Gaussian process. *arXiv e-prints*, page arXiv:2005.07709, May 2020.

- [79] P. Jetley, F. Gioachin, L. Mendes, C. Kale, and T. Quinn. Massively parallel cosmological simulations with ChaNGa. *Proceedings of IEEE International Parallel and Distributed Processing Symposium*, 2008.
- [80] A. Johansen, M.-M. Mac Low, P. Lacerda, and M. Bizzarro. Growth of asteroids, planetary embryos, and Kuiper belt objects by chondrule accretion. *Science Advances*, 1:1500109, April 2015.
- [81] A. Johansen, J. S. Oishi, M.-M. Mac Low, H. Klahr, T. Henning, and A. Youdin. Rapid planetesimal formation in turbulent circumstellar disks. *Nature*, 448:1022–1025, August 2007.
- [82] A. Kataoka, H. Tanaka, S. Okuzumi, and K. Wada. Fluffy dust forms icy planetesimals by static compression. *A&A*, 557:L4, September 2013.
- [83] Scott J. Kenyon and Benjamin C. Bromley. Terrestrial Planet Formation. I. The Transition from Oligarchic Growth to Chaotic Growth. *AJ*, 131(3):1837–1850, Mar 2006.
- [84] Diederik P. Kingma and Jimmy Ba. Adam: A Method for Stochastic Optimization. *arXiv e-prints*, page arXiv:1412.6980, December 2014.
- [85] David R. Kirsh, Martin Duncan, Ramon Brasser, and Harold F. Levison. Simulations of planet migration driven by planetesimal scattering. *Icarus*, 199(1):197–209, Jan 2009.
- [86] E. Kokubo and S. Ida. Orbital evolution of protoplanets embedded in a swarm of planetesimals. *Icarus*, 114:247–257, April 1995.
- [87] E. Kokubo and S. Ida. On Runaway Growth of Planetesimals. *Icarus*, 123:180–191, September 1996.
- [88] E. Kokubo and S. Ida. Oligarchic Growth of Protoplanets. *Icarus*, 131:171–178, January 1998.
- [89] E. Kokubo and S. Ida. Formation of Protoplanet Systems and Diversity of Planetary Systems. *ApJ*, 581:666–680, December 2002.
- [90] E. Kokubo and S. Ida. Dynamics and accretion of planetesimals. *Progress of Theoretical and Experimental Physics*, 2012(1):01A308, October 2012.

- [91] Eiichiro Kokubo and Shigeru Ida. Formation of Protoplanets from Planetesimals in the Solar Nebula. *Icarus*, 143:15–27, January 2000.
- [92] J. Laskar. Large scale chaos and the spacing of the inner planets. *A&A*, 317:L75–L78, January 1997.
- [93] Jacques Laskar. Large Scale Chaos and Marginal Stability in the Solar System. *Celestial Mechanics and Dynamical Astronomy*, 64(1-2):115–162, March 1996.
- [94] David W. Latham, Jason F. Rowe, Samuel N. Quinn, Natalie M. Batalha, William J. Borucki, Timothy M. Brown, Stephen T. Bryson, Lars A. Buchhave, Douglas A. Caldwell, Joshua A. Carter, Jessie L. Christiansen, David R. Ciardi, William D. Cochran, Edward W. Dunham, Daniel C. Fabrycky, Eric B. Ford, III Gautier, Thomas N., Ronald L. Gilliland, Matthew J. Holman, Steve B. Howell, Khadeejah A. Ibrahim, Howard Isaacson, Jon M. Jenkins, David G. Koch, Jack J. Lissauer, Geoffrey W. Marcy, Elisa V. Quintana, Darin Ragozzine, Dimitar Sasselov, Avi Shporer, Jason H. Steffen, William F. Welsh, and Bill Wohler. A First Comparison of Kepler Planet Candidates in Single and Multiple Systems. *ApJL*, 732(2):L24, May 2011.
- [95] M. Lecar and S. J. Aarseth. A numerical simulation of the formation of the terrestrial planets. *ApJ*, 305:564–579, June 1986.
- [96] Eve J. Lee and Eugene Chiang. Magnetospheric Truncation, Tidal Inspiral, and the Creation of Short-period and Ultra-short-period Planets. *ApJ*, 842(1):40, June 2017.
- [97] Z. M. Leinhardt. Terrestrial Planet Formation: A Review and Current Directions. In D. Fischer, F. A. Rasio, S. E. Thorsett, and A. Wolszczan, editors, *Extreme Solar Systems*, volume 398 of *Astronomical Society of the Pacific Conference Series*, page 225, 2008.
- [98] Z. M. Leinhardt and D. C. Richardson. Planetesimals to Protoplanets. I. Effect of Fragmentation on Terrestrial Planet Formation. *ApJ*, 625:427–440, May 2005.
- [99] Zoë M. Leinhardt, Jack Dobinson, Philip J. Carter, and Stefan Lines. Numerically Predicted Indirect Signatures of Terrestrial Planet Formation. *ApJ*, 806:23, June 2015.
- [100] H. F. Levison, M. J. Duncan, and E. Thommes. A Lagrangian Integrator for Planetary Accretion and Dynamics (LIPAD). *AJ*, 144:119, October 2012.
- [101] Harold F. Levison and Craig Agnor. The Role of Giant Planets in Terrestrial Planet Formation. *AJ*, 125(5):2692–2713, May 2003.

- [102] Jack J. Lissauer. Planet formation. *ARA&A*, 31:129–174, January 1993.
- [103] Jack J. Lissauer, Daniel Jontof-Hutter, Jason F. Rowe, Daniel C. Fabrycky, Eric D. Lopez, Eric Agol, Geoffrey W. Marcy, Katherine M. Deck, Debra A. Fischer, Jonathan J. Fortney, Steve B. Howell, Howard Isaacson, Jon M. Jenkins, Rea Kolbl, Dimitar Sasselov, Donald R. Short, and William F. Welsh. All Six Planets Known to Orbit Kepler-11 Have Low Densities. *ApJ*, 770(2):131, June 2013.
- [104] Jack J. Lissauer, Geoffrey W. Marcy, Stephen T. Bryson, Jason F. Rowe, Daniel Jontof-Hutter, Eric Agol, William J. Borucki, Joshua A. Carter, Eric B. Ford, Ronald L. Gilliland, Rea Kolbl, Kimberly M. Star, Jason H. Steffen, and Guillermo Torres. Validation of Kepler’s Multiple Planet Candidates. II. Refined Statistical Framework and Descriptions of Systems of Special Interest. *ApJ*, 784(1):44, March 2014.
- [105] Jack J. Lissauer, Geoffrey W. Marcy, Jason F. Rowe, Stephen T. Bryson, Elisabeth Adams, Lars A. Buchhave, David R. Ciardi, William D. Cochran, Daniel C. Fabrycky, Eric B. Ford, Francois Fressin, John Geary, Ronald L. Gilliland, Matthew J. Holman, Steve B. Howell, Jon M. Jenkins, Karen Kinemuchi, David G. Koch, Robert C. Morehead, Darin Ragozzine, Shawn E. Seader, Peter G. Tanenbaum, Guillermo Torres, and Joseph D. Twicken. Almost All of Kepler’s Multiple-planet Candidates Are Planets. *ApJ*, 750(2):112, May 2012.
- [106] Jack J. Lissauer, Darin Ragozzine, Daniel C. Fabrycky, Jason H. Steffen, Eric B. Ford, Jon M. Jenkins, Avi Shporer, Matthew J. Holman, Jason F. Rowe, Elisa V. Quintana, Natalie M. Batalha, William J. Borucki, Stephen T. Bryson, Douglas A. Caldwell, Joshua A. Carter, David Ciardi, Edward W. Dunham, Jonathan J. Fortney, III Gautier, Thomas N., Steve B. Howell, David G. Koch, David W. Latham, Geoffrey W. Marcy, Robert C. Morehead, and Dimitar Sasselov. Architecture and Dynamics of Kepler’s Candidate Multiple Transiting Planet Systems. *ApJS*, 197(1):8, November 2011.
- [107] Y. Lithwick. After Runaway: The Trans-Hill Stage of Planetesimal Growth. *ApJ*, 780:22, January 2014.
- [108] D. Lynden-Bell and A. J. Kalnajs. On the generating mechanism of spiral structure. *MNRAS*, 157:1, January 1972.
- [109] Renu Malhotra. Nonlinear resonances in the solar system. *Physica D Nonlinear Phenomena*, 77(1-3):289–304, October 1994.
- [110] Robert A. Marcus, Sarah T. Stewart, Dimitar Sasselov, and Lars Hernquist. Collisional Stripping and Disruption of Super-Earths. *ApJL*, 700(2):L118–L122, August 2009.

- [111] J. P. McMullin, B. Waters, D. Schiebel, W. Young, and K. Golap. CASA Architecture and Applications. In R. A. Shaw, F. Hill, and D. J. Bell, editors, *Astronomical Data Analysis Software and Systems XVI*, volume 376 of *Astronomical Society of the Pacific Conference Series*, page 127, October 2007.
- [112] Carl Melis, B. Zuckerman, Joseph H. Rhee, Inseok Song, Simon J. Murphy, and Michael S. Bessell. Rapid disappearance of a warm, dusty circumstellar disk. *Nature*, 487(7405):74–76, July 2012.
- [113] H. Menon, L. Wesolowski, and G. et al. Zheng. Adaptive Techniques for Clustered N-Body Cosmological Simulations. *Computational Astrophysics and Cosmology*, 2:1, 2015.
- [114] Michael R. Meyer, Nuria Calvet, and Lynne A. Hillenbrand. Intrinsic Near-Infrared Excesses of T Tauri Stars: Understanding the Classical T Tauri Star Locus. *AJ*, 114:288–300, July 1997.
- [115] Y. Miguel, O. M. Guilera, and A. Brunini. The diversity of planetary system architectures: contrasting theory with observations. *MNRAS*, 417(1):314–332, Oct 2011.
- [116] Sarah Millholland, Songhu Wang, and Gregory Laughlin. Kepler Multi-planet Systems Exhibit Unexpected Intra-system Uniformity in Mass and Radius. *ApJL*, 849(2):L33, Nov 2017.
- [117] Sarah C. Millholland and Joshua N. Winn. Split Peas in a Pod: Intra-system Uniformity of Super-Earths and Sub-Neptunes. *ApJL*, 920(2):L34, October 2021.
- [118] Sean Mills, Daniel C. Fabrycky, Cezary Migaszewski, Eric B. Ford, Erik Petigura, and Howard T. Isaacson. Kepler-223: A Resonant Chain of Four Transiting, Sub-Neptune Planets. In *AAS/Division of Dynamical Astronomy Meeting #47*, volume 47 of *AAS/Division of Dynamical Astronomy Meeting*, page 101.03, May 2016.
- [119] A. Morbidelli, W. F. Bottke, D. Nesvorný, and H. F. Levison. Asteroids were born big. *Icarus*, 204:558–573, December 2009.
- [120] A. Morbidelli, J. I. Lunine, D. P. O’Brien, S. N. Raymond, and K. J. Walsh. Building Terrestrial Planets. *Annual Review of Earth and Planetary Sciences*, 40:251–275, May 2012.
- [121] R. Morishima. A particle-based hybrid code for planet formation. *Icarus*, 260:368–395, November 2015.

- [122] R. Morishima. Onset of oligarchic growth and implication for accretion histories of dwarf planets. *Icarus*, 281:459–475, January 2017.
- [123] R. Morishima, J. Stadel, and B. Moore. From planetesimals to terrestrial planets: N-body simulations including the effects of nebular gas and giant planets. *Icarus*, 207:517–535, June 2010.
- [124] Gijs D. Mulders, Ilaria Pascucci, Dániel Apai, and Fred J. Ciesla. The Exoplanet Population Observation Simulator. I. The Inner Edges of Planetary Systems. *AJ*, 156(1):24, July 2018.
- [125] C. D. Murray and S. F. Dermott. *Solar system dynamics*. 1999.
- [126] C. D. Murray and S. F. Dermott. *Solar System Dynamics*. February 2000.
- [127] C. D. Murray and S. F. Dermott. *Solar System Dynamics*. February 2000.
- [128] R. A. Murray-Clay and E. I. Chiang. Brownian Motion in Planetary Migration. *ApJ*, 651:1194–1208, November 2006.
- [129] Y. Nakagawa, M. Sekiya, and C. Hayashi. Settling and growth of dust particles in a laminar phase of a low-mass solar nebula. *Icarus*, 67:375–390, September 1986.
- [130] Erika R. Nesvold and Marc J. Kuchner. Gap Clearing by Planets in a Collisional Debris Disk. *ApJ*, 798:83, Jan 2015.
- [131] D. P. O’Brien, A. Morbidelli, and H. F. Levison. Terrestrial planet formation with strong dynamical friction. *Icarus*, 184:39–58, September 2006.
- [132] Masahiro Ogiara, Eiichiro Kokubo, Takeru K. Suzuki, and Alessandro Morbidelli. Formation of close-in super-Earths in evolving protoplanetary disks due to disk winds. *A&A*, 615:A63, July 2018.
- [133] K. Ohtsuki, G. R. Stewart, and S. Ida. Evolution of Planetesimal Velocities Based on Three-Body Orbital Integrations and Growth of Protoplanets. *Icarus*, 155:436–453, February 2002.
- [134] S. Okuzumi, H. Tanaka, H. Kobayashi, and K. Wada. Rapid Coagulation of Porous Dust Aggregates outside the Snow Line: A Pathway to Successful Icy Planetesimal Formation. *ApJ*, 752:106, June 2012.

- [135] C. W. Ormel, C. P. Dullemond, and M. Spaans. Accretion among preplanetary bodies: The many faces of runaway growth. *Icarus*, 210:507–538, November 2010.
- [136] S. J. Peale. Orbital resonance in the solar system. *ARA&A*, 14:215–246, January 1976.
- [137] Tim D. Pearce and Mark C. Wyatt. Dynamical evolution of an eccentric planet and a less massive debris disc. *MNRAS*, 443:2541–2560, Sep 2014.
- [138] Tim D. Pearce, Mark C. Wyatt, and Grant M. Kennedy. Constraining the orbits of sub-stellar companions imaged over short orbital arcs. *MNRAS*, 448:3679–3688, Apr 2015.
- [139] Laura M. Pérez, John M. Carpenter, Sean M. Andrews, Luca Ricci, Andrea Isella, Hendrik Linz, Anneila I. Sargent, David J. Wilner, Thomas Henning, Adam T. Deller, Claire J. Chandler, Cornelis P. Dullemond, Joseph Lazio, Karl M. Menten, Stuart A. Corder, Shaye Storm, Leonardo Testi, Marco Tazzari, Woojin Kwon, Nuria Calvet, Jane S. Greaves, Robert J. Harris, and Lee G. Mundy. Spiral density waves in a young protoplanetary disk. *Science*, 353:1519–1521, Sep 2016.
- [140] Erik A. Petigura, Geoffrey W. Marcy, Joshua N. Winn, Lauren M. Weiss, Benjamin J. Fulton, Andrew W. Howard, Evan Sinukoff, Howard Isaacson, Timothy D. Morton, and John Asher Johnson. The California-Kepler Survey. IV. Metal-rich Stars Host a Greater Diversity of Planets. *AJ*, 155(2):89, February 2018.
- [141] Andrew Pontzen, Rok Roškar, Greg Stinson, and Rory Woods. pynbody: N-Body/SPH analysis for python. Astrophysics Source Code Library, May 2013.
- [142] R. R. Rafikov. Dynamical Evolution of Planetesimals in Protoplanetary Disks. *AJ*, 126:2529–2548, November 2003.
- [143] S. N. Raymond, D. P. O’Brien, A. Morbidelli, and N. A. Kaib. Building the terrestrial planets: Constrained accretion in the inner Solar System. *Icarus*, 203:644–662, October 2009.
- [144] S. N. Raymond, T. Quinn, and J. I. Lunine. High-resolution simulations of the final assembly of Earth-like planets I. Terrestrial accretion and dynamics. *Icarus*, 183:265–282, August 2006.
- [145] Sean N. Raymond, Thibault Boulet, Andre Izidoro, Leandro Esteves, and Bertram Bitsch. Migration-driven diversity of super-Earth compositions. *MNRAS*, 479(1):L81–L85, September 2018.

- [146] Sean N. Raymond, Thomas Quinn, and Jonathan I. Lunine. Making other earths: dynamical simulations of terrestrial planet formation and water delivery. *Icarus*, 168:1–17, March 2004.
- [147] Sean N. Raymond, Thomas Quinn, and Jonathan I. Lunine. Terrestrial Planet Formation in Disks with Varying Surface Density Profiles. *ApJ*, 632(1):670–676, October 2005.
- [148] L. Ricci, A. Isella, S. Liu, and H. Li. Imaging Planetary Systems in the Act of Forming with the ngVLA. In Eric Murphy, editor, *Science with a Next Generation Very Large Array*, volume 517 of *Astronomical Society of the Pacific Conference Series*, page 147, December 2018.
- [149] D. C. Richardson. Tree Code Simulations of Planetary Rings. *MNRAS*, 269:493, July 1994.
- [150] D. C. Richardson, T. Quinn, J. Stadel, and G. Lake. Direct Large-Scale N-Body Simulations of Planetesimal Dynamics. *Icarus*, 143:45–59, January 2000.
- [151] Viktor Sergeevich Safronov. *Evoliutsiia doplanetnogo oblaka*. 1969.
- [152] Kevin Schawinski, Ce Zhang, Hantian Zhang, Lucas Fowler, and Gokula Krishnan Santhanam. Generative adversarial networks recover features in astrophysical images of galaxies beyond the deconvolution limit. *MNRAS*, 467(1):L110–L114, May 2017.
- [153] A. Shannon, Y. Wu, and Y. Lithwick. Conglomeration of Kilometer-sized Planetesimals. *ApJ*, 801:15, March 2015.
- [154] V. Silva Aguirre, G. R. Davies, S. Basu, J. Christensen-Dalsgaard, O. Creevey, T. S. Metcalfe, T. R. Bedding, L. Casagrande, R. Handberg, M. N. Lund, P. E. Nissen, W. J. Chaplin, D. Huber, A. M. Serenelli, D. Stello, V. Van Eylen, T. L. Campante, Y. Elsworth, R. L. Gilliland, S. Hekker, C. Karoff, S. D. Kawaler, H. Kjeldsen, and M. S. Lundkvist. Ages and fundamental properties of Kepler exoplanet host stars from asteroseismology. *MNRAS*, 452(2):2127–2148, September 2015.
- [155] Jason H. Steffen and Jason A. Hwang. The period ratio distribution of Kepler’s candidate multiplanet systems. *MNRAS*, 448(2):1956–1972, Apr 2015.
- [156] Maryam Tabeshian and Paul A. Wiegert. Detection and Characterization of Extrasolar Planets through Mean-motion Resonances. I. Simulations of Hypothetical Debris Disks. *ApJ*, 818:159, Feb 2016.

- [157] Maryam Tabeshian and Paul A. Wiegert. Applying a Particle-only Model to the HL Tau Disk. *ApJ*, 857:3, Apr 2018.
- [158] Daniel Tamayo, Miles Cranmer, Samuel Hadden, Hanno Rein, Peter Battaglia, Alysa Obertas, Philip J. Armitage, Shirley Ho, David N. Spergel, Christian Gilbertson, Naireen Hussain, Ari Silburt, Daniel Jontof-Hutter, and Kristen Menou. Predicting the long-term stability of compact multiplanet systems. *Proceedings of the National Academy of Science*, 117(31):18194–18205, August 2020.
- [159] Hidekazu Tanaka, Taku Takeuchi, and William R. Ward. Three-Dimensional Interaction between a Planet and an Isothermal Gaseous Disk. I. Corotation and Lindblad Torques and Planet Migration. *ApJ*, 565(2):1257–1274, Feb 2002.
- [160] Scott Tremaine and Subo Dong. The Statistics of Multi-planet Systems. *AJ*, 143(4):94, Apr 2012.
- [161] Tilman Tröster, Cameron Ferguson, Joachim Harnois-Déraps, and Ian G. McCarthy. Painting with baryons: augmenting N-body simulations with gas using deep generative models. *MNRAS*, 487(1):L24–L29, July 2019.
- [162] Vincent Van Eylen and Simon Albrecht. Eccentricity from Transit Photometry: Small Planets in Kepler Multi-planet Systems Have Low Eccentricities. *ApJ*, 808(2):126, Aug 2015.
- [163] Kathryn Volk and Brett Gladman. Consolidating and Crushing Exoplanets: Did It Happen Here? *ApJL*, 806(2):L26, June 2015.
- [164] Spencer C. Wallace and Thomas R. Quinn. N-body simulations of terrestrial planet growth with resonant dynamical friction. *MNRAS*, 489(2):2159–2176, Oct 2019.
- [165] William R. Ward. Protoplanet Migration by Nebula Tides. *Icarus*, 126:261–281, April 1997.
- [166] S. J. Weidenschilling. Aerodynamics of solid bodies in the solar nebula. *MNRAS*, 180:57–70, July 1977.
- [167] S. J. Weidenschilling. Initial sizes of planetesimals and accretion of the asteroids. *Icarus*, 214:671–684, August 2011.
- [168] S. J. Weidenschilling and D. R. Davis. Orbital resonances in the solar nebula: Implications for planetary accretion. *Icarus*, 62(1):16–29, Apr 1985.

- [169] S. J. Weidenschilling, D. Spaute, D. R. Davis, F. Marzari, and K. Ohtsuki. Accretional Evolution of a Planetesimal Swarm. *Icarus*, 128(2):429–455, Aug 1997.
- [170] M. D. Weinberg and N. Katz. The bar-halo interaction - II. Secular evolution and the religion of N-body simulations. *MNRAS*, 375:460–476, February 2007.
- [171] Martin D. Weinberg and Neal Katz. The bar-halo interaction - I. From fundamental dynamics to revised N-body requirements. *MNRAS*, 375(2):425–459, February 2007.
- [172] G. W. Wetherill. An alternative model for the formation of the asteroids. *Icarus*, 100:307–325, December 1992.
- [173] G. W. Wetherill and G. R. Stewart. Accumulation of a swarm of small planetesimals. *Icarus*, 77:330–357, February 1989.
- [174] G. W. Wetherill and G. R. Stewart. Formation of planetary embryos - Effects of fragmentation, low relative velocity, and independent variation of eccentricity and inclination. *Icarus*, 106:190, November 1993.
- [175] F. Windmark, T. Birnstiel, C. Güttler, J. Blum, C. P. Dullemond, and T. Henning. Planetesimal formation by sweep-up: how the bouncing barrier can be beneficial to growth. *A&A*, 540:A73, April 2012.
- [176] O. C. Winter and C. D. Murray. Resonance and chaos. I. First-order interior resonances. *A&A*, 319:290–304, March 1997.
- [177] Jack Wisdom and Matthew Holman. Symplectic maps for the N-body problem. *AJ*, 102:1528–1538, October 1991.
- [178] M. C. Wyatt. Evolution of debris disks. *Annual Review of Astronomy and Astrophysics*, 46:339–383, Sep 2008.
- [179] Lei Xu, Maria Skoularidou, Alfredo Cuesta-Infante, and Kalyan Veeramachaneni. Modeling Tabular data using Conditional GAN. *arXiv e-prints*, page arXiv:1907.00503, June 2019.
- [180] A. N. Youdin and F. H. Shu. Planetesimal Formation by Gravitational Instability. *ApJ*, 580:494–505, November 2002.
- [181] Tiziano Zingales and Ingo P. Waldmann. ExoGAN: Retrieving Exoplanetary Atmospheres Using Deep Convolutional Generative Adversarial Networks. *AJ*, 156(6):268, December 2018.

## Appendix A **WHERE TO FIND THE FILES**

The uwthesis class file, `uwthesis.cls`, contains the parameter settings, macro definitions, and other `TEX`nical commands which allow `LATEX` to format a thesis. The source to the document you are reading, `uwthesis.tex`, contains many formatting examples which you may find useful. The bibliography database, `uwthesis.bib`, contains instructions to BibTeX to create and format the bibliography. You can find the latest of these files on:

- My page.

`https://staff.washington.edu/fox/tex/thesis.shtml`

- CTAN

`http://tug.ctan.org/tex-archive/macros/latex/contrib/uwthesis/`

(not always as up-to-date as my site)

## VITA

Jim Fox is a Software Engineer with IT Infrastructure Division at the University of Washington. His duties do not include maintaining this package. That is rather an avocation which he enjoys as time and circumstance allow.

He welcomes your comments to `fox@uw.edu`.